

Design of superconducting AC machines for hybrid-electric aircraft

Von der KIT-Fakultät für
Elektrotechnik und Informationstechnik
des Karlsruher Instituts für Technologie (KIT)

zur Erlangung
des akademischen Grades eines

Doktors der Ingenieurwissenschaften

genehmigte

Dissertation

vorgelegt von
Master of Science
Matthias Corduan
geboren in Eisenhüttenstadt

Tag der mündlichen Prüfung: 23.11.2020

Referent: Prof. Dr.-Ing. Mathias Noe
Korreferent: Prof. Dr.-Ing. Martin Doppelbauer



This document is licensed under a Creative Commons Attribution-ShareAlike 4.0 International License (CC BY-SA 4.0): <https://creativecommons.org/licenses/by-sa/4.0/deed.en>

Acknowledgment

This thesis was written at the Corporate Technology department of Siemens AG in cooperation with the Institute for Technical Physics (ITEP) at Karlsruhe Institute of Technology. The successful completion of this thesis would not have been achieved without the help of several people. I would like to express my sincere gratitude to all of them.

Firstly, I would like to thank my advisor Dr. Martin Boll for his in-company mentoring and unremitting support anytime. His suggestions for improvement were a priceless help to raise the quality of this work. In addition to his academic guidance, I would also like to express my thanks on a personal level for the off-topic discussions, his positive spirit and social activities.

Special gratitude I would also like to extend to my doctoral supervisor Prof. Dr.-Ing. Mathias Noe for his continuous support and advice to raise the scientific quality of this thesis. I highly appreciated his helpful comments and constructive feedback as well as our technical discussions at our regular meetings.

I would like to thank my second referee Prof. Dr.-Ing. Martin Doppelbauer for the helpful discussions on electric machines, for his interest in my work and for his valuable comments to improve this thesis.

I am very thankful to Dr. Mykhaylo Filipenko for his support during the last years and his profound regular feedback. Special thanks go to Dr. Marijn P. Oomen and Dr. Francesco Grilli for their support and guidance on AC loss calculation of superconducting wires. Moreover, I want to thank Prof. Dr. Bernhard Holzapfel and Dr. Sonja Schlachter for the opportunity of measurements and the supply of equipment. Many measurements could not have been completed without the technical support and persistent help of Quoc Huang Pham and Dr. Mayraluna Lao. I would also like to thank all my colleagues Dr. Lars Kühn, Dr. Jörn Grundmann, Prof. Dr. Tabea Arndt, Roman Bause, Stefan Biser, Mabroor Ahmed, Torsten Müller, Dr. Fabian Utzmann, Dr. Marc Lessmann, Dr. Thomas Gleixner and Dr. Stefan Moldenhauer.

Finally, I would like to express my sincere thanks to my family and friends, especially my parents. Without their permanent support, great encouragement, infinite patience I would not have been able to complete this thesis.

Matthias Corduan
Nuremberg, 09.09.2020

Abstract

The aviation industry is challenged to develop environmentally and economically sustainable propulsion systems to deal with growing air traffic passenger demand and emission reduction goals. Electrification of the propulsion system offers benefits regarding these goals due to novel variable concepts such as hybrid-electric or distributed propulsion. Due to the multiple energy conversion, the propulsion system has to be highly efficient to achieve a fuel consumption benefit compared to a conventional propulsion system. Furthermore, a significantly reduced weight is required to reach the power-to-weight ratio of conventional engines. However, state-of-the-art electric machines are unable to achieve these goals due to their thermal and magnetic limitations. Superconductors are promising to overcome these limitations due to the high current carrying capacity and the negligible direct current (DC) resistance. This thesis investigates superconducting alternating current (AC) machines as a part of a cryogenic hybrid-electric propulsion system. A detailed machine design process is developed, that integrates the interaction between electromagnetics and thermics of the superconductor. Thus, the technical fields of superconductivity, electric machine and aircraft are combined in one tool under consideration of their respective requirements in order to investigate mutual dependencies.

Various machine topologies create a large design space of synchronous radial flux machines and require for exploration fast holistic analytical approaches. In this work, the focus is on the modeling of superconducting coils based on magnesium diboride (MgB_2), which are penetrated by alternating magnetic fields in the stator. A 114 filament MgB_2 wire is characterized and the impact of its AC loss on the current carrying capacity is integrated in the machine design. Moreover, a two-phase flow of hydrogen is implemented for the cooling of MgB_2 coils, which also allows to determine the hydrogen consumption of machines. Hence, the design is subdivided into the analytical electro-thermal model and electromagnetic model. The magnetic flux density distribution is computed in two dimensions with high accuracy in all machine regions and is compared with finite element method. This allows to determine the field sensitive AC loss of the stator coils. The mechanical and thermal support components within the magnetic air gap are adapted and designed according to the machine topology. Both active mass and passive mass from the main structural parts are calculated.

To evaluate the potential of fully and partially superconducting machines, the design of a 21.6 MW machine is performed, which substitutes the core engine and directly powers the conventional fan of an Airbus A321neo-LR engine. These machine topologies based on superconducting as well as normal conducting coils and magnets are compared with each other by optimizing the number of pole pairs, the diameter of the machine as well as the coil and magnet thickness. This also includes the design of a tank for liquid hydrogen, which is integrated four times in the fuselage and stores 280 kg of liquid hydrogen per tank. Furthermore, the range of this aircraft for a specific flight mission is calculated for a selection of optimized machines. In addition, the reduction of stator AC loss by an optimized control strategy of rotor and stator current is studied.

It is shown that the current density of a MgB_2 stator coil at an operating temperature of 20 K is up to 18 times higher compared to a conventional coil based on copper litz wires at 453 K. This leads to the fact that superconducting machines enable both high power-to-weight ratio¹ and low stator AC loss. The lightest fully superconducting machine based on MgB_2 stator coils and high-temperature superconductor (HTS) rotor coils achieves a maximum power-to-weight ratio of 56.8 kW kg^{-1} , which is the lightest machine of all topologies. The most efficient machine of this topology reaches a minimal stator AC loss of 6.4 kW. Partially superconducting machines consisting of MgB_2 stator coils and Halbach rotor array generate even lower stator AC loss of minimal 3.9 kW. Moreover, low loss is required in order to avoid burdening the weight balance of the entire propulsion system by a large liquid hydrogen tank or a heat exchanger, as necessary for copper stators. Hence, a maximum flight time of about 600 min is achieved with one of four liquid hydrogen tanks taking into account the cooling demand of the fan motors, which is higher than the fuel range limit of the hybridized Airbus A321neo-LR. It can be summarized that after reaching a minimum power-to-weight ratio in the machine design in order to fulfill requirements given by the installation space, the optimization of the stator AC loss becomes a priority.

Finally, two design proposals are offered for detailed engineering and manufacturing studies under consideration of economic conditions.

¹The power-to-weight ratio is determined by taking into account the nominal power as well as the active mass and various passive masses of the machine, as described in more detail in Chapter 4.

Zusammenfassung

Die Luftfahrtindustrie steht vor großen Herausforderungen. Die wachsende Anzahl an Passagieren bei gleichzeitiger Reduzierung der Emissionen erfordert die Entwicklung ökologisch und ökonomisch nachhaltiger Antriebssysteme. Die Elektrifizierung des Antriebssystems bietet aufgrund neuartiger variabler Konzepte, wie hybrid-elektrische oder verteilte Antriebe, Vorteile, diese Ziele zu erreichen. Infolge der mehrfachen Energiewandlung muss ein solches Antriebssystem hocheffizient sein, um im Vergleich zu einem konventionellen Triebwerk einen Vorteil im Kraftstoffverbrauch zu erzielen. Weiterhin ist ein deutlich reduziertes Gewicht erforderlich, um das Leistungsgewicht konventioneller Triebwerke zu erlangen. Modernste elektrische Maschinen erreichen diese Ziele aufgrund ihrer thermischen und magnetischen Beschränkungen nicht. Mit Supraleitern können diese Grenzen überwunden werden. Sie zeichnen sich durch eine hohe Stromtragfähigkeit und einen vernachlässigbaren DC Widerstand aus. In dieser Arbeit werden supraleitende AC Maschinen, welche Teil eines kryogenen hybrid-elektrischen Antriebssystems sind, untersucht. Dazu wird ein detaillierter Prozess zum Auslegen einer solchen Maschine entwickelt, der die Wechselwirkungen zwischen Elektromagnetik und Thermik des Supraleiters berücksichtigt. Es werden die technischen Bereiche Supraleitung, elektrische Maschine und Flugzeug unter Berücksichtigung ihrer jeweiligen Anforderungen in einem Tool zusammengefasst, um gegenseitige Abhängigkeiten zu betrachten.

Die Untersuchung mehrerer Maschinentopologien, welche auf synchronen Radialflussmaschinen basieren, eröffnet einen großen Lösungsraum und erfordert schnelle ganzheitliche analytische Lösungsansätze. In dieser Arbeit liegt der Schwerpunkt auf der Modellierung von supraleitenden Statorspulen auf der Basis von Magnesiumdiborid (MgB_2), die von magnetischen Wechselfeldern durchsetzt werden. Dazu wird ein Draht aus MgB_2 mit 114 Filamenten charakterisiert und der Einfluss seiner AC Verluste auf die Stromtragfähigkeit in die Maschinenauslegung integriert. Darüber hinaus wird eine zweiphasige Wasserstoffkühlung für MgB_2 -Spulen implementiert, die es ermöglicht, den Wasserstoffverbrauch der Maschine zu bestimmen. Die Auslegung wird in das analytische elektro-thermische Modell und das elektromagnetische Modell unterteilt. Die zweidimensionale Berechnung der magnetischen Flussdichte erfolgt mit hoher Rechengenauigkeit in allen Maschinenbereichen und wird mit der Finite-Elemente-Methode verglichen. Dadurch lassen sich die feldsensitiven AC Verluste der Statorspulen bestimmen. Die mechanisch und thermisch unterstützenden Strukturen innerhalb des magnetischen Luftspalts werden an die Maschinentopologie angepasst und ausgelegt. Dabei werden sowohl die Aktivmasse als auch die Passivmasse diverser struktureller Komponenten berechnet.

Um das Potential von voll und teilweise supraleitenden Maschinen zu beurteilen, wird eine 21.6 MW Maschine ausgelegt, die das Kerntriebwerk ersetzt und den konventionellen Fan eines Airbus A321neo-LR Triebwerks direkt antreibt. Diese Maschinentopologien, die sowohl auf supraleitenden als auch auf normalleitenden Spulen und Magneten basieren, werden miteinander verglichen, indem die Anzahl der Polpaare, der Durchmesser der Maschine sowie die Spulen- und Magnetdicke optimiert werden. Dazu gehört auch die Auslegung eines Tanks für Flüssigwasserstoff, der vier

Mal in den Rumpf integriert ist und pro Tank 280 kg Flüssigwasserstoff speichert. Des Weiteren wird die Reichweite dieses Flugzeugs, unter Beachtung einer spezifischen Flugmission, für eine Auswahl von optimierten Maschinen berechnet. Eine optimierte Regelstrategie des Rotor- und Statorstromes ermöglicht die Reduzierung der AC Verluste in den MgB_2 -Statorspulen.

Es wird gezeigt, dass die Stromdichte einer MgB_2 -Statorspule bei einer Betriebstemperatur im Bereich von 20 K im Vergleich zu einer konventionellen Spule auf Basis von Kupferlitzen bei 453 K bis zu 18 mal höher ist. Dies führt dazu, dass supraleitende Maschinen sowohl ein hohes Leistungsgewicht¹ als auch geringe AC Verluste im Stator aufweisen. Die leichteste voll supraleitende Maschine, die auf MgB_2 -Statorspulen und HTS-Rotorspulen basiert, erreicht ein maximales Leistungsgewicht von 56.8 kW kg^{-1} und ist damit ebenfalls die leichteste Maschine aller Topologien. Die effizienteste Maschine dieser Topologie erreicht minimale AC Verluste von 6.4 kW im Stator. Teilweise supraleitende Maschinen, die aus MgB_2 -Statorspulen und Halbach-Array im Rotor bestehen, erzeugen noch geringere AC Verluste von minimal 3.9 kW im Stator. Diese geringen Verluste sind erforderlich, um nicht die Gewichtsbilanz des gesamten Antriebssystems durch einen großen Flüssigwasserstofftank oder einen Wärmetauscher zu belasten, wie er bei Kupferstatoren notwendig ist. Mit einem der vier Flüssigwasserstofftanks des hybridisierten Airbus A321neo-LR wird eine maximale Flugzeit von etwa 600 min unter Berücksichtigung des Kühlbedarfs der Fanmotoren erreicht, welche die Reichweite dieses Flugzeuges übersteigt. Zusammenfassend lässt sich in der Maschinenauslegung feststellen, dass nach Erreichen eines minimalen Leistungsgewichtes zur Erfüllung der Anforderungen durch den limitierten Einbauraum die Optimierung der AC Verluste des Stators in den Fokus rückt.

Abschließend werden unter Berücksichtigung von wirtschaftlichen Aspekten Designvorschläge für zwei supraleitende Maschinen erstellt, welche detaillierte Auslegungs- und Fertigungsstudien erlauben.

¹Das Leistungsgewicht wird unter Berücksichtigung der Nennleistung sowie der aktiven Masse und verschiedener passiver Massen der Maschine bestimmt, wie in Kapitel 4 näher beschrieben ist.

Table of Contents

Acknowledgment	I
Abstract	III
Zusammenfassung	V
Table of Contents	VII
1. Introduction	1
1.1. Emission by Aviation	1
1.2. Hybrid-Electric Propulsion System	5
1.2.1. Topologies	5
1.2.2. Cryogenic Hybrid-Electric Propulsion System	7
1.3. Superconductivity	9
1.4. Electric Machine	10
1.4.1. Conventional Machine	10
1.4.2. Superconducting Machine	10
1.5. Basic Idea and Solution Approach	13
1.6. Structure of this Thesis	15
2. Magnesium Diboride	17
2.1. Conductor Manufacturing and Architectures	17
2.2. Critical Parameters	21
2.3. AC Loss	24
2.3.1. Analytical Calculation	26
2.3.2. Finite Element Method	36
2.3.3. Results	40
2.4. Summary and Recommendation	45
3. Electro-Thermal Model of Magnesium Diboride Wires	47
3.1. Properties of Hydrogen	49
3.2. Heat Transfer	50
3.2.1. Single-Phase Flow	50
3.2.2. Two-Phase Flow	52
3.2.3. Feasibility Analysis	53
3.3. Pressure Drop	55
3.3.1. Single-Phase Flow	55
3.3.2. Two-Phase Flow	56
3.4. Temperature Distribution Inside the Wire	56
3.4.1. Analytical Calculation	57
3.4.2. Numerical Calculation	59
3.5. Coupled Model Results of Electromagnetics and Thermal	61
3.5.1. Copper Litz Wire	62
3.5.2. Magnesium Diboride Wire	65

3.6. Summary	68
4. Electromagnetic Machine Design	71
4.1. Introduction	71
4.2. Stator Winding System	74
4.3. Air Gap Design	76
4.3.1. Sleeve	79
4.3.2. Cryo Wall	82
4.4. Excitation Methods	84
4.5. Analytical Field Calculation	89
4.5.1. Field Generated by Coils	89
4.5.2. Field Generated by Magnets	90
4.5.3. Field Generated by Halbach Array	92
4.5.4. Boundary Conditions	93
4.5.5. Validation	94
4.6. Torque Calculation	102
4.6.1. Analytical Calculation	102
4.6.2. Validation	102
4.7. Yoke Design	103
4.8. Summary	105
5. Design of Superconducting Machines for Flight Mission	107
5.1. Fundamental Design Process	107
5.2. Stator Coil Working Point	112
5.3. Stator Coil AC Loss	115
5.4. Maximum Torque per AC Loss	117
5.5. Liquid Hydrogen Tank Model	121
5.5.1. Mechanical Design	124
5.5.2. Thermal Design	124
5.5.3. Parameter Study	126
5.6. Summary	128
6. Design Example for an Airbus A321neo-LR	129
6.1. Turbofan	131
6.2. Hybrid-Electric Propulsion System Overview	133
6.3. Flight Mission and Material Parameters	135
6.4. Topology Comparison	138
6.4.1. Partially Superconducting Machines	142
6.4.2. Fully Superconducting Machines	147
6.5. Influence of Flight Mission	154
6.6. Design Proposal	155
7. Summary, Conclusion and Outlook	161
7.1. Extension Options for Machine Design	164
7.1.1. Stator Coils with Multifilament Coated Superconductor	164
7.1.2. Multi Shell Stator Coils	165
7.2. Next Steps	166

Appendix	167
A. Temperature Distribution by Thermal Conduction	167
B. Detailed Calculation Procedures	169
C. Properties of Various Materials	171
D. Magnetic Field Distributions for Validation	177
E. Derivation of Mean Torque	181
F. Collection of Superconducting Machines from Various Areas	184
List of Figures	187
List of Tables	195
Abbreviations	197
Index of Symbols	199
Bibliography	213

1. Introduction

1.1. Emission by Aviation

Since industrialization, carbon dioxide (CO_2) emissions by humans have increased dramatically and the rising level of CO_2 in the atmosphere leads to social and economic consequences [1, 2, 3].

Figure 1.1a shows the global CO_2 emissions of the most influential sectors in 2018. The power industry has the largest share, followed by other industrial combustion. The transportation sector, including road, aviation and shipping, contribute 18.8% to the total emissions [4]. Among these 6.9 Gt, the aviation sector contributes 797 Mt,

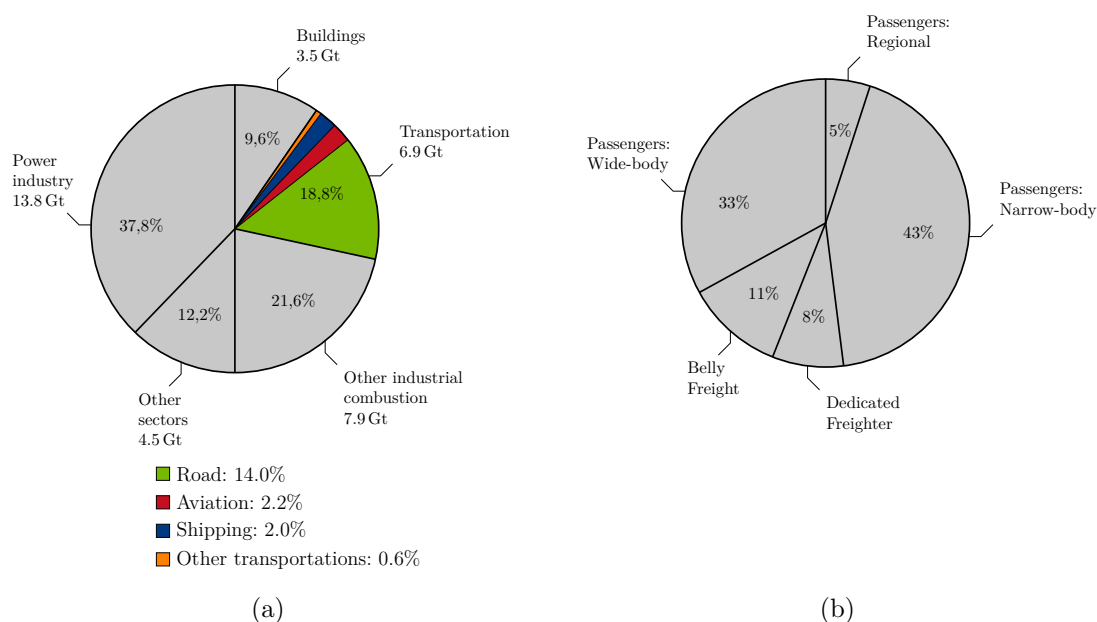


Figure 1.1.: Global annual fossil CO_2 emissions for the year 2018 by:

(a) Main activity sectors [4, 5].

(b) Aviation subdivided into the operations and aircraft class. Adapted from [6].

which is 2.2% of the entire CO_2 emissions. Aviation releases emissions in the atmosphere consisting mainly of CO_2 , nitrogen oxide (NO_x), sulfur oxide (SO_x), water (H_2O) and soot particles [7]. Typical emission levels at the cruise of a long-haul flight are 3160 g of CO_2 , approximately 13.3 g of NO_x , 1 g of SO_x and 1230 g of H_2O per kilogram of jet fuel [8]. Since these emissions mostly occur in altitudes between 8 km – 13 km, they are attributed to have a stronger effect. The formation of ozone is particularly effective in the upper troposphere due to NO_x emissions [9].

An additional emission is noise, which is emitted by the engine and the airframe. Modern aircraft such as the Airbus A320neo reaches a sound pressure level of 85 dB at flyover in the take-off phase with maximum take-off weight, full take-off thrust and at an flyover altitude which is reached after 6500 m from the start of roll [10, 11].

1. Introduction

Carbon dioxide emissions by civil aviation can be divided into their operation in freight and passenger transportation as well as according to their aircraft class, as presented in Figure 1.1b.

The class of passenger aircraft is subdivided into narrow-body, wide-body as well as regional and accounts 81% of CO₂ emissions by civil aviation. The narrow-body aircraft, contributing 43% of the emissions, have a single aisle and typical representatives are the jet-powered aircraft Airbus A320 and Boeing 737 for short- to medium-range operations. In contrast, wide-body aircraft, like the Airbus A350 and A380 or the Boeing 777 and 747, have a larger cabin as well as multiple aisles and is designed for long range operations. [6]

A further comparison of CO₂ emissions by aviation is given by Figure 1.2, where the percentage distribution of total passenger CO₂ emissions and the carbon intensity are shown as a function of the mission length. Approximately one-third of the

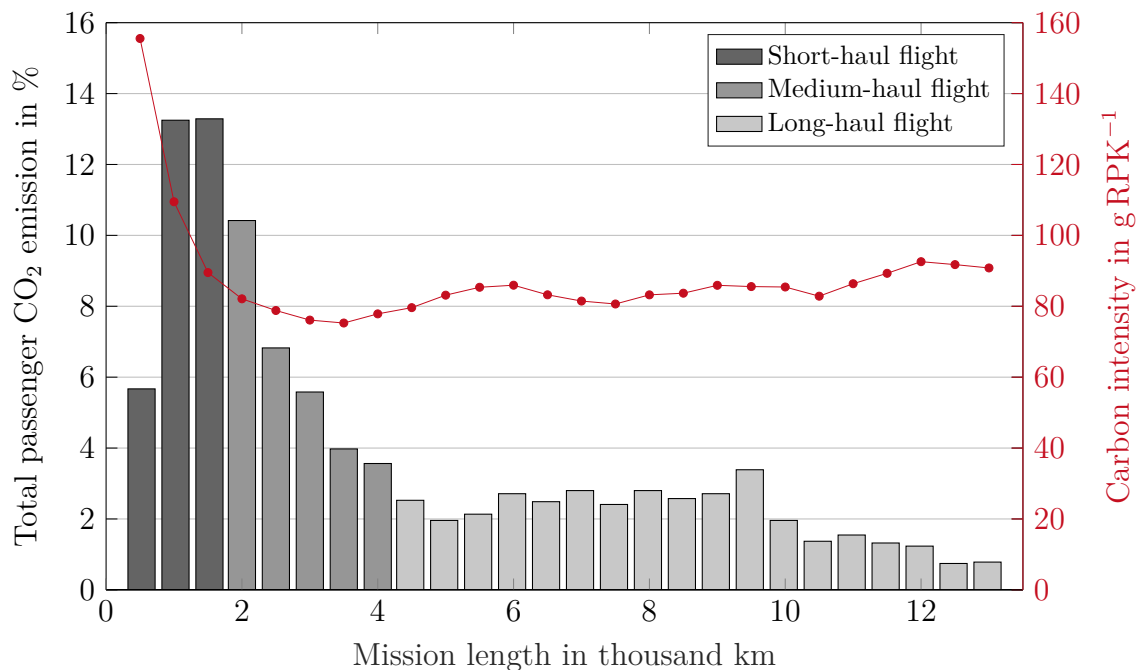


Figure 1.2.: Total passenger CO₂ emission and the carbon intensity as a function of the mission length. Adapted from [6].

passenger CO₂ emissions are emitted on short-haul flights of less than 1500 km. The next third occurs on medium-haul flights of 1500 km–4000 km and the last third is caused by long-haul flights greater than 4000 km. On regional flights less than 500 km, where aircraft compete with other modes of transport, the emissions are less than 6% of total passenger CO₂ emissions. [6]

It is common practice to specify the transport performance by the revenue passenger kilometer (RPK), which is given by the product of the number of passengers and the distance traveled. Figure 1.2 shows further that the carbon intensity of short-haul flights is on average 118 g CO₂ per RPK. This is approximately 40% higher than the average at medium- and long-haul flights with 85 g RPK⁻¹ [6]. On regional flights of 500 km or less the carbon intensity rises up to 155 g RPK⁻¹ [6]. This is due to

the greater influence of the take-off and climb phase at high thrust demand compared to missions with a longer fuel-efficient cruise flight phase at medium thrust demand [12]. Moreover, regional aircraft are operated with less fuel-efficient engines [6]. However, short- and medium-haul flights cause 5–10 times higher CO₂ emissions per RPK compared to high-speed trains with 15 g RPK⁻¹ [13].

Thus, the statistics highlight that there is a high potential for emission reductions, especially for short-haul flights with narrow-body aircraft and routes where no alternative modes of transport are available.

History of CO₂ emissions

The number of passengers traveling by aircraft rises almost every year. This fact is illustrated by the revenue passenger kilometer in dependence of the year from 1978 to 2018 in Figure 1.3. This leads to a continuous increase in CO₂ emissions,

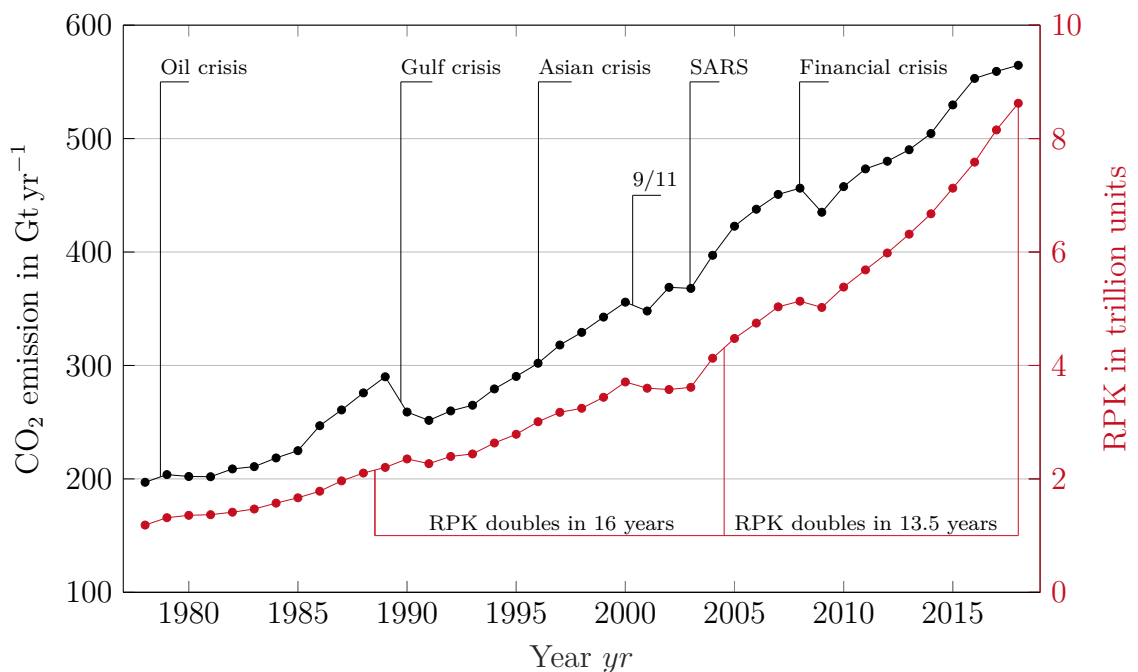


Figure 1.3.: CO₂ emission and revenue passenger kilometer (RPK) as a function of the year yr . Global crises which affecting the aircraft industry are marked at the respective beginning. Adapted from [14] and extended with data from [4].

which is also shown in the figure. In the past 13.5 years the RPKs have doubled to 8.623 trillion RPK in 2018, causing 565 Gt of CO₂ emissions. Even though, global crisis as the Gulf crisis in 1990 or the financial crisis in 2008 lead to a temporal decrease of emissions, they did not interrupt this steady increase on a long term basis and are not expected to do so in the future [14]. In the years from 2016 onwards, a less strong increase in emissions is visible, although the RPKs continue to increase strongly with approximately 6% per year. This can be explained by the launch of larger aircraft and more efficient engines, which effect is overwhelmed and therefore does not lead to a reduction in CO₂ emissions over all.

Forecast of CO₂ emissions

How the CO₂ emissions of the civil aviation will continue in the future is presented in Figure 1.4 for the time period from 2000 to 2050. The emission forecasts FAST-A1

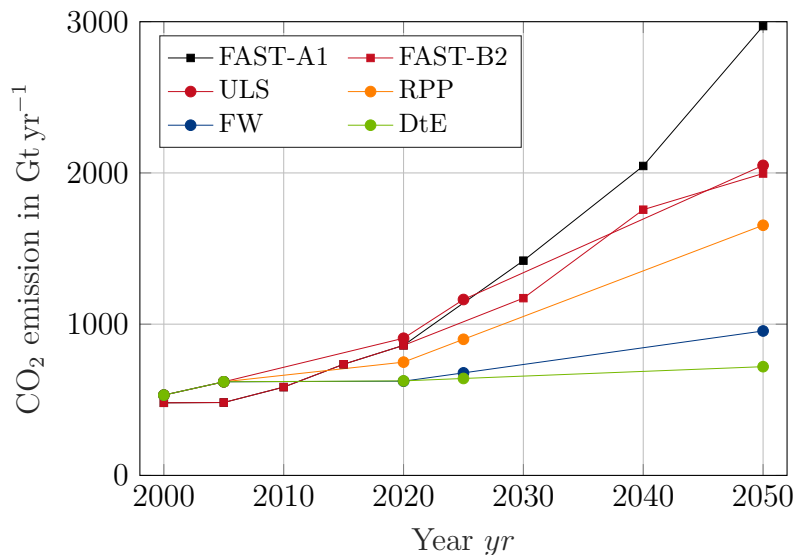


Figure 1.4.: Forecast of CO₂ emission of the civil aviation for the years between 2020 and 2050. Produced with data from [15, 16].

and FAST-B2 are estimated by [15] in 2006 and the forecasts Unlimited Skies (ULS), Regulatory Push & Pull (RPP), Fractured World (FW) and Down to Earth (DtE) are estimated by [16] in 2005. Both approaches take into account different political, economic and technological constraints and forecast emissions of 719 Gt yr⁻¹ up to 2971 Gt yr⁻¹ in 2050. The comparison of the scenarios with the emissions in 2018 shows, that the high emissions from the scenarios FAST-A1, FAST-B2 and ULS have not been achieved. This can be explained by the financial crisis in 2007 and the launch of larger aircraft and more efficient engines.

The Covid-19 epidemic, which started in 2019, is another global crisis that is still continuing and significantly affecting civil aviation and forecasts. This led to a temporary reduction of 80% in the global air traffic in spring 2020 [17]. It is expected that the pre-crisis level and a further increase in air traffic will be reached again after two to six years depending on the course of the pandemic [18].

However, each of these scenarios are standing in contrast to the goal of the European Union to reduce the absolute CO₂ emissions of the aviation sector by 50% until 2050. Moreover, technologies and procedures should be available in 2050 for a reduction in NO_x emission of 90% and perceived noise emission of 65% compared to a typical new aircraft in 2000 [19]. Engine optimizations also pointed out that modifications to reduce NO_x emissions lead to increased fuel consumption. Therefore, a trade-off between CO₂ and NO_x emissions is present [8, 20]. Furthermore, the noise requirements will not be achievable by noise reduction technologies at the level of single components [21, 22]. For this reason, new aircraft technologies and aircraft configurations are necessary to achieve these goals. The most promising approaches for the reduction of CO₂ emission are described in the following.

Technologies to reduce CO₂ emissions

There are several approaches that aim to lower the specific CO₂ emission per revenue passenger kilometer. Firstly, sustainable aviation fuels such as bio-based fuels are obtained from biomass, hydrogenated fats, oils and recycled waste [23]. These bio-based fuels must be certified in order to mix them with conventional fossil-based aviation fuel [23, 24, 25]. Several production pathways certified and blends of bio-based aviation fuel with a low percentage of the total fuel is used on regular flights in the European Union [26, 27].

A further approach is the replacement of the hydraulic and pneumatic subsystems of an aircraft by equivalent electrical components. Such an approach is called a more electric aircraft and the aim is to increase the operational efficiency of the overall aircraft system [28]. Some of these approaches are used in the Boeing 787, resulting in fuel savings of about 3% [29].

The electric taxiing system also belongs to this process of electrification. Currently, the aircraft uses its engines in idle trust to navigate to the runway of the airport, which is inefficient and causes high emissions. These emissions by ground operations can be reduced by using an electric taxiing system, which allows to taxi and pushback. Therefore, an electric motor is installed in the main landing gear, which is powered by the auxiliary power unit that normally generates the energy for non-propulsion functions. The advantage is that this solution is more efficient in the required power range [30]. Due to the additional weight, this system is beneficial for relatively shorter flights and saves fuel in the range of 1%–2% [31].

These electric options for CO₂ reduction consider the subsystems, which offer only low saving potentials, and not the propulsion system, which is the next step in electrification of an aircraft. The current research focus aims at the development of battery-electric and hybrid-electric propulsion systems which replace the conventional engines. However, a technological leap is necessary in the storage of energy in order to enable long range flight with a battery-electric aircraft [32, 33, 34]. For this reason, the hybrid-electric approach is considered in this thesis as the most promising for aircraft above the regional class.

1.2. Hybrid-Electric Propulsion System

1.2.1. Topologies

In a hybrid-electric propulsion system, the propulsion energy is provided by two or more different energy sources. At least one source must generate electrical energy. Therefore, the energy can be provided for example by batteries, solar cells, fuel cells or generators powered by a combustion engine. According to this definition many combinations are possible to create a hybrid-electric propulsion system. Due to the high energy consumption to power an aircraft, the system is limited to the combination of combustion engines, electric machines and batteries as a energy buffer. Fuel cells are currently a focus of research, but their maximum power-to-weight ratio of about 1.6 kW kg^{-1} and efficiencies of less than 60% at medium to high power demand are not jet high enough for narrow-body aircraft [35, 36]. Based on this restriction, three different system topologies are determined in Figure 1.5. In each topology, the distribution of electric energy between motor, generator and battery

is controlled and monitored by the electric power distribution center (EPDC). Firstly, the turbo-electric topology is given in Figure 1.5a with only one energy source. According to the definition above, this variation is not a hybrid-electric

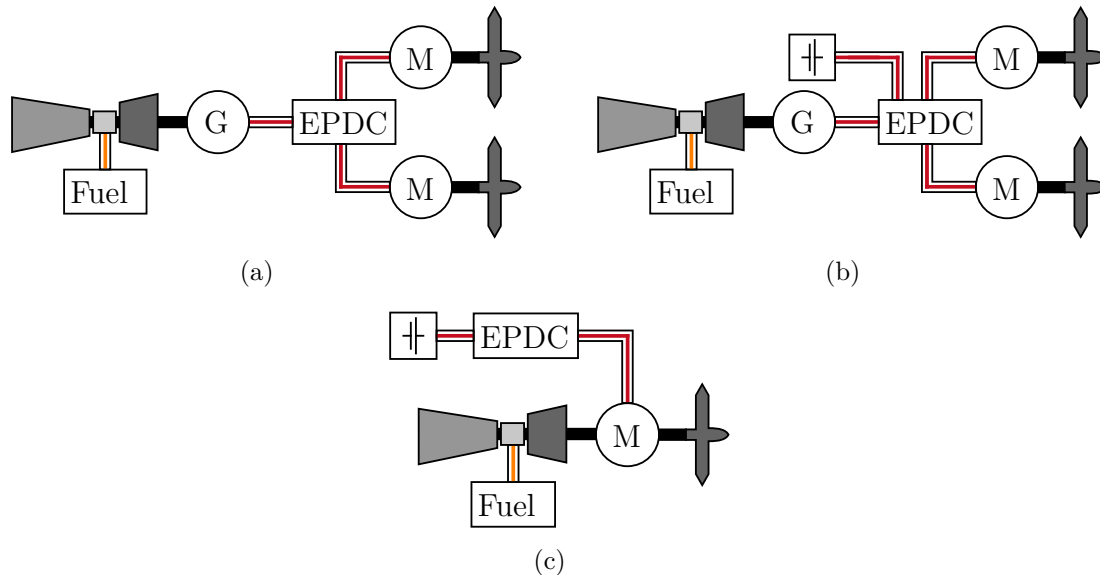


Figure 1.5.: Topologies of hybrid-electric propulsion systems divided into:

- (a) Turbo-electric.
- (b) Serial-hybrid.
- (c) Parallel-hybrid.

Illustrated are the combustion engine, fuel tank, motor (M), generator (G), fan, electric power distribution center (EPDC) and battery.

system, due to the missing second energy source. However, several concepts are developed based on this configuration [37, 38, 39]. Adding a battery leads to the serial-hybrid topology, as shown in Figure 1.5b. The advantage of both serial approaches is that the power generation is completely mechanically decoupled from the electric propulsion. This enables an optimized operation of both components in terms of total efficiency of the propulsion system. The disadvantage is that both components have to be designed for the total propulsion power.

Figure 1.5c presents the parallel-hybrid topology. This approach is based on the fact that both, the electric system and the engine provide propulsion energy simultaneously. The shaft of both components are mechanically coupled, optionally also via a gearbox. The advantage is that the electric propulsion supports the engine and therefore does not have to be designed for the total propulsion power. This offers a high flexibility as investigated in [40, 41]. The disadvantage is that both components cannot be operated independently of each other.

The propulsion units in Figure 1.5, consisting of an electric motor and a fan, can be distributed along each wing, which is known as distributed electric propulsion. This is possible due to the relatively small size and low weight of electric machines, which can be scaled without a significant decrease of efficiency or power-to-weight ratio. This results in an additional degree of freedom in aircraft design and enables

completely novel concepts [42, 43]. In contrast, traditional engines strongly influence the aircraft design due to scaling effects and the large size and weight of turbines. With such hybrid systems the advantages of all technologies can be used simultaneously. The energy density of a conventional engine with a turbine is very high due to the huge energy density of the jet fuel, as shown in Table 5.3. However, these engines have a lower efficiency when they do not operate in their optimum operating point. This disadvantage can be compensated by the electric machine, which has a high efficiency over the entire performance range. The fuel consumption and the emissions of such a system are reduced because the engine almost always operates at its most efficient operating point and surplus energy is stored for example in a battery or is used for other loads [44]. Further advantages of such a system are that the heat signature of the aircraft is reduced and almost all noise emissions of the propulsion system are eliminated with the exception of the propeller or fan noise.

Two aspects are particularly critical in a hybrid-electric propulsion system. Firstly, the power-to-weight ratio of the entire propulsion system must be on the level of a conventional propulsion system. Therefore, a power-to-weight ratio of about 7 kW kg^{-1} has to be achieved compared to the jet engine of an Airbus A320neo [45]. This ensures that a hybrid-electric aircraft can be operated economic with the same payload compared to conventional aircraft. Secondly, the loss of the entire propulsion system must be very low in order to efficiently remove the energy loss from a system of several mega watt [46]. The required cooling systems would be very heavy and reduce the power-to-weight ratio of the system. These requirements can generally not be achieved by conventional propulsion systems with a maximum efficiency of about 95%, for example as designed for electric trains or battery electric vehicles [47]. This is due to the fact that optimum power-to-weight ratio and optimum efficiency cannot be reached simultaneously in the design process.

A further challenge is given by the present voltage levels at aircraft, which are typically designed so that no possibility of electrical discharge can occur due to Paschen's law across an air gap at typical flight altitude. This results in a maximum voltage of 327 V DC and 231 V AC and improves safety and simplifies the electric system [48]. However, it is not designed to transmit high levels of electrical power. To prevent an increase in the voltage drop and conductor size as well as weight a voltage increase while avoiding electrical discharges is necessary [49, 50]. First more electric aircraft are designed with a voltage level of 540 V DC [51].

Superconductivity has the potential to overcome these limitations and the application of this technology as superconducting propulsion system is presented in the following section.

1.2.2. Cryogenic Hybrid-Electric Propulsion System

A cryogenic hybrid-electric propulsion system consists of superconducting and cryogenic-cooled components, as shown in Figure 1.6. Liquid hydrogen (LH_2) is used as coolant, which is stored in tanks in the fuselage of the aircraft. Furthermore, this is a serial concept in which the thrust is produced by two electric propulsion units (EPU) and they are mainly energized by two power generation units (PGU). Each electric propulsion unit contains a fan that is driven by a superconducting machine powered by an inverter unit. These units convert the DC voltage that is

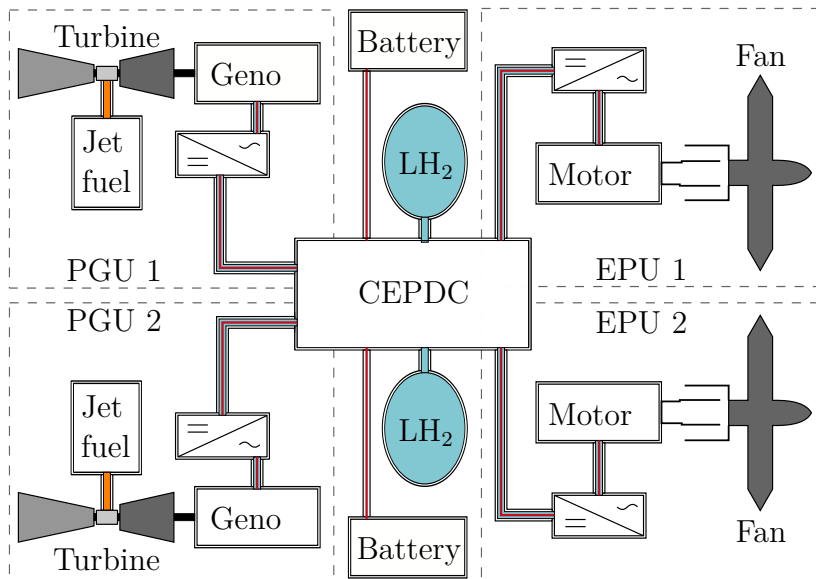


Figure 1.6.: Cryogenic hybrid-electric propulsion system consists of the subsystems cryogenic electric power distribution center (CEPDC), power generation unit (PGU) and electric propulsion unit (EPU). All electrical components and the transmission lines are cooled with liquid hydrogen (LH_2) except the batteries. Adapted from [52].

provided by superconducting DC transmission lines into AC voltage feeding the AC machines. Optionally, machine and fan can also be connected via a gearbox. This allows both components to be optimized regarding their optimum rotational speed independently of each other. All units are connected by the cryogenic electric power distribution center (CEPDC) as the head of this architecture. The cooling medium is distributed via this unit to the electric machines, the inverter units and the cables. The turbine as part of the power generation units are mainly supplied with jet fuel but are also able to burn hydrogen after it has been used to cool the components of the electric propulsion system. One superconducting generator per engine produces the required electric power, which is afterwards converted into DC voltage by the inverter unit [52]. In addition, power is provided by batteries in order to compensate peak power.

This concept allows a flexible arrangement of electric propulsion unit, power generation unit and cryogenic electric power distribution center, keeping the system simple. Additionally, the number of electric propulsion units and power generation units can also be further increased to improve the reliability by distributed propulsion. The disadvantage is that at least three rotating components are required and the electric propulsion unit has to be designed for maximum power.

Due to the high current carrying capabilities of superconductors, components such as electric machines and cables can be designed much lighter. Additionally, the voltage level can be reduced in order to transfer the same electric power. In this thesis the focus is on the design of electric machines in this system in combination with cooling by liquid hydrogen. The effect of superconductivity and its technical application in electric machines is explained in more detail in the following sections.

1.3. Superconductivity

Superconductivity as a physical phenomenon has been known since 1911 and is generally characterized by a vanishing direct current electrical resistance and an ideal diamagnetic behavior which excludes the interior magnetic field of the superconductors [53, 54].

The temperature at which the transition from the normal conducting state to the superconducting state as well as from the superconducting state to the normal conducting state occurs is defined as the critical temperature T_c and is reached under normal conditions at cryogenic temperatures. Figure 1.7 presents the critical temperature and the year of discovery of several superconducting elements and compounds. Furthermore, the boiling temperature of the cooling liquids helium, hydro-

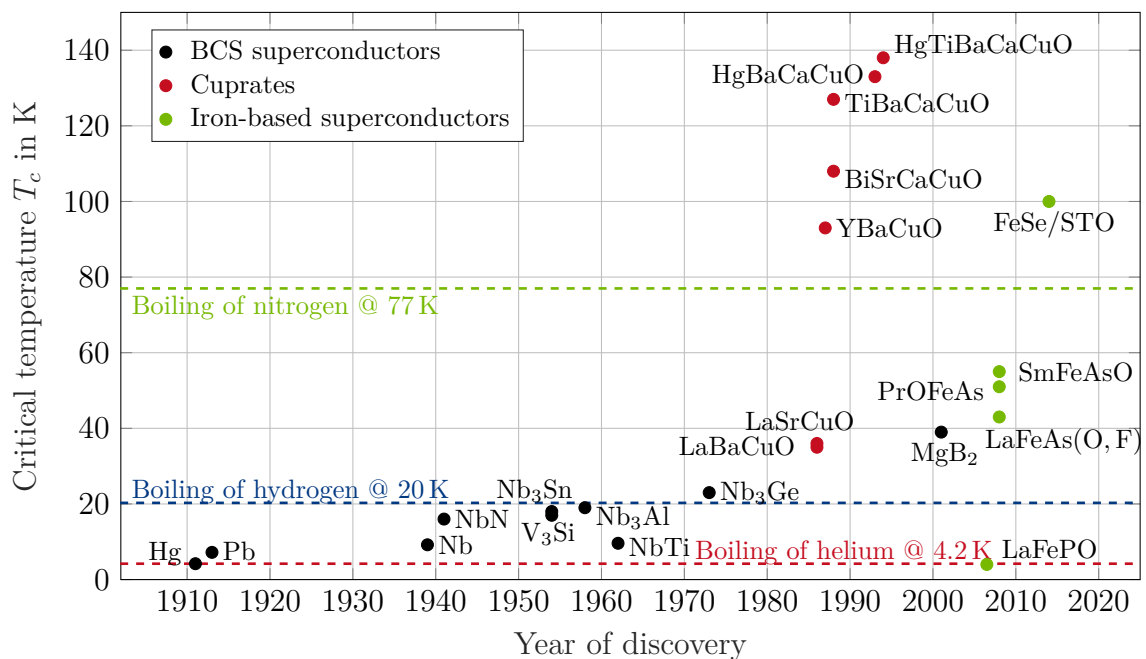


Figure 1.7.: Critical temperature T_c and the year of discovery for several superconducting compounds. It is distinguished between bardeen-cooper-schrieffer (BCS) superconductors, cuprates, iron-based superconductors and the boiling points of some cooling liquids are marked. Adapted from [55] and [56].

gen and nitrogen are marked. It is divided between BCS superconductors named on the Bardeen-Cooper-Schrieffer theory, cuprates and iron-based superconductors. A further distinction can be made according to the critical temperature in high-temperature superconductor (HTS) and low-temperature superconductor (LTS). The copper oxide compounds are the main representatives of HTS, which typically have a critical temperature above the boiling point of nitrogen at 77.35 K. The first stable compound discovered above this temperature was $\text{YBa}_2\text{Cu}_3\text{O}_{7-x}$ (YBCO). The rare earth element yttrium (Y) can be substituted by other rare earth elements such as dysprosium, gadolinium or samarium and is then named rare-earth barium copper oxide (REBCO) [57]. The compound with the currently highest critical tem-

perature is $\text{HgTiBa}_2\text{Ca}_2\text{Cu}_3\text{O}_8$ with 138 K [58]. Another important representative of HTS for technical applications is $\text{Bi}_2\text{Sr}_2\text{CaCu}_2\text{O}_y$ or $\text{Bi}_2\text{Sr}_2\text{Ca}_2\text{Cu}_3\text{O}_y$ (BSCCO) with a critical temperature of 108 K.

The critical temperature of LTS is typically below 23 K, because until 1986 all discovered superconductors had their critical temperature below this temperature. However, this value is historically determined and does not represent a fixed distinction. An important representative for technical applications especially in the health technology are Nb_3Sn and NbTi with a critical temperature of 18 K and 9.6 K, respectively. These applications are cooled by liquid helium (LHe) which has its boiling point at 4.2 K. In 2001, the compound MgB_2 was discovered with a critical temperature of 39 K which is also a member of LTS.

The first iron-based superconductors were discovered in 2006 and are currently of scientific interest and not relevant for technical applications.

HTS materials generally have significant advantages compared to LTS materials, because they can be cooled at economically and commercially feasible temperatures due to the decreasing efficiency of cryocoolers with decreasing temperature [59]. This fact can significantly reduce the efficiency of technical applications. However, they are used in technical applications such as medical diagnostic tools and superconducting machines.

1.4. Electric Machine

1.4.1. Conventional Machine

The basic property of electric machines is that the torque is proportional to the product of the stator current per circumferential length and the flux density in the air gap. Therefore, this product has to be maximized for light machines. However, this approach is limited both thermally and magnetically in a conventional machine design. This means that the current density in the windings is limited due to their ohmic loss which has to be removed by cooling. Liquid cooling is one option for an effective removal of this loss, resulting in a maximum current densities of about 10 A mm^{-2} for well-designed standard electric machines with copper windings [60]. This effect also limits the maximum flux density in the air gap of approximately 1 T for machines with rotor excitation windings [61]. This value is similar for excitations with permanent magnets due to their limited remanence and coersivity. Furthermore, the saturation flux density of conventional ferromagnetic sheets reaches about 2 T. This restricts the flux density in the iron teeth of the machine.

Thus, the material selection has a significant influence on the design and power-to-weight ratios of around 10 kW kg^{-1} have already been achieved in the design of normal conducting machines [62]. However, higher power-to-weight ratios and above all lower power losses are required. Superconductivity is expected to be a key enabling technology to solving this trade-off between current density and power loss.

1.4.2. Superconducting Machine

Superconducting machines have been developed mainly for applications in mobility and power generation with a power greater than 1 MW. Figure 1.8 presents machines

from the areas marine, wind, utility and aerospace in dependence of the power P and the rotational speed n . Additionally, the development status of the machines is divided into concepts and demonstrators.

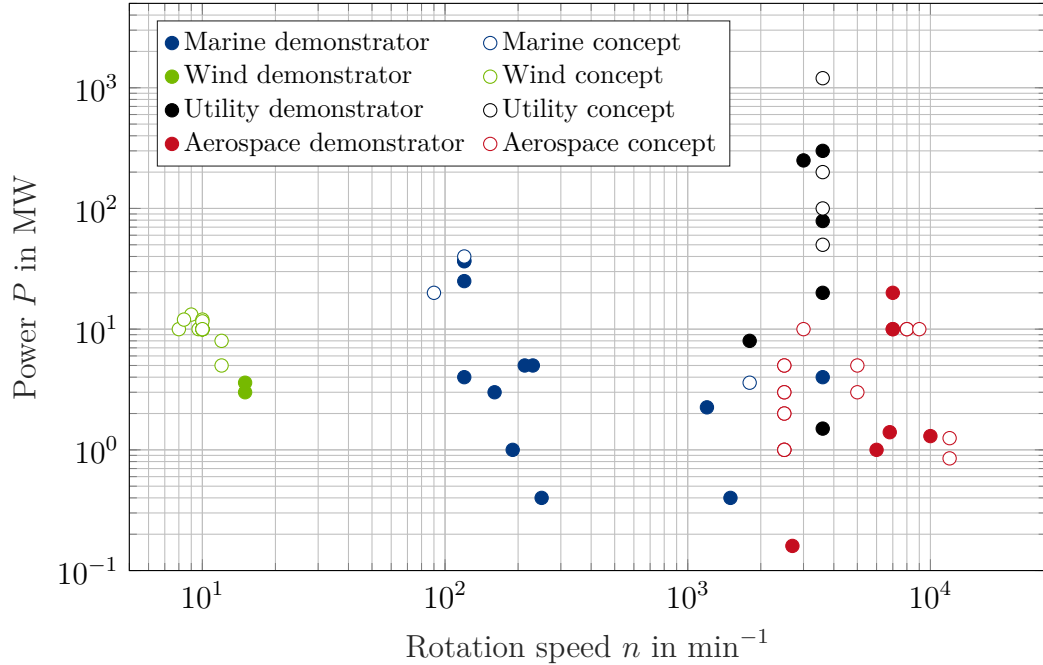


Figure 1.8.: Power P as a function of the rotational speed n of superconducting machines from the areas marine, wind, utility and aerospace which are divided into the development stages concept and demonstrator. The data are summarized in Table 1.1 as well as in the Appendix in Table F.1, F.2 and F.3.

Superconducting machines for wind turbines operate in the rotational speed range around 10 min^{-1} and powers around 10 MW as direct drives. The key parameters such as power-to-weight ratio, efficiency, superconducting material and operation temperature of these machines are listed in the Appendix in Table F.1. Both LTS with NbTi and MgB₂ as well as HTS with YBCO and BSCCO have been investigated and realized as generators since 2007.

The identical superconductors can also be found in machines for marine propulsion systems as direct drive with around 120 min^{-1} . Furthermore, the first demonstrator was developed with NbTi in 1983 [63]. The key parameters of all further machines which are mainly based on HTS are summarized in the Appendix in Table F.3.

Machines for utility are operating typically at the line frequency of 50 Hz or 60 Hz which corresponds to a rotational speed of 3000 min^{-1} or 3600 min^{-1} for one pole pair. The power range is very wide and extends from a few MW to the GW range, as listed in the Appendix in Table F.2. Due to the high power and continuous operation in power plants, superconductors can be used particularly economically. This can also be seen from the early application in several demonstrators with NbTi from 1978 onwards.

High rotational speeds are required for aviation applications, for example to further

increase the power-to-weight ratio or to couple the machine directly to a turbofan. The power ranges are in the single-digit and lower two-digit MW range, as listed in Table 1.1. The first LTS demonstrator was built in 1980 and since 2017 many more demonstrators and concepts have been launched. This is due to the necessity to reduce the fossil CO₂ emissions in civil aviation, as described in Section 1.1. It can be concluded that in the last few years, the majority of superconducting machine demonstrators and concepts were designed with HTS, due to the more economic cooling. Additionally, some machines with MgB₂ are also present. In nearly all presented areas, the superconducting machine has not progressed beyond the status of a demonstrator. This can change in the aviation area, because the technical solution alternatives are more limited than in the other areas.

Table 1.1.: Main properties of the superconducting machines for aerospace application corresponding to Figure 1.8.

Year	Power ¹	Speed ²	PTW ³	Efficiency ⁴	SC	Temp. ⁵	Source
1980	20	7000	0.06	99.5	NbTi\Nb3Sn	4	[64]
2008	1.3	10000	8.8	98.0	BSCCO	30	[65]
2009	0.16	2700	5.3	–	YBCO\BSCCO	30	[66]
2017	1	2500	11.5	–	REBCO	–	[67]
2017	1	2500	14.5	–	REBCO	–	[67]
2017	1	2500	18.2	–	REBCO	–	[67]
2017	2	2500	18.6	–	REBCO	–	[67]
2017	2	2500	24.1	–	REBCO	–	[67]
2017	3	2500	21.4	–	REBCO	–	[67]
2017	3	2500	31.9	–	REBCO	–	[67]
2017	5	2500	23.1	–	REBCO	–	[67]
2017	5	2500	37.0	–	REBCO	–	[67]
2017	10	7000	–	–	MgB ₂	20	[68]
2017	10	8000	–	81.9	MgB ₂	20	[69]
2017	10	8000	–	99.8	Nb ₃ Sn	4	[69]
2018	0.85	12000	11.7	–	MgB ₂	20	[70]
2018	1.25	12000	6.5	–	MgB ₂	20	[70]
2018	1.4	6800	17.4	98.9	YBCO	63	[71]
2019	1	6000	20.0	99.0	YBCO	25	[72, 73, 74]
2019	3	5000	19.4	–	YBCO\MgB ₂	20	[75]
2019	5	5000	25.2	–	YBCO\MgB ₂	20	[75]
2019	10	3000	25.0	–	Nb ₃ Sn	–	[76]
2019	10	7000	20.0	98.0	YBCO	30	[77]
2019	10	9000	25.6	99.3	REBCO	20	[78]

¹ in MW

² in min⁻¹

³ in kW kg⁻¹

⁴ in %

⁵ in K

1.5. Basic Idea and Solution Approach

Most of the listed and presented superconducting machines in the section before are synchronous machines and their improved performance characteristics are based on increasing the excitation flux density due to the high current carrying capabilities of superconductors under DC conditions. This is based on the fact that the torque of an electric machine is proportional to the product of the stator current per circumferential length and the flux density in the air gap. Therefore, superconducting coils are integrated in the rotor and the stator is equipped with conventional copper (Cu) coils. Such a topology is shown in Figure 1.9a with an air gap stator winding and is defined as partially superconducting rotor machine. Due to the high flux density generated by the rotor coils, it is advantageous to design such machines without stator teeth to avoid high saturation of the iron. Detailed machine concept designs

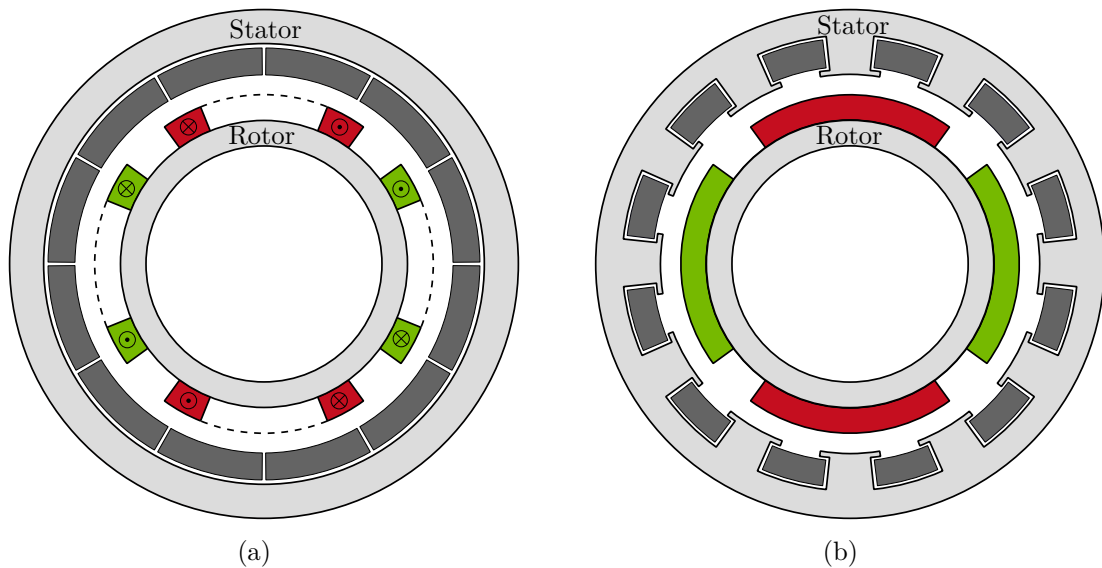


Figure 1.9.: Minimal sketch of radial flux synchronous machines with:
 (a) Air gap stator winding of copper and superconducting rotor coil.
 (b) Slotted superconducting stator and permanent magnet rotor.

including verification of specific components have already been realized and show that a maximum power-to-weight ratio of about 20 kW kg^{-1} can be achieved with this topology at high rotational speeds around 7000 min^{-1} [71, 77]. However, it is necessary to achieve even higher power-to-weight ratios to meet the power-to-weight requirement for the entire system and this also in cases of lower rotational speeds. This approach offers less potential because it is limited due to the saturation of the iron yoke and the copper loss in the stator windings.

Another topology is the partially superconducting stator machine with superconducting coils in the stator and normal conducting coils or permanent magnets (PM) in the rotor, as shown in Figure 1.9b. However, in this configuration the superconductors would be exposed to a rotating magnetic field and have to carry an alternating current. This leads to AC loss and explains why in the past superconductors were used mainly in machines with DC excitation. It is essential to consider the influence

of AC loss on the current carrying capacity of the superconductor in the design of such machines. Therefore, conductors with high transport properties and low AC losses are required. A superconducting stator can also be combined with a superconducting rotor, which is called a fully superconducting machine.

Magnesium diboride (MgB_2) is a candidate for a machine with superconducting stator coils because good transport properties at moderate magnetic fields up to 4 T are demonstrated with lower cost, wide availability of raw materials and improved mechanical stability compared to coated high-temperature superconductors [79, 80, 81, 82]. However, the price target of $1 \text{ € kA}^{-1} \text{ m}^{-1}$, which is cheaper than a copper wire, has not yet been achieved [83]. The higher current-carrying capacity of HTS tapes compared to MgB_2 wires at identical temperature and magnetic field cannot compensate the higher AC loss in alternating fields and would lead to an uneconomical high cooling effort, which is particularly disadvantageous in an aircraft application [84]. Magnesium diboride wires are beneficial compared to conventional LTS wires due to the higher temperature operation range and an increased stability [85]. Moreover, MgB_2 wires are characterized by low AC loss, explained by the manufacturing of thin MgB_2 filaments with a radius of a few micrometers. Many filaments are twisted and combined by a metallic matrix to a round wire [86, 87]. Furthermore, MgB_2 enables the production of conductors in kilometer length, which is essential for the development of many commercial applications. The critical temperature of MgB_2 is 39 K and allows cooling with liquid hydrogen. This combination is promising for hybrid-electric aircraft when using the hydrogen for cooling and as a source to generate electric energy. Thus, the cooling capacity is already on board and does not need to be generated. Therefore the disadvantage of less economical cooling due to the lower critical temperature compared to HTS is compensated.

This thesis discusses the design of electric machines with MgB_2 stator windings. The influence of the AC loss generated by the superconductor in alternating magnetic fields is considered in the machine design process. The heating of the coils during two-phase cooling with liquid hydrogen is calculated by taking into account varying fields, frequencies and currents. In the stator design, an air gap winding is regarded as more promising than a slotted stator, because the stator teeth are saturated due to the high magnetic fields. The superconducting stator is combined with different rotor topologies, which allows the investigation of both partially and fully superconducting machines. This includes superconducting coils, superconducting bulks, permanent magnets and Halbach array as custom design of permanent magnets.

The models are variable and characterized by a reasonable simulation time due to the holistic analytical design approach. Furthermore, the comparison of different machine topologies and the investigation of parameter studies are enabled. This is an advantage compared to an approach based on the finite element method (FEM), where the design of superconducting machines has to be solved as a complex multi-physics problem with a high computational effort.

The machine model is applied in a case study that aims to retrofit a state of the art single aisle aircraft with a hybrid-electric propulsion system. The core engine is replaced by a superconducting machine and propels directly the fan. Finally, a design proposal for the most promising superconducting machine topologies is made.

1.6. Structure of this Thesis

In order to investigate the above mentioned topics, mainly three different disciplines need to be considered. These are superconductivity, electric machine and hybrid-electric aircraft, as illustrated in Figure 1.10.

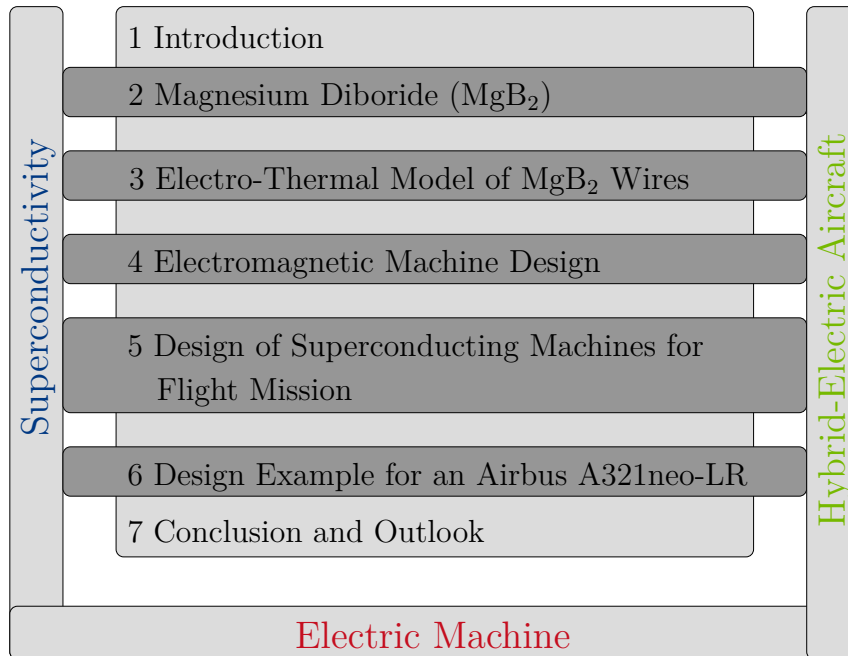


Figure 1.10.: Content of this thesis which is surrounded by the main topics superconductivity, electric machine and hybrid-electric aircraft.

Furthermore, the thesis is structured in five main chapters, which include the theoretical fundamentals of these technical fields up to the calculation and discussion of a specific use case. The content of these main chapters is introduced in the following.

Content of main chapters

In Chapter 2, MgB_2 is presented as superconductor for technical applications and its critical properties are discussed. For this reason the critical current of a MgB_2 multifilament wire is measured under varying temperature and external magnetic flux density penetrating the wire. This provides the basis for implementing a model to calculate the AC loss components in the different materials of the wire with a combination of analytical formulas and finite element method.

Chapter 3 describes the analytical calculation of a two-phase flow to cool multifilament wires and coils of these wires. A thermal model is developed from this knowledge, which separates between the heat transfer, the temperature distribution inside the wire and the pressure drop. Since hydrogen is used as the cooling medium, its thermal properties are discussed in detail. Subsequently, both models, the AC loss model and the thermal model, are combined to the electro-thermal model. For comparison reasons, a single-phase flow cooling model is implemented, in order to compare a two-phase cooled MgB_2 wire with liquid hydrogen and a state-of-the-art single-phase cooled Cu wire with a synthetic oil regarding their maximum current

density.

In Chapter 4, a machine model has been created for radial flux synchronous machines with air gap windings. Different machine topologies are defined which are divided into partial and fully superconducting machines. Both superconducting and normal conducting coils, superconducting bulks as well as permanent magnets are calculated. Analytical equations are used to determine the magnetic flux density distribution in the entire machine, except the stator yoke. The thickness of the magnetic air gap is calculated model internally, taking into account mechanical and thermal functionalities. This includes the calculation of the thickness of the sleeve, which fixes the magnets or coils on the rotor by a press fit, and the thickness of the cryogenic walls, which separate different temperature areas. In addition, the thickness of the yoke is designed and its loss is determined. By calculating the passive and active mass of the main components of the machine as well as the torque, the power-to-weight ratio is determined.

Chapter 5 presents the fundamental design process of superconducting machines for hybrid-electric aircraft under consideration of a flight mission. This includes how the working point of the stator coils is adjusted and the determination of the total AC loss in stator coils. Additionally, the AC loss minimization with optimized control strategies is also being investigated. In order to consider the influence of the flight mission on the machine design, a liquid hydrogen tank model is introduced, which takes into account the thermal and mechanical effects.

In Chapter 6, the results for a machine design for an Airbus A321neo-LR are presented and the hybridization approach of this aircraft is explained in detail. Furthermore, the machine topologies are compared under consideration of all boundary conditions and a design proposal is presented.

Finally, the thesis is completed with a summary and an outlook in which the next development steps and possible extensions of the models are described.

In order to provide the reader with all necessary information to reproduce the presented results the appendix contains further explanations and data.

2. Magnesium Diboride

Magnesium diboride (MgB_2) is a type-II superconductor and was discovered in the year 2001 [88]. Bulks, wires and thin films are promising for many applications in energy technology. This thesis utilizes wires which are available commercially [85].

2.1. Conductor Manufacturing and Architectures

Magnesium diboride wires are basically divided into monofilament and multifilament wires. Both architectures have advantages and disadvantages, especially in their electromagnetic, thermal and mechanical properties. The manufacturing process also influences the wire properties, as described in the following [89].

Powder in Tube

One very popular method for achieving good quality MgB_2 wires is the powder in tube (PIT) method. Various pure metallic or alloy tubes are filled with precursor powder in this process [85, 90, 91, 92, 93, 94]. The tube material is chosen by their common workability, different hardness and tensile strength properties. Further criteria are the thermal conductivity and bonding as well as the specific resistance of the material. The powder is packed inside the tube by pressing with a steel piston. Furthermore, doping the powder with silicon carbide (SiC) or carbon (C) leads to higher critical current densities [89]. In the subsequent deformation process by rolling and drawing, monofilament wires are manufactured. These wires can be combined in a metallic matrix to form a multifilament wire, followed by further deformation until the desired dimensions are reached. Afterwards, a heat treatment in vacuum or oxygen protective atmosphere is applied to the wire. The powder in tube method can be performed by either an ex-situ or in-situ process.

In the ex-situ process, the tube is filled with pre-reacted MgB_2 and sintered at around 950°C [95]. In contrast, in the in-situ process a stoichiometric mixture of magnesium (Mg) and boron (B) powder is sintered at a temperature around 650°C , which is approximately the melting point of magnesium. This process results in a volume reduction and thus the powder in tube method is distinguished by high superconductor porosity and lower current carrying capability compared to the internal magnesium diffusion process, as presented in the next section [96].

Internal Magnesium Diffusion

The fabrication of wires with the internal magnesium diffusion (IMD) process was successfully carried out by [97] and [98]. In this process, the starting materials are a pure magnesium rod which is positioned in the centre of a metal tube and the gap between rod and tube is filled with boron powder or a powder mixture. Subsequently, the filled powder is packed by pressing with a steel tube. This starting billet is rod rolled, swaged and drawn alternately until the final outer diameter is reached. During heat treatment at a temperature of 650°C , the magnesium diffuses into the boron powder. At higher reaction temperatures, a decrease of the critical current density must be expected for silicon carbide doped wires [97]. A high density MgB_2 of higher phase purity is achieved, compared with the powder in tube method. Furthermore,

the porosity in the MgB_2 layer is much smaller compared to powder in tube processed wires [89]. The diffusion reaction results in a circular MgB_2 layer with a hole at the place where the magnesium rod was [96].

However, wires manufactured with the internal magnesium diffusion process are not commercially available, therefore only powder in tube manufactured wires are considered in this thesis.

Properties of two commercially available multifilament wires

Two low AC loss multifilamentary wires are investigated in this thesis which are manufactured by the in-situ PIT process by Hyper Tech Research. The first is a 114 filament wire (114F) and the second is a 54 filament wire (54F) shown in Figure 2.1a and 2.2a, respectively. Moreover, the adapted geometry of both wires is shown in Figure 2.1b and 2.2b which are used later in FEM calculations.

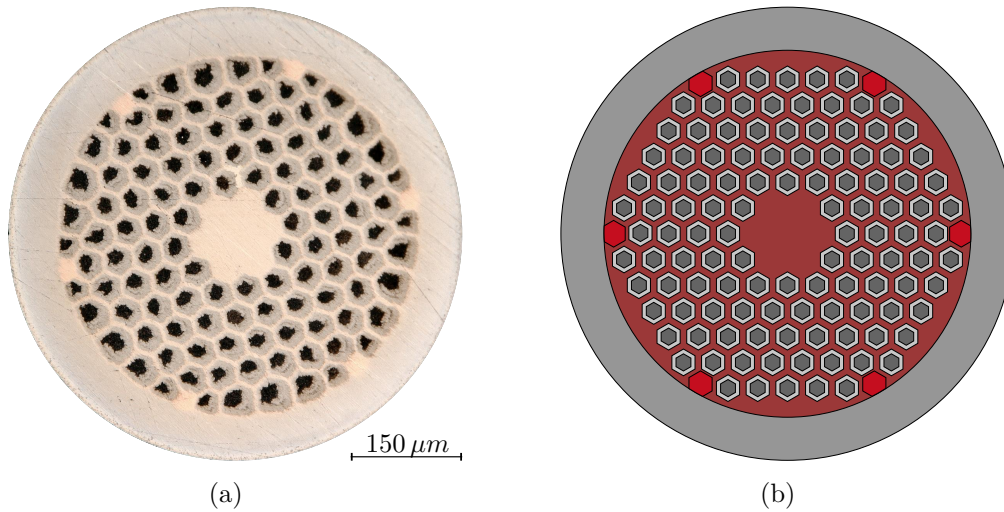


Figure 2.1.: Cross section of the 114 filament MgB_2 wire according to Table 2.1 shown as:

(a) Microscopic image.

(b) Adapted geometry for FEM simulations.

MgB_2 ■, Nb barrier □, Cu10Ni matrix ■, Cu interfilaments ■ and Cu30Ni outer sheath ■ are marked.

The 114 filament wire has a filament diameter of $20 \mu\text{m}$ and the filaments are surrounded by niobium (Nb) which is used as diffusion barrier. Furthermore, the matrix and the central core are manufactured with Cu10Ni and the outer sheath is made of Cu30Ni to improve the mechanical strength. The Nb barrier avoids reactions of the MgB_2 powder with the cupronickel matrix. The outermost filament ring includes 6 Cu interfilaments to provide electrical and thermal protection for the superconducting wire in the event of a sudden loss of superconductivity. In total, the wire has a diameter of $610 \mu\text{m}$ and was delivered already reacted.

The 54 filament wire has a similar design to the 114 filament wire. The filaments, with a diameter of $13 \mu\text{m}$, are coated with Nb and embedded in a Cu10Ni matrix. Copper interfilaments are not present and the wire diameter is $290 \mu\text{m}$. Further ge-

ometric and material properties, such as the volumetric mass density, the electrical resistivity and the thermal conductivity, of the two wires are summarized in Table 2.1 and 2.2, respectively. Magnesium diboride is about four times lighter than copper but due to the low fill factor in the wires, this has only a marginal effect on the total density of the MgB_2 wires compared to a copper wire. In contrast to the 114 filament wire, this wire was delivered unreacted, which makes a heat treatment necessary. This process is described in the following section.

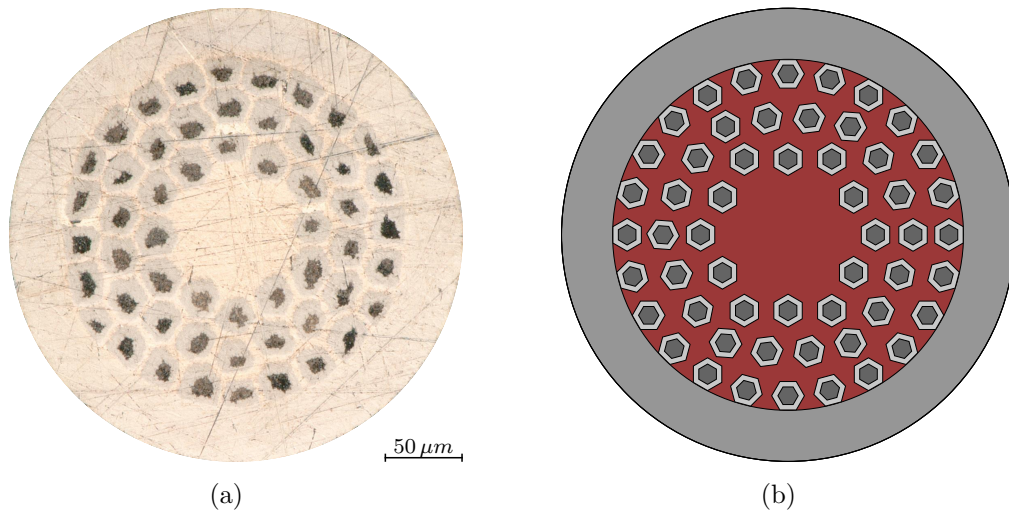


Figure 2.2.: Cross section of the 54 filament MgB_2 wire according to Table 2.1 shown as:

(a) Microscopic image.

(b) Adapted geometry for FEM simulations.

MgB_2 ■, Nb barrier □, Cu10Ni matrix ■ and Cu30Ni outer sheath ■ are marked.

Table 2.1.: Geometric properties of the 54 filament (54F) and 114 filament (114F) MgB_2 wire.

Property	Unit	54F	114F
Wire diameter	μm	290	610
Filament diameter	μm	$10^1, 13^2$	20
Number of SC filaments	-	54	114
Number of NC filaments	-	-	6
Fill factor with MgB_2	-	0.11	0.135
Thickness of outer sheath	μm	35	65
Thickness of barrier	μm	7.5	12
Twist pitch	mm	5	5

¹ mean value by measurement of the MgB_2 area in Figure 2.2a

² from data sheet

Table 2.2.: Material properties of the investigated multifilament MgB_2 wires which are presented in detail in Appendix C [87, 86].

Part	Material	Density ¹	Electrical resistivity ²	Thermal conductivity ³
SC filament	MgB_2	2550 [99]	–	6.8 [100]
NC filament	Cu^4	8940 [101]	0.026 [101]	8564.4 [101]
Barrier	Nb	8570 [102]	5.64 [102]	8.5 [103]
Matrix	Cu10Ni	8940 [104]	140 [102]	18.2 [105]
Outer sheath	Cu30Ni	8800 [106]	365 [102]	9.1 [107]

¹ in kg m^{-3}

² in $\text{n}\Omega\text{m}$ and at 20 K and 0 T

³ in $\text{W m}^{-1}\text{K}^{-1}$ and at 20 K

⁴ RRR equals 1000

Heat treatment

Heat treatments are performed in an electrically heated furnace under an argon atmosphere with slight overpressure. Hydrogen gas with a concentration of 5% traps any remnant oxygen in the furnace chamber. The non-reacted 54 filament wire is wound to hollow steel cylinders with a radius of 8 cm which is far above the critical bending radius defined in the next section. The wire is fixed at its ends by screws and the furnace temperature is measured inside this hollow cylinder. The temperature profile is shown in Figure 2.3. It is important that a temperature of over 600°C is reached for a period of 90 min and a temperature of 650°C for a period of 45 min, allowing magnesium and boron to react. The duration of the cool-down phase is determined by the thermal capacity of the furnace and the ambient temperature. The slow cooling-down phase reduces internal stresses which result from the deformation process.

After heat treatment, the critical parameters of the conductors are examined.

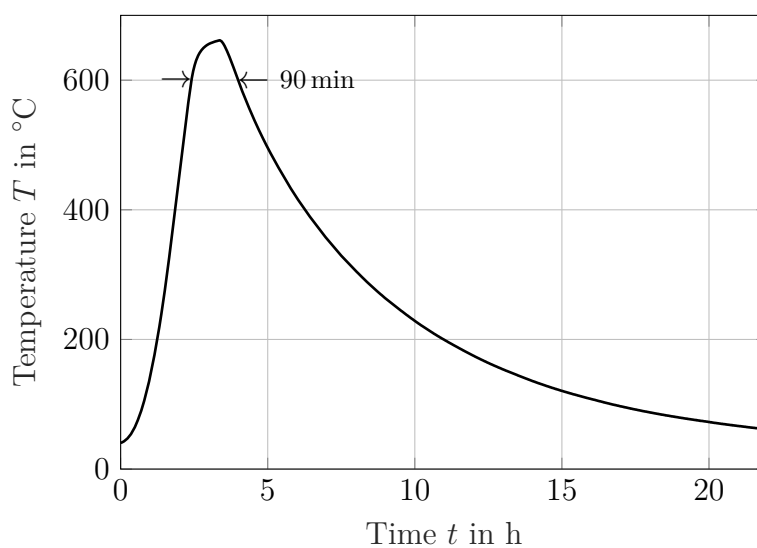


Figure 2.3.: Measured temperature T at the sample of the 54 filament wire as a function of the time t .

2.2. Critical Parameters

A superconductor has several critical parameters, which have a major impact on the superconducting properties and must be taken into account when designing applications.

Critical temperature

The characteristic critical temperature T_c of MgB_2 is 39 K, below which the electrical resistance vanishes [88]. Above this temperature the superconducting state cannot exist. Sufficient temperature margin must be maintained from this limit during operation of the application to ensure safe operation. Furthermore, the critical current and critical field of the conductor decreases with increasing temperature, which will be presented in the following sections. [54]

Critical field

The superconducting state is lost if the critical magnetic field H_c is exceeded. Furthermore, the Meissner effect describes the expulsion of the magnetic field of a material during its transition to the superconducting state. [55]

This means that a type-I superconductor behaves like a perfect diamagnet, that expels the magnetic field from its interior. The critical magnetic field depends strongly on the temperature and is zero at the critical temperature, as shown as an example in Figure 2.4a.

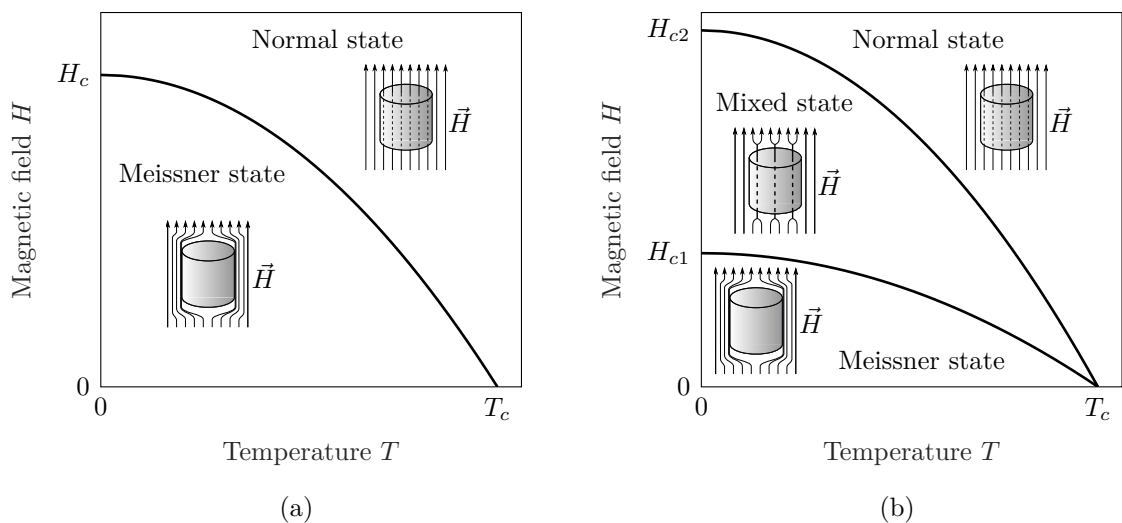


Figure 2.4.: Magnetic field H as a function of the temperature T for:

(a) Type-I superconductors. Adapted from [108].

(b) Type-II superconductors. Adapted from [108].

The penetration of a cylindrical superconductor by a parallel magnetic field \vec{H} is illustrated.

Type-II superconductors are characterized by two critical magnetic field values which define two areas presented in Figure 2.4b. Firstly, the area between zero and lower critical field H_{c1} is defined for magnetic fields, which are completely excluded from the superconductor by screening currents flowing in a very thin layer at the surface.

Secondly, the field area between the lower critical field and upper critical field H_{c2} in which the superconductor is penetrated in the form of flux tubes.

Nowadays, the upper critical field is increased by doping MgB_2 [109]. Carbon doping is one of the most effective variants for increasing this value. This was done by the manufacturer in the 54 filament and 114 filament wire with 2% [86].

Critical current

The most important characteristic property of a superconductor for practical applications is the critical current I_c . This value defines the maximum electrical transport current that the superconductor is able to carry without DC resistance. Due to the importance for further calculations, the critical current is measured as a function of the temperature and the external magnetic field. This measurement is done in an electrical characterization system for superconductors [110]. Only straight samples with a maximum length of 9 cm can be mounted, of which 5 cm are taken by the current contacts. The maximum applied current is 1 kA and the temperature can be adjusted between 1.8 K and 200 K. DC fields up to 6 T can be reached.

Due to the necessary two-phase hydrogen cooling in the electric machine and the critical temperature of MgB_2 , the conductor is measured at the discrete temperatures of 20 K, 22 K, 25 K, 27 K, 30 K and 33 K. The magnetic flux density is varied between 0 T and 2 T in 0.1 T steps. No higher fields are to be expected due to the typical saturation of iron in electric machines beyond 2 T and the strongly decreasing current carrying capacity of MgB_2 at increasing magnetic flux density.

The resistance of the conductor is determined by measuring the transport current I_t and the voltage difference U , which can also be represented as electric field E . By increasing the transport current, the critical current is determined by definition when the critical electric field E_c of $1 \mu\text{V cm}^{-1}$ has been reached. As an example, a curve of the strongly non-linear electric field current characteristic is shown in Figure 2.5.

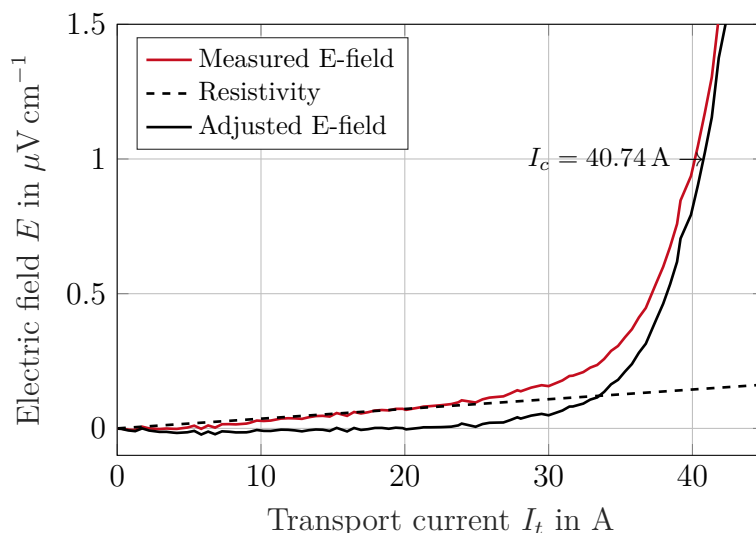


Figure 2.5.: Measured electric field E of the 114 filament wire as a function of the transport current I_t to determine the critical current I_c at a critical electric field E_c of $1 \mu\text{V cm}^{-1}$.

The measurement results are then modified in two steps. Firstly, the DC resistance generated by the current injection is removed. Secondly, the curve is fitted to the power law in Equation 2.1 [111] with the parameters critical current density J_c and n -value.

$$E = E_c \left(\frac{J}{J_c} \right)^n \quad (2.1)$$

The measurement results for both wires are summarized in Figure 2.6.

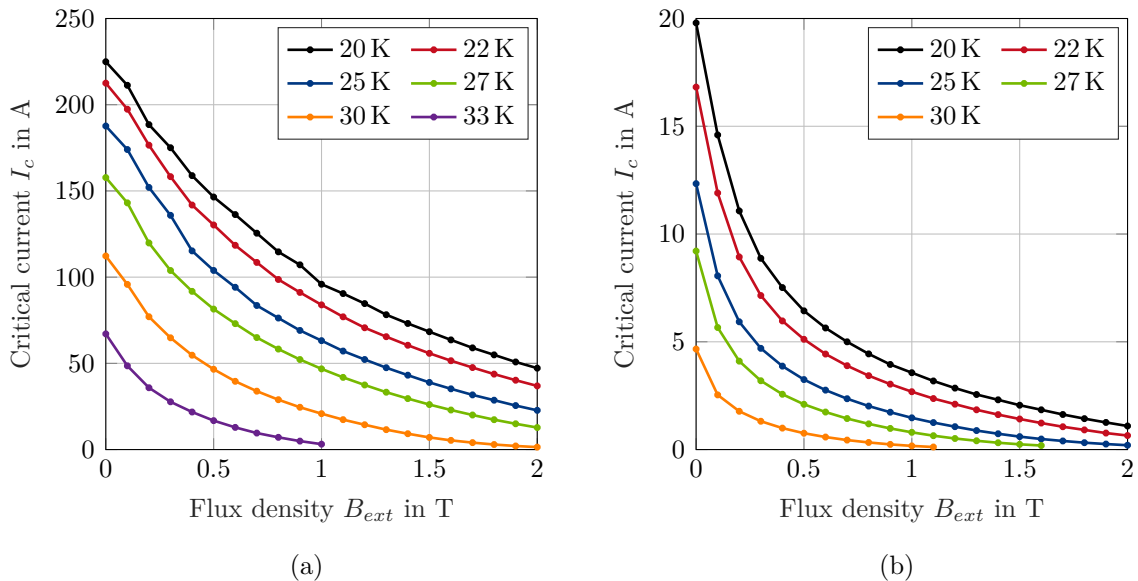


Figure 2.6.: Critical current I_c as a function of the external flux density B_{ext} measured at temperatures between 20 K – 33 K for the:

- (a) 114 multifilament wire.
- (b) 54 multifilament wire.

It is conspicuous that the current carrying capacity of the 54 filament wire is considerably lower than that of the 114 filament wire. A comparison of the current densities at 20 K and self-field shows that the current density of the 54 filament wire reaches a value of 300 A mm^{-2} and the 114 filament wire reaches a value of 770 A mm^{-2} . Their ratio difference increases with increasing flux density due to the stronger field sensitivity of the 54 filament wire and is 9.8 at 20 K and 2 T. No improvement could be achieved by changing the heat treatment. It can be concluded that the conductor quality is not yet sufficient for this application. Another indication of this is that the filament diameter varies strongly, as can be seen in Figure 2.2a, and the measured mean value is only $10 \mu\text{m}$ and not $13 \mu\text{m}$ as specified by the manufacturer. The fill factor is therefore also lower.

For this reason, the 54 filament wire is not further taken into account in this thesis because the difference would be reflected in the overall machine design. The 114 filament wire shows much better current carrying capacity in dependence of flux density and therefore it will be taken into account in the further design.

Critical bending radius

The critical bending radius $r_{b,c}$ is important for conductors used in coils operated in an external magnetic field and thus subjected to large stress and strain. If a J_c -degradation occurs through bending, the critical bending radius is achieved. This point mainly depends on the outer sheath material [112, 113]. Equation 2.2 can be used to calculate the critical bending strain $\varepsilon_{b,c}$ with the distance of the outer filaments from the neutral axis d_{of} .

$$\varepsilon_{b,c} = \frac{d_{of}}{d_{of} + r_{b,c}} \quad (2.2)$$

Measurements at room temperature show that a critical current degradation occurs at bending strains greater than 0.3%–0.5% for MgB₂ wires with CuNi outer sheath [114, 115]. This leads to a minimum bending radius of 22 mm–37 mm for the 54 filament wire and 48 mm–80 mm for the 114 filament wire. The strain tolerance can be improved with an outer sheath made of stainless steel [116].

Furthermore, bending before the heat treatment is advantageous so that no I_c -degradation occurs. Cracks occur during bending, which are healed by the heat treatment process. This results in advantages in the manufacturing of coils. However, bending after heat treatment causes a significant I_c -degradation [112].

The J_c -degradation in dependence of the bending radius is not investigated in this thesis. If the machine design reaches bending radii smaller than the critical values, these designs will be dismissed.

2.3. AC Loss

The determination of the AC loss is a key task in this thesis because it limits the current carrying capacity of the superconductor in alternating fields through heating of the wire. There is a mutual influence: The transport current influences the external field loss component and the external field influences the transport current loss component [117]. Thus, this calculation forms the basis for the design of electric machines.

The AC loss in a superconducting wire consists essentially of five components, listed in Table 2.3 and shown in Figure 2.7. They are distinguished according to the location of their origin, superconducting (SC) or normal conducting (NC) material, and essential influence parameters.

The loss is mainly caused by two sources. Firstly, the superconducting wire is penetrated by an external sinusoidal field with the amplitude B_{ext} and frequency f_{ext} which generates the magnetization loss. This alternating field is generated in electric machines by adjacent AC coils or by the DC field of the moving rotor. Secondly, the transport current I_t produces an alternating magnetic self-field around the wire, which is penetrating the wire and causes the self-field transport current loss [117]. In addition, the loss is influenced by various material parameters, such as the electrical resistivity ρ_{nc} or a ferromagnetic behavior of normal conducting materials.

The loss components in the superconducting filaments and the normal conducting materials, as shown in Figure 2.7, are the magnetization loss $P_{v,mag}$ ① and the coupling-current loss $P_{v,cc}$ ③, respectively. Further loss components are the

eddy current loss $P_{v,e}$ ③ in normal conducting materials and possible overcurrent transport loss $P_{v,oc}$ ④ for example in the thermal and mechanical stabilizer. The ferromagnetic loss $P_{v,fe}$ ⑤ is generated in the sheath material if this is magnetic.

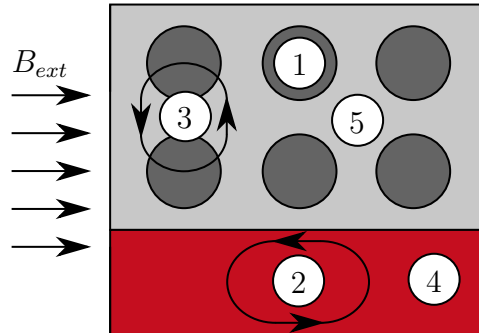


Figure 2.7.: Sketch illustrating the different loss components in SC filaments ■, NC sheath material □ and NC stabilizer ■ dedicated to different effects and materials listed in Table 2.3.

Table 2.3.: AC loss components in a superconducting wire with the major influence parameters and point of origin.

Loss component	Point of origin	Major influence parameters
① Magnetization loss $P_{v,mag}$	SC filament	B_{ext}, f_{ext}, I_t
③ Eddy current loss $P_{v,e}$	NC stabilizer/sheath	$B_{ext}, f_{ext}, \rho_{nc}$
② Coupling-current loss $P_{v,cc}$	NC sheath	$B_{ext}, f_{ext}, \rho_{nc}$
④ Overcurrent transport loss $P_{v,oc}$	NC stabilizer	I_t, ρ_{nc}
⑤ Ferromagnetic loss $P_{v,fe}$	NC sheath	$B_{ext}, f_{ext}, Q_{v,fe}$

It is common to specify the loss per wire length. All loss components summarized result in the total AC loss per unit length $P'_{v,tot}$:

$$P'_{v,tot} = P'_{v,mag} + P'_{v,e} + P'_{v,cc} + P'_{v,oc} + P'_{v,fe} \quad (2.3)$$

The analytical determination of the loss is very complex and different boundary conditions have to be considered, which are explained below.

It is assumed that the external field B_{ext} and transport current I_t in the wire are in-phase. No analytical expression is known to calculate the loss if this field and this current are not in-phase. If this is the case, the total loss becomes lower because of Faraday's Law. The electric field drives screening and coupling currents and has its maximum at the moment when the time derivative of the flux density has its maximum and thus, the flux density is zero [118]. At the same time and if external field and current are in-phase, the current is also zero due to the inductive behavior and leaves maximum space for screening and coupling currents. Thus, if they are not in-phase, the external field and current are never zero simultaneously and the

screening as well as coupling currents cannot be so high as in the in-phase case. [117] Furthermore, no analytical expression is known to determine the alternating transport current loss and the magnetization loss of a wire by an alternating external field separately. Moreover, the calculation is independent of external thermal as well as mechanical influences.

A more detailed description of the summarized loss components of Table 2.3 are presented in the following sections of this chapter. Two different approaches to compute the individual loss contributions are used in this thesis. In Section 2.3.1 general analytical calculation methods are presented for each loss component. In contrast, Section 2.3.2 shows the procedure to use numerical methods to calculate the magnetization loss. In the subsequent Section 2.3.3 the results of both approaches are presented and compared for the 114 filament wire.

2.3.1. Analytical Calculation

The static analytical calculation of the AC loss described in the next sections is based on the work of Wilson [119], Bean [120], Carr [121] and Oomen [117]. The calculations differentiate between a multifilament wire in a normal conducting matrix and a cable made of monofilaments. Even if no sample of a cable based on monofilaments is available, this wire architecture can be considered theoretically to discuss the general superconductor characteristics.

Magnetization loss

In type-II superconductors, an alternating magnetic field causes magnetization loss being linked with two energy sources: an external magnetic field and the self-field of the conductor when applying a transport current. These two superimposed sources penetrate the superconducting material in the form of flux tubes. If the field is changing, the internal magnetic field of the superconductor changes as well and induces an electric field. This leads to screening currents at the level of the critical current density in the outer part of the superconductor. The inner part of the superconductor is field-free. If a current is transported through a superconductor, Lorentz forces are moving the flux tubes which is known as flux creep. [117]

The magnetization loss is calculated for an external sinusoidal magnetic field perpendicular to the conductor, carrying a sinusoidal transport current in-phase with the magnetic field [117]. Initially two important quantities are introduced to describe the actual state and the AC loss of a superconductor. Firstly, the normalized current I_n is defined in Equation 2.4 which describes the ratio of transport current I_t to critical current I_c .

$$I_n = \frac{I_t}{I_c} \quad (2.4)$$

Secondly, the normalized flux density amplitude β in Equation 2.5 is introduced and is defined by the ratio of external flux density B_{ext} to penetration flux density B_p .

$$\beta = \frac{B_{ext}}{B_p} \quad (2.5)$$

Furthermore, the penetration flux density B_p in Equation 2.6 is defined by the required magnetic field, perpendicular to the superconductor, to penetrate the centre

of a cylindrical superconductor [120]. This quantity depends only on the radius of the superconductor r_{sc} and its critical current density J_c .

$$B_p = \frac{2 r_{sc} \mu_0 J_c}{\pi} \quad (2.6)$$

The magnetization loss density of a superconducting wire $Q_{v,mag}$, given as loss per cycle and per unit of volume, is calculated according to Equation 2.7 [121].

$$Q_{v,mag} = \begin{cases} \frac{\Gamma_{cyl,\perp}(\beta)}{\Gamma_{slab,\parallel}(\beta)} \frac{2 B_{ext}^2}{\mu_0} \left(\frac{I_n^3}{3 \beta^2} + I_n \right) & \text{if } \beta \leq I_n \\ \frac{\Gamma_{cyl,\perp}(\beta)}{\Gamma_{slab,\parallel}(\beta)} \frac{2 B_{ext}^2}{\mu_0} \left(\frac{\beta}{3} + \frac{I_n^2}{\beta} \right) & \text{if } I_n \leq \beta \leq 1 \\ \frac{\Gamma_{cyl,\perp}(\beta)}{\Gamma_{slab,\parallel}(\beta)} \frac{2 B_{ext}^2}{\mu_0} \left(\frac{3 + I_n^2}{3 \beta} - \frac{2(1 - I_n^3)}{3 \beta^2} \right) & \text{if } \beta \geq 1 \text{ and } I_n \leq 1 \\ + \frac{6 I_n^2 (1 - I_n)^2}{3 \beta^2 (\beta - I_n)} - \frac{4 I_n^2 (1 - I_n)^3}{3 \beta^2 (\beta - I_n)^2} & \end{cases} \quad (2.7)$$

This equation was originally developed for an infinite slab parallel to a sinusoidal magnetic field and can be extended with the ratio of the loss factors $\Gamma(\beta)$ to a cylindrical wire penetrated by a perpendicular field shown in Figure 2.8 [119].

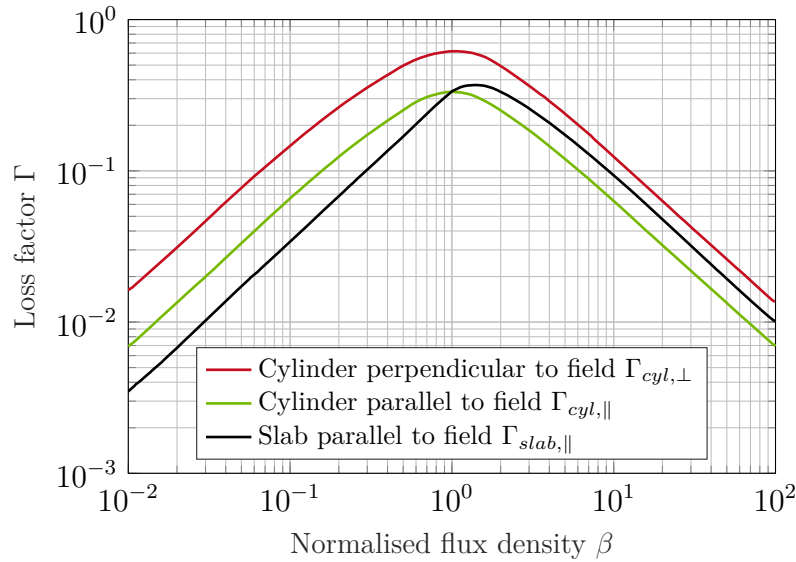


Figure 2.8.: Loss factor Γ for the magnetization loss density per cycle and per unit volume as a function of normalized flux density amplitude β in different shapes of superconductors [119].

Furthermore, it is assumed that the critical current is independent of the flux density [117]. No expressions are known to separate the two physical contributions during external alternating magnetic field and transport current. An important parameter

for the characterization of a superconductor is the n -value which is used to describe the sharpness of the E - J transition. Its influence on the magnetization loss is not taken into account in this analytical approach because the equations are given for Bean's critical-state model [120]. This model assumes three current density states in the superconductor which are the zero current density in field-free regions and the positive and negative critical current density in the regions penetrated by a magnetic field.

Finally, the magnetization loss per unit length $P'_{v,mag}$ is determined by Equation 2.8 with the filament area A_{fil} and the external frequency f_{ext} .

$$P'_{v,mag} = Q_{v,mag} A_{fil} f_{ext} \quad (2.8)$$

As an example, Figure 2.9a shows results of Equation 2.7 as a function of the normalized flux density amplitude β and normalized current I_n for a single filament of the 114 filament wire with the input parameters according to Table 2.4. It is clearly

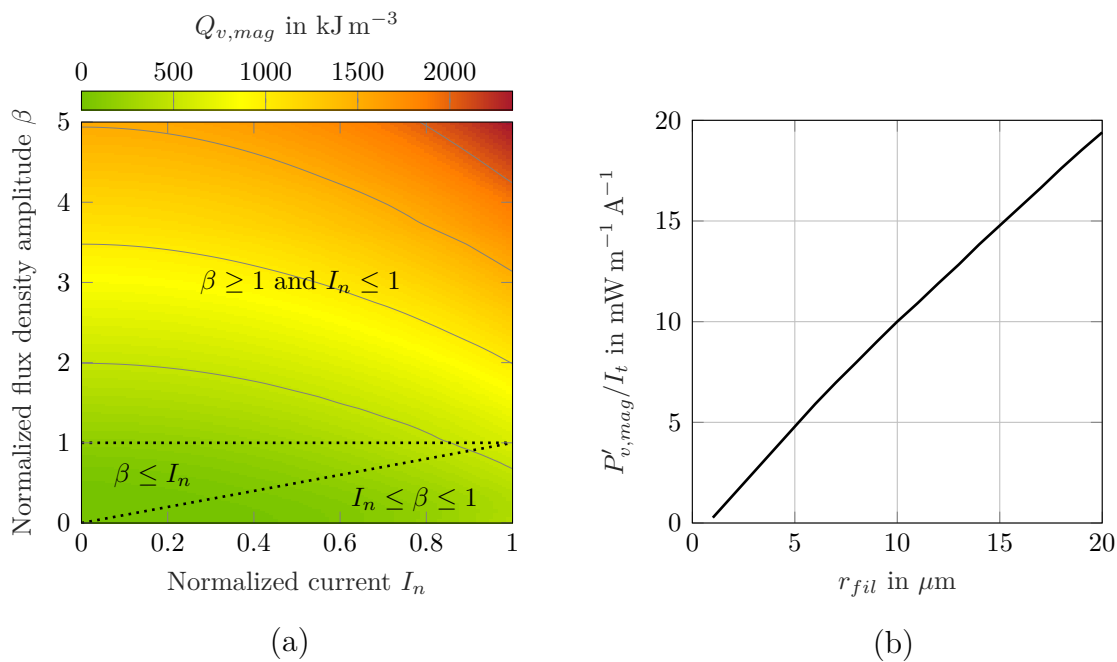


Figure 2.9.: Magnetization loss results for an exemplary filament of the 114 filament wire with the input parameters in Table 2.4.

(a) Magnetization loss density $Q_{v,mag}$ as a function of the normalized flux density amplitude β and the normalized current I_n . The three cases from Equation 2.7 are shown.

(b) Magnetization loss per unit length and per transport current $P'_{v,mag}/I_t$ as a function of the filament radius r_{fil} .

visible that after reaching the penetration flux density at a normalized flux density amplitude of 1, the magnetization loss increases rapidly and the normalized flux density amplitude has a greater influence than the normalized current in the value range investigated.

For applications with a medium field lower than 2 T, such as electric machines, the penetration flux density is rapidly exceeded in wires with small filament radii. In these cases applies $\beta \gg 1$ and only the first summand in the last case of Equation 2.7 is significant.

Furthermore, Figure 2.9b shows the influence of the filament radius r_{fil} on the magnetization loss per unit length and per transport current $P'_{v,mag}/I_t$. This loss representation is chosen to compare the filaments with each other [122]. With decreasing filament radius, the loss per current decreases linearly.

Table 2.4.: Input parameters for the analytical magnetization loss calculation of the 114 filament wire shown in Figure 2.9.

Symbol	Value	Unit	Explanation
I_n	0.7	–	Normalized current
f_{ext}	500	Hz	External frequency
J_c	$2.083 \cdot 10^9$	A m^{-2}	Critical current density
B_p	0.4	T	Penetration flux density

The magnetization loss can be reduced by operation of the superconductor significantly below the critical current. Furthermore, the reduction of the dimensions of the superconducting filaments reduces the magnetization loss, but this increases the critical bending radius and is limited by the manufacturing process [122]. In Section 2.3.3 the influence of the filament radius is presented in more detail for the 114 filament wire.

Eddy current loss in normal conducting materials

The electromagnetic alternating fields induce eddy currents in normal conducting materials. According to Figure 2.7, there are two sources of magnetic fields. Firstly, the external field B_{ext} and secondly the field which is generated by the adjacent superconducting wires. Both fields superimposed generate loss in a normal conductor known as proximity effect. A further loss component is known as skin effect, which results from the self-field of a current carrying normal conductor. This effect occurs in a superconducting application only if the superconductor is overloaded and thus a part of the transport current I_t is flowing in the normal conductor. This current is defined as external current I_{ext} .

The eddy current loss per unit length $P'_{v,e}$ is calculated by Equation 2.9 [123]. The first summand represents the skin effect and the second summand represents the proximity effect.

$$P'_{v,e} = R'_{dc} \left(2 C_s I_{ext}^2 + C_p \left(\frac{B_{ext}}{\mu_0} \right)^2 \right) \quad (2.9)$$

Parameters that influence the eddy current loss are the DC resistance per unit length R'_{dc} , which depends on the resistivity ρ_{nc} , and the area of the respective material.

$$R'_{dc} = \frac{\rho_{nc}}{\pi r_{nc}^2} \quad (2.10)$$

Further parameters are the factors C_s and C_p in Equation 2.11 and 2.12, respectively, which include the Kelvin functions $K_{Ber}(\nu, \xi)$ and $K_{Bei}(\nu, \xi)$ in dependence of the relative thickness ξ .

$$C_s = \frac{\xi}{4\sqrt{2}} \left(\frac{K_{Ber}(0, \xi) K_{Bei}(1, \xi) - K_{Ber}(0, \xi) K_{Ber}(1, \xi)}{K_{Ber}(1, \xi)^2 + K_{Bei}(1, \xi)^2} + \frac{K_{Bei}(0, \xi) K_{Ber}(1, \xi) + K_{Bei}(0, \xi) K_{Bei}(1, \xi)}{K_{Ber}(1, \xi)^2 + K_{Bei}(1, \xi)^2} \right) \quad (2.11)$$

$$C_p = -\sqrt{2} \xi \pi^2 r_{nc}^2 \left(\frac{K_{Ber}(2, \xi) K_{Ber}(1, \xi) + K_{Ber}(2, \xi) K_{Bei}(1, \xi)}{K_{Ber}(0, \xi)^2 + K_{Bei}(0, \xi)^2} + \frac{K_{Bei}(2, \xi) K_{Bei}(1, \xi) - K_{Bei}(2, \xi) K_{Ber}(1, \xi)}{K_{Ber}(0, \xi)^2 + K_{Bei}(0, \xi)^2} \right) \quad (2.12)$$

$$\xi = \frac{\sqrt{2} r_{nc}}{\delta_s} \quad (2.13)$$

The skin depth δ_s is defined as:

$$\delta_s = \sqrt{\frac{2\rho_{nc}}{\omega\mu_0}} \quad (2.14)$$

and the Kelvin functions are the real and imaginary parts of the ν^{th} Bessel function J_ν [124]:

$$J_\nu \left(\nu, \xi e^{\frac{3\pi i}{4}} \right) \quad (2.15)$$

Equation 2.9 describes the two cases of partially and fully penetrated normal conductors, as shown in Figure 2.10. It can be seen that the two loss effects as a function of the resistivity ρ_{nc} generate losses of different levels. These can also become extremely large with a several hundred watts per meter, which should be avoided by an appropriate wire design.

A further calculation option for eddy current loss is introduced according to [125]. For zero external current and full penetration Equation 2.16 can be used with the second moment of area I_a . It is specified for circular cross-section in Equation 2.17.

$$P'_{v,e} = I_a \frac{\omega^2 B_{ext}^2}{2\rho_{nc}} \quad \text{if } \delta_s \geq r_{nc} \quad (2.16)$$

$$I_a = \frac{\pi}{4} r_{nc}^4 \quad (2.17)$$

An advantage compared to the first approach with Bessel functions is that the calculation effort is greatly reduced, without loss of accuracy, as illustrated in Figure 2.10. The eddy current loss increases in a partially penetrated conductor with increasing resistivity until the maximum eddy current loss is reached, as shown and marked in Figure 2.10. At this point, the conductor is completely penetrated by the magnetic field. A further increase of the resistivity leads to decreasing eddy current loss in a

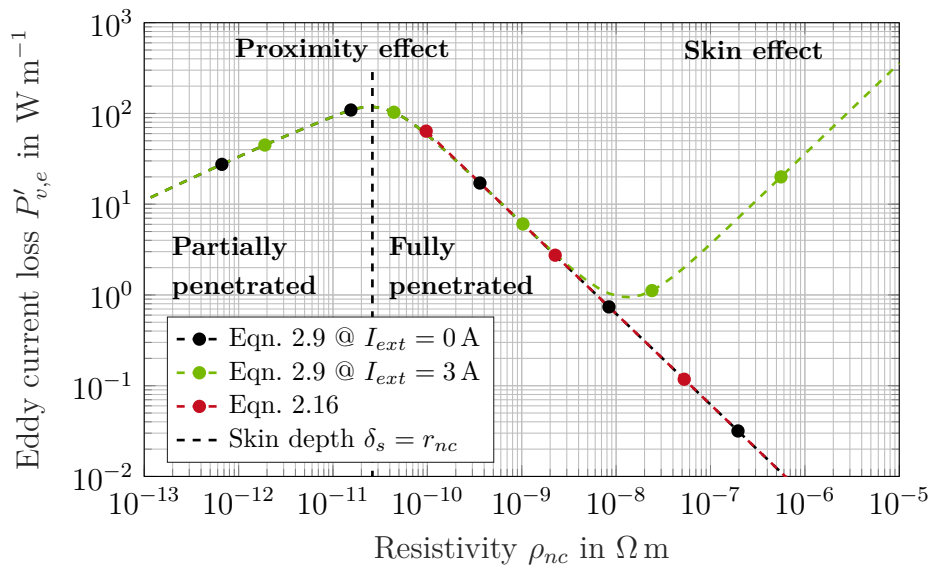


Figure 2.10.: Eddy current loss per unit length $P'_{v,e}$ as a function of the resistivity ρ_{nc} for a NC material with circular cross-section, a radius r_{nc} of 200 μm , an external field B_{ext} of 1 T and a frequency f_{ext} of 500 Hz.

fully penetrated conductor.

Eddy current losses can be reduced through an optimal choice of the normal conducting material. So far, the electrical resistivity has been assumed to be temperature independent, but especially in the case of copper, it strongly varies in the cryogenic temperature range, as presented in Appendix C.2. Further influencing parameters are the residual-resistance ratio (RRR) and the external flux density.

In the further calculation, the detailed variant with Bessel functions for determining the eddy current loss is chosen, because there are no limits to the electrical resistivity to be considered.

Coupling current loss in multi-stage-twisted cable

An alternating external magnetic field induces an electric field according to Faraday's law, which causes cross-over currents in superconductors from one filament to the other.

Figure 2.11 illustrates the origin of this coupling current loss. At first, Figure 2.11a shows two parallel filaments in a normal conducting matrix, penetrated by a perpendicular external field B_{\perp} . This magnetic field induces an electric field which in turn drives a coupling current i_{coup} around the loop. Furthermore, the current flows through the normal conducting matrix and generates loss in this matrix. If the conductor length increases, the filaments can reach their critical current very fast. This condition is called critical length l_c where the filaments are full coupled [119].

$$l_c = 2\sqrt{\frac{\rho_{nc} J_{c,fil} d_{fil}}{\pi f_{ext} B_{ext}}} \quad (2.18)$$

This results in a higher loss in a multifilament wire compared with a equivalent monofilament wire. For this reason, multifilament superconductors in AC applications must always be twisted.

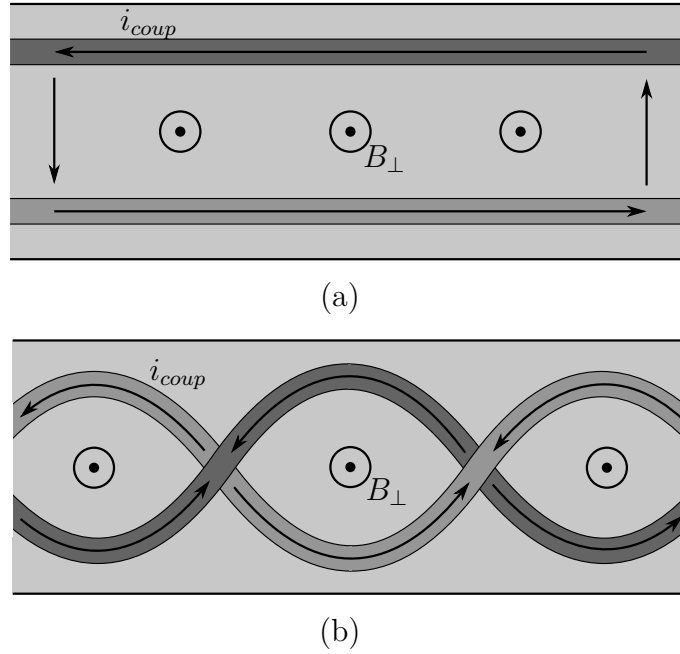


Figure 2.11.: Sketch of the current path of coupling currents i_{coup} between two filaments $\blacksquare, \blacksquare$ embedded in a matrix \square and penetrated by a perpendicular magnetic field B_{\perp} in a:

(a) Non-twisted conductor. Adapted from [117].

(b) Twisted conductor. Adapted from [117].

Figure 2.11b presents two twisted superconductors where the voltage is induced in each loop. Differently from Figure 2.11a, the cross-over current flows parallel to the magnetic field through the matrix and not perpendicular. The distance between two twisted filaments in a round wire is independent of the direction of the cross-over current. The coupling currents are decreased to an acceptable level by choosing the twist pitch l_{tw} shorter than $2l_c$ [117].

If filaments are combined into a wire or wires into a cable, in addition to twisting, the increase of the effective resistivity ρ_b between the wires in the cable can also reduce coupling current loss. Equation 2.19 is used for the calculation of the coupling current loss per unit length $P'_{v,cc}$ with the cable area A_{cab} and the external frequency f_{ext} .

$$P'_{v,cc} = Q_{v,cc} A_{cab} f_{ext} \quad (2.19)$$

Further, the coupling current loss density $Q_{v,cc}$ is defined in Equation 2.20 with the total coupling time constant τ_{tot} .

$$Q_{v,cc} = \frac{2 B_{ext}^2 \pi \omega \tau_{tot}}{\mu_0 (1 + (\omega \tau_{tot})^2)} \quad (2.20)$$

This time constant describes the decay time of a coupling current and depends on the number of twisting stages n . For a better understanding, Figure 2.12 illustrates as an example the situation of a cable with multifilament wires and three twisting stages.

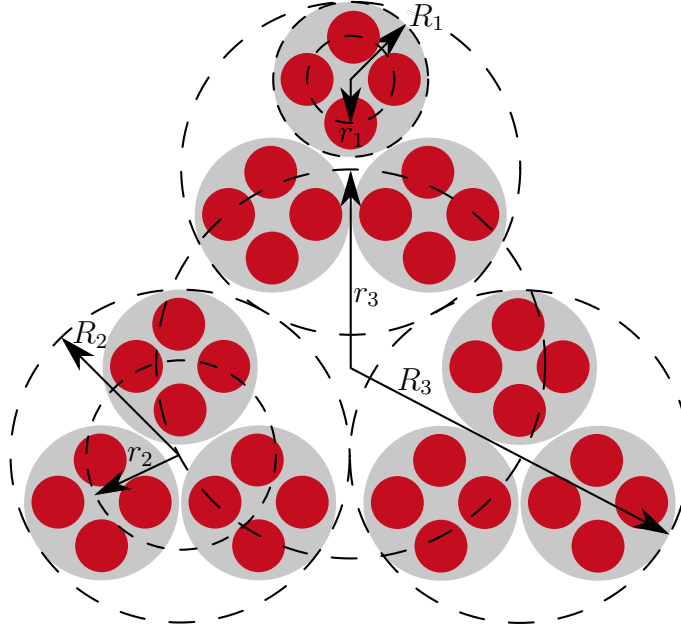


Figure 2.12.: Cable consisting of multifilament wires with SC filaments \blacksquare and NC matrix \square in three twisting stages. The outer radius R_n and the twist radius r_n of each twisting stage n are illustrated.

The first stage is from the basic filament twist. It is also possible to calculate twisted multifilament wires, which are combined to a twisted cable. The total coupling time constant τ_{tot} of cables, manufactured by twisted composite wires, are calculated for one or more stages, as follows in Equation 2.21.

$$\tau_{tot} = \begin{cases} \frac{\mu_0 l_{tw}^2}{8 \pi^2 \rho_b} & \text{if } n = 1 \\ \sum_{n=0}^N \tau_n & \text{if } n > 1 \end{cases} \quad (2.21)$$

First of all, the case for more than one stage is considered. The total time constant is summed over all stage time constants τ_n [126]. Every new twisting stage n causes a decrease of coupling current loss, which is smaller than for an untwisted cable. The general stage time constant is defined as:

$$\tau_n = \frac{\mu_0}{2 \rho_n^*} \left(\frac{l_{tw,n}^*}{2 \pi} \right)^2 \frac{1}{1 - \varepsilon_{n-1}} \quad (2.22)$$

with the effective twist pitch length $l_{tw,n}^*$, the effective resistivity ρ_n^* and the average void fraction ε_n between the cable stages. These parameters are defined as:

$$l_{tw,n}^* = l_{tw,n} - \frac{r_{n-1}}{R_{n-1}} l_{tw,n-1} \quad (2.23)$$

$$\rho_n^* = \frac{\rho_b d_b}{\eta_n R_{n-1}} \quad (2.24)$$

with the apparent twist pitch length $l_{tw,n}$, the outer radius R_n , the twist radius r_n , the contact area ratio η_n , the resistivity ρ_b and thickness d_b of the contact resistive barrier. The twist radius describes the path on which the centers of the filaments move when twisting. If there are multiple materials in the barrier, the different products $\rho_b d_b$ are summed. For cables consisting of monofilament wires the first-stage time constant τ_1 in Equation 2.22 is zero.

Coupling current loss in mono-stage-twisted wire

Equation 2.20 can also be used to calculate the coupling current loss in multifilament wires with one twisting stage. First the coupling time constant τ_{tot} has to be determined with the effective resistivity ρ_b given in Equation 2.25 with the radius of filamentary core r_{fc} shown in Figure 2.13.

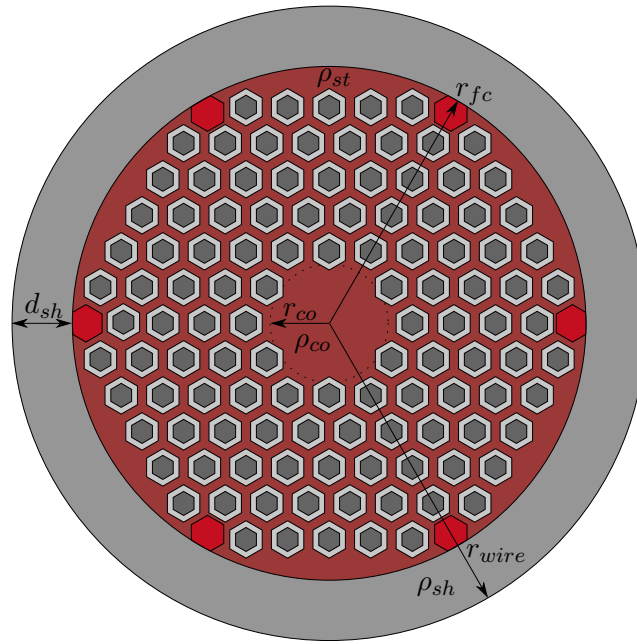


Figure 2.13.: Multifilament wire divided into the inner matrix core, the filamentary zone and the outer sheath with the corresponding outer radii r_{co} , r_{fc} and r_{wire} , respectively.

$$\rho_b = \frac{1}{\rho_{m,eff}} + \frac{d_{sh}}{r_{fc} \rho_{sh}} \quad (2.25)$$

The effective transverse resistivity $\rho_{m,eff}$ of the matrix is determined by the matrix material and by the shape as well as structure of the inner filaments. This resistivity can be calculated by Equation 2.26 with the fraction of filaments in filamentary core ε_f and if it is assumed that the filaments have good electrical contact with the matrix material [121].

$$\rho_{m,eff} = \rho_{st} \frac{1 - \varepsilon_f}{1 + \varepsilon_f} \quad (2.26)$$

Another calculation method is described in [127, 128]. In this approach, the geometric structure of the wire, as shown in Figure 2.13, is taken into account in more

detail compared to the first approach. The wire is divided into the inner matrix core with the radius r_{co} , the filamentary zone with the radius r_{fc} and the outer sheath with its outer radius r_{wire} . Each area has a corresponding resistivity. The coupling current loss per unit length $P'_{v,cc}$ is given by the following equation:

$$P'_{v,cc} = A_{cab} \left(\frac{r_{fc}}{r_{wire}} \right)^2 B_{ext}^2 \omega^2 \left(\frac{l_{tw}}{2\pi} \right)^2 \left(\frac{1}{\rho_{sh}} \frac{r_{wire}^2 - r_{fc}^2}{r_{wire}^2 + r_{fc}^2} + \frac{1}{\rho_{st}} \frac{r_{fc}^2 - r_{co}^2}{r_{fc}^2} - \frac{1}{\rho_{co}} \frac{r_{co}^2}{r_{fc}^2} \right) + A_{cab} \frac{1}{4\rho_{sh}} B_{ext}^2 \omega^2 \left(\frac{r_{wire}^4 - r_{fc}^4}{r_{wire}^2} \right) \quad (2.27)$$

Figure 2.14 shows the comparison of both calculation methods in Equations 2.19 and 2.27. Both approaches show similar behavior. With increasing flux density and frequency the loss increases rapidly. Furthermore, the approach with the loss calculation through the coupling current time constant provides more pessimistic values, which are about 15% higher. This variant is selected for further calculations in order to achieve a conservative design.

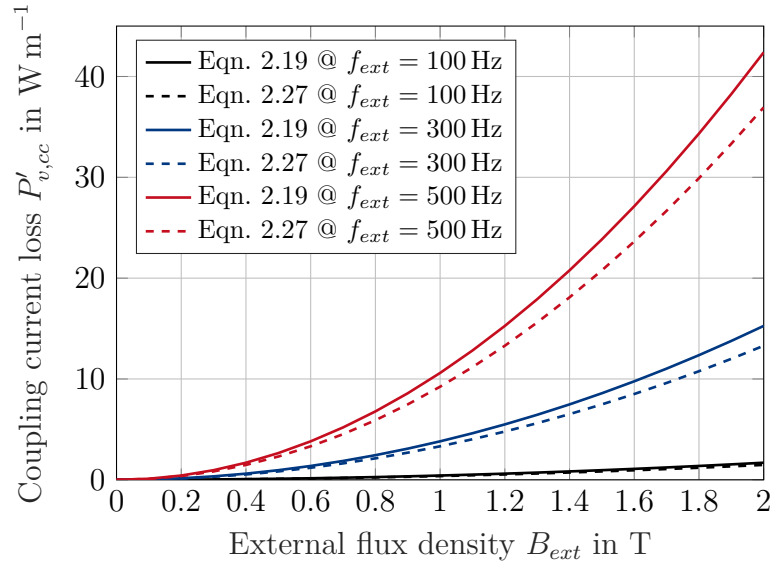


Figure 2.14.: Coupling current loss per unit length $P'_{v,cc}$ as a function of the external flux density B_{ext} at different external frequencies f_{ext} for the 114 filament wire.

Overcurrent loss

Overcurrent loss occurs when the superconducting filaments of a wire are overloaded in the case of a quench and, as a consequence, a part of the transport current I_t flows as overcurrent in the normal conducting material. This is only possible for limited time, otherwise the wire will be destroyed due to high AC loss.

The parallel resistance per unit length R'_{nc} from all normal conducting materials in the cable must be determined for the calculation of the overcurrent loss per unit length $P'_{v,oc}$ in Equation 2.28.

$$P'_{v,oc} = \begin{cases} R'_{nc} (I_t - I_c)^2 & \text{if } I_n > 1 \\ 0 & \text{if } I_n \leq 1 \end{cases} \quad (2.28)$$

In this event, the skin effect and proximity effect presented in Equation 2.9 also occur as additional AC loss.

This exceptional condition is neglected in the machine design and is therefore not taken into account in the loss calculation. Furthermore, quenching is prevented by having transport currents equal to a small fraction of the critical current. In this work, the normalized current is limited to less than 0.7.

Ferromagnetic loss

Ferromagnetic loss $P_{v,fe}$ is caused by hysteresis behavior of ferromagnetic non-superconducting materials. During manufacturing of the wires, undesirable ferromagnetic impurities can occur [68]. Apart from impurities, some MgB₂ wires are manufactured with magnetic material [129, 130]. The loss density $Q_{v,fe}$ can be determined by integration over the closed hysteresis curve area A_h :

$$Q_{v,fe} = \int_{A_h} H dB \quad (2.29)$$

The hysteresis curve is non-linear and thus no closed-form expression is known to calculate its loss density. With the approximation according to Steinmetz in Equation 2.30 the ferromagnetic loss density $Q_{v,fe}$ and subsequently the ferromagnetic loss per unit length $P'_{v,fe}$ in Equation 2.31 is determined. The material dependent constant C_{fe} and the exponent n , which varies in the range from 1.5–3, have to be determined empirically by measurements [131].

$$Q_{v,fe} = C_{fe} B^n \quad (2.30)$$

$$P'_{v,fe} = Q_{v,fe} A_{fe} f_{ext} \quad (2.31)$$

The basic equations to analytically derive the different terms contributing to the total AC loss in Equation 2.3 of a superconducting wire carrying an alternating transport current when being exposed to an alternating magnetic field are now described. Assuming that no quench occurs and non-magnetic normal conducting materials are used in the further investigation, the most influential loss terms are the magnetization loss, the eddy current loss and the coupling current loss. Therefore, in the next sections, they will be investigated in more detail using finite element method (FEM) to understand the profound behavior.

2.3.2. Finite Element Method

The FEM calculation is based on the H-formulation of Maxwell's equations. Faraday's Law in Equation 2.32 and Ampère's Law in Equation 2.33 are incorporated in commercial FEM software (Comsol 5.3a) as user-defined partial differential equations (PDE) using the components of the magnetic field \vec{H} as state variables. Addition-

ally, special features in the simulation of the non-linear behavior of superconductors are applied [132].

$$\nabla \times \vec{E} = -\frac{\partial \vec{B}}{\partial t} \quad (2.32)$$

$$\nabla \times \vec{H} = \vec{J} \quad (2.33)$$

For isotropic materials and time invariant systems the following relations are given:

$$\vec{J} = \frac{\vec{E}}{\rho} \quad (2.34)$$

$$\vec{B} = \mu_0 \mu_r \vec{H} \quad (2.35)$$

The electrical resistivity ρ and the relative permeability μ_r could be non-linear.

Two dimensional modeling

In this case, the model is reduced to the cross sections of the wire shown in Figure 2.1 as a two-dimensional problem. If the magnetic flux is limited to the x - y plane, the electric field \vec{E} as well as the current density \vec{J} have only non-zero components in z -direction. Ampere's Law in Equation 2.33 simplifies too:

$$J_z = \frac{\partial H_y}{\partial x} - \frac{\partial H_x}{\partial y} \quad (2.36)$$

Compared to the electromagnetics of normal conductors, where the electric field and the current density have a linear correspondence, for superconductors the non-linear E - J power law is applied [111]. This relation can be used to describe the phenomenon of flux creep and is defined as follows in Equation 2.37.

$$E_z = E_c \left(\frac{J_z}{J_c(B)} \right)^n \quad (2.37)$$

The critical electric field E_c is $1 \mu\text{V cm}^{-1}$ and characterizes the voltage drop per meter, which is commonly used to define the critical current density $J_c(B)$ of the superconductor presented in Section 2.2. The n -value characterizes the transition behavior between superconducting state and normal conducting state. For an n -value of 1 linear resistivity is set and if the n -value increases the behavior gets closer to Bean's critical state model. The measured critical current density, as presented in Section 2.2, is fitted now to one of the following models.

The Bean model [120] is extended in [133] by introducing the dependence of the critical current density on the magnetic field, which is called Kim model and is described by following equation with the fitting parameters β and B_0 :

$$J_c(B) = \frac{\beta}{B + B_0} \quad (2.38)$$

This Kim model is modified in [134] by adding the fitting parameter α , as given in Equation 2.39. This allows the adjustment of the steepness of the J - B correlation from α equals 0 for the Bean model and α equals 1 for the Kim model.

$$J_c(B) = J_{c0} \frac{1}{\left(1 + \frac{B}{B_0}\right)^\alpha} \quad (2.39)$$

A further adaptation is given by [135] where an additional parameter has been added. In Equation 2.40 the fitting parameter B_1 describes the flux density where the critical current of the superconductor reaches zero.

$$J_c(B) = \begin{cases} J_{c0} \frac{1 - \frac{B}{B_1}}{\left(1 + \frac{B}{B_0}\right)^\alpha} & \text{if } B < B_1 \\ 0 & \text{if } B \geq B_1 \end{cases} \quad (2.40)$$

In this work is Equation 2.39 used and Table 2.5 presents the fit results for the measured critical currents from Section 2.2.

Table 2.5.: Fit parameters for the critical current density according to Equation 2.39 of the 114 filament wire.

T^1	J_{c0}^2	B_0^3	α
20	$0.770 \cdot 10^9$	7.581	6.654
22	$0.727 \cdot 10^9$	5.696	5.760
25	$0.642 \cdot 10^9$	6.810	8.005
27	$0.540 \cdot 10^9$	7.003	9.343
30	$0.384 \cdot 10^9$	4426	7778

¹ in K
² in $A m^{-2}$
³ in T

To solve the presented equations, boundary conditions are necessary, as explained in the next section.

Boundary conditions

First of all, at interfaces between two materials with the magnetic field \vec{H}_1 and \vec{H}_2 the tangential component of the field is continuous if no surface current density \vec{K} occurs, as described by the following equation with the normal vector \vec{n} .

$$\vec{n} \times (\vec{H}_1 - \vec{H}_2) = \vec{K} = 0 \quad (2.41)$$

Two boundary conditions are required to solve the partial differential equation. The first one is the magnetic insulation at the edge of a simulation area defined in Equation 2.42.

$$\vec{n} \cdot \begin{pmatrix} H_x \\ H_y \end{pmatrix} = 0 \quad (2.42)$$

The second boundary condition is defined in Equation 2.43 by the line integral of the tangential component of the magnetic field H_θ equal to the sinusoidal transport current I_t .

$$\sqrt{2} I_t \sin(\omega t) = \oint H_\theta ds \quad (2.43)$$

If a twisted cable is calculated in a two-dimensional model, additional boundary conditions can be set. In a perfectly twisted cable, the same current flows in every filament. This condition is realized for the k^{th} filament by Equation 2.44.

$$I_k(t) = \int_A J_{z,k} dA \quad (2.44)$$

Not all filaments are transposed in the 114 filament wire. The filaments are only transposed in the five superconducting shells, as shown in Figure 2.1. Therefore, the same current flows in the filaments of a shell, but the current splitting between the shells remains free. This fact is taken into account by adjusting the condition in Equation 2.44 in the FEM model.

AC loss calculation

The determination of the different AC loss components is made by integration over the surface area. Accordingly, the magnetization loss of the superconducting filaments is calculated by integration over the area of the filaments in Figure 2.7 and the eddy current loss is determined by integration over the area of the normal conducting material.

The instantaneous value of loss per unit length is given by:

$$p'_v(t) = \int_A J_z E_z dA \quad (2.45)$$

and the time averaged value per unit length by:

$$P'_v = \int p'_v(t) dt \quad (2.46)$$

Coupling current loss can only be determined in a three-dimensional model, which will be discussed in the next section.

Three dimensional modelling

A three-dimensional model is advantageous to calculate the coupling current loss more precisely compared to the analytical approach. Especially at high external fields and frequencies, this loss component takes up the main part of the total AC loss, as shown in Figure 2.20.

In the past, three-dimensional calculations were successfully carried out on simplified models or wires with a low number of filaments [136, 137]. The number of nodes increases due to the additional nodes in the third dimension. Consequently, the computation time increase approximately by a factor proportional to the number of inserted mesh points along the third dimension [138]. This would lead to a huge calculation effort and for this reason three-dimensional models are not performed in this thesis.

2.3.3. Results

This section presents the results of the AC loss calculation generated by finite element method (FEM) and compares them with analytical results. Firstly, a monofilament is calculated with FEM to explain the basic superconductor behavior. Afterwards, the 114 filament wire is investigated. Finally, design suggestions and guidelines are derived from the findings.

Magnetization loss of a monofilament

The magnetization loss per unit length $P'_{v,mag}$ is presented according to the input parameters in Table 2.6. The constant current density at a temperature of 20 K and a flux density of 1 T is used in the analytical calculation only. In the FEM calculation the measured $J_c(B)$ -characteristic at a temperature of 20 K is used.

Figure 2.15a presents the magnetization loss per unit length and per transport current $P'_{v,mag}/I_t$ of a monofilament wire as a function of the filament radius r_{fil} and the analytical approach from Equation 2.8 is compared with FEM results. The loss is

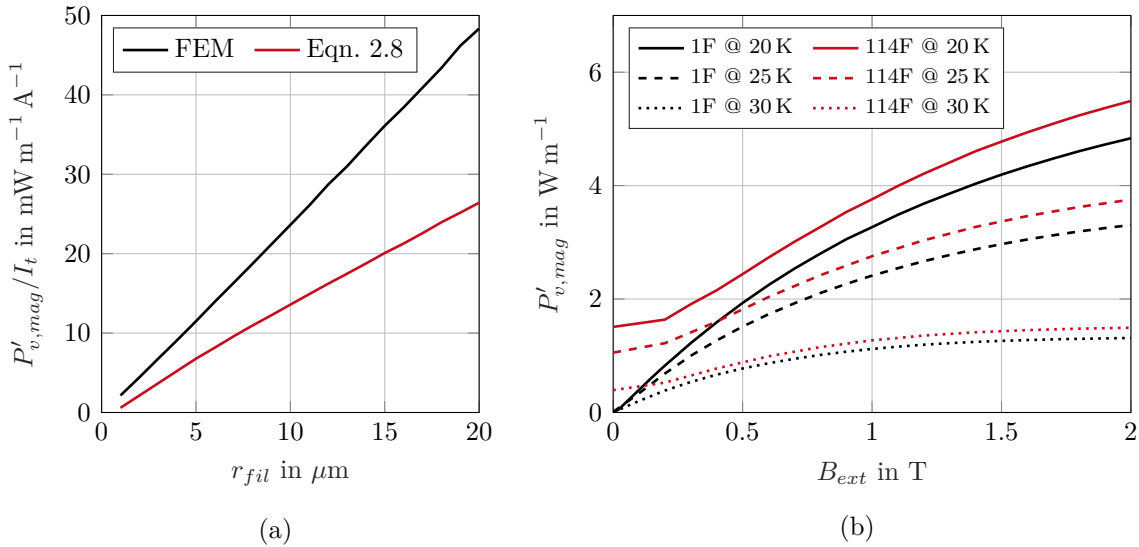


Figure 2.15.: Magnetization loss results with the input parameters in Table 2.6:

- (a) Influence of the filament radius r_{fil} on the magnetization loss per unit length and per transport current $P'_{v,mag}/I_t$ of a monofilament wire.
- (b) Comparison of the magnetization loss per unit length $P'_{v,mag}$ between the monofilament (1F) and the 114 filament (114F) wire depending on the external flux density B_{ext} . The loss of the monofilament is scaled with a factor of 114 to those of the 114 filament wire.

normalized to the transport current in order to achieve comparability. As expected, the loss increases linearly with increasing filament radius as already shown in Figure 2.9b. However, the loss results for the analytical approach are too low with a deviation of 43% percent at a filament radius of 10 μm . This is a too high inaccuracy, so the FEM is taken to calculate this loss component.

Next, the difference in magnetization loss per unit length $P'_{v,mag}$ between the monofilament and the 114 filament wire in dependence of the external flux density B_{ext}

is examined. This verifies whether it would be possible to determine the loss of a multifilament wire by a quicker calculable monofilament model. For a better comparison, the loss of the monofilament is scaled to the loss of the 114 monofilament wires by multiplication with 114. The results for different temperatures are presented in Figure 2.15b. Over the entire field range, the losses of the monofilament are lower than those of the 114 filament wire.

In the field range smaller than the penetration flux density of around 0.2 T at a temperature of 20 K, large deviations occur because the self-field and the shielding effect of several filaments are not taken into account. Furthermore, eddy current effects are not considered in the monofilament. Due to the high deviation a monofilament cannot be used to describe the loss behavior of the 114 filament wire accurately.

Table 2.6.: Input parameters for the analytical and FEM magnetization loss calculation for a monofilament and the 114 filament wire presented in Figure 2.15, 2.16 and 2.17.

Symbol	Value	Unit	Explanation
I_n	0.7	–	Normalized current
B_{ext}	1	T	External flux density
f_{ext}	500	Hz	External frequency
J_c^1	$2.567 \cdot 10^9$	$A m^{-2}$	Critical current density
T	20	K	Temperature

¹ only used in the analytical calculation

Magnetization loss of the 114 filament wire

Figure 2.16 presents the behavior of the 114 filament wire depending on the time t . An external flux density of 1 T, an external frequency f_{ext} of 500 Hz and a normalized current of 0.7 is selected as the operating point of the wire. The phase angle between current and external field varies between 0° and 90° , as shown in Figure 2.16a and 2.16b, respectively. The instantaneous critical current i_c of the wire is calculated by integration of the instantaneous critical current density over all filaments to represent the instantaneous utilization rate of the wire. It should be noted that the critical current is a DC quantity and is in general frequency dependent for alternating currents [139]. However, the critical current can be measured only for DC field and direct current with the electrical characterization system presented in Section 2.2.

The highest instantaneous utilization rate of the wire occurs in Figure 2.16a when the external field and the transport current are exactly in phase. The minimum instantaneous critical current and the maximum instantaneous transport current i_t arises at the same time and the maximum instantaneous normalized current is reached with represents the target normalized current of 0.7. A comparison with Figure 2.16b shows that the maximum instantaneous normalized current is significantly lower with 0.4.

The phase angle between magnetic field and transport current cannot be fixed in electric machines, because this parameter can be changed by the machine control.

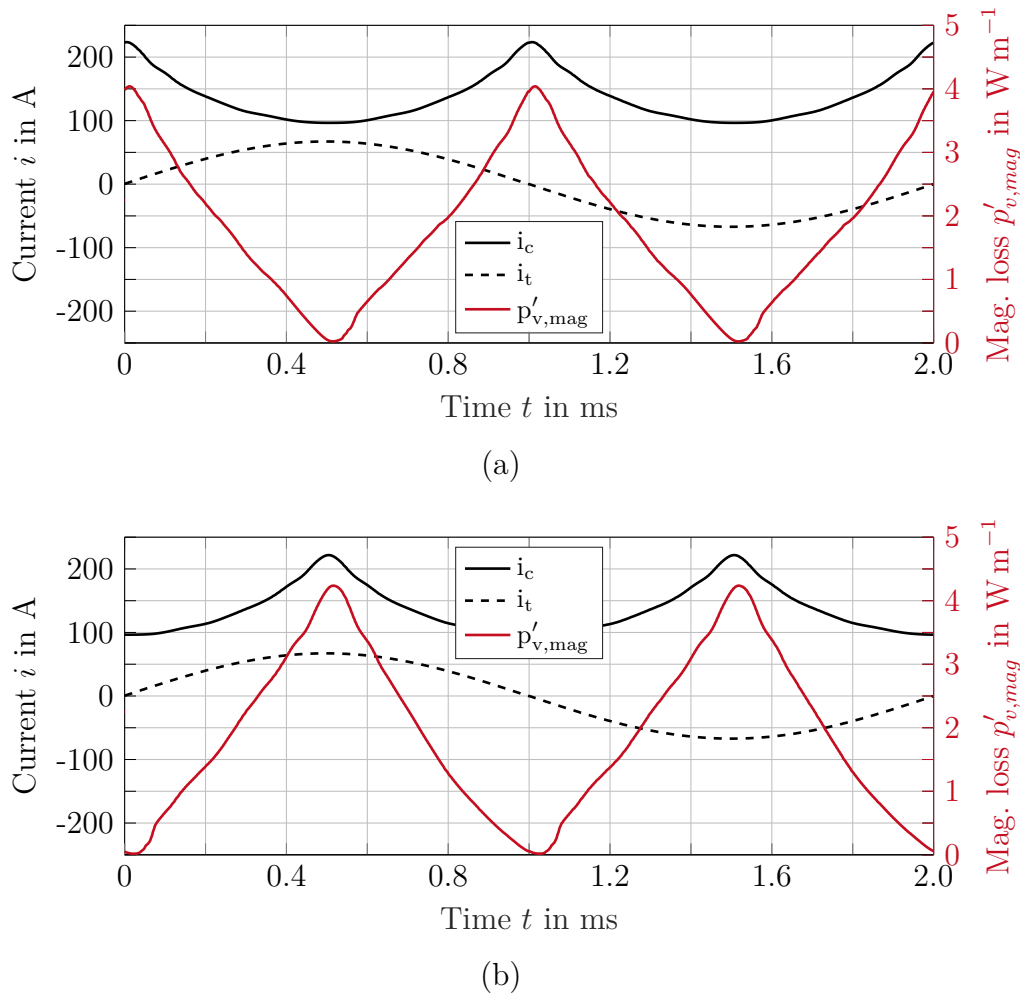


Figure 2.16.: Instantaneous transport current i_t , the instantaneous critical current i_c and the instantaneous magnetization loss per unit length $p'_{v,mag}$ as a function of the time t for the 114 filament wire with the input parameters in Table 2.6 and for a:

- (a) Phase angle of 0° between external field and transport current.
- (b) Phase angle of 90° between external field and transport current.

The peak of magnetization loss occurs when $\partial B/\partial t$ becomes maximal and therefore the flux density is zero. Furthermore, the non-linearity of the superconductor is visible in the loss curve. However, the time average of the magnetization loss is practically independent from the phase angle and due to the minimal impact, it is neglected in further AC loss calculations.

The adapted geometry of the 114 filament wire in Figure 2.1b is not rotationally symmetrical. For this reason, the influence of the spatial rotation angle θ_{sc} on the magnetization loss per unit length $P'_{v,mag}$ is investigated and the results are shown in Figure 2.17a. The adaptation of the geometry has no significant influence on the magnetization losses and therefore requires no detailed consideration.

A further investigation is done regarding the frequency dependence of magnetization loss. The target is to reduce the loss calculation to the magnetization loss density

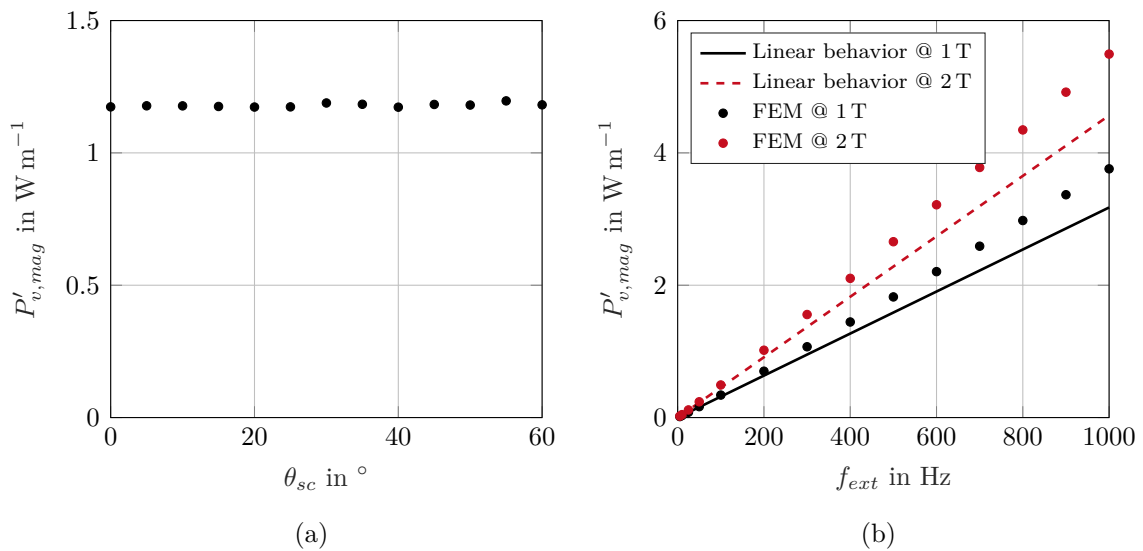


Figure 2.17.: Magnetization loss results for the 114 filament wire with the input parameters in Table 2.6:

- (a) Magnetization loss per unit length $P'_{v,mag}$ as a function of the rotation angle θ_{sc} .
- (b) Magnetization loss per unit length $P'_{v,mag}$ as a function of the external frequency f_{ext} .

$Q_{v,mag}$ by using Equation 2.8 and thus to be independent of the frequency. Figure 2.17b compares FEM results with an ideal linear dependence. It can be seen that the loss has a moderate quadratic dependence on the frequency, which results in a maximum deviation of 20% between linear approximation and FEM result at 1000 Hz and 2 T. The amount of deviation also varies with the magnitude of the magnetic flux density visible as an example for 1000 Hz and 1 T with a maximum deviation of a 18%. This means that even a field-dependent correction cannot be introduced. To eliminate the frequency dependence, the magnetic flux density is calculated at 1000 Hz, whereby the losses for frequencies less than 1000 Hz are determined slightly too high. Thus, it is possible to determine the magnetization loss density $Q_{v,mag}$ in an acceptable calculation time depending on the three most important influencing parameters: the flux density, the normalized current and the temperature. The calculation is based on the measured temperatures shown in Figure 2.6a and is limited to temperatures below 30 K.

It can be seen in Figure 2.18 that with decreasing temperature, the magnetization loss density decreases, because the critical current density and thus the penetration flux density decreases according to Equation 2.6. This increases the normalized flux density amplitude, which decreases the loss density according to Equation 2.7 case 3. Furthermore, the flux density has a much greater influence on the magnetization loss density than the normalized current. This can also be seen in Figure 2.19a at a normalized current of 0.7. The impact of the normalized current is visible at low flux densities and at a temperature of 20 K in Figure 2.18a, due to the high critical current densities at this temperature. With increasing temperature and flux density the influence of the normalized current is decreasing. This fact is additionally shown

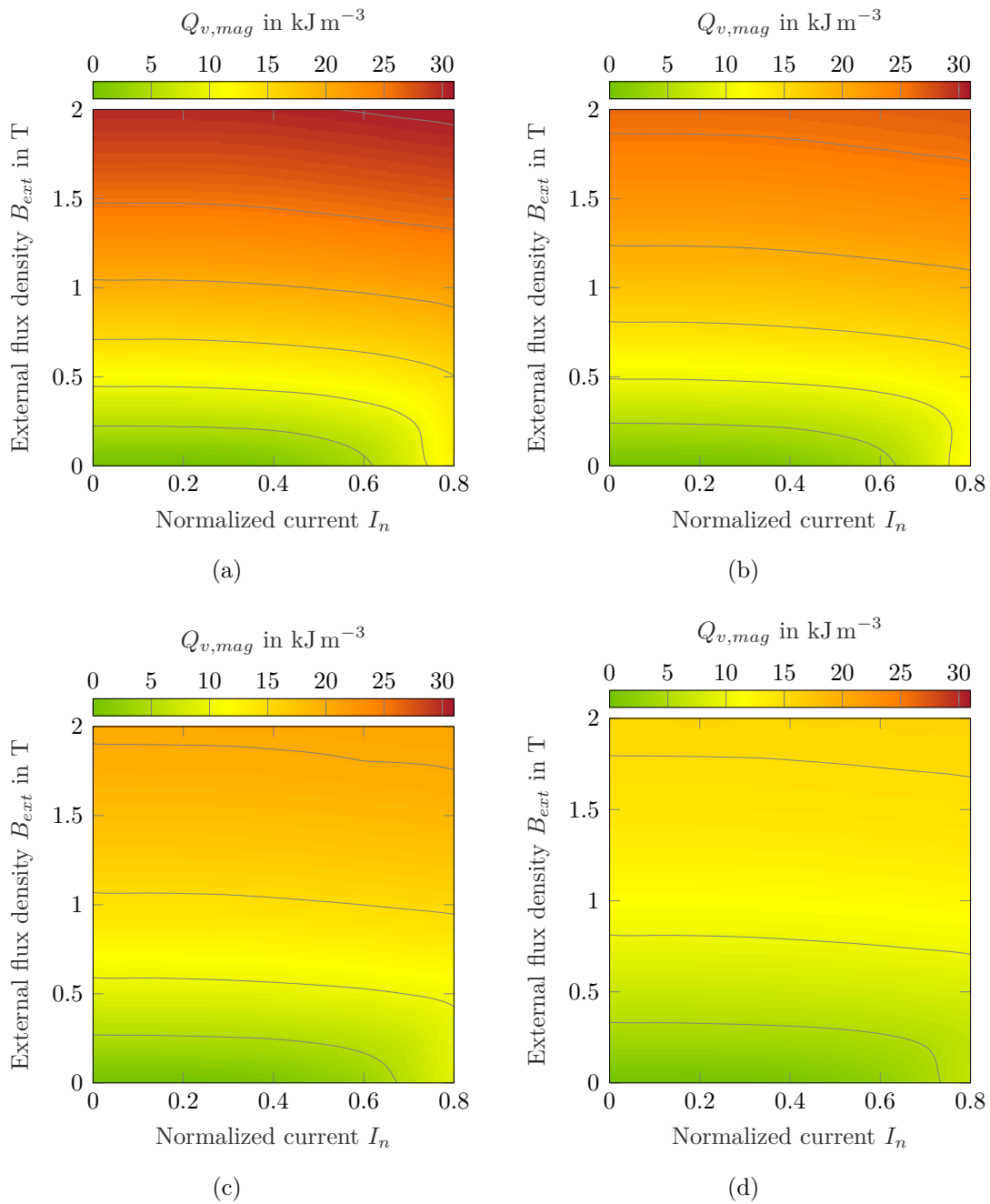


Figure 2.18.: Magnetization loss density $Q_{v,mag}$ of the 114 filament wire as a function of the external flux density B_{ext} and the normalized current I_n for a: (a) Temperature T of 20 K. (b) Temperature T of 22 K. (c) Temperature T of 25 K. (d) Temperature T of 27 K.

in Figure 2.19b at a flux density of 0.1 T.

Due to the higher accuracy of the magnetization loss calculated by FEM, these results are integrated into the analytical calculation and replace the loss component according to Equation 2.8.

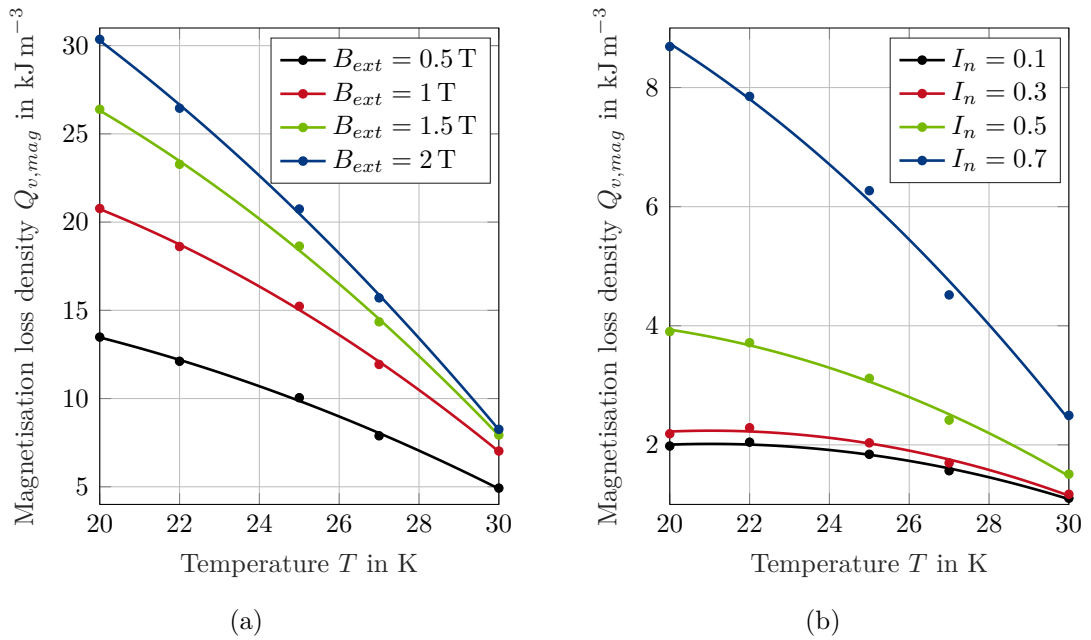


Figure 2.19.: Magnetization loss density $Q_{v,mag}$ of the 114 filament wire as a function of the temperature T for a:
 (a) Normalized current of 0.7 and different external flux densities B_{ext} .
 (b) External flux density of 0.1 T and different normalized currents I_n .
 The points present the loss at the measured temperature values and the line illustrates the quadratic fit between these points.

2.4. Summary and Recommendation

The major loss components are the magnetization loss, the eddy current loss and the coupling current loss, which add up to the total AC loss. In the AC loss model of this work, the magnetization loss is calculated by FEM and all other components are calculated analytically. They are mainly influenced by the external alternating magnetic field penetrating the wire, the normalized current of the wire and the wire design. For the latter, design specifications can be collected in the following, which characterizes an AC loss optimized MgB_2 multifilament wire.

Firstly, if the filament radius is reduced, the magnetization loss is decreasing as long as no critical current degradation due to mechanical stress occurs. This can happen, for example, by bending and twisting the wire, which is essential in AC coils. Twisting reduces efficaciously the coupling current loss, which is further influenced by the specific resistance of the matrix material. The matrix ensures thermal and mechanical stability of the filaments and must therefore have sufficient thermal conductivity for more robustness during operation [140]. Coupling current loss cannot be completely prevented in such wires. In the 114 filament wire, it generates the majority of total loss and is strongly field and frequency dependent, as can be seen in Figure 2.20 at fields between 0.5 T–1.5 T and frequencies between 100 Hz–500 Hz. The magnetization loss is significantly lower and with less field and frequency dependence, which can be explained by the high number of filaments. The eddy current loss is very low due to the low copper fraction in the conductor.

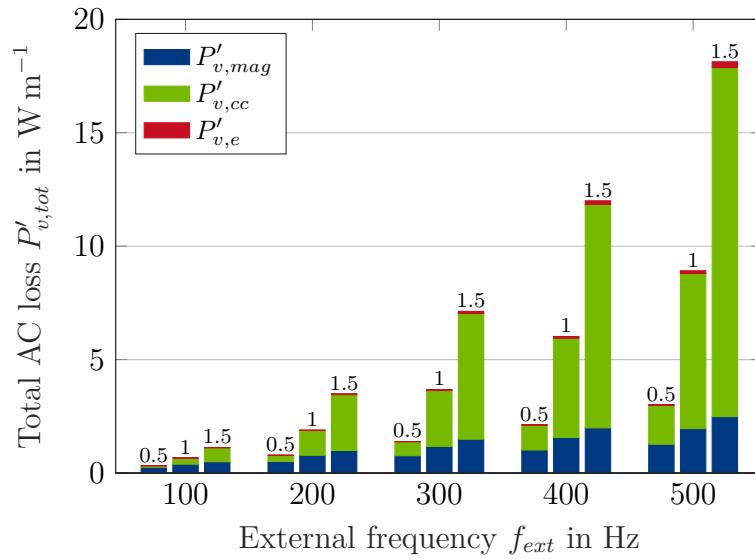


Figure 2.20.: Comparison of the loss components per unit length of the 114 filament wire depending on the external frequency f_{ext} and the flux density B_{ext} (on the bars) at a normalized current I_n of 0.7 and a temperature T of 20 K.

In the future, the aim will be to characterize the AC loss of a superconductor by measurement at high field and frequency as well as cryogenic temperatures [141]. Overall, it is demonstrated that the AC loss of MgB₂ wires can be calculated with analytical approaches with integrated FEM results. This is a fast and sufficient possibility to calculate the AC loss within the machine design.

The temperature dependencies of the critical current density and the AC loss are not taken into account in the developed model so far. Therefore, the following chapter examines the temperature increase of the superconducting wire while cooling.

3. Electro-Thermal Model of Magnesium Diboride Wires

The critical current density of a superconducting wire depends on the wire temperature and the magnetic field, which is specified by the respective application in general. Especially the wire temperature is affected by the AC loss of the wire. This non-negligible effect is considered through the development of an electro-thermal coupled model in this section. Therefore, the static temperature distribution in a cooling slot and inside a MgB_2 wire is calculated at different operating points. For comparison, a copper wire is considered for the design of machines with a normal conducting stator.

The calculation procedure includes the electro-magnetic behavior of the superconductor (SC behavior) and a model of the cooling process (cooling), as shown in Figure 3.1. Both parts, which are described in detail below, influence each other and are therefore calculated iteratively until a static state is reached. The input parameters of the model are the geometry and the normalized current I_n of the superconductor as well as the flux density B_{ext} and the frequency f_{ext} of the external field. The various components of the AC loss that are described in Section 2.3

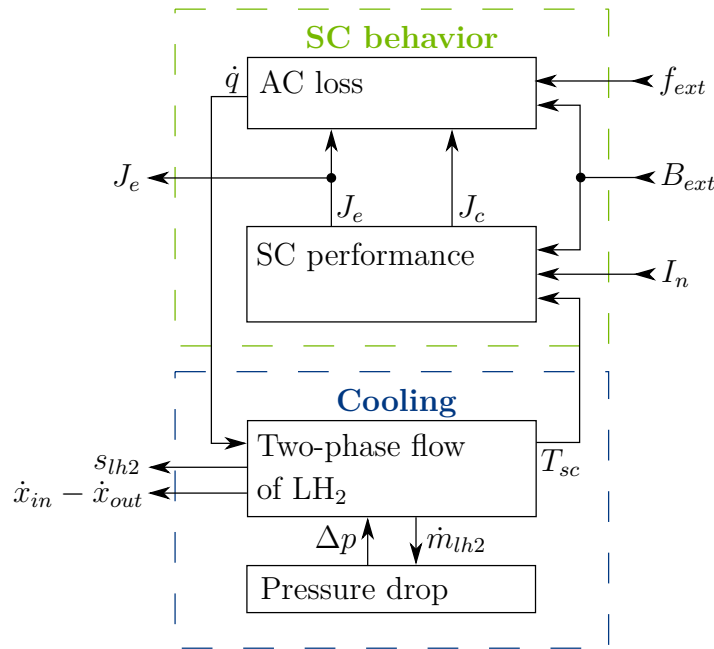


Figure 3.1.: Calculation procedure of the electro-thermal model divided into SC behavior and cooling. [142]

cause heat fluxes \dot{q} that occur at different locations in the wire, as shown in Figure 2.7. These local sources of heat affect the temperature distribution T_{sc} in the wire, which is cooled by a two-phase flow of liquid hydrogen (LH_2). Furthermore, the evaporation of liquid hydrogen is calculated analytically and the pressure drop Δp is considered. Both processes are described in more detail in Section 3.2 for the heat

transfer and Section 3.3 for the pressure drop. The new temperature of the MgB_2 is defined at the local maximum at the innermost point of the wire and results a new critical current density J_c . This current density is used to determine the engineering current density J_e by multiplication with the normalized current. The calculation loop is closed with the new AC loss for this new current density. In addition, this calculation procedure is illustrated by the flowchart in Figure B.1. The cooling slot thickness s_{lh2} and the vapor quality at the beginning \dot{x}_{in} and ending \dot{x}_{out} of the cooled wire are additional output parameters, as shown in Figure 3.1 and 3.2.

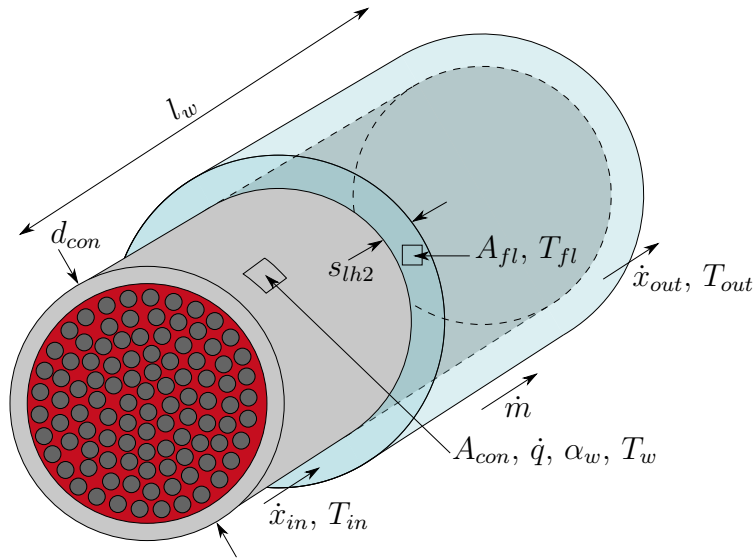


Figure 3.2.: Three-dimensional view of a multifilament MgB_2 wire with a normal conducting matrix ■ cooled with evaporating liquid hydrogen ■ in axial flow direction through the whole superconductor surface. The filaments and the outer sheath are marked ■ and ■, respectively.

Equation 3.1 defines the vapor quality \dot{x} by the quotient of the vapor mass flow rate \dot{m}_v and the total mass flow rate \dot{m} .

$$\dot{x} = \frac{\dot{m}_v}{\dot{m}} \quad (3.1)$$

It is assumed that the heat emitted over the wire surface must be equal to the heat output during evaporation of liquid hydrogen. This equilibrium is determined by the left and right parts of Equation 3.2.

$$\dot{m} A_{fl} \Delta \dot{x} \Delta h_v = \dot{q} A_{con} \quad (3.2)$$

The cross section of the cooling slot A_{fl} and the conductor shell surface A_{con} are defined in Equation 3.3 as well as 3.4 and are illustrated in Figure 3.2. The specific enthalpy Δh_v and further properties of hydrogen are explained in more detail in Section 3.1.

$$A_{fl} = \frac{\left((d_{con} + s_{lh2})^2 - d_{con}^2 \right) \pi}{4} \quad (3.3)$$

$$A_{con} = \pi d_{con} l_w \quad (3.4)$$

In this model, the assumption is made that only already hydrodynamically formed flows occur. Anomalies at the inlet of the cooling slot are neglected. In addition, the thermal properties of the cooling medium and the materials along the cooling slot change due to the continuous input of heat. Therefore it is essential to calculate the temperature distribution iteratively along the cooling slot.

3.1. Properties of Hydrogen

This section introduces the most important thermodynamic properties of hydrogen to allow a better understanding of the wire cooling.

Figure 3.3 presents the T - s diagram with the specific entropy s of liquid hydrogen depending on the temperature T . In addition, isobars and constant vapor qualities \dot{x} are shown. The evaporation enthalpy Δh_v is calculated at the temperature, the pressure p and the free optimization parameters the vapor qualities \dot{x}_{in} and \dot{x}_{out} .

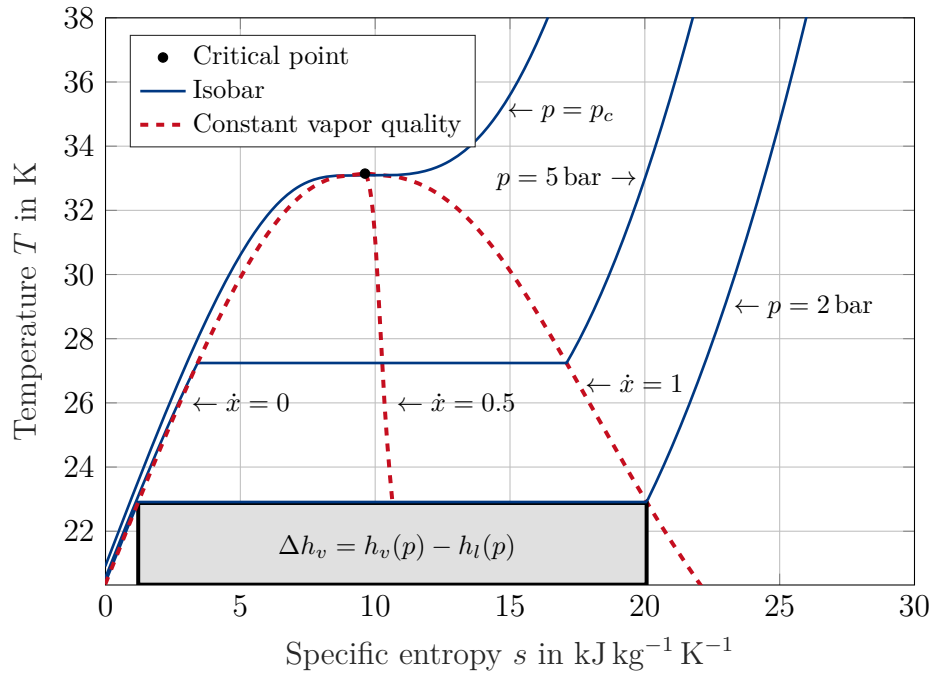


Figure 3.3.: T - s diagram of hydrogen with a descriptive determination of the evaporation enthalpy Δh_v at different pressures p and vapor qualities \dot{x} . Produced with data from [143].

An example for the determination of the evaporation enthalpy at a pressure of 2 bar and a vapor quality from 0 to 1 is shown in the T - s diagram. The evaporation enthalpies at boiling and dew point are h_l and h_v , respectively. The operating point for the two-phase cooling can be freely adjusted below the entire vapor curve, which is limited at the critical pressure of hydrogen p_c .

Figure 3.4 shows the three phases of hydrogen in a p - T diagram. The triple point is defined at the corresponding pressure p_{tri} and temperature T_{tri} at which solid,

liquid and vapor phases of a substance coexist in equilibrium. Furthermore, the liquid-vapor critical point is given at the end point of the pressure-temperature curve at which a liquid and its vapor can coexist. This point is defined at the critical pressure p_c and critical temperature T_c . Both points must not be exceeded and thus are limiting the operational range.

The operating temperature of liquid hydrogen, as marked in Figure 3.4, is defined between 20 K and 30 K due to the minimum pressure of 1 bar and the critical current measurements of the 114 filament wire in Section 2.2, respectively.

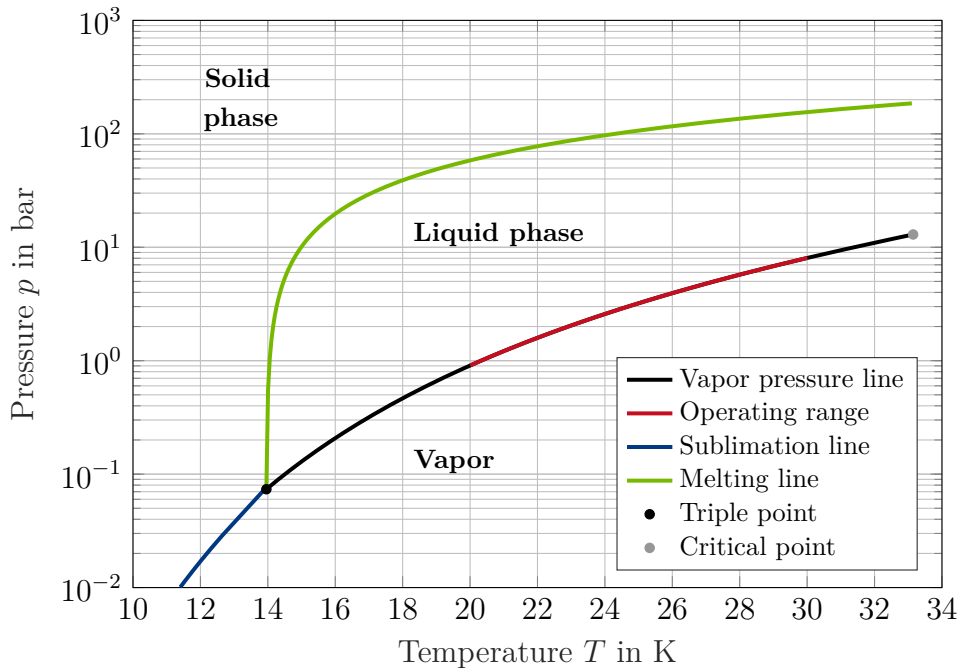


Figure 3.4.: Phase diagram of hydrogen with the marked operating range between 20 K and 30 K. Produced with data from [143].

Thermodynamic and transport properties of hydrogen are provided by the library for fluid properties REFPROP and the electro-thermal model is implemented in Matlab 2019b [143].

3.2. Heat Transfer

The heat transfer is mainly characterized by the heat transfer coefficient of the wall α_w and can be implemented by a single-phase flow or two-phase flow. For this reason, the calculation of both variants, based on [144], are presented in the next sections and a comparison of the variants is carried out.

3.2.1. Single-Phase Flow

The heat transfer coefficient for single-phase flows α_{sp} is given by Equation 3.5 with the thermal conductivity λ_m at average liquid temperature, the hydraulic diameter d_h and the Nusselt number Nu_{sp} [144].

$$\alpha_{sp} = \frac{\lambda_m Nu_{sp}}{d_h} \quad (3.5)$$

The hydraulic diameter is a commonly used quantity to describe flow conditions in non-circular tubes and is defined by its area A_{fl} and circumference U_{fl} of this non-circular geometry. For an annular gap and a rectangular duct the hydraulic diameters are given by Equation 3.6 and Equation 3.7, respectively.

$$d_{h,ann} = 4 \frac{A_{fl}}{U_{fl}} = 4 \frac{\frac{\pi}{4} (d_{out}^2 - d_{in}^2)}{\pi (d_{out} + d_{in})} = d_{out} - d_{in} = s \quad (3.6)$$

$$d_{h,rec} = 4 \frac{A_{fl}}{U_{fl}} = 4 \frac{a b}{2(a + b)} \quad (3.7)$$

The Nusselt number is mainly determined by the Reynolds number Re , which characterizes the type of flow and is given in Equation 3.8 with the dynamic viscosity η_m , the volumetric mass density ρ_m and the flow velocity w_m at average temperature. It is distinguished between laminar flow ($Re \leq 2300$), turbulent flow ($Re \geq 10^4$) and the transition between both.

$$Re = \frac{\rho_m w_m d_h}{\eta_m} \quad (3.8)$$

Consequently, the Nusselt number at laminar flows $Nu_{sp,lam}$, which is valid for the entire cooling slot length, is given by Equation 3.9 including the Prandtl number Pr in Equation 3.10 with the specific heat capacity $c_{p,m}$ at average temperature [144].

$$Nu_{sp,lam} = \left(4.634^3 + 0.6^3 + \left(1.953 \left(Re Pr \frac{d_h}{l} \right)^{-3} - 0.6 \right)^3 \right)^{-3} \quad (3.9)$$

$$Pr = \frac{\eta_m c_{p,m}}{\lambda_m} \quad (3.10)$$

Further, the Nusselt number at turbulent flows $Nu_{sp,tur}$, which is valid for the local cooling slot position z , is defined in Equation 3.11 with the factor ξ in Equation 3.12.

$$Nu_{sp,tur} = \frac{\frac{\xi}{8} Re Pr}{1 + 12.7 \sqrt{\frac{\xi}{8}} (Pr^{\frac{2}{3}} - 1)} \left(1 + \frac{1}{3} \left(\frac{d_h}{z} \right)^{\frac{2}{3}} \right) \quad (3.11)$$

$$\xi = (1.8 \log(Re) - 1.5)^{-2} \quad (3.12)$$

The Nusselt number at intermediate flow $Nu_{sp,int}$ is determined by Equation 3.13.

$$Nu_{sp,int} = \left(1 - \frac{Re - 2300}{10^4 - 2300} \right) Nu_{sp,lam}(Re = 2300) + \frac{Re - 2300}{10^4 - 2300} Nu_{sp,tur}(Re = 10^4) \quad (3.13)$$

3.2.2. Two-Phase Flow

The heat transfer coefficient for two-phase flows α_{tp} is a combination of the heat transfer coefficient of convective boiling α_k and the heat transfer coefficient of nucleate boiling α_b according to Equation 3.14 [144].

$$\alpha_{tp} = \sqrt[3]{\alpha_k^3 + \alpha_b^3} \quad (3.14)$$

Both heat transfer coefficients are given by the empirical estimated Equations 3.15 and 3.19 and are valid for two-phase flows of liquids in horizontal pipes [144, 145]. This is the worst case compared to a vertical arrangement. Due to gravity, the liquid phase can be stratified. This results in partial wetting of the heating wall with a generally reduced heat transfer.

$$\begin{aligned} \alpha_k = \alpha_{l0} & \left((1 - \dot{x})^{0.01} \left((1 - \dot{x}) + 1.2\dot{x}^{0.4} \left(\frac{\rho_l}{\rho_v} \right)^{0.37} \right)^{-2.2} \right. \\ & \left. + \dot{x}^{0.01} \left(\frac{\alpha_{v0}}{\alpha_{l0}} \left(1 + 8(1 - \dot{x})^{0.7} \left(\frac{\rho_l}{\rho_v} \right)^{0.67} \right) \right)^{-2} \right)^{-0.5} \end{aligned} \quad (3.15)$$

In the following, the heat transfer coefficients α_{l0} and α_{v0} are defined if the whole cooling medium is flowing in the liquid or the vapor phase with the corresponding Nusselt number and thermal conductivity.

$$\alpha_{l0} = \frac{Nu_l \lambda_l}{d_h} \quad (3.16)$$

$$\alpha_{v0} = \frac{Nu_v \lambda_v}{d_h} \quad (3.17)$$

Nucleate boiling activates if the heat flux \dot{q}_{on} is exceeded at the wire wall, as given in Equation 3.18 with the surface tension of the liquid σ_l , the roughness of the wall R_w and the volumetric mass density of the vapor ρ_v . If this overheating does not occur, only convective boiling has to be considered in Equation 3.14. This is especially the case in the range of vapor qualities smaller than 0.3 [144].

$$\dot{q}_{on} = \frac{2 \sigma_l T \alpha_{l0}}{R_w \rho_v \Delta h_v} \quad (3.18)$$

The heat transfer coefficient of nucleate boiling is defined by the following equation:

$$\alpha_b = \begin{cases} \alpha_n \left(C_n \left(\frac{\dot{q}}{\dot{q}_n} \right)^{n^*} \left(2.692 p^{*0.43} + \frac{1.6 p^{*6.5}}{1 - p^{*4.4}} \right) \right. \\ \cdot \left(\frac{d_n}{d} \right)^{0.5} \left(\frac{R_w}{R_{w,n}} \right)^{0.133} \left(\frac{\dot{m}}{\dot{m}_n} \right)^{0.25} & \text{if } \dot{q} \geq \dot{q}_{on} \\ \cdot \left(1 - p^{*0.1} \frac{\dot{q}}{\dot{q}_{cr,PB}} \right)^{0.3} \dot{x} & \end{cases} \quad (3.19)$$

The normalization values d_n , $R_{w,n}$, \dot{m}_n , α_n , \dot{q}_n and the constant value C_n that are used in Equation 3.15 and 3.19 are summarized in Table 3.1. The exponent n^* and the normalized pressure p^* are given in Equation 3.20 and 3.21 with the inlet pressure p_{in} and the critical pressure p_c . A detailed calculation of the reference heat flux $\dot{q}_{cr,PB}$ is presented in [144].

Table 3.1.: Constants and normalization values of evaporating hydrogen for the heat transfer coefficient calculation [144].

Parameter	Value	Parameter	Value
d_n	$1 \cdot 10^{-2} \text{ m}$	α_n	$12\,220 \text{ W m}^{-2} \text{ K}^{-1}$
$R_{w,n}$	$1 \cdot 10^{-6} \text{ m}$	\dot{q}_n	$10\,000 \text{ W m}^{-2}$
\dot{m}_n	$100 \text{ kg s}^{-1} \text{ m}^{-2}$	C_n	0.79
p_c	12.97 N m^{-2}		

$$n^* = 0.9 - 0.44 p^{*0.085} \quad (3.20)$$

$$p^* = \frac{p_{in}}{p_c} \quad (3.21)$$

After the heat transfer coefficients α_w of both flows have been calculated, the wall temperature T_w of the wire can be determined. As schematically illustrated in Figure 3.2, this temperature is computed with the heat flux \dot{q} generated by the total AC loss of the wire in the following equation:

$$T_w = T_{fl} + \frac{\dot{q}}{\alpha_w} \quad (3.22)$$

3.2.3. Feasibility Analysis

The heat dissipation of a multifilament MgB₂ wire with a single-phase flow and a two-phase flow of hydrogen are compared at expected operating temperatures in this section.

In the following, the 114 filament wire described in Section 2.1 is assumed to be cooled at the conditions according to Table 3.2. The heat flux \dot{q} is calculated by

Table 3.2.: Input parameters for a benchmark cooling calculation for single-phase flow and two-phase flow of liquid hydrogen.

Parameter	Value	Parameter	Value
T_{in}	20.0 K	\dot{q}	0.43 W cm^{-2}
p	1 bar	s_{lh2}	1 mm
\dot{x}_{in}	0	w_{sp}	57.4 m s^{-1}
\dot{x}_{out}	1	l_w	1 m

the total AC loss of the 114 filament wire at a flux density of 1 T, a frequency of 500 Hz and a normalized current of 0.7. Furthermore, an inlet temperature T_{in} of 20 K is chosen for both flow states. To simplify the calculation, the pressure drop is neglected and the pressure p is set to 1 bar. For comparison, both calculations are carried out with the same cooling slot thickness s_{lh2} and heat flux \dot{q} . The velocity of the single-phase flow w_{sp} is selected such that a turbulent flow occurs and the vapor quality of the two-phase flow at the beginning \dot{x}_{in} and ending \dot{x}_{out} of the cooling slot are specified as 0 and 1, respectively.

Figure 3.5 shows that the heat transfer coefficient of a two-phase flow is about five times higher compared to single-phase flow. Accordingly, the wall temperatures are

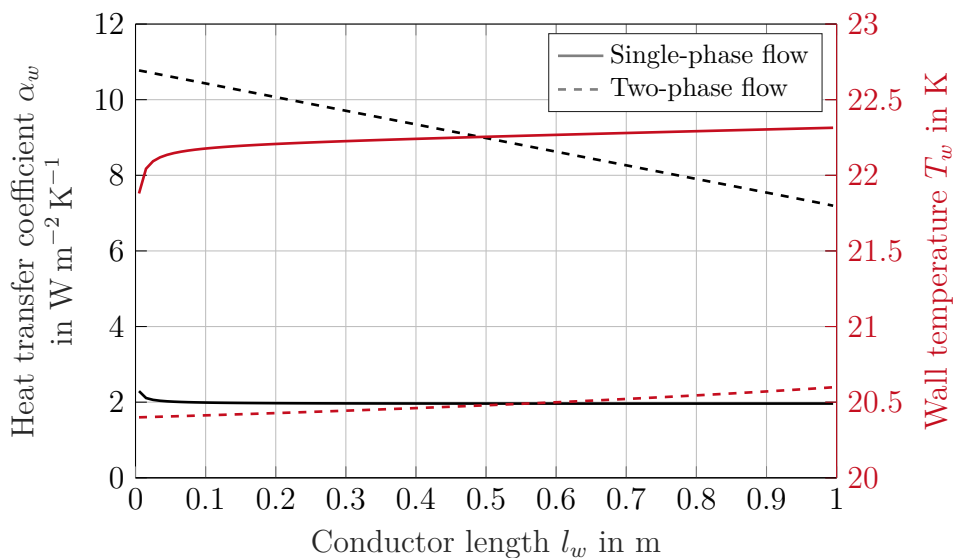


Figure 3.5.: Heat transfer coefficient α_w and wall temperature T_w as a function of the wire length l_w for an exemplary wire cooling at single-phase and two-phase flow.

lower with two-phase cooling. The difference is about 1.75 K over the entire length of the wire. This temperature difference would lead to an essential reduction of the critical current density, as shown in Figure 2.6a. To counteract this, sub-cooled liquid hydrogen could be used.

However, turbulent single-phase flows have a higher heat transfer coefficient than laminar flows. But this requires high flow velocities and thus high volume flows, which are about $100 \text{ cm}^3 \text{ s}^{-1}$ in case of a single-phase flows. This is much higher compared to the two-phase cooling with about $0.26 \text{ cm}^3 \text{ s}^{-1}$, because it requires large amounts of liquid hydrogen. Therefore, single-phase cooling is not feasible due the high necessary volume flow caused by the AC loss in the superconductor. Furthermore, the amount of hydrogen for single-phase flow would also be too high for an application in an aircraft. The cooling energy is provided by a hydrogen tank with limited space on board of an aircraft, as introduced in Section 6.2. As a consequence, a large amount of the cooling energy of the hydrogen would be unused due to the low usable temperature range in a MgB_2 application.

The high flow velocity would also lead to a high pressure drop which would be

another disadvantage. The calculation of the pressure drop in both flow states is presented in the next section.

3.3. Pressure Drop

The determination of the pressure drop Δp is an important part of the calculation to stay within the operating range shown in Figure 3.3 and 3.4. The total pressure drop Δp_{tot} consists of the frictional pressure drop Δp_{fric} , gravitational pressure drop Δp_{grav} and accelerational pressure drop Δp_{acce} according to Equation 3.23 [144].

$$\Delta p_{tot} = \Delta p_{fric} \pm \Delta p_{grav} + \Delta p_{acce} \quad (3.23)$$

It is assumed that the gravitational and acceleration pressure drop are much smaller than the frictional pressure drop for steady state flows [146]. Consequently, only the frictional pressure drop is considered:

$$\Delta p_{tot} = \Delta p_{fric} = \Delta p$$

The pressure drop calculation starts with the single-phase flow situation and afterwards the two-phase flow is considered, because the calculations are based on each other.

3.3.1. Single-Phase Flow

The single-phase pressure drop Δp_{sp} depends on the mass flow rate \dot{m} , the length of the cooling channel section Δl_w , the volumetric mass density ρ and the hydraulic diameter d_h [147].

$$\Delta p_{sp} = f_{sp} \frac{2 \Delta l_w \dot{m}^2}{\rho d_h} \quad (3.24)$$

The Fanning friction factor f_{sp} given in Equation 3.26 depends on the Reynolds number Re , which determines the flow regime as laminar or turbulent.

$$Re = \frac{\dot{m} d_h}{\eta} \quad (3.25)$$

It is expected that only turbulent flows occur with a Reynolds number Re larger than 2300 and different correlations for different ranges [144]:

$$f_{sp} = \begin{cases} \frac{0.3164}{\sqrt[4]{Re}} & \text{if } 2300 \leq Re < 10^4 \\ (1.8 \lg(Re) - 1.5)^{-2} & \text{if } 10^4 \leq Re \leq 10^6 \\ \left(2 \lg(Re \sqrt{f_{sp}}) - 0.8\right)^{-2} & \text{if } Re > 10^6 \end{cases} \quad (3.26)$$

3.3.2. Two-Phase Flow

The two-phase frictional pressure drop is modeled by the Lockhart-Martinelli correlation [148] with the multiplier Φ^2 to relate the two-phase pressure drop Δp_{tp} to the reference single-phase pressure drop Δp_{sp} . It is assumed that only one of the two phases is flowing in the annular gap.

$$\Delta p_{tp} = \Phi_{l,tt}^2 2 f_{sp} \frac{\Delta l_w \dot{m}^2 (1 - \dot{x})^2}{d_h \rho_l} \quad (3.27)$$

McFarlane [149] describes a simple equation, which approximates the Lockhart-Martinelli multiplier $\Phi_{l,tt}^2$ for the case of turbulent flow in both phases:

$$\Phi_{l,tt}^2 = 1 + \frac{20}{X_{tt}} + \frac{1}{X_{tt}^2} \quad (3.28)$$

The Martinelli parameter X_{tt} is defined in Equation 3.29 with the volumetric mass densities ρ_l and ρ_v as well as the dynamic viscosities η_l and η_v at boiling and dew point, respectively.

$$X_{tt} = \left(\frac{1 - \dot{x}}{\dot{x}} \right)^{0.9} \left(\frac{\rho_v}{\rho_l} \right)^{0.5} \left(\frac{\mu_l}{\mu_v} \right)^{0.1} \quad (3.29)$$

An additional approach is presented by Equation 3.30 with the mean flow velocity $w_{m,lv}$ and the mean volumetric density $\rho_{m,lv}$ between liquid and vapor state [144]. Furthermore, the empirical coefficient f_{tp} is given in Equation 3.31.

$$\Delta p_{tp} = f_{tp} \frac{2 \rho_{m,lv} w_{m,lv}^2 \Delta l_w}{d_h} \quad (3.30)$$

$$f_{tp} = 0.00925 Re^{-0.2534} + \frac{13.98 Re^{-0.9501} - 0.0925 Re^{-0.2534}}{\left(1 + \left(\frac{Re}{293} \right)^{4.864} \right)^{0.1972}} \quad (3.31)$$

In the electro-thermal model, the calculation according to Equation 3.30 is applied, because this variant is based on a large number of measurements and is suitable if the flow type is unknown.

With the known heat transfer coefficient and the pressure drop, the temperature distribution inside the wire is calculated in the next section.

3.4. Temperature Distribution Inside the Wire

To determine the current density at the modified temperature T_{sc} according to Figure 3.1, the temperature distribution inside the wire is calculated. In this section, an analytic model is presented and cross-checked with finite element method (FEM) to compute this temperature distribution.

Due to the widely varying AC losses in the different materials of the wire, there is a high requirement on the computing time of the thermal model. Therefore, a one-dimensional temperature model is developed. For this purpose, the wire cross-section from Figure 2.1b needs to be transferred and simplified to a shell model to calculate the temperature distribution in a cylindrical coordinate system, as shown in

Figure 3.6b. In this operation, the surface ratios remain constant and the insulation thickness of the wire is taken into account. Additionally, the calculation in a cartesian coordinate system is introduced to calculate the temperature distribution in a coil, as illustrated in Figure 3.6a.

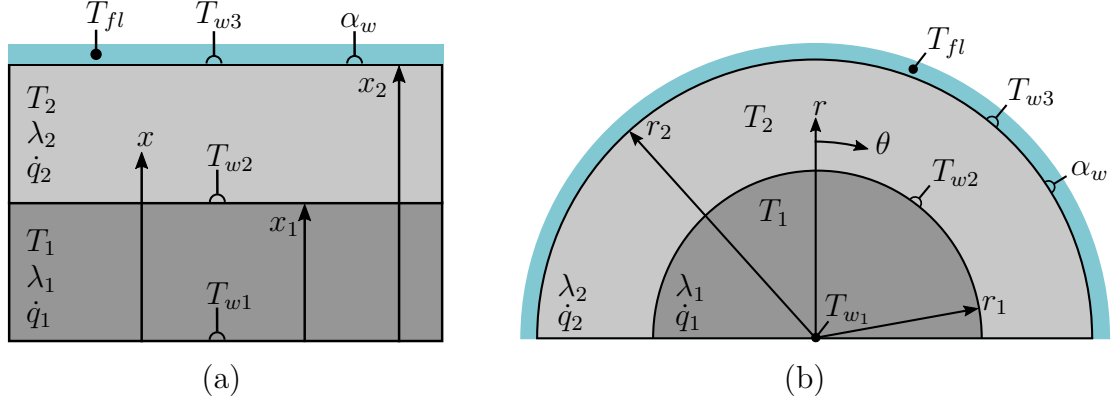


Figure 3.6.: Minimal sketch for the heat conduction calculation through a shell model in a:
 (a) Cartesian coordinate system.
 (b) Cylindrical coordinate system.
 Evaporating hydrogen is marked \blacksquare .

3.4.1. Analytical Calculation

Cartesian coordinate system

The differential heat conduction equation in cartesian coordinates is defined in Equation 3.32 with the heat flux \dot{q} , the thermal conductivity λ , the volumetric mass density ρ and the specific heat capacity at constant pressure c_p [150].

$$\lambda \frac{\partial^2 T}{\partial x^2} + \lambda \frac{\partial^2 T}{\partial y^2} + \lambda \frac{\partial^2 T}{\partial z^2} + \dot{q} = \rho c_p \frac{\partial T}{\partial t} \quad (3.32)$$

For a one-dimensional problem in x -direction, as shown in Figure 3.6a, and steady state conditions the Partial differential equation 3.32 reduces to:

$$\lambda \frac{\partial^2 T}{\partial x^2} + \dot{q} = 0 \quad (3.33)$$

with the general solution:

$$T(x) = C_1 x + C_2 - \frac{\dot{q}}{2\lambda} x^2 \quad (3.34)$$

Figure 3.6a illustrates the convective heat transfer in cartesian coordinates between two layers and the cooling fluid. The heat transfer depends on the temperature differences between the walls T_w , the fluid T_{fl} and the heat transfer coefficient α_w . Each shell is characterized by a specific heat flux \dot{q} and thermal conductivity λ . Furthermore, the outermost shell is always assumed to be insulation material.

Equation 3.33 requires several boundary conditions for the determination of the coefficients C_1 and C_2 in Equation 3.34. The first boundary condition is defined by the heat transfer between the coolant and outer wall in Equation 3.35.

$$\alpha_w (T_{fl} - T_{w3}) = \lambda_2 \left. \frac{\partial T_2}{\partial x} \right|_{x=x_2} \quad (3.35)$$

Between two layers with different thermal conductivities, the same temperature occurs if the contact resistance is neglected. This correlation is defined by Equation 3.36 and represents the next boundary condition.

$$T_1 \Big|_{x=x_1} = T_2 \Big|_{x=x_1} \quad (3.36)$$

Additionally, the heat fluxes between two layers are identical and given by Equation 3.37.

$$\lambda_1 \left. \frac{\partial T_1}{\partial x} \right|_{x=x_1} = \lambda_2 \left. \frac{\partial T_2}{\partial x} \right|_{x=x_1} \quad (3.37)$$

With these boundary conditions it is now possible to calculate the coefficients C_1 and C_2 of Equation 3.34 and the detailed calculation results are listed in the Appendix A.1.

Cylindrical coordinate system

The differential heat conduction equation in cylindrical coordinates is given by [150]:

$$\frac{1}{r} \frac{\partial}{\partial r} \left(\lambda r \frac{\partial T}{\partial r} \right) + \frac{1}{r^2} \frac{\partial}{\partial \theta} \left(\lambda \frac{\partial T}{\partial \theta} \right) + \frac{\partial}{\partial z} \left(\lambda \frac{\partial T}{\partial z} \right) + \dot{q} = \rho c_p \frac{\partial T}{\partial t} \quad (3.38)$$

The calculation of the temperature distribution in the wire after the simplification to a one-dimensional problem with temperature gradients only in radial direction is shown in Figure 3.6b. In steady state conditions Equation 3.38 is reduced to:

$$\frac{1}{r} \frac{\partial}{\partial r} \left(\lambda r \frac{\partial T}{\partial r} \right) + \dot{q} = 0 \quad (3.39)$$

with the general solution:

$$T(r) = -\frac{\dot{q}}{4\lambda} r^2 + C_1 \ln(r) + C_2 \quad (3.40)$$

Figure 3.6b presents a minimal sketch of this temperature distribution in a cylindrical coordinate system. The boundary conditions are similar to these in the cartesian coordinate system and are therefore not presented. The detailed calculation results are summarized in the Appendix A.1.

For the determination of the critical current density according to Figure 3.1, the maximum temperature in the superconducting material is crucial. Therefore, only the maximum temperature of the innermost MgB₂ shell has to be calculated.

3.4.2. Numerical Calculation

The influence of the geometric simplifications on the temperature distribution inside the wire is verified by finite element simulations using COMSOL 5.3a. Table 3.3 shows the input parameters for the operation point at an external flux density B_{ext} of 1 T, a frequency f_{ext} of 500 Hz and a normalized current I_n of 0.7. It is assumed that the heat flux generation by the different AC loss components in the different materials presented in Table 2.3 are constant. Furthermore, when comparing finite element simulations to analytic calculations, the temperature dependency of the thermal conductivities are neglected. In the temperature distribution calculations according to Figure 3.1, the conductivity is temperature dependent.

Table 3.3.: Input parameters of the temperature distribution calculation at an external flux density B_{ext} of 1 T, a frequency f_{ext} of 500 Hz and a normalized current of 0.7.

Parameter	Value	Parameter	Value
\dot{q}_{sc}^1	47.6	λ_{sc}^3	6.8
\dot{q}_b^1	-	λ_b^3	8.4
\dot{q}_{cu}^1	5.6	λ_{cu}^3	8564.4
\dot{q}_{ma}^1	77.4	λ_{ma}^3	18.1
\dot{q}_{sh}^1	0.0	λ_{sh}^3	8.4
\dot{q}_{ins}^1	0.0	λ_{ins}^3	0.048
α_w^2	10.0	T_{fl}^4	20.0

¹ in W m^{-3}

² in $\text{W m}^{-2} \text{K}^{-1}$

³ in $\text{W m}^{-1} \text{K}^{-1}$

⁴ in K

Figure 3.7a shows the temperature profile of the 114 filament wire calculated by the finite element simulation with the cooling conditions presented in Table 3.3. The wire insulation thickness is assumed to be $5 \mu\text{m}$ of the polyimide Kapton and is cooled over the entire surface. The dielectric strength of Kapton is approximately $291 \text{ V } \mu\text{m}^{-1}$ [151]. This is the maximum electric field that the material can withstand without an electrical breakdown under ideal conditions. Furthermore, the thermal conductivity λ_{ins} is assumed according to [152]. The thermal conductivity of this polyimide is presented in Appendix C.3. This represents a conservative assumption, because higher thermal conductivities were also measured by [153]. For comparison, Figure 3.7b shows the simplified geometry of the wire as a shell model whose temperature distribution is reduced to a one-dimensional problem in cylindrical coordinates. The area ratios and the total loss of the wire remains constant.

Furthermore, the temperature distribution in radial direction is shown in Figure 3.8a for both the finite element models and the analytical approach. The simplification of the wire geometry shows no significant effect on the temperature profile. Therefore, the analytical approach presented in Section 3.4.1 can be used. Due to its low thermal conductivity, the insulation layer has the strongest influence and is mainly responsible for the temperature gradient in the wire. For example, the thermal con-

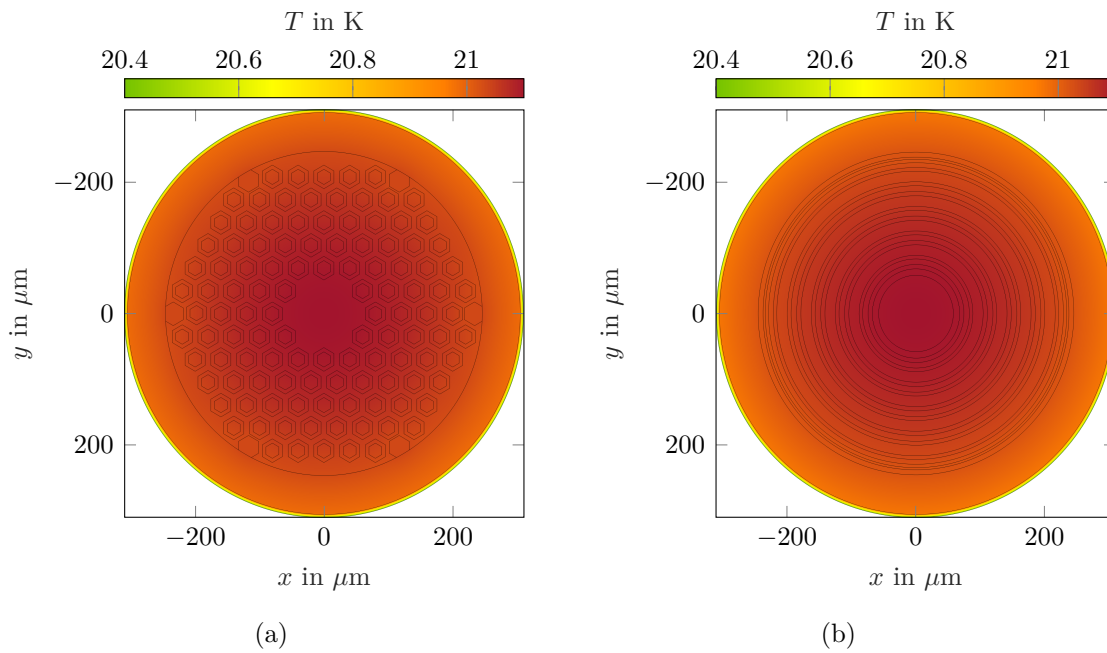


Figure 3.7.: Temperature profile of the perfect cooled:
 (a) Round 114 filament wire model.
 (b) Round shell model.

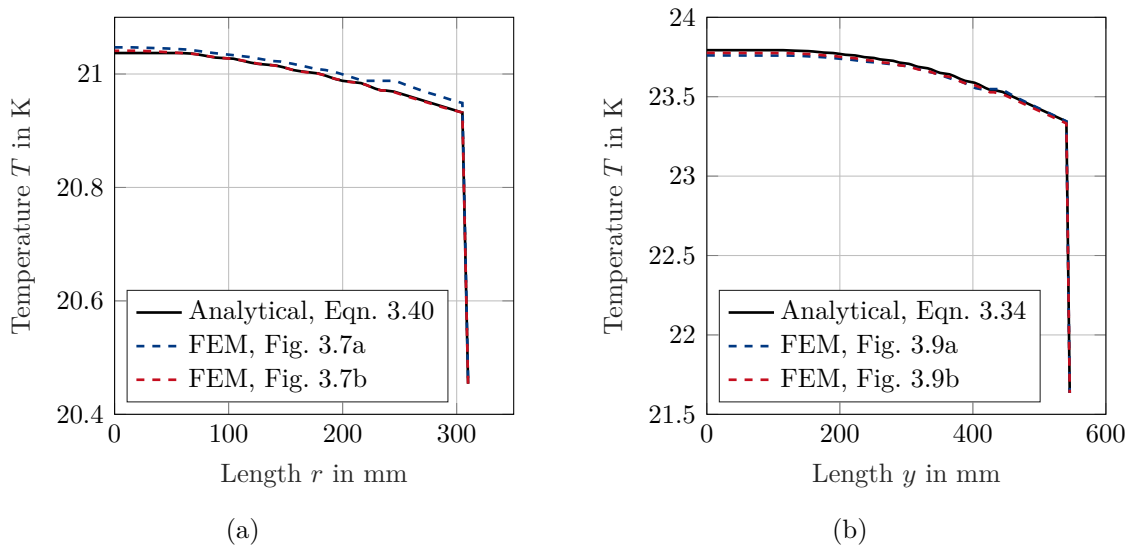


Figure 3.8.: Temperature distribution in:
 (a) r -direction of the round wire model.
 (b) y -direction of the quadratic wire model.

ductivity is about 175 times lower compared to the outer sheath material of the wire Cu30Ni. For this reason only the turn-to-turn insulation is considered by this insulation layer. Such insulation separates wires and turns of a coil. Moreover, the

slot insulation, which is implemented for the galvanical separation of a coil from earthed parts, as well as the phase-to-phase insulation are distanced and separated from the heat transfer into the liquid hydrogen. They are integrated in the support structure of the coils, as introduced in Chapter 4.

The assumption that a wire is cooled on its entire surface cannot be realized in practical applications. For this reason, the cooling area is reduced to a quarter. This has the consequence that a one-dimensional calculation in cylindrical coordinates is no longer possible. However, the round wire is transformed into a quadratic geometry, as shown in Figure 3.9a. Subsequently, this geometry is transformed in Figure 3.9b

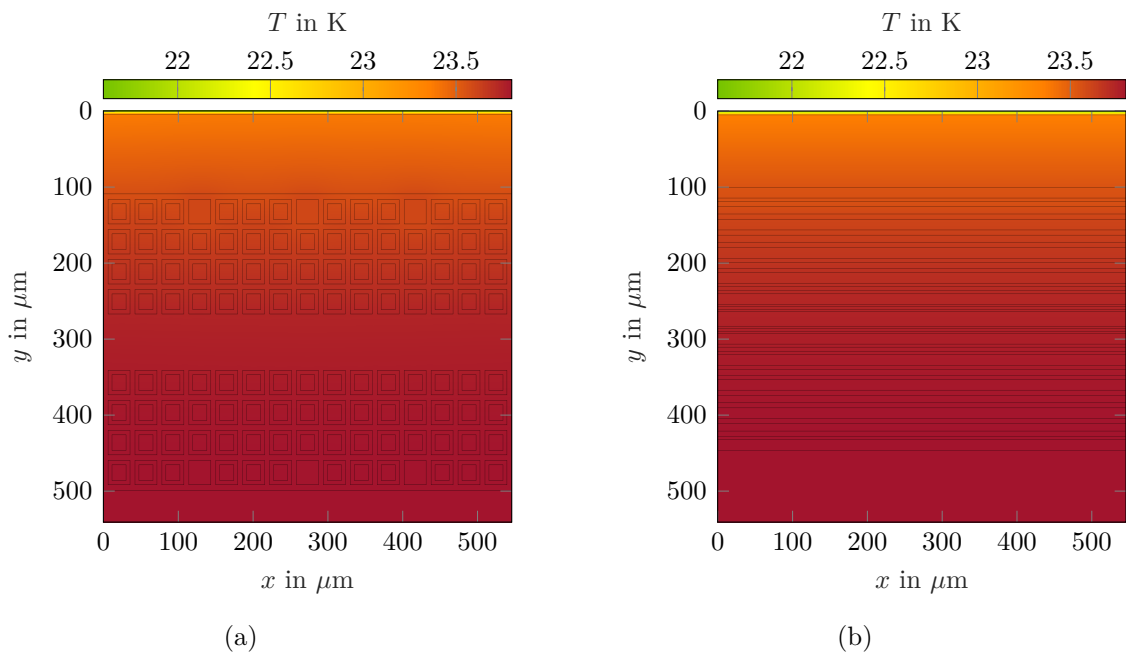


Figure 3.9.: Temperature profile of the one-side cooled:
 (a) Quadratic 114 filament wire.
 (b) Quadratic shell model.

into a shell model in order to obtain a one-dimensional problem in cartesian coordinates. Again, the insulation is responsible for the largest temperature gradient inside the wire, as shown in Figure 3.8b.

This comparison demonstrates that the analytical and one-dimensional approaches can be used to determine the temperature inside the conductor with sufficient precision.

3.5. Coupled Model Results of Electromagnetics and Thermal

In this section the coupled model results are presented according to Figure 3.1 for the 114 filament MgB_2 wire cooled with liquid hydrogen. For comparison reason a copper litz wire cooled with a silicone oil at non-cryogenic temperatures is firstly analyzed

in the next section. Furthermore, two wire cooling arrangements are presented in each case to achieve a realistic air gap winding design. It is important to note that the current densities are related to the wire cross-section and cooling area.

3.5.1. Copper Litz Wire

For the design of partially superconducting machines with a copper stator, it is necessary to calculate the engineering current density under single-phase cooling conditions. This is mainly the same procedure as for MgB_2 wires with the difference that the total conductivity of the insulated copper litz wire λ_w is known by measurement [154]. The cooling arrangement is designated as single one-side cooled, as shown in Figure 3.10. Furthermore, the silicone oil Novec is used as liquid coolant [155].

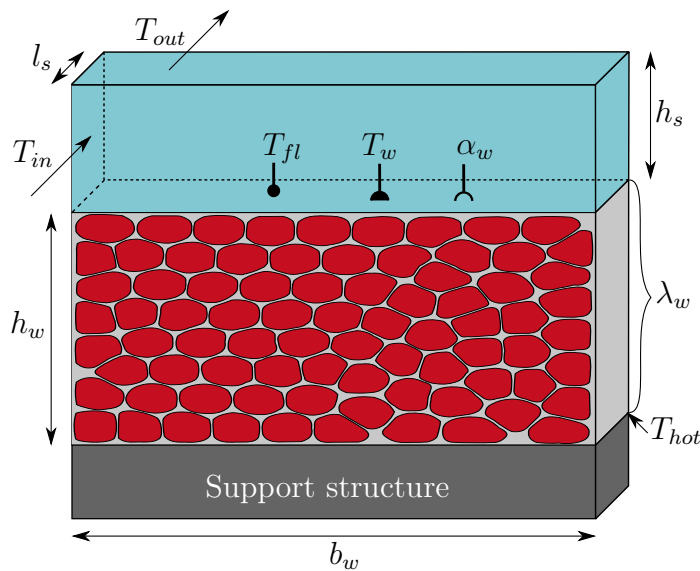


Figure 3.10.: Single one-side cooled arrangement of a potted and pressed copper litz wire ■ including insulation □.

The copper litz wire geometry is defined by the wire height h_w and the wire width b_w . Additionally, the cooling slot width is identical to the wire width and the cooling slot length l_s is identical to the wire length. An important optimization parameter is the cooling slot height h_s , because this influences the flow type and thus the heat transfer coefficient α_w . Another free parameter is the inlet temperature T_{in} , by which the outlet temperature T_{out} is calculated according to Equation 3.41 with the specific heat capacity c_p and the mass flow \dot{M} .

$$T_{out} = \frac{P_{v,tot}}{c_p \dot{M}} + T_{in} \quad (3.41)$$

The cooling slot is discretized in direction of the cooling flow, whereby input and output temperature are calculated for each segment. However, the highest cooling fluid temperature is reached in the final segment. Subsequently, the wall temperature T_w is calculated by Equation 3.42 with the cooling fluid temperature T_{fl} corresponding to the outlet temperature of the final segment.

$$T_w = \frac{P_{v,tot}}{l_s b_w \alpha_w} + T_{fl} \quad (3.42)$$

This results in a hot spot temperature T_{hot} at the inner most position of the wire given in Equation 3.43, which defines the maximum allowable temperature of the insulation.

$$T_{hot} = \frac{h_w P_{v,tot}}{l_s b_w \lambda_w} + T_w \quad (3.43)$$

The single one-side cooled arrangement described above can also be designed as double one-side cooled, as illustrated in Figure 3.13b for MgB₂ wires. This means that there is an additional copper litz wire above the cooling channel, which doubles the heat input in the cooling slot. This saves area in the stator for example through less support structure and is calculated in the following for an example.

Figure 3.11 presents the impact of the cooling slot height on the engineering current density J_{cu} of the copper litz wire and the pressure drop Δp . Further input param-

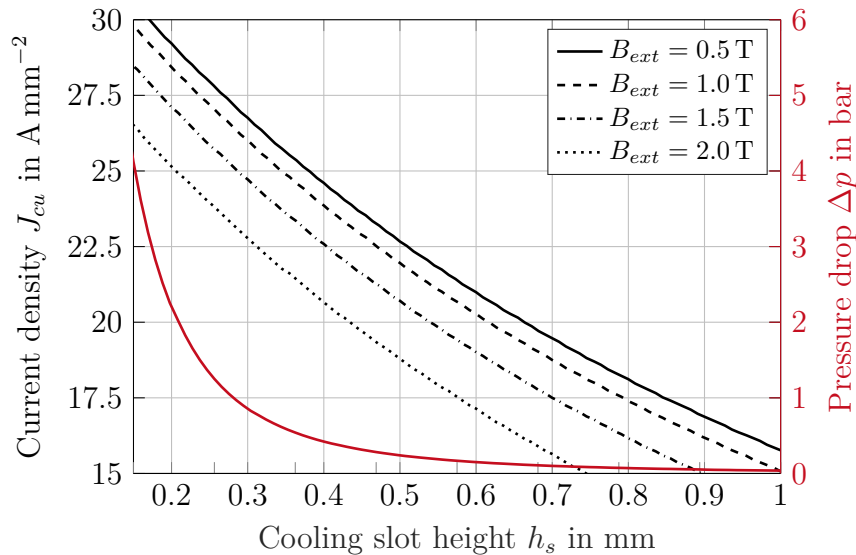


Figure 3.11.: Engineering current density of copper J_{cu} and pressure drop Δp as a function of cooling slot height h_s for a slot with double one-side cooling. The input parameters are listed in Table 3.4.

eters are the fill factor f_{fil} , the filament diameter d_{fil} as well as the volume flow rate \dot{V}_s . All parameters are summarized in Table 3.4. Additionally, the copper litz wire is penetrated by fields between 0.5 T and 2.0 T at a frequency of 500 Hz. With decreasing cooling slot height the cooling improves, because the Reynolds number rises and thus the heat transfer coefficient. This allows a higher loss which is limited by the maximum temperature T_{max} . In addition, the area of the cooling slot decreases, which also increases the maximum engineering current density, because the current density is related to the cross-section of wire and cooling slot. Furthermore, higher current densities are possible at lower external fields and frequencies. In practice, this effect is limited by the pressure drop, which rises sharply when the cooling slot

3. Electro-Thermal Model of Magnesium Diboride Wires

Table 3.4.: Input parameters of the electro-thermal calculation for an exemplary copper litz wire.

Parameter	Value	Parameter	Value
h_w	3 mm	h_s	0.5 mm
b_w	6 mm	l_s	0.5 m
f_{fil}	0.75	\dot{V}_s	$4 \text{ cm}^3 \text{ s}^{-1}$
d_{fil}	0.4 mm	T_{in}	353.15 K
λ_w	$3 \text{ W m}^{-1} \text{ K}^{-1}$ [154]	T_{max}	453.15 K

decreases. Cooling slot heights smaller than 0.28 mm lead to pressure drops of more than 1 bar at a cooling slot length of 0.5 m. For this reason, a cooling slot height of 0.5 mm is specified for further investigation. Additionally, the pressure drop is generally independent of the loss.

The current density of the copper litz wire J_{cu} as a function of the external flux density B_{ext} and frequency f_{ext} is especially important for an optimal machine design. Figure 3.12 shows this dependency for the wire geometry and cooling conditions according to Table 3.4 and for double one-side cooling. At small fields and frequencies, the maximum of the current density is around 28.5 A mm^{-2} . It is limited by the DC resistance of the copper litz wire. Furthermore, a transition with quadratic dependence between field and frequency to lower current densities is visible. As a result, the AC losses at high fields and frequencies cannot be cooled and the current density decreases to zero.

These results can now be compared with the 114 filament MgB_2 wire in the next section.

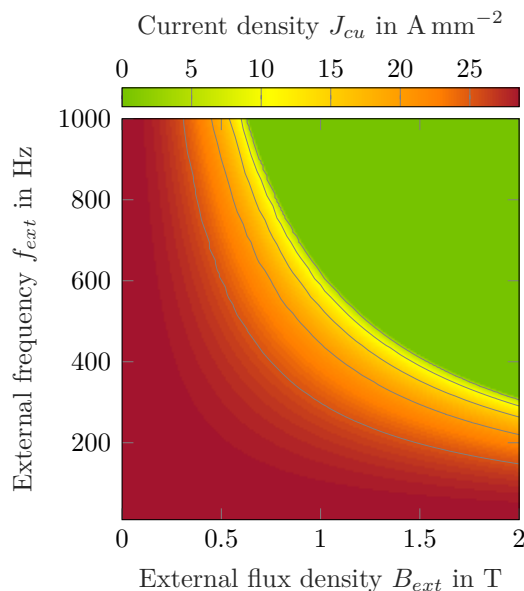


Figure 3.12.: Current density of the copper litz wire J_{cu} as a function of external flux density B_{ext} and frequency f_{ext} for the cooling conditions as well as wire properties summarized in Table 3.4.

3.5.2. Magnesium Diboride Wire

In this section the 114 filament MgB_2 wire is characterized with the electro-thermal model. For comparison, three conductor arrangements are considered. These are the perfectly cooled wire known from Figure 3.2 and the single one-side cooled wire shown in Figure 3.13a. The third arrangement is the double one-side cooled wire in Figure 3.13b.

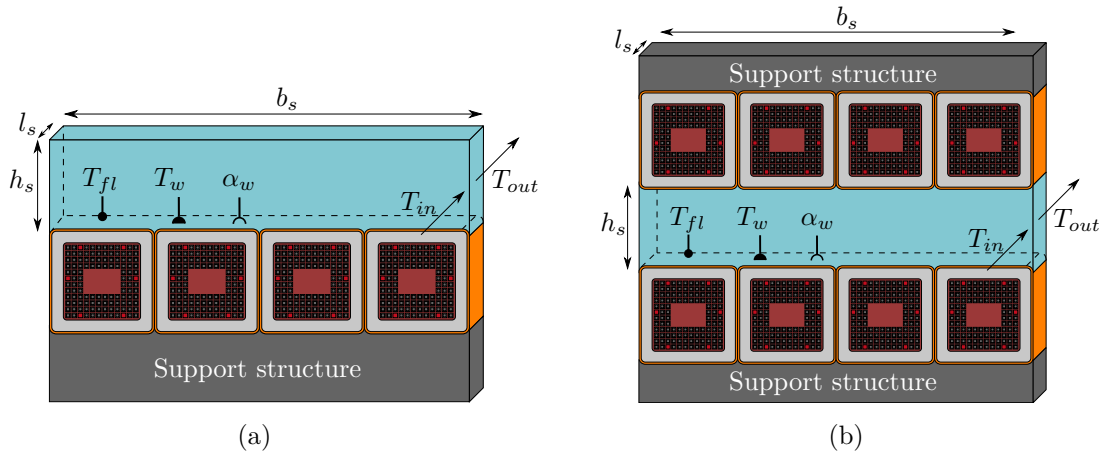


Figure 3.13.: Minimal sketch of periodic cooling arrangements in the MgB_2 stator based on the insulated 114 filament wire and divided into:

- (a) Single one-side cooling.
- (b) Double one-side cooling.

Table 3.5 summarizes the input parameters of the electro-thermal calculation of the 114 filament MgB_2 wire.

Table 3.5.: Input parameters of the electro-thermal calculation for the 114 filament MgB_2 wire.

Parameter	Value	Parameter	Value
h_w	546 μm	h_s	1.0 mm
l_s	3.0 m	b_s	12.0 mm
\dot{x}_{in}	0.0	T_{in}	20.3 K
\dot{x}_{out}	1.0	p_{out}	1.0 bar

Most important optimization parameters are the slot height h_s and the insulation thickness d_{ins} . The slot length is 3 m and corresponds to the iron length of the machine. The slot length must be estimated according to the maximum expected iron length because the electro-thermal calculation is completed before a specific machine is designed. This is possible because the slot length has only a minimal impact on the current density as long as the influence of pressure drop on cooling is negligible. Furthermore, the inlet pressure p_{in} is adjusted such that the outlet pressure p_{out} is 1 bar. Due to the slot width b_s of 12 mm, 20 windings can be arranged next to each other. Further, it is assumed that the hydrogen is evaporated in a cooling slot

between the vapor quality at the beginning \dot{x}_{in} and ending \dot{x}_{out} of the cooling slot. Figure 3.14 shows the engineering current density $J_{e,sc}$ and the maximum MgB_2 temperature $T_{sc,max}$ as a function of the insulation thickness d_{ins} . Furthermore, the

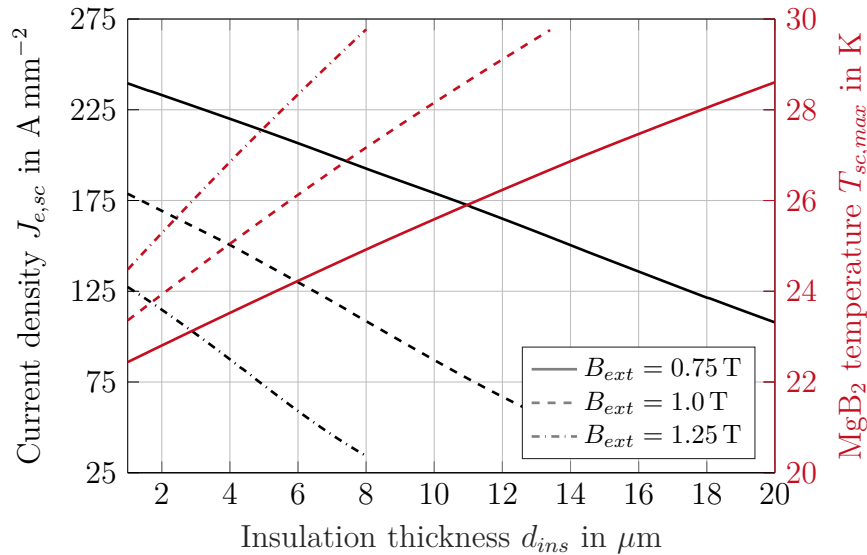


Figure 3.14.: Engineering current density $J_{e,sc}$ of the 114 filament MgB_2 wire and the maximum MgB_2 temperature $T_{sc,max}$ as a function of the insulation thickness d_{ins} for a slot with double one-side cooling. The input parameters are listed in Table 3.5.

insulation thickness is varied between $1 \mu\text{m} - 20 \mu\text{m}$ and the external field is 0.75 T, 1 T and 1.25 T at a frequency of 500 Hz. It is shown that the insulation thickness has a strong influence on the engineering current density and this influence increases at higher flux densities. This behavior is caused by the 175 times smaller thermal conductivity between insulator and outer sheath of the wire, which results in a high temperature gradient inside the insulator. For this reason, the insulation must be designed as thin as possible and must be in direct contact with the cooling medium. An insulation thickness of $5 \mu\text{m}$ is chosen and represents a compromise between dielectric strength and cooling performance.

Figure 3.15 presents the engineering current density $J_{e,sc}$ and the inlet pressure p_{in} as a function of the cooling slot height h_s , which is varied between 0.1 mm and 2 mm. Additionally, the external field is 0.75 T, 1 T and 1.25 T at a frequency of 500 Hz. With decreasing cooling slot height, the engineering current density increases because the flow conditions improve and the total area consisting of wire and cooling decreases. This effect ends when the pressure drop becomes too large with about 0.2 bar and the cooling conditions deteriorate considerably. In this example, this point is reached at a cooling slot height of 0.39 mm. In order to have a safety margin to this point, a cooling slot height of 0.5 mm is selected for further calculations.

Figure 3.16 shows contour lines of the current density J as a function of the external flux density B_{ext} and frequency f_{ext} . This enables the comparison between the single one-side cooled wire, the perfect cooled wire and the current density measurement in DC field.

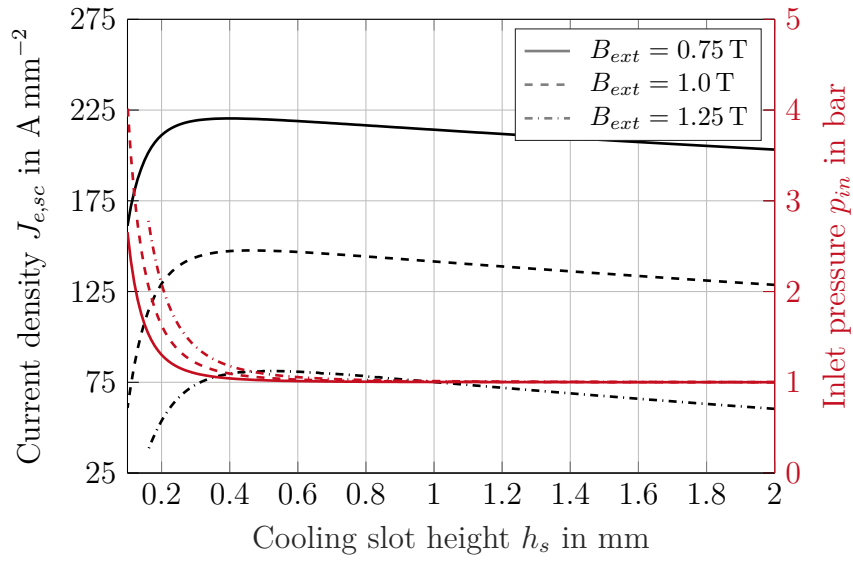


Figure 3.15.: Engineering current density $J_{e,sc}$ of the 114 filament MgB_2 wire and the inlet pressure p_{in} as a function of the cooling slot height h_s for a slot with double one-side cooling. The input parameters are listed in Table 3.5.

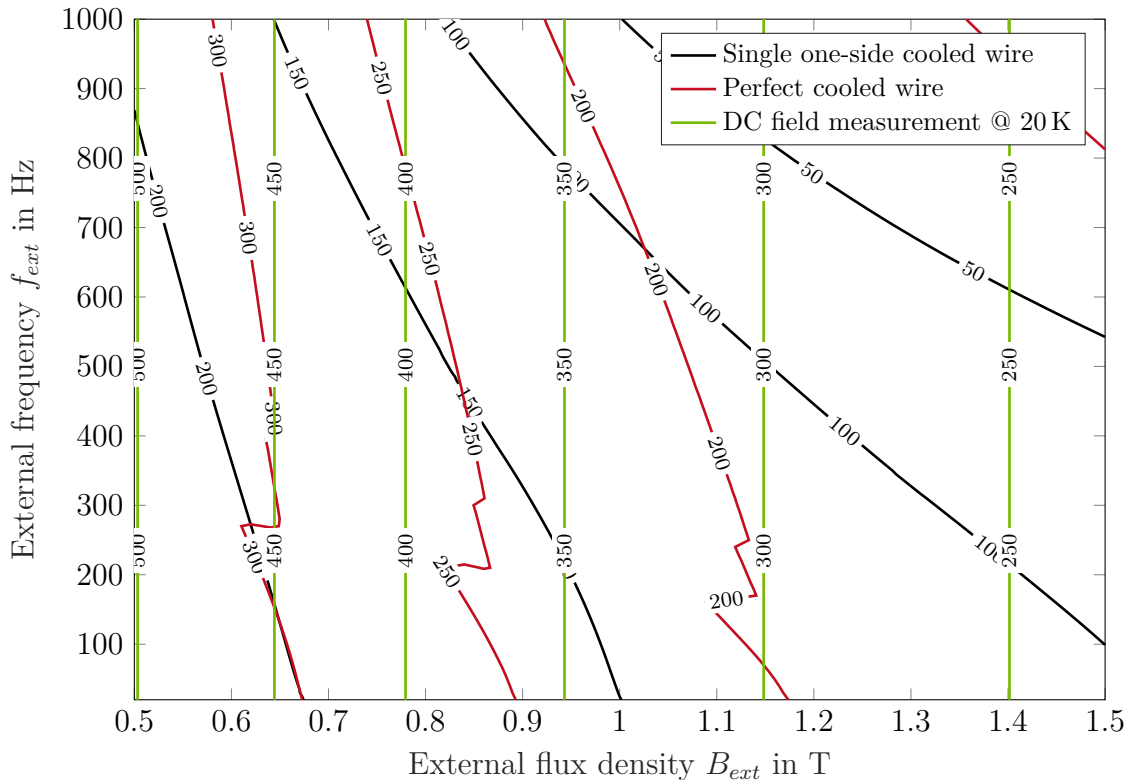


Figure 3.16.: Current density J in $A\ mm^{-2}$ of the 114 filament MgB_2 wire in the cases single one-side cooled as well as perfect cooled at a normalized current of 0.7 and the measured values at a temperature of 20 K.

Even at low fields and frequencies, the perfect cooled 114 filament MgB_2 wire achieves considerably higher current densities than the single one-side cooled 114 filament MgB_2 wire. This is due to the 4 times smaller cooling surface of the one-side cooled wire. With increasing field and frequency, this difference becomes larger and larger. This effect is caused by a higher temperature gradient, especially in the insulation. The measured current densities, which are frequency independent and presented in Section 2.1, clearly show the influence of the electro-thermal model. A significant reduction of the current density is thereby achieved and forms the basis for a realistic machine design. The sudden change of the current density between 150 Hz and 300 Hz in the case of the perfectly cooled wire results from the additional nucleate boiling, which is activated above a specific heat flux defined in Equation 3.18. This transition is not visible for the single one-side cooled multifilament MgB_2 wire, because the specific heat flux is 4 times higher due to the cooling surface reduction.

3.6. Summary

Figure 3.17 shows the engineering current density J_e as a function of the external flux density B_{ext} and frequency f_{ext} . Furthermore, the contour lines of the single one-side cooled MgB_2 wire, the double one-side cooled MgB_2 wire and the copper litz wire are plotted. MgB_2 wires achieve a much higher current density in the en-

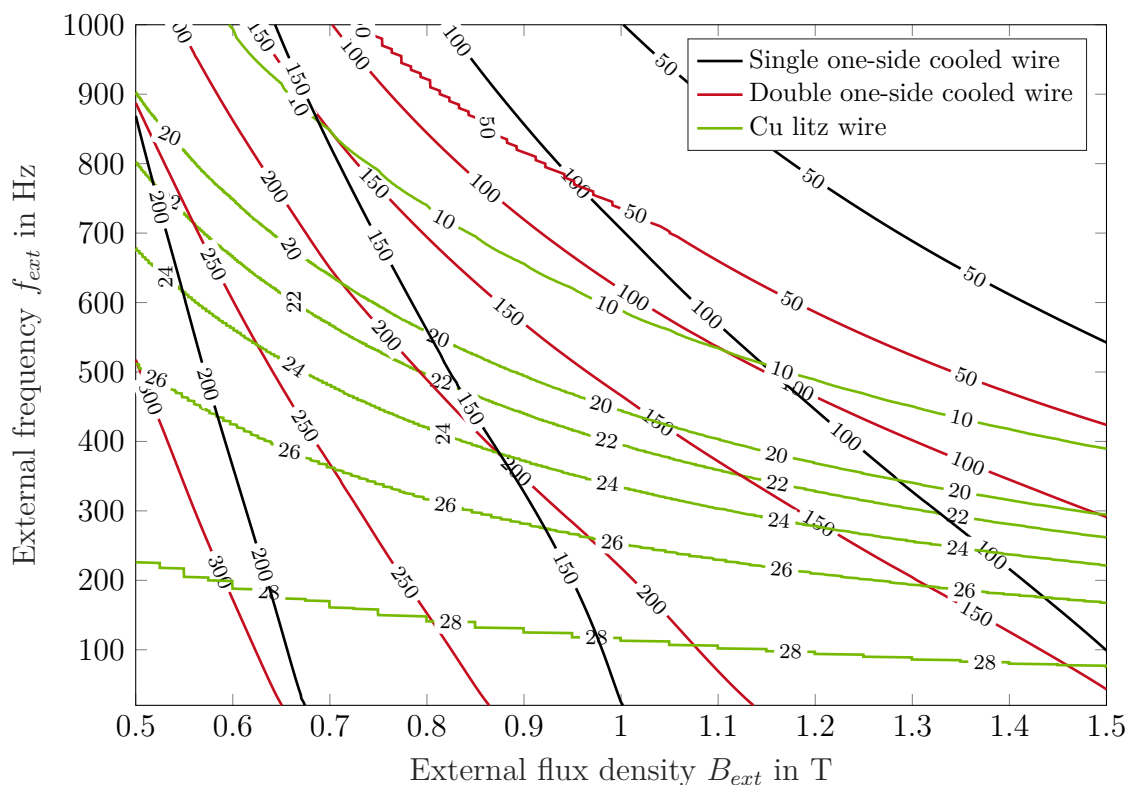


Figure 3.17.: Engineering current density J_e in A mm^{-2} of the 114 filament MgB_2 wire in the cases single one-side cooled as well as double one-side cooled at a normalized current of 0.7 and the copper litz wire.

tire field and frequency range than copper litz wires. This is a great advantage in the machine design, because this leads to a significant torque increase compared to copper. The current density of copper litz wires have a higher frequency dependence compared to MgB_2 wires. This is due to the AC loss characteristic of the MgB_2 wire. Figure 3.18 presents a further comparison of the three wires. For this purpose, the current density ratios as a function of the external flux density B_{ext} and frequency f_{ext} are shown.

A comparison of the single one-side cooled and double one-side cooled wire in Figure 3.18a shows that the single one-side cooled wire performs better than the double one-side cooled wire in the high field and frequency area ($J_{e,sc,d}/J_{e,sc,s} > 1$). This is due to the higher AC losses in this area, which have to be removed via the identical cooling slot width. In the low field and frequency area ($J_{e,sc,d}/J_{e,sc,s} < 1$), the double one-side cooled wire reaches a current density that is up to 1.5 times higher than the current density of the single one-side cooled wire. This factor results from the area ratio between the two cooling arrangements of MgB_2 in the case of negligible losses.

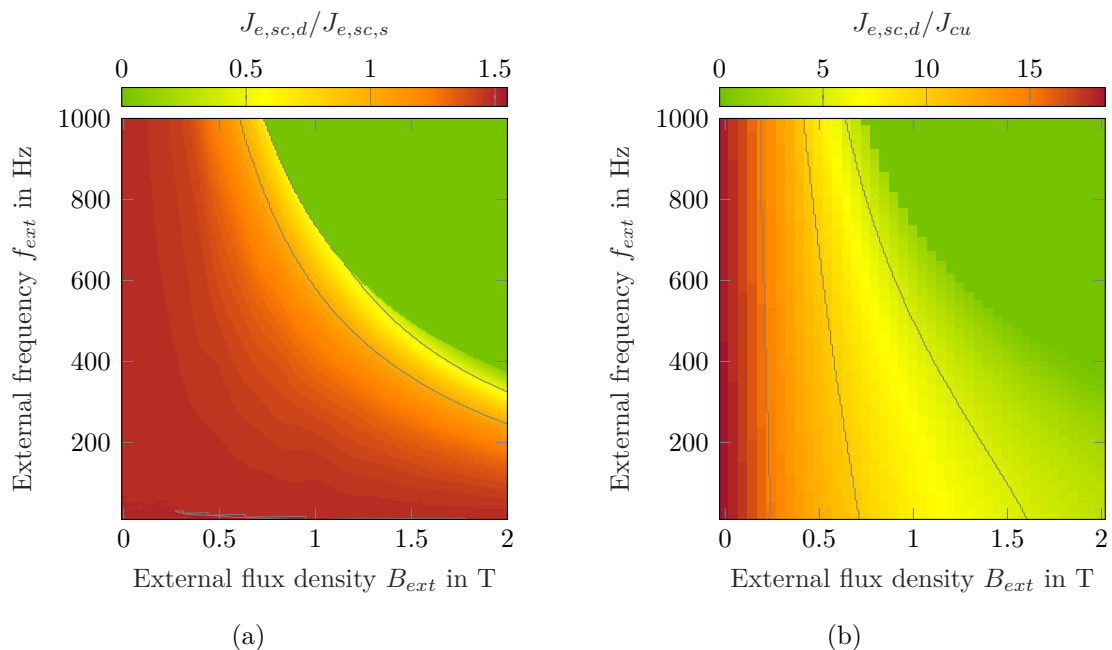


Figure 3.18.: Current density ratio between the:

- (a) 114 filament MgB_2 wire double one-side cooled $J_{e,sc,d}$ and single one-side cooled $J_{e,sc,s}$.
- (b) 114 filament MgB_2 wire double one-side cooled $J_{e,sc,d}$ and the copper litz wire J_{cu} .

Figure 3.18b presents the current density ratios between the double-one side cooled wire and the copper litz wire. The MgB_2 wire achieves for 1 T and 500 Hz a current density that is 5 times higher than that of the copper litz wire. For very small fields close to zero this factor increases up to 18.

As design recommendations, it remains to be concluded that the MgB_2 wire in-

sulation must be designed as thin as possible to guarantee effective heat transfer in the small temperature range between 20 K–30 K. For this reason, the insulated superconductor must be in direct contact with the liquid hydrogen. For cooling, the cooling slot must be chosen as small as possible to guarantee excellent heat transfer. However, the pressure drop has to be limited to an insignificant level to prevent a deterioration of the heat transfer.

It is recommended to investigate the total thermal conductivity of insulated MgB_2 wires in the future to improve the model, which also takes contact resistances into account. Furthermore, the development of insulation materials for cryogenic temperatures is important. The two-phase cooling can be validated by practical examination of the heat transfer coefficient of liquid hydrogen.

4. Electromagnetic Machine Design

4.1. Introduction

The calculation of the engineering current density in superconducting coils under different conditions is explained in the electro-thermal model in the sections before. The results show a strong dependence on the AC loss which has an influence on the machine design. This can be justified by the fact that the maximum flux density penetrating the stator coils depends strongly on the machine geometry. Another example is that changing the number of pole pairs results in a change of the electrical frequency and thus in the loss as well as the engineering current density. The dependencies mentioned are shown in Figure 3.17.

Therefore, a machine model is developed that includes the electro-thermal model into the machine design, according to [142]. Its calculation procedure is presented in Figure 4.1. In this figure, the electro-thermal model of Figure 3.1 is simplified to its superior functionalities of superconductor (SC) behavior and cooling. For a given

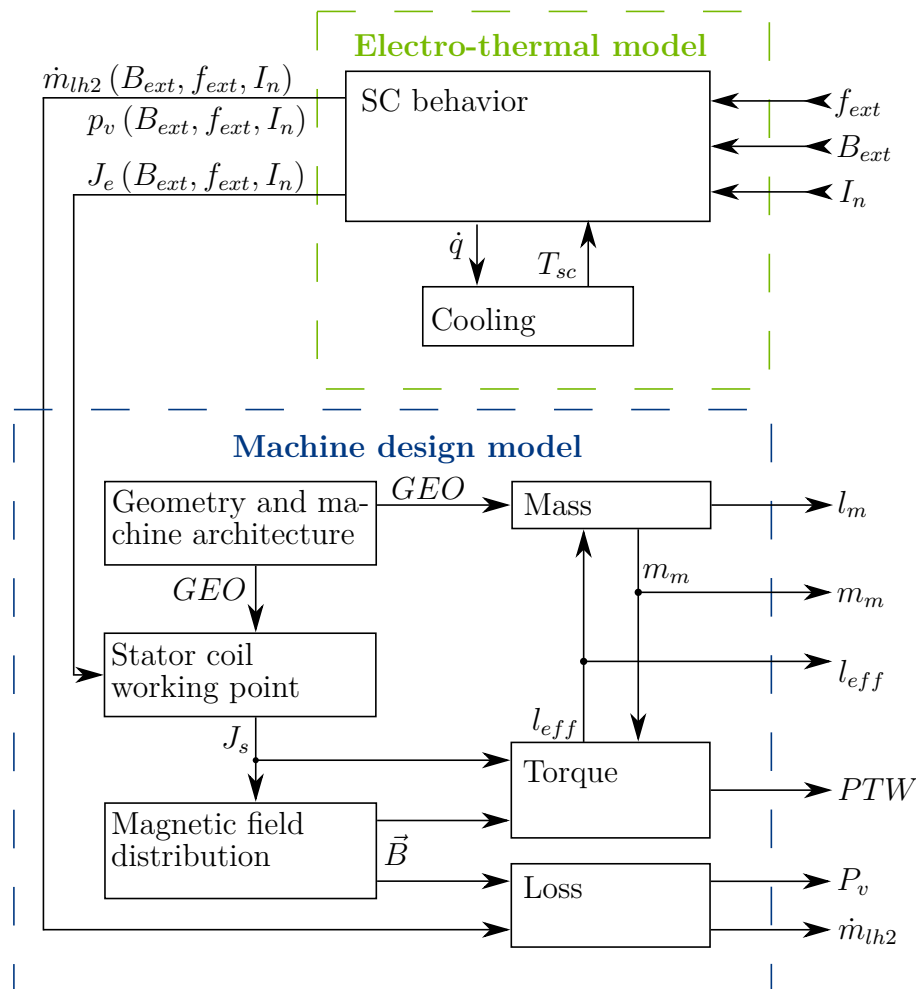


Figure 4.1.: Calculation procedure of the analytical machine design model including results by the electro-thermal model. [142]

alternating field and a normalized transport current that are related to a specific machine design, the engineering current density J_e , the loss density p_v and the mass flow rate of liquid hydrogen (LH₂) \dot{m}_{lh2} are calculated in the electro-thermal model and feed back into the machine model. This approach allows to design a machine with a specific engineering current density that depends on the alternating external flux density B_{ext} with frequency f_{ext} , the normalized stator current I_n and the cooling conditions [142]. The external flux density penetrating the superconductors is mainly generated by the rotor magnets or coils and the stator coils.

The main purpose of the machine design model, which is illustrated as flowchart in Figure B.2, is the determination of the machine geometry and architecture according to Table 4.1. This variability allows to calculate different machine topologies: fully superconducting machines, partially superconducting machines as well as normal conducting machines. Thus, the advantages and disadvantages of the individual topology can be analyzed in detail. Active parts, support structures and housing are included in the geometry and consist of different materials depending on their respective functionality. A couple of examples of these are magnets, coils, carriers, sleeves and cryogenic parts. Moreover, the entire geometry is adapted to the machine architecture to be calculated [142]. This allows to compute the mass of several parts and enables the distinction between active and passive mass. Excluded from the passive mass are the masses for the bearing shields, bearings, torque transmission elements, shaft, measuring systems and cooling connections as well as electrical connections, such as current leads.

The geometry forms the basis to calculate the magnetic field distribution inside the machine. An exact calculation of the field distribution is essential due to the high sensitivity of the AC loss in dependence of the flux density, as presented in Figure 2.20. Therefore, a large programming effort in the two-dimensional field calculation is required. Furthermore, an exact field information is indispensable in the calculation of torque, loss and hydrogen consumption. [142]

The equations that describe the electromagnetic fields are solved in the frequency domain [156]. The solutions are calculated in Python 3.7.2. using mainly the packages NumPy and SymPy.

The main features of the machine design tool are as follows [142]. Firstly, the model supports the design of synchronous radial flux machines with air gap windings, shown in Figure 4.2. In this example, a three-phase machine is shown, but in general the number of phases is a free parameter.

In this model a slotted stator and rotor is not foreseen. The work [157], [158] and [159] claim that an analytical calculation is feasible and that a good match for the magnetic field in the air gap is achieved. However, in these works the stator slot field is not compared with FEM. In contrast, the work [160] presents a strong deviation of the stator slot field, caused by the infinite permeability of the iron teeth. They found the deviation rises for an increasing stator current. Furthermore, it is expected that the iron teeth experience high saturation due to the high magnetic flux densities in superconducting machines.

Secondly, the rotor is free of iron and the stator is enclosed by a yoke of iron. This reduces weight in the rotor and the stator shields the environment from electromagnetic fields. Regardless of the machine topology, the stator iron is assumed to

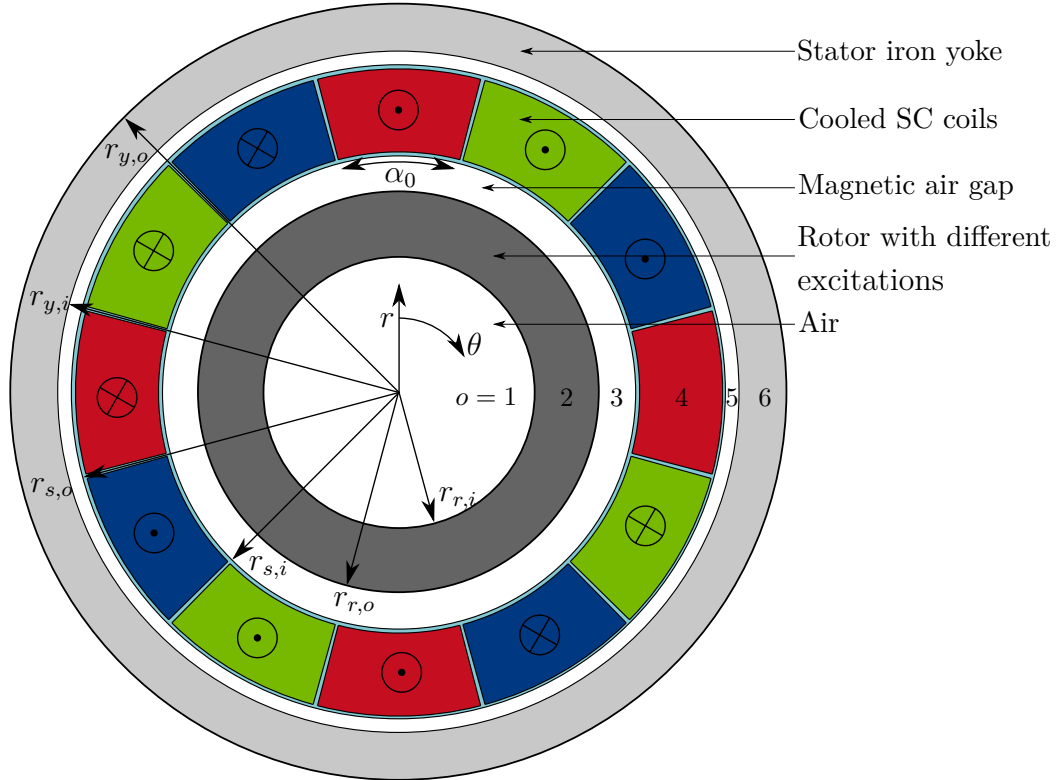


Figure 4.2.: General superconducting machine model with a cold air gap winding and variable rotor excitation presented in Figure 4.8. The sketch is reduced to the relevant information for the electromagnetic calculation and the regions correspond to the parameter o in Section 4.5. [142]

be operated at ambient temperatures. This has several reasons as investigated by [185]. Due to the increased relative permeability of iron it seems advantageous to operate at cryogenic temperatures. However, since the iron loss grow rapidly with decreasing temperature and would burden the cryogenic system, this variant is not considered. Moreover, the machines are designed for a high power-to-weight ratio, which requires to operate the stator magnetic steel close to the saturation point to keep its mass low. This leads to a further increase of the iron loss.

The following effects are neglected in the model. Firstly, due to the two-dimensional static calculation, end effects are not considered. This effects occur at the end region of electric machines for example, by the winding heads or a field component in axial direction, which can cause additional loss [60]. Furthermore, mechanical loss, such as bearing friction loss and air gap loss due to air friction, as well as additional loss caused by harmonics are neglected. This also includes loss in permanent magnets and superconducting magnets or coils in the rotor. It is also assumed that eddy currents in the permanent magnets generate low heating due to the low harmonics caused by the air gap winding approach, the large air gap and a high level of magnet segmentation. However, neodymium iron boron magnets, for example, are particularly temperature-sensitive and effective cooling of the magnets must be ensured in a detailed machine design [60].

Secondly, the thickness of the stator yoke and its relative permeability are assumed as infinite during the computation of the field distribution. This assumption makes it impossible to calculate residual fields outside the machine. The thickness of the yoke is adapted in the machine design process and is described in more detail in Section 4.7.

The computational effort would grow significantly with the introduction of a finite thick yoke of finite permeability. However, this functionality is not necessary for topology comparisons and can be considered in the detail engineering by finite element method. Finally, the current density distribution in the coil is assumed as constant, by which skin effects in normal conductors and shielding in superconductors are neglected.

In the following chapters, the different parts of the model are explained and derived, starting with the stator winding system followed by the different excitations. This also includes the adaptation and design of the air gap according to the machine topology. Subsequently, the magnetic fields are compared with finite element method in detail. Finally, the yoke is designed including the calculation of the iron loss.

4.2. Stator Winding System

The stator is built up by an m -phase air gap winding system, as shown in Figure 4.2, and the various coils are shaped race track coils for simplification. Furthermore, it is assumed that the manufacturing of such a coil is possible and only the bending radius limits the coil. Figure 4.3 shows a sketch of the coil along two different axes. The inner bending radius of a stator coil $r_{s,b,i}$ is defined in Equation 4.1 at the middle stator radius $r_{s,m}$, which is shown in Figure 4.11.

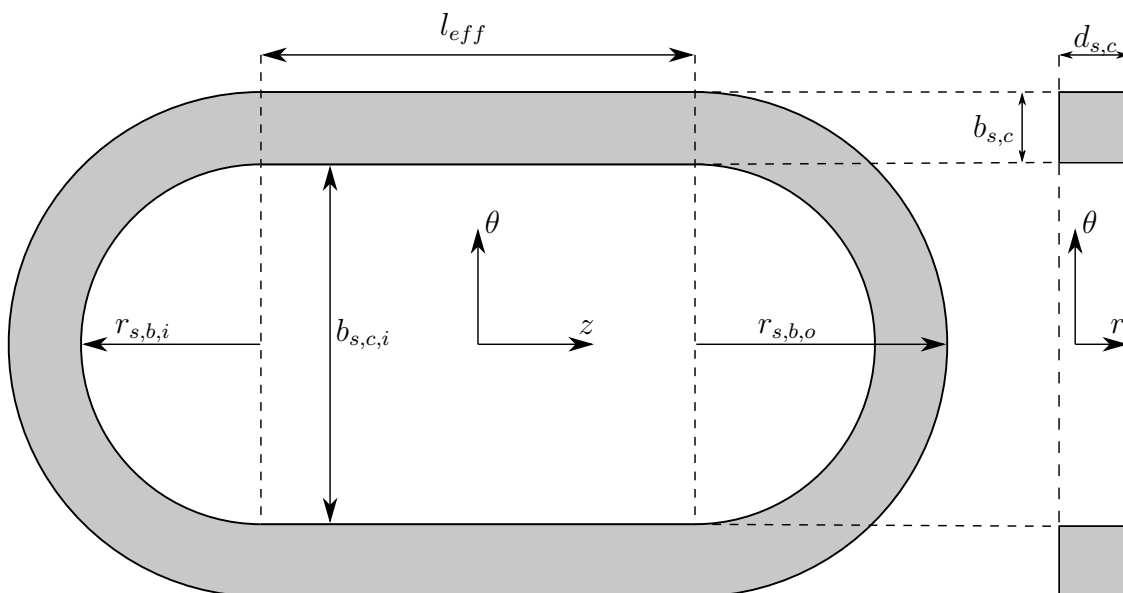


Figure 4.3.: Sketch of a flat coil with the top view (left) if the stator coil area in Figure 4.2 is sectioned in the z - θ plane and the cross section (right) as cut through the r - θ plane.

$$r_{s,b,i} = r_{s,m} \left(1 - \frac{\alpha_0}{2m} \right) \sin \left(\frac{\pi}{2p} \right) \quad (4.1)$$

The bedding radius of a rotor coil is presented in Section 4.4. Further parameters to characterize the coil are the width $b_{s,c}$, the thickness $d_{s,c}$ and the inner diameter $b_{s,c,i}$ of the stator coil as well as the effective machine length l_{eff} . The effective machine length is valid for the rotor and stator.

The spatial and time depending stator current density J_s is defined in Equation 4.2 for an m -phase system with constant spatial distribution and phase shift. Further parameters of this equation are the number of pole pairs p , angular coordinate θ , angular frequency ω and time t .

$$J_s(\theta, t) = \sum_{k=0}^{m-1} \sum_n J_n \cos \left(n \left(p\theta - \frac{2\pi k}{m} \right) \right) F_n \cos \left(n \left(p\omega t - \frac{2\pi k}{m} \right) \right) \quad (4.2)$$

The shape of the coils and the current waveform are described by the Fourier coefficients J_n and F_n of the n^{th} harmonic. The Fourier coefficient of a rectangular spatial shape can be calculated by Equation 4.3 with the maximum current density over one period of time J_{max} . Additionally, the coverage α_0 denotes the percentage share of the stator area that is covered by the coils.

$$J_n = 2\alpha_0 J_{max} \text{sinc} \left(\frac{n\alpha_0}{2} \right) \quad (4.3)$$

In time domain with sinusoidal supply only the fundamental wave is necessary, but for example, harmonics generated by an inverter can be taken into account or even square wave mode, which is among the simplest waveform an inverter can produce [162]. It is shown in Section 4.6.1 that the calculation of torque is much faster by assuming a sinusoidal current.

Figure 4.4 shows the ideal spatial current density distribution of a three-phase system over a pole pair with a coverage α_0 of 0.8, introduced in Figure 4.2 at the time t equals 0s. The electrical angle θ_{el} is defined by the mechanical angle θ as follows:

$$\theta_{el} = \theta p \quad (4.4)$$

Furthermore, the deviation between ideal current density distribution and the model is visualized if Equation 4.2 is solved up to the 19th harmonic order. The differences between ideal and model spatial current density distribution are clearly visible and the influence of the maximum harmonic n_{max} is discussed in Section 4.5.5.

The load angle θ_{load} is defined over the spatial angular displacement from the fundamental wave of stator field and rotor field. Thus, an angle of 0 denotes that the positive and negative maxima of both fields are opposite each other. In the model, this is achieved via setting the position and orientation of the magnets or coils in the rotor.

In the calculation it is assumed that the coil has a homogeneous current density. This is not feasible in practice because a support structure is also necessary to protect the wire and to guide the cooling fluid. Therefore, forces are absorbed as well as transferred and cooling channels are defined by it. The design of such a structure

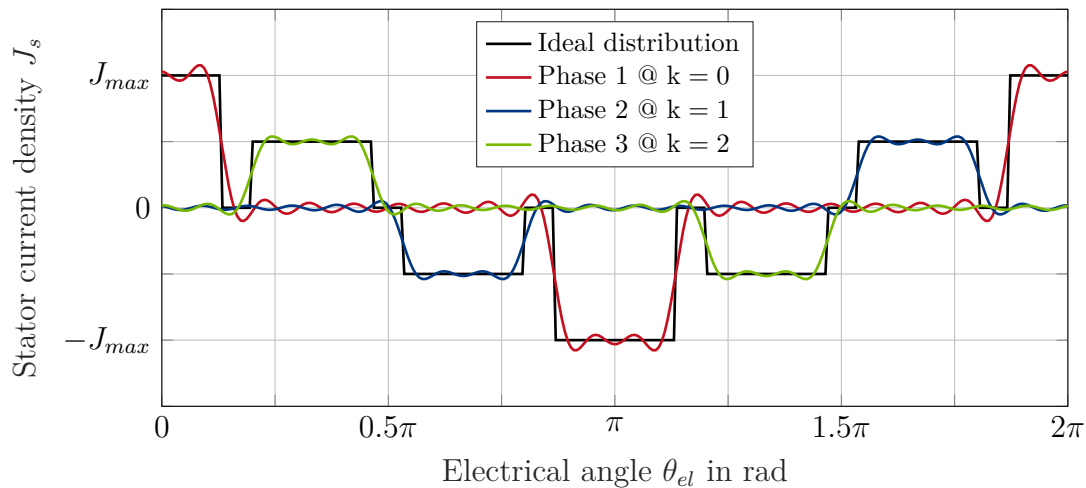


Figure 4.4.: Spatial stator current density distribution of a three-phase system at a coverage α_0 of 0.8 in an ideal model under load which is defined at a load angle θ_{load} of 90 deg and in comparison with a limited model at n_{max} of 19 at the time t equals 0 s.

is not discussed in depth in this work, because this is part of the detailed design of a specific machine. However, the required cross-sectional ratio between wire and support structure in the stator is estimated by the coil support ratio f_{csr} .

After the stator current density is defined, the air gap can now be described in more detail to determine the magnetically effective air gap depending on the machine topology.

4.3. Air Gap Design

The design of the air gap depends on the machine topology. All topologies that can be computed with the machine design model are presented in Table 4.1.

Table 4.1.: Machine topologies and corresponding architectures in the machine design model.

Generic term	Topology	Architecture
Fully superconducting	SC stator / SC rotor	MgB ₂ coil / HTS coil
		MgB ₂ coil / HTS bulk
Partially superconducting	SC stator / NC rotor	MgB ₂ coil / Cu coil
		MgB ₂ coil / HA
	NC stator / SC rotor	MgB ₂ coil / PM
Normal conducting	NC stator / NC rotor	Cu coil / HTS coil
		Cu coil / HTS bulk
		Cu coil / Cu coil
		Cu coil / HA
		Cu coil / PM

Figure 4.5 shows different machine architectures which differ in the air gap design mainly due to the high temperature gradient between rotor and stator or stator and yoke. To enable such high gradients a vacuum in the rotor and stator housing must be supported, providing the required thermal isolation. For this reason, cryo walls, which enable the vacuum, are designed mechanically for this functionality, as described in Section 4.3.2. Thus, the radial thickness of the designed air gap is very different, affecting the profile and amplitude of the magnetic field that penetrates the stator winding strongly. Consequently, this leads to a non-negligible effect on the AC loss of the stator coils and the stator current density according to the results of Section 3.5. The radial distance between rotor magnets or rotor coils and stator coils is defined as magnetic air gap d_{air} and sums the thicknesses of all air gap components. Furthermore, the corresponding radial distance between stator coils and yoke is defined as coil-to-yoke distance d_{c2y} .

Furthermore, the mechanical forces of the coils or magnets in the rotor must be transferred to the rotor carrier at high circumferential speeds. For this reason, a retention sleeve is installed through a press fit around the circumference, as explained in Section 4.3.1. Depending on the topology, the stator requires also a carrier structure.

Most of these parts in the air gap can be made out of materials with an electrical conductivity much larger than zero. Thus, the functionality of a field shield can also be realized by these parts, such as the housing, the carrier of stator or rotor and the sleeve, depending on the machine topology. Harmonics can be shielded due to the effect, that electro-magnetic fields are mitigated by conductive shells. By an appropriate choice of the shell thickness, AC losses can be locally shifted and thus are reduced in machines with cryogenic parts, because the losses are already generated in the respective conductive shells. The eddy current losses in a hollow cylinder can be calculated analytically, as shown in [163, 164]. Due to the high computational effort, this functionality is not implemented because the influence on the torque of the machine is estimated to be low. In a detailed design of a machine, these losses can be determined by finite element method.

In detail, Figure 4.5a shows a fully superconducting machine with two cryogenic systems in stator and rotor. It should be noted, that the air gap is evacuated from air to combine functionalities, resulting in a smaller magnetic air gap. The rotor carrier is partly used to guide the coolant in the case of superconducting excitation. In Figure 4.5b the first of two partially superconducting topologies is presented. The rotor is surrounded by a vacuum area and rotor housing. In this configuration, this part of the cryogenic system of the machine needs to be designed to withstand the mechanical loads due to rotation. This can additionally increase the required wall thickness. However, in the other partially superconducting architecture with a cryogenic stator, as shown in Figure 4.5c, the requirements for the cryogenic system are reduced by the absence of rotational movement, which reduces the thickness of the air gap. The total air gap of normal conducting machines is illustrated in Figure 4.5d. In relation, this is much thinner than the previously presented architectures due to its simple structure.

All these functionalities will be discussed and calculated in the following sections starting with the sleeve.

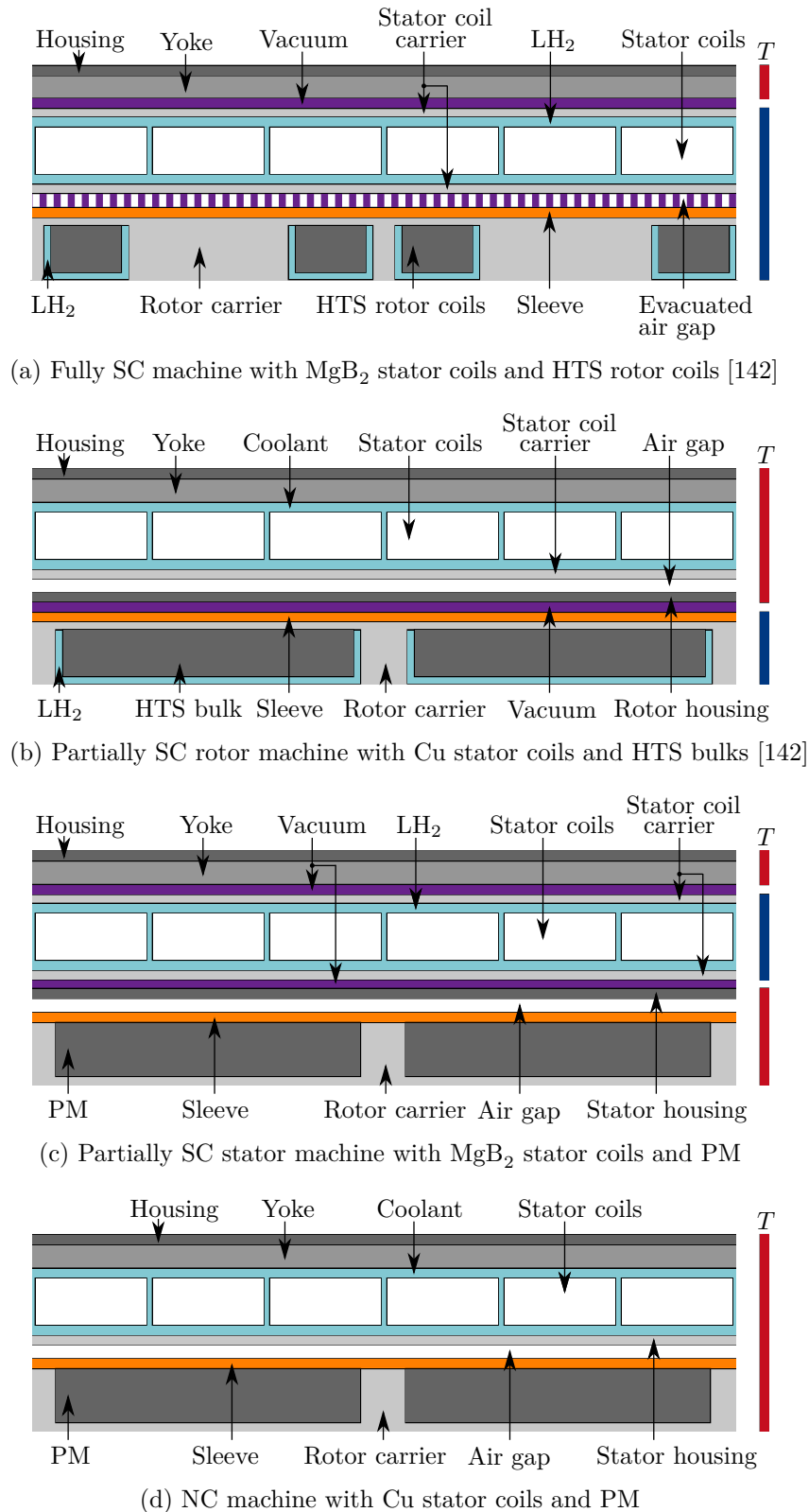


Figure 4.5.: Exemplary air gap design with marked temperature areas for cryogenic ■ and ambient temperature ■ of:

(a) Fully SC machines. (b) Partially SC rotor machines.
(c) Partially SC stator machines. (d) NC machines.

4.3.1. Sleeve

In this section, an analytical approach is developed to calculate the sleeve thickness. To achieve this, a press-fit model is used to assess the static strength of the composite sleeve. The homogenized tangential stress in the sleeve is calculated as a result of its radial overclosure.

To allow an analytical calculation, various simplifications must be made. Firstly, the geometry is assumed to be rotationally symmetric with constant load conditions. Furthermore, the model is simplified to a two-dimensional plane strain state without stress in the axial direction. A uniform contact pressure distribution is assumed between the interfaces. The load is transmitted in the radial direction and no tangential load carrying capability is assumed. Finally, there is a homogeneous temperature distribution and a linear elastic behavior in the materials.

The computation of the stress components and the radial displacement in rotating hollow cylinders is based on the work of [165] and [166]. Furthermore, the rotor is modeled as a compound of three adjacent hollow cylinders which represent a rotor carrier, permanent magnets or coils and the sleeve. In the case of a machine architecture that features coils in the rotor, its entire surface is assumed to be covered by the coils for the computation of the sleeve, leading to a slightly too large sleeve thickness.

All components are shown in Figure 4.6 and the total inner pressure $p_{tot,i}$ and total outer pressure $p_{tot,o}$ on the segmented magnets are illustrated. The total radial displacement $\delta_{tot,r}$ describes the total deformation of the rotor after press-fitting due to applied forces. It is the sum of the radial displacements caused in the sleeve $\delta_{sl,r}$, magnet $\delta_{mag,r}$ and rotor carrier $\delta_{rot,r}$ according to Equation 4.5.

$$\delta_{tot,r} = \delta_{rot,r} + \delta_{mag,r} + \delta_{sl,r} \quad (4.5)$$

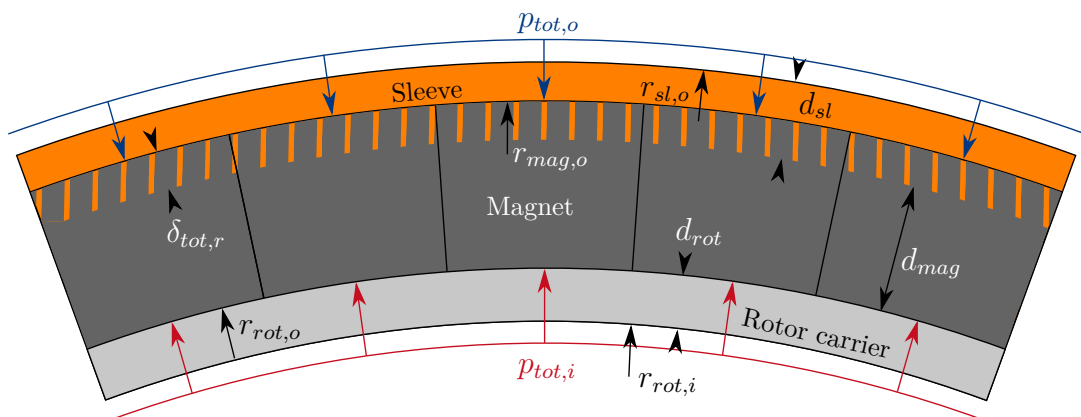


Figure 4.6.: Press-fit model of a rotor with rotor carrier, segmented magnets and covered by a sleeve. The hatched area symbolizes the radial displacement due to the occurring forces. Adapted from [167].

These three displacements are caused by three different effects. Firstly, the displacement $\delta_{p,r}$ due to the inner pressure p_i or outer pressure p_o presented in Equation 4.6 with the inner radius r_i and the outer radius r_o of the hollow cylinder has to be

mentioned. The material is characterized by the Young's modulus E and Poisson's ratio ν .

$$\delta_{p,r} = \begin{cases} \frac{p_i r_i}{E} \left(\frac{r_i^2 + r_o^2}{r_o^2 - r_i^2} + \nu \right) & \text{if } p_o = 0 \\ -\frac{p_o r_o}{E} \left(\frac{r_i^2 + r_o^2}{r_o^2 - r_i^2} - \nu \right) & \text{if } p_i = 0 \end{cases} \quad (4.6)$$

Secondly, the displacement $\delta_{t,r}$ caused by thermal expansion is given by Equation 4.7 with the radius r or thickness d , the thermal expansion coefficient α_t and temperature difference ΔT between installation temperature (press-fit temperature) and various ambient temperatures. These can be divided into the states minimum operation temperature $T_{r,min}$ and maximum operation temperature $T_{r,max}$ of the rotor as well as room temperature T_{rt} . There is a distinction between cylinders that are tangentially open or closed.

$$\delta_{t,r} = \begin{cases} r \alpha_t \Delta T & \text{if open hollow cylinder} \\ d \alpha_t \Delta T & \text{if closed hollow cylinder} \end{cases} \quad (4.7)$$

Thirdly, the displacement $\delta_{\omega,r}$ due to centrifugal forces is calculated by Equation 4.8 with the angular speed ω and the volumetric mass density of the material ρ . The angular speed is differentiated between the nominal angular speed ω_n and the whirl angular speed ω_w , defined in Equation 4.9 with the whirl safety factor f_w .

$$\delta_{\omega,r} = \frac{r_i \rho \omega^2}{4 E} \left(\left(1 - \frac{\nu}{1 - \nu} \right) r_i^2 + \left(3 + \frac{\nu}{1 - \nu} \right) r_o^2 \right) \quad (4.8)$$

$$\omega_w = f_w \omega_n \quad (4.9)$$

By summing the different contributions to the displacements of the regions sleeve, magnet and rotor carrier, Equations 4.10, 4.11 and 4.12 result, respectively. Since the magnets are not contacted tangentially and do not form a closed ring, only the deformations due to the internal pressure and thermal expansion are considered.

$$\delta_{sl,r} = \frac{p_{tot,o} r_{sl,i}}{E_{sl,\theta}} \left(\frac{r_{sl,o}^2 + r_{mag,o}^2}{r_{sl,o}^2 - r_{mag,o}^2} + \nu_{sl} \right) + \frac{r_{sl,i} \rho_{sl} \omega^2}{4 E_{sl,\theta}} \cdot \left(\left(1 - \frac{\nu_{sl}}{1 - \nu_{sl}} \right) r_{sl,i}^2 + \left(3 + \frac{\nu_{sl}}{1 - \nu_{sl}} \right) r_{sl,o}^2 \right) + r_{sl,i} \alpha_{sl,t,\theta} \Delta T \quad (4.10)$$

$$\delta_{mag,r} = \frac{d_{mag}}{2 E_{mag}} (p_{tot,o} + p_{tot,i}) + d_{mag} \alpha_{mag,t,r} \Delta T \quad (4.11)$$

$$\delta_{rot,r} = -\frac{p_{tot,i} r_{rot,o}}{E_{rot}} \left(\frac{r_{rot,o}^2 + r_{rot,i}^2}{r_{rot,o}^2 - r_{rot,i}^2} - \nu_{rot} \right) + \frac{r_{rot,o} \rho_{rot} \omega^2}{4 E_{rot}} \cdot \left(\left(1 - \frac{\nu_{rot}}{1 - \nu_{rot}} \right) r_{rot,o}^2 + \left(3 + \frac{\nu_{rot}}{1 - \nu_{rot}} \right) r_{rot,i}^2 \right) + r_{rot,o} \alpha_{rot,t,\theta} \Delta T \quad (4.12)$$

By using the Equations 4.10, 4.11, 4.12 and 4.13 in Equation 4.5, the total outer pressure $p_{tot,o}$ can be calculated.

$$p_{tot,i} = \frac{p_{tot,o} r_{sl,i} - \frac{1}{2} \rho_{mag} \omega^2 (r_{sl,i}^2 - r_{rot,o}^2) r_{sl,i}}{r_{rot,o}} \quad (4.13)$$

Thus, the tangential stress $\sigma_{sl,\theta}$ in the sleeve can be determined with the following equation:

$$\sigma_{sl,\theta} = \frac{r_{sl,o}^2 + r_{mag,o}^2}{r_{sl,o}^2 - r_{mag,o}^2} p_{tot,o} + \frac{\rho_{sl} \omega^2}{4} \left(\left(1 - \frac{\nu_{sl}}{1 - \nu_{sl}} \right) r_{sl,i}^2 + \left(3 + \frac{\nu_{sl}}{1 - \nu_{sl}} \right) r_{sl,o}^2 \right) \quad (4.14)$$

Two fundamental requirements must be fulfilled for the sleeve in order to comply with the static strength proof. Firstly, the tangential stress according to Equation 4.14 must be allowed for the sleeve material under consideration of all load cases in Table 4.2. The load cases differ in terms of temperature, speed as well as torque and thus include all possible loads. This condition is defined by Equation 4.15 with the allowable tangential stress $\sigma_{sl,\theta,allow}$ and stress safety factor $f_{sl,\sigma}$.

$$\sigma_{sl,\theta} < \sigma_{sl,\theta,allow} f_{sl,\sigma} \quad (4.15)$$

Secondly, a minimum pressure between magnets and rotor carrier interface is required to transfer the mean torque \overline{M} through the tangential shear stress $\tau_{m,\theta}$ defined in Equation 4.16 with the inner magnet radius $r_{i,mag}$, the effective length of the machine l_{eff} and the non-slip safety factor f_m . By dividing this quantity by the static friction coefficient μ_θ between magnets and rotor, the frictional shear stress is calculated. For this reason, the internal pressure must be greater than the frictional shear stress to prevent the magnets from slipping on the rotor carrier surface expressed by Equation 4.17.

$$\tau_{m,\theta} = \frac{\overline{M} f_m}{2 r_{mag,i}^2 \pi l_{eff}} \quad (4.16)$$

$$p_{tot,i} \geq \frac{\tau_{m,\theta}}{\mu_\theta} \quad (4.17)$$

Table 4.2.: Design points of the sleeve thickness at different temperature T , angular speed ω and mean torque \overline{M} .

Config.	Characteristics		
	Temperature	Speed	Torque
1	T_{rt}	0	0
2	$T_{r,max}$	ω_w	0
3	$T_{r,max}$	ω_n	\overline{M}
4	$T_{r,min}$	ω_w	0
5	$T_{r,min}$	ω_n	\overline{M}

By varying the thickness of the sleeve d_{sl} and the total radial displacement $\delta_{tot,r}$ in a given range, the thickness of the sleeve can be determined. For this purpose, the thickness is increased iteratively until all boundary conditions are fulfilled. If one condition is not fulfilled, the calculation of a thickness and radial displacement value pair is terminated. Furthermore, this ensures that the minimum thickness is computed. In addition, the minimum air gap thickness is an output, which is necessary due to the displacement described.

4.3.2. Cryo Wall

The cryo wall separates different pressure and temperature areas in the machine from each other. For example, a cryo wall is in between a vacuum isolation layer and an area containing a cryogenic cooling liquid, as shown for different machine topologies in Figure 4.5. This section deals with the mechanical design of the cryo wall. The thermal design is neglected because it is assumed that the AC loss of the stator coils are much higher than the heat input through residual heat conduction as well as heat radiation and thus responsible for the main coolant consumption.

Consequently, the cryo wall is a part of the air gap design. In the model, it is assumed as a hollow cylinder. It is distinguished between the cases overpressure, where the inner pressure $p_{cw,i}$ is greater than the outer pressure $p_{cw,o}$ and the case negative pressure, where the conditions are reversed. Both cases are illustrated for a parametric cylindrical vessel in Figure 4.7 and the arrows indicate the direction of the force. Furthermore, the vessel is characterized by the outer radius $r_{cw,o}$ and length l_{cw} . The goal is to calculate the thickness of the cryo wall d_{cw} in dependence of the machine length and pressure conditions for given materials. Therefore, the calculation is implemented according to [168, 169]. It should be noted, that all units

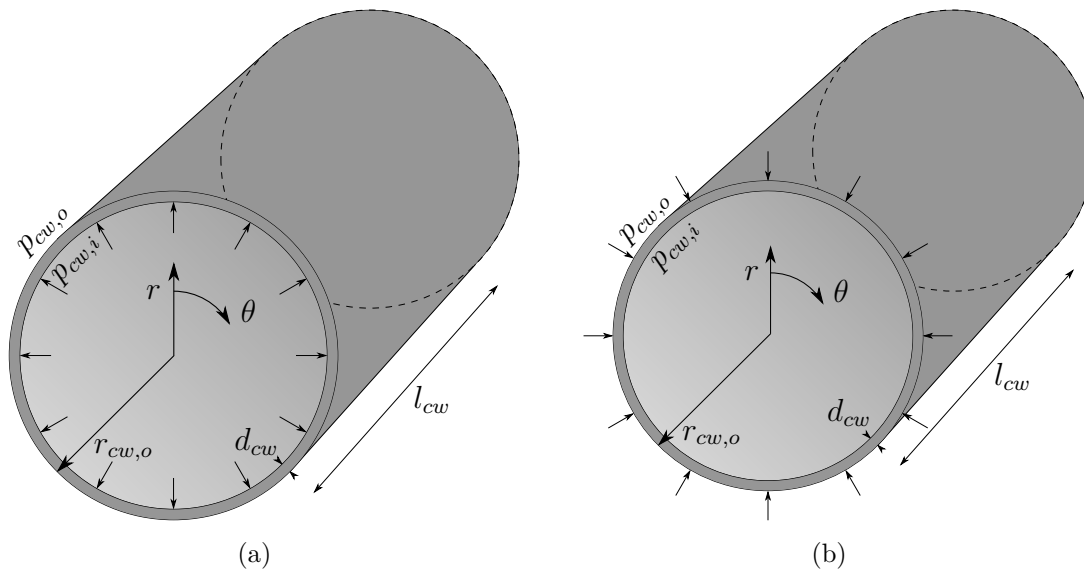


Figure 4.7.: Sketch of a cryo wall in cylindrical form under:

- (a) Overpressure.
- (b) Negative pressure.

The arrows illustrates the direction of force.

of lengths are given in mm in the following equations. Firstly, the overpressure case is presented and secondly the negative pressure case which is additionally divided into elastic buckling and plastic buckling.

Overpressure

The calculation is done with analytical formulas according to [170] considering the safety factor f_{cw} , the structural strength K_{cw} and the Poisson's ratio ν_{cw} in Equation 4.19. The pressure difference Δp is defined as:

$$\Delta p = |p_{cw,i} - p_{cw,o}| \quad (4.18)$$

$$d_{cw} = \frac{2 r_{cw,o} \Delta p}{20 \frac{K_{cw}}{f_{cw}} \nu_{cw} + \Delta p} \quad (4.19)$$

Negative pressure

At negative pressures the wall thickness is calculated iteratively for elastic buckling and for plastic buckling. Therefore, the critical buckling pressure is determined according to [171].

Firstly, for elastic buckling the critical buckling pressure $p_{cw,e}$ is given by Equation 4.20 with the Young's modulus E_{cw} of the selected material and by using Equation 4.21. The calculation is performed for different numbers of buckling waves n_{cw} . Afterwards, the lowest critical pressure is taken to determine the minimum wall thickness in the case of elastic buckling.

$$p_{cw,e} = \frac{E_{cw}}{f_{cw}} \left(\left(\frac{20}{(n_{cw}^2 - 1) \left(1 + \left(\frac{n_{cw}}{Z} \right)^2 \right)^2} \right) \frac{d_{cw}}{2 r_{cw,o}} \right. \quad (4.20)$$

$$\left. + \frac{80}{12(1 - \nu_{cw}^2)} \left(n_{cw}^2 - 1 + \frac{2n_{cw}^2 - 1 - \nu_{cw}}{1 + \left(\frac{n_{cw}}{Z} \right)^2} \right) \left(\frac{d_{cw}}{2 r_{cw,o}} \right)^3 \right)$$

$$Z = \frac{\pi r_{cw,o}}{l_{cw}} \quad (4.21)$$

Secondly, the critical buckling pressure $p_{cw,p}$ in the case of plastic buckling is taken into account by Equation 4.22 with the out of roundness factor u_{cw} .

$$p_{cw,p} = \frac{10 K_{cw}}{f_{cw} r_{cw,o}} \frac{100 d_{cw}^2}{100 d_{cw} + 3 u_{cw} \left(1 - 0,4 \frac{r_{cw,o}}{l_{cw}} \right) r_{cw,o}} \quad (4.22)$$

Finally, the thickness of the cryo wall d_{cw} can be determined by choosing the maximum value of the minimum wall thicknesses of both buckling types.

A special variant occurs in a partially superconducting rotor machine shown in Figure 4.5b [142]. There, the innermost cryo wall is part of the rotor and thus the centrifugal forces must be considered. The static strength proof is similar to that in Section 4.3.1. The critical point is located at the inner radius of the cylinder in tangential direction. The total tangential stress $\sigma_{cw,\theta}$ is calculated by the sum of the

tangential stress through centrifugal forces $\sigma_{cw,\omega,\theta}$ and the tangential stress through the external pressure $\sigma_{cw,p,\theta}$ in Equation 4.23 to 4.25 [165, 172].

$$\sigma_{cw,\theta} = \sigma_{cw,\omega,\theta} + \sigma_{cw,p,\theta} \quad (4.23)$$

$$\sigma_{\omega,\theta} = \frac{3 + \nu_{cw}}{4} \rho_{cw} r_{cw,o}^2 \omega^2 \left(1 + \frac{1 - \nu_{cw} r_{cw,i}^2}{3 + \nu_{cw} r_{cw,o}^2} \right) \quad (4.24)$$

$$\sigma_{p,\theta} = -\frac{2 \Delta p r_{cw,o}^2}{r_{cw,o}^2 - r_{cw,i}^2} \quad (4.25)$$

4.4. Excitation Methods

To compare as many machine architectures as possible, the rotor excitation is kept variable. All types of excitation are shown in Figure 4.8 and named in Table 4.1. A detailed description of all types follows in the next subsections. If superconducting parts are used, a specific cooling area is taken into account, which is visualized through the light blue area. The variants are basically divided into coils and magnets and thus have different magnetizations. For this reason, the description of the field profile in the frequency domain is particularly important.

Superconducting coil

As it can be seen in Figure 4.8a, the superconducting coils are periodically distributed around the circumference and the exact position as well as size of the coils are determined by the inner coil angle α_2 , which defines the distance between the two legs within a coil, and the adjacent coil angle α_3 , which defines the distance between the legs of adjacent coils. The radial thickness of the coils is also given by d_{mag} . Depending on these quantities, the spatial shape of the rotor current density J_r in axial direction over a pole pair is illustrated in Figure 4.10a.

This profile is now transformed into the frequency domain for further processing. The Fourier series is given by Equation 4.26 with Fourier coefficients J_n in Equation 4.27 [142].

$$J_r = \sum_{n \text{ odd}} J_n \cos(np\theta) \quad (4.26)$$

$$J_n = J_{max} \frac{-2 \sin(\alpha_3 n) + 2 \sin(n(\alpha_3 - \pi)) + 4 \cos(\alpha_2 n) \sin\left(\frac{n\pi}{2}\right)}{n \pi} \quad (4.27)$$

It should be noted, that the coils are shifted with an electrical angle θ_{el} of 90 deg to make use of the cosine formulation in Equation 4.26 possible. This is corrected via an offset on the electrical angle after solving the equation.

Furthermore, the inner bending radius of a rotor coil $r_{r,b,i}$ is given at the middle rotor radius $r_{r,m}$ as follows:

$$r_{r,b,i} = r_{r,m} \sin\left(\frac{\alpha_2}{p}\right) \quad (4.28)$$

High-temperature superconductor coils have to be reliably manufactured as a flat race track coil since high mechanical stress can destroy the conductor. This causes

a discrepancy between coil and model geometry, which leads to geometry errors for small number of pole pairs. This fact is neglected in the calculation.

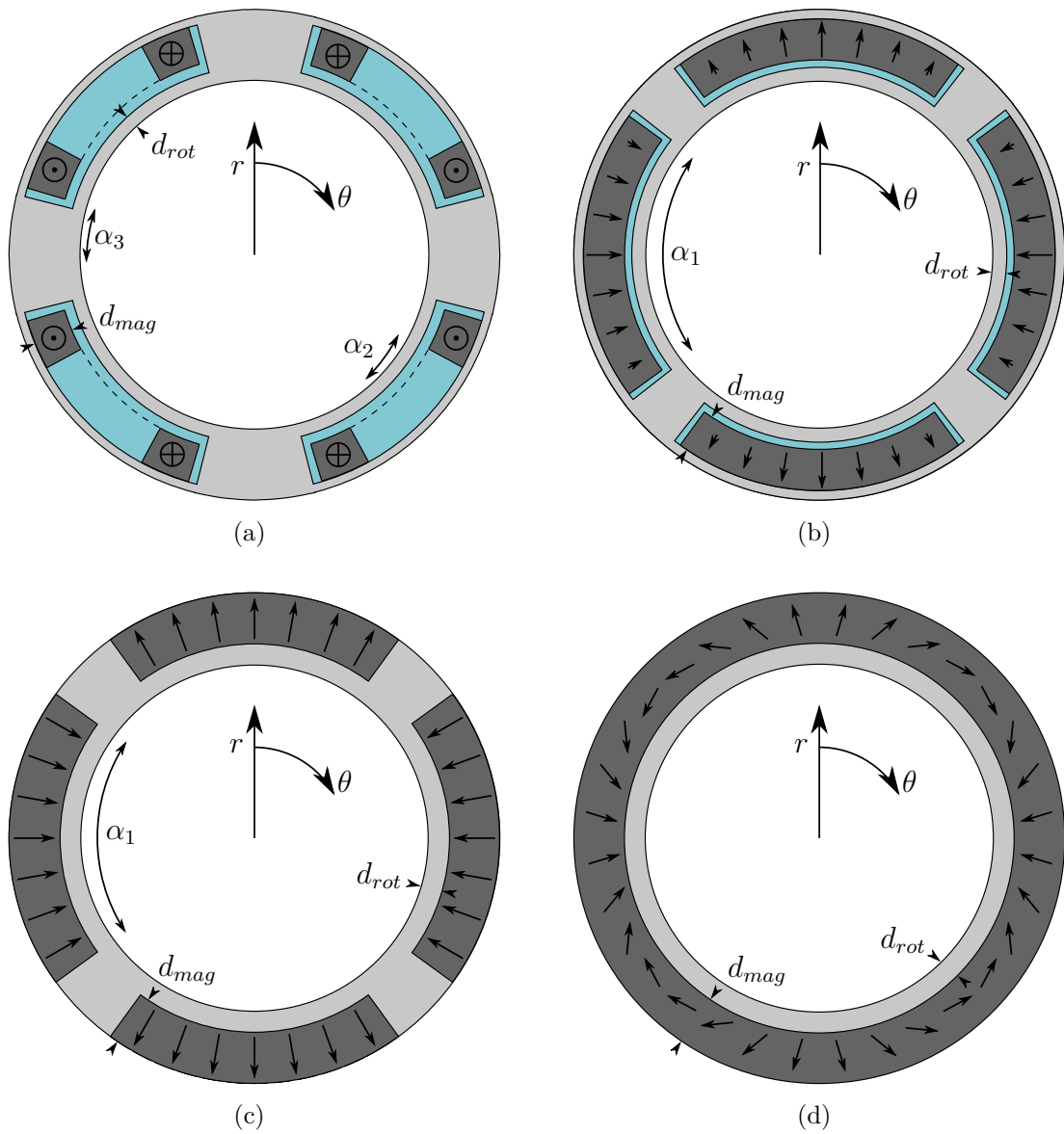


Figure 4.8.: Rotor excitation in region o equals 2 of the general superconducting machine model, as shown in Figure 4.2, with:

- (a) Superconducting coil.
- (b) HTS bulk.
- (c) Permanent magnet.
- (d) Halbach array.

Exemplary drawn for a machine with 4 poles and the arrows describe the direction and amount of magnetization. The rotor carrier, the coil or magnet and the liquid hydrogen are illustrated \square , \blacksquare , and \blacksquare , respectively.

HTS bulk

To model the electromagnetic behavior of HTS bulks, the Bean model is used [120]. It assumes the current density within a bulk to be constant, resulting in a triangle wave instead of a square wave generated by permanent magnets in the r - θ plane. The spatial shape of the radial component of the remanence $M_{tri,r}$ over a pole pair for HTS bulks is shown in Figure 4.10b and defined in Equation 4.29. Furthermore, the tangential component $M_{tri,\theta}$ is zero [173].

$$M_{tri,r} = \sum_{n \text{ odd}} M_{tri,n} \cos(np\theta) \quad (4.29)$$

$$M_{tri,\theta} = 0 \quad (4.30)$$

The Fourier coefficients $M_{n,tri}$ for the n^{th} harmonic can be calculated by Equation 4.31 for triangular remanence.

$$M_{tri,n} = \alpha_1 M_{max} \left(\text{sinc} \left(\frac{n \alpha_1}{4} \right) \right)^2 \quad (4.31)$$

$$M_{max} = \frac{B_{peak}}{\mu_0} \quad (4.32)$$

The coverage of the rotor surface α_1 is defined with magnets from the two-dimensional perspective and d_{mag} is the thickness of the bulk. Both values are shown in Figure 4.8b. The maximum remanence M_{max} of the bulk is calculated over a specific maximum flux density which occurs in the middle of the surface of the respective bulk shape. This point has been established in literature [174, 175, 176, 177] as a logical comparison point for the maximum flux density and is named peak flux density B_{peak} .

Three arrangements of HTS bulk arrays are distinguished in continuous, rectangular and cylindrical shape, as shown in Figure 4.9. They differ in the coverage of the

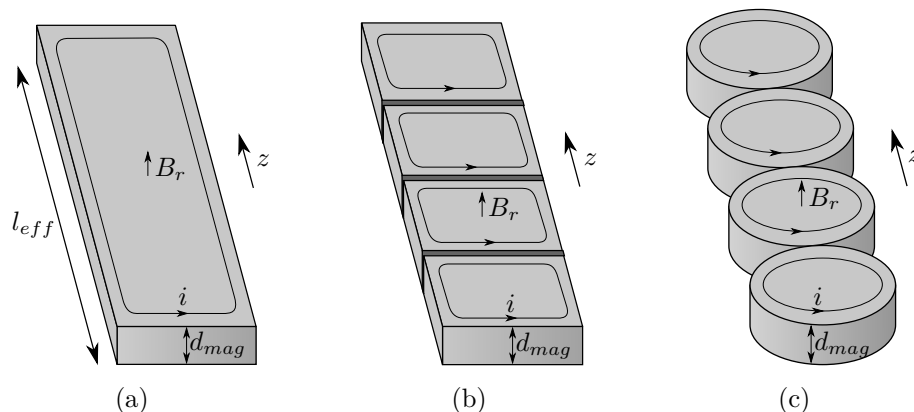
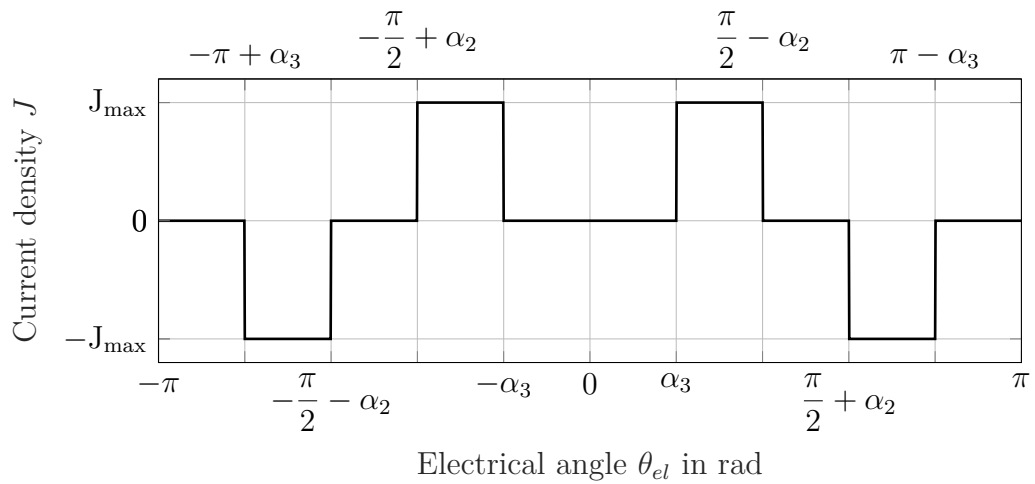


Figure 4.9.: HTS bulk arrangements for one pole distinguished in:

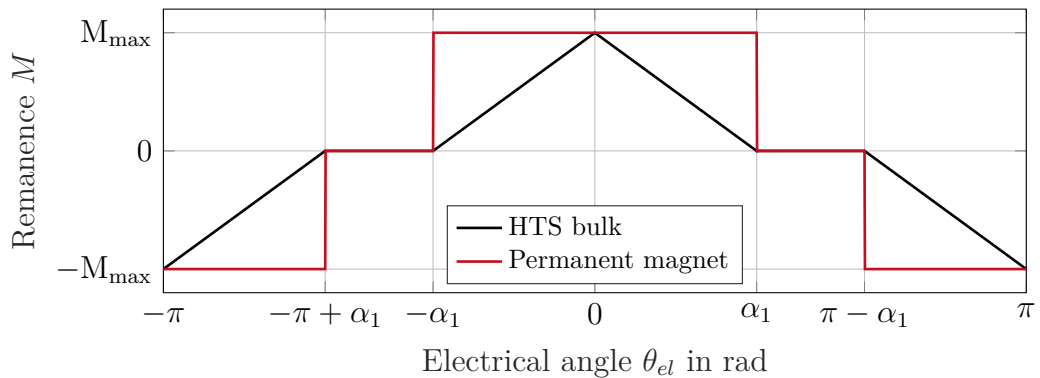
- (a) Continuous.
- (b) Rectangular.
- (c) Cylindrical.

rotor surface and their magnetic flux even in z -direction [178].

Due to the two-dimensional approach, the flux generated by the rotor must be corrected. A correction factor is defined as flux factor f_Φ in Equation 4.33 by comparing the total magnetic flux from an infinitely long bar of bulk HTS material, whose flux corresponds to the volume of a three sided prism and the flux from an infinitely long series of cylindrical or rectangular bulk arrays or a continuous bulk [179]. It should be note, that this factor does not consider the flux leakage in the axial direction of the rotor, which results in an overestimation of the torque as well as the AC loss of the stator [179]. Such factors are also determined in [180] by a three-dimensional FEM simulation and show sufficient agreement with the flux factor f_Φ in this work. Due to this different shapes, the true coverage is taken into account only when calculating the necessary effective machine length l_{eff} for a specific torque.



(a)



(b)

Figure 4.10.: Spatial shape as a function of the electrical angle θ_{el} over a pole pair of the:

- (a) Current density J in rotor coils.
- (b) Remanence M in radial direction of conventional permanent magnets and HTS bulks.

$$f_{\Phi} = \begin{cases} 1 - \frac{\alpha_1 \pi r_{r,m}}{3 l_{eff} p} & \text{if continuous HTS bulk} \\ \frac{2}{3} & \text{if rectangular HTS bulk array} \\ \frac{\pi}{6} & \text{if cylindrical HTS bulk array} \end{cases} \quad (4.33)$$

It is neglected that only discrete machine lengths are realizable with bulk arrays. However, due to reduced magnetic flux per rotor surface of bulk arrays, only the continuous bulk is suitable to achieve lightweight and efficient machines.

Even with these limitations, this approach seems sufficient to investigate the potential of HTS bulk machines. Since the power-to-weight ratio of such machines is overestimated, a further discussion is given in Section 6.4.

Permanent magnet

The geometry of machines in which the excitation is realized by permanent magnets, as shown in Figure 4.8c, is defined by the coverage α_1 and thickness d_{mag} . The radial and the tangential components of the magnetic remanence $M_{rec,r}$ and $M_{rec,\theta}$ for a radial magnetization only are given in Equation 4.34 and 4.35, respectively [181]. The utilized material defines the maximum remanence M_{max} .

$$M_{rec,r} = \sum_{n \text{ odd}} M_{rec,n} \cos(np\theta) \quad (4.34)$$

$$M_{rec,\theta} = 0 \quad (4.35)$$

The Fourier coefficients $M_{rec,n}$ are given by:

$$M_{rec,n} = 2 \alpha_1 M_{max} \operatorname{sinc} \left(\frac{n \alpha_1}{2} \right) \quad (4.36)$$

Halbach array

An Halbach array is a special arrangement of several individual permanent magnets to reach a magnetic pole with a approximately sinusoidal field profile [182]. For this purpose, the magnet of a pole is divided into several parts and the magnetization rotates within a pole pair around its own axis in longitudinal direction of the machine. Therefore, the magnetic flux increases on one side of the array while canceling the field to near zero on the other side. This offers the advantage that a rotor back-iron is not necessary and that the amplitude of the fundamental field is increased [183]. In radial flux machines with rotor excitation, this is the side facing the air gap [184]. The entire circumference is covered with segmented magnets and the thickness is defined over d_{mag} , shown in Figure 4.8d.

The magnetization of an ideal Halbach array is inherently sinusoidal and defined by Equation 4.37 for the radial component and by Equation 4.38 for the tangential component. Thus, the calculation for higher orders n is not necessary.

$$M_{hal,r} = M_1 \cos(p\theta) \quad (4.37)$$

$$M_{hal,\theta} = -M_1 \sin(p\theta) \quad (4.38)$$

4.5. Analytical Field Calculation

The following chapters introduce the calculation of the flux density in the entire machine for general coils, magnets and Halbach array. The necessary boundary conditions are also defined and the results are compared with finite element method (FEM).

4.5.1. Field Generated by Coils

A magnetic vector potential $\vec{\Phi}$ is used to calculate the field generated by coils. This potential has only a z -direction, if the field distribution is solved in the x - y plane and the current density has only a z -component. The Laplace equation 4.39 allows the calculation of the magnetic field outside of the stator coil area in the regions o equals 1, 2, 3, 5 and 6, as shown in Figure 4.2.

$$\frac{\partial^2 \Phi_{z,o}}{\partial r^2} + \frac{1}{r} \frac{\partial \Phi_{z,o}}{\partial r} + \frac{1}{r^2} \frac{\partial^2 \Phi_{z,o}}{\partial \theta^2} = 0 \quad (4.39)$$

The Poisson equation 4.40 is used to solve the field inside the coils in region o equals 4 with the current density J_z and the vacuum permeability μ_0 .

$$\frac{\partial^2 \Phi_{z,4}}{\partial r^2} + \frac{1}{r} \frac{\partial \Phi_{z,4}}{\partial r} + \frac{1}{r^2} \frac{\partial^2 \Phi_{z,4}}{\partial \theta^2} = -\mu_0 J_z \quad (4.40)$$

The Laplace equation and Poisson equation can be solved by the general solutions given in Equations 4.41 and 4.42, including the singularity at np equals 2 [161].

$$\Phi_{z,o}(r, \theta) = \sum_{n \text{ odd}} \left(A_{n,o} r^{np} + C_{n,o} r^{-np} \right) \cos(np\theta) \quad (4.41)$$

$$\Phi_{z,4}(r, \theta) = \begin{cases} \sum_{n \text{ odd}} \left(A_{n,4} r^{np} + C_{n,4} r^{-np} - \frac{J_n r^2}{4 - (np)^2} \right) \cos(np\theta) & \text{if } np \neq 2 \\ \sum_{n \text{ odd}} \left(A_{1,4} r^2 + C_{1,4} r^{-2} - \frac{1}{4} J_1 r^2 \ln(r) \right) \cos(2\theta) & \text{if } np = 2 \end{cases} \quad (4.42)$$

Afterwards, the radial and tangential component B_r and B_θ are given in Equation 4.44 and 4.45 by curl of the magnetic vector potential:

$$\nabla \times \Phi_{z,o} = \vec{B} \quad (4.43)$$

$$B_{r,o}(r, \theta) = \frac{1}{r} \frac{\partial \Phi_{z,o}}{\partial \theta} \quad (4.44)$$

$$B_{\theta,o}(r, \theta) = -\frac{\partial \Phi_{z,o}}{\partial r} \quad (4.45)$$

Subsequently, the derivation is solved to get the radial component $B_{r,o}$ in Equation 4.46 and 4.47 as well as

$$B_{r,o} = - \sum_{n \text{ odd}} np \left(A_{n,o} r^{np-1} + C_{n,o} r^{-np-1} \right) \sin(np\theta) \quad (4.46)$$

$$B_{r,4}(r, \theta) = \begin{cases} - \sum_{n \text{ odd}} np \left(A_{n,4} r^{np-1} + C_{n,4} r^{-np-1} \right) \sin(np\theta) & \text{if } np \neq 2 \\ - \frac{J_n r}{4 - (np)^2} \sin(np\theta) & \\ - \left(2 \left(A_{1,4} r + C_{1,4} r^{-3} \right) - \frac{1}{2} J_1 r \ln(r) \right) \sin(2\theta) & \text{if } np = 2 \end{cases} \quad (4.47)$$

the tangential component $B_{\theta,o}$ in Equation 4.48 and 4.49.

$$B_{\theta,o} = \sum_{n \text{ odd}} np \left(A_{n,o} r^{np-1} - C_{n,o} r^{-np-1} \right) \cos(np\theta) \quad (4.48)$$

$$B_{\theta,4}(r, \theta) = \begin{cases} \sum_{n \text{ odd}} \left(np \left(A_{n,4} r^{np-1} - C_{n,4} r^{-np-1} \right) - \frac{2 J_n r}{4 - (np)^2} \right) \cos(np\theta) & \text{if } np \neq 2 \\ \left(2 \left(A_{1,4} r - C_{1,4} r^{-3} \right) - \frac{1}{2} J_1 r \ln(r) - \frac{1}{4} J_1 r \right) \cos(2\theta) & \text{if } np = 2 \end{cases} \quad (4.49)$$

This solution is also valid if coils in the rotor are calculated. Only the corresponding region has to be changed.

4.5.2. Field Generated by Magnets

A further possibility for excitation of the machine are magnets. The derivation of magnetic fields generated by these is described in the following section. The solution can be used for permanent magnets as well as for HTS bulks.

In contrast to the section before, a magnetic scalar potential ϕ is used to calculate the two-dimensional field produced by magnets. The Laplace equation 4.50 describes the magnetic field outside of the magnet area in the regions o equals 1, 3, 4, 5 and 6, as shown in Figure 4.2.

$$\frac{\partial^2 \phi_o}{\partial r^2} + \frac{1}{r} \frac{\partial \phi_o}{\partial r} + \frac{1}{r^2} \frac{\partial^2 \phi_o}{\partial \theta^2} = 0 \quad (4.50)$$

The Poisson equation 4.51 is used in region o equals 2 to solve the field inside the magnets with the remanence M_r and the relative permeability μ_r .

$$\frac{\partial^2 \phi_2}{\partial r^2} + \frac{1}{r} \frac{\partial \phi_2}{\partial r} + \frac{1}{r^2} \frac{\partial^2 \phi_2}{\partial \theta^2} = \frac{M_r}{\mu_r r} \quad (4.51)$$

For both equations the general solutions are given in the Equations 4.52 and 4.53 by [186], including the singularity at np equals 1.

$$\phi_o(r, \theta) = \sum_{n \text{ odd}} \left(A_{n,o} r^{np} + C_{n,o} r^{-np} \right) \cos(np\theta) \quad (4.52)$$

$$\phi_2(r, \theta) = \begin{cases} \sum_{n \text{ odd}} \left(A_{n,2} r^{np} + C_{n,2} r^{-np} \right. \\ \left. + \frac{M_n r}{\mu_r (1 - (np)^2)} \right) \cos(np\theta) & \text{if } np \neq 1 \\ \sum_{n \text{ odd}} \left(A_{1,2} r + C_{1,2} r^{-1} + \frac{1}{2} \frac{M_1}{\mu_r} r \ln(r) \right) \cos(\theta) & \text{if } np = 1 \end{cases} \quad (4.53)$$

The radial component H_r and the tangential component H_θ are given in Equation 4.55 and 4.56 by gradient of the magnetic scalar potential:

$$\nabla \phi_o = -\vec{H} \quad (4.54)$$

$$H_{r,o}(r, \theta) = -\frac{\partial \phi_o}{\partial r} \quad (4.55)$$

$$H_{\theta,o}(r, \theta) = -\frac{1}{r} \frac{\partial \phi_o}{\partial \theta} \quad (4.56)$$

In region o equals 2, the magnetization M_r of the magnet must be considered:

$$B_{r,2} = \mu_0 \mu_r H_{r,2} + \mu_0 M_r \quad (4.57)$$

After solving the derivation, the radial component $B_{r,o}$ in Equation 4.58 and 4.59 as well as

$$B_{r,o} = \sum_{n \text{ odd}} -\mu_0 \mu_r np \left(A_{n,o} r^{np-1} - C_{n,o} r^{-np-1} \right) \cos(np\theta) \quad (4.58)$$

$$B_{r,2}(r, \theta) = \begin{cases} \sum_{n \text{ odd}} -\mu_0 \mu_r \left(np \left(A_{n,2} r^{np-1} - C_{n,2} r^{-np-1} \right) \right. \\ \left. + \frac{M_n (np)^2}{\mu_r (1 - (np)^2)} \right) \cos(np\theta) & \text{if } np \neq 1 \\ -\mu_0 \mu_r \left(A_{1,2} - C_{1,2} r^{-2} + \frac{1}{2} \frac{M_1}{\mu_r} (\ln(r) + 1) \right. \\ \left. - \frac{M_1}{\mu_r} \right) \cos(\theta) & \text{if } np = 1 \end{cases} \quad (4.59)$$

the tangential component $B_{\theta,o}$ in Equation 4.60 and 4.61 result.

$$B_{\theta,o} = \sum_{n \text{ odd}} \mu_0 \mu_r np \left(A_{n,o} r^{np-1} + C_{n,o} r^{-np-1} \right) \sin(np\theta) \quad (4.60)$$

$$B_{\theta,2}(r, \theta) = \begin{cases} \sum_{n \text{ odd}} \mu_0 \mu_r np \left(A_{n,o} r^{np-1} + C_{n,o} r^{-np-1} + \frac{M_n}{\mu_r (1 - (np)^2)} \right) \sin(np\theta) & \text{if } np \neq 1 \\ \mu_0 \mu_r \left(A_{1,2} + C_{1,2} r^{-2} + \frac{1}{2} \frac{M_1}{\mu_r} \ln(r) \right) \sin(\theta) & \text{if } np = 1 \end{cases} \quad (4.61)$$

Thus, the field generated by the magnets is determined by the presented equations for all machine regions.

4.5.3. Field Generated by Halbach Array

Similar to the computation of the fields for permanent magnets by a magnetic scalar potential ϕ , the solution for fields by an Halbach array is given in the following.

According to [187] the Laplace equation 4.62 for the regions o equals 1, 3, 4, 5 and 6 as well as the Poisson equation 4.63 for the region o equals 2 are given.

$$\frac{\partial^2 \phi_o}{\partial r^2} + \frac{1}{r} \frac{\partial \phi_o}{\partial r} + \frac{1}{r^2} \frac{\partial^2 \phi_o}{\partial \theta^2} = 0 \quad (4.62)$$

$$\frac{\partial^2 \phi_2}{\partial r^2} + \frac{1}{r} \frac{\partial \phi_2}{\partial r} + \frac{1}{r^2} \frac{\partial^2 \phi_2}{\partial \theta^2} = \frac{\nabla \vec{M}}{\mu_r} = \frac{M_1}{\mu_r r} (1 - p) \cos(p\theta) \quad (4.63)$$

These differential equations are solved with the general solutions in Equation 4.64 and 4.65.

$$\phi_o(r, \theta) = (A_o r^p + C_o r^{-p}) \cos(p\theta) \quad (4.64)$$

$$\phi_2(r, \theta) = \left(A_2 r^p + C_2 r^{-p} + \frac{M_1 r}{\mu_r (1 + p)} \right) \cos(p\theta) \quad (4.65)$$

By using the Equations 4.54 to 4.56 the radial and tangential component of the magnetic field $H_{r,o}$ and $H_{\theta,o}$ is solved and the components of the flux density can be calculated with the following equations:

$$B_{r,o} = \mu_0 \mu_r H_{r,o} = -\mu_0 \mu_r p (A_o r^{p-1} - C_o r^{-p-1}) \cos(p\theta) \quad (4.66)$$

$$\begin{aligned} B_{r,2} &= \mu_0 \mu_r H_{r,2} + \mu_0 M_r \\ &= -\mu_0 \mu_r p \left(A_2 r^{p-1} - C_2 r^{-p-1} - \frac{M_1}{\mu_r (1 + p)} \right) \cos(p\theta) \end{aligned} \quad (4.67)$$

$$B_{\theta,o} = \mu_0 \mu_r H_{\theta,o} = \mu_0 \mu_r p (A_o r^{p-1} + C_o r^{-p-1}) \sin(p\theta) \quad (4.68)$$

$$\begin{aligned} B_{\theta,2} &= \mu_0 \mu_r H_{\theta,2} + \mu_0 M_\theta \\ &= \mu_0 \mu_r p \left(A_o r^{p-1} + C_o r^{-p-1} - \frac{M_1}{\mu_r p (1 + p)} \right) \sin(p\theta) \end{aligned} \quad (4.69)$$

In order to calculate the magnetic flux density presented in the Sections 4.5.1 to 4.5.3, suitable boundary conditions are missing.

4.5.4. Boundary Conditions

By setting boundary conditions for the coordinate origin, between adjacent regions and in the inner yoke radius, the flux density equations presented in Section 4.5.1 to 4.5.3 can be solved. The coefficients $A_{n,o}$ and $C_{n,o}$ are symbolically calculated one-time with Python and the solution is saved to minimize the calculation time. At interfaces between two materials, the tangential component of the magnetic field $H_{\theta,o}$ and the radial component of the flux density $B_{r,o}$ are constant. Additionally, the magnetic scalar potential ϕ or the vector potential $\vec{\Phi}$, depending on the excitation type, are zero in the coordinate origin. To reduce the computation time, the yoke is not included in the field calculation. Therefore, since the permeability of the yoke is assumed to be infinite, only a radial component occurs. All boundary conditions are summarized in Equation 4.70.

$$\begin{aligned}
 \phi_1 |_{r=0} &= 0 & \Phi_{z,1} |_{r=0} &= 0 \\
 H_{\theta,1} |_{r=r_{r,i}} &= H_{\theta,2} |_{r=r_{r,i}} & B_{r,1} |_{r=r_{r,i}} &= B_{r,2} |_{r=r_{r,i}} \\
 H_{\theta,2} |_{r=r_{r,o}} &= H_{\theta,3} |_{r=r_{r,o}} & B_{r,2} |_{r=r_{r,o}} &= B_{r,3} |_{r=r_{r,o}} \\
 H_{\theta,3} |_{r=r_{s,i}} &= H_{\theta,4} |_{r=r_{s,i}} & B_{r,3} |_{r=r_{s,i}} &= B_{r,4} |_{r=r_{s,i}} \\
 H_{\theta,4} |_{r=r_{s,o}} &= H_{\theta,5} |_{r=r_{s,o}} & B_{r,4} |_{r=r_{s,o}} &= B_{r,5} |_{r=r_{s,o}} \\
 H_{\theta,5} |_{r=r_{y,i}} &= 0 & &
 \end{aligned} \tag{4.70}$$

4.5.5. Validation

The validation of the analytical field calculation is an important step in the model development. Due to the complex formulas and relationships, programming errors are difficult to detect. For this reason, each machine type is compared individually with finite element method. In addition, the influence of the maximum harmonic on the absolute and relative error is examined.

Ansys Maxwell version 19.1.0 is used as FEM software. For every machine type an identical two dimensional static model is created. The comparison of the different field components is done at specific circular arcs, as shown in Figure 4.11. The mid-

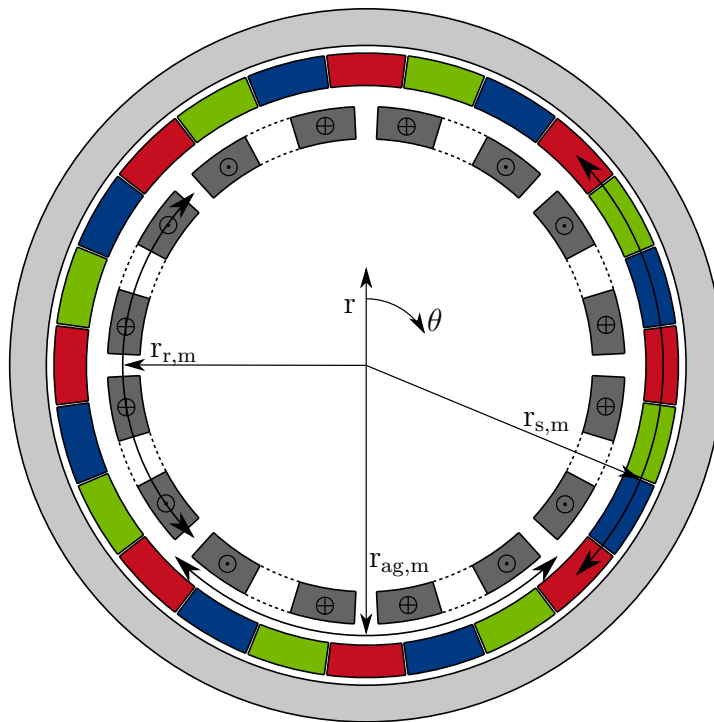


Figure 4.11.: Machine model with 4 pole pairs and specific circular arcs for the validation of the analytical calculation.

dle rotor radius $r_{r,m}$, the middle air gap radius $r_{ag,m}$ and the middle stator radius $r_{s,m}$ are selected as possible radii, so that the field is comprehensively analyzed. The presentation of the results is always identical. The analytical solution is displayed continuously (—, —) and the FEM solution is only compared at selected points (+, ×) for the radial component of the flux density B_r and tangential component of the flux density B_θ to keep the figures clear. Important machine input parameters are given by Table 4.3. Please note that this parameters are only examples to compare the analytical method and are not optimized. However, the parameters have been chosen meaningfully and are focused besides the different excitations on the singularities presented in Section 4.5.1 and 4.5.2. Furthermore, the results, such as torque, machine length or yoke thickness will not be discussed further. All configurations are calculated up to a maximum harmonic n_{max} of 59.

In the following examples the absolute error ε_a and relative error ε_r are computed, given by Equation 4.71 and 4.72, respectively. This equation is presented in general

Table 4.3.: Important input parameters of the electromagnetic machine model for validation.

Parameter	Unit	Config. 1	Config. 2	Config. 3	Config. 4
Rotor	-	HTS coil	HTS bulk	PM	Halbach
p	-	4	1	4	4
m	-	3	3	3	3
$r_{r,i}$	mm	150.0	150.0	150.0	150.0
$r_{r,o}$	mm	170.0	170.0	170.0	170.0
$r_{ag,m}$	mm	177.5	177.5	177.5	177.5
$r_{s,i}$	mm	185.0	185.0	185.0	185.0
$r_{s,o}$	mm	205.0	205.0	205.0	205.0
$r_{y,i}$	mm	210.0	210.0	210.0	210.0
J_s	A mm ⁻²	50	50	50	50
J_r	A mm ⁻²	100	-	-	-
B_{peak}	T	-	2	-	-
B_{rem}	T	-	-	1.44	1.44
α_0	%	95	95	95	95
α_1	%	-	80	60	100
α_2	deg	60.0	-	-	-
α_3	deg	5.625	-	-	-
n_{max}	-	59	59	59	59

form for a specific physical quantity given by finite element method x_{fem} or by the analytical machine model x_{ana} .

$$\varepsilon_a = |x_{fem} - x_{ana}| \quad (4.71)$$

$$\varepsilon_r = \left| 1 - \frac{x_{fem}}{x_{ana}} \right| \quad (4.72)$$

The influence of the maximum harmonic that is taken into account on the absolute and relative error is examined more accurately after the individual comparison. In the following the configurations 1 to 4, as listed in Table 4.3, are compared and discussed. Three further examples can be found in the Appendix D.

High-temperature superconductor coils are used as rotor excitation in configuration 1, as shown in Figure 4.12. The position of these coils around the circumference, including the stator coils, is marked. If the stator is powered by a current density distribution according to Figure 4.4 and under load which is the case at a load angle θ_{load} of 90 deg, the stator field distribution at the middle stator radius $r_{s,m}$ is given in Figure 4.12a. The three phase system is clearly visible in the radial field, just as the fundamental wave. The transition between the phases is also visible because the coverage α_0 is 95%. Figure 4.12b shows the field generated by two rotor coils at the middle rotor radius $r_{r,m}$. North and south pole are shown. Within the coils the radial field increases linearly. The largest mismatch of the radial and tangential

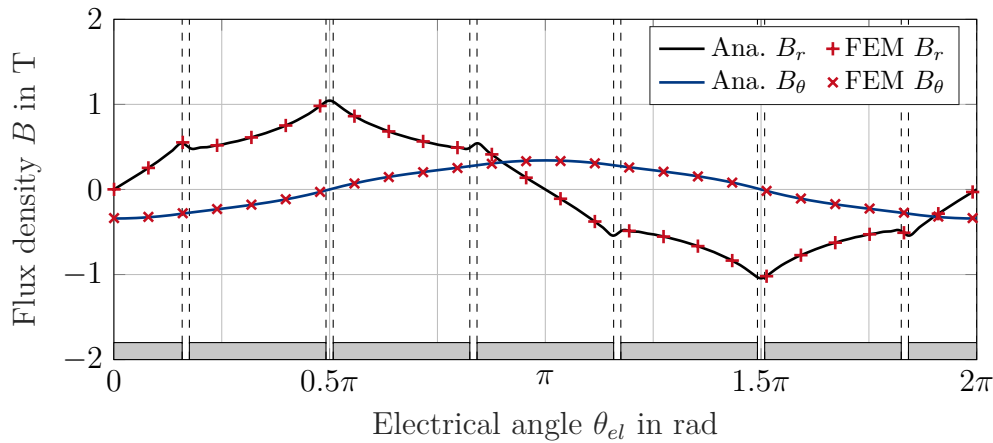
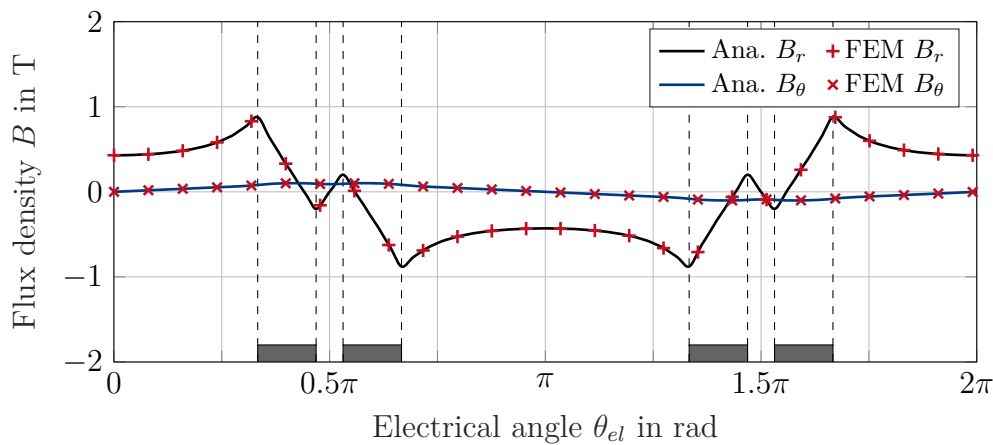
(a) Stator field at middle stator radius $r_{s,m}$ (b) Rotor field at middle rotor radius $r_{r,m}$

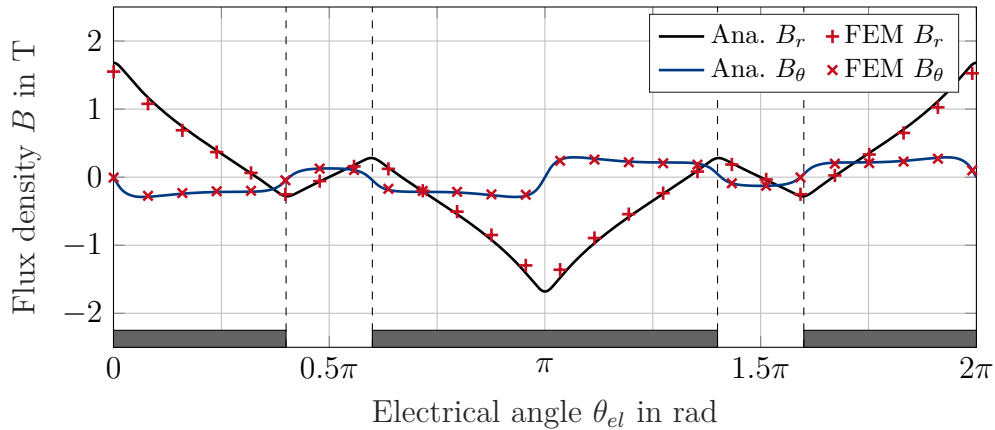
Figure 4.12.: Validation of the analytical machine model according to **config. 1** in Table 4.3 through a comparison with FEM over the radial and tangential flux density B_r and B_θ at different radii **without** exception np equals **2**. Coils are used as rotor excitation and the position around the circumference, including stator coils, are marked \blacksquare and \square , respectively.

component between analytical and FEM calculation is around 3% and occurs at middle stator radius in Figure 4.12a. The strongest peaks are in the radial field, which requires high harmonics to increase the accuracy in this point. However, this is limited by the chosen maximum harmonic n_{max} . Furthermore, the calculation is limited by the data type, because an overflow can occur in the exponent np in the general Solution 4.41.

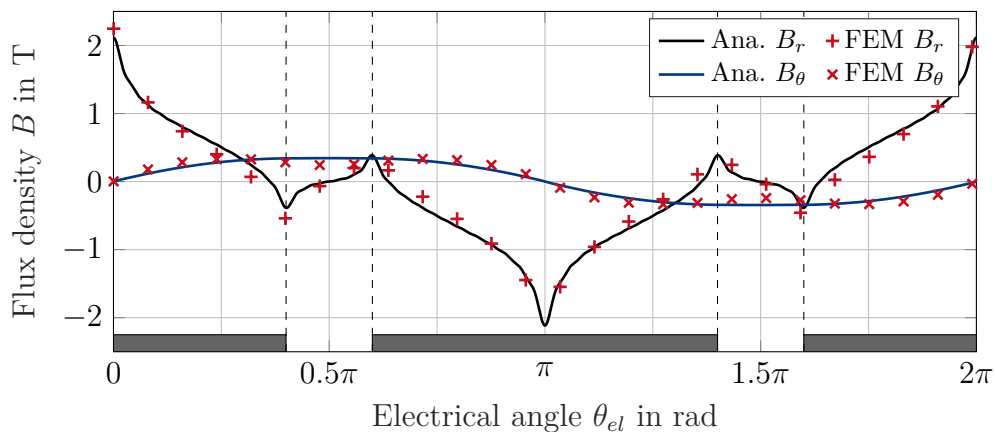
For comparison, configuration 5 is given in Table D.1 in the appendix with the same machine set-up, except the number of pole pairs, which is changed to 2. Accordingly, the singularity in Equation 4.42 arises and for the calculation of the fundamental wave the exceptional solution is used. This also affects the mismatch between analytical and FEM solution. Figure D.1c shows a significant relative deviation of 13.5%. By transforming the FEM results with a Fourier analysis, the deviant harmonics

are apparent. A larger deviation with 15 % can be found if the 3rd harmonics are compared. Errors cannot be found in the stator field in Figure D.1a, because a three-phase machine is calculated. In the air gap in Figure D.1b, the error is also missing, because the exception is only used in the rotor coil region.

In Figure 4.13 the results in case of HTS bulks as excitation, summarized as configuration 2 in Table 4.3, are shown. The triangular radial magnetization is recognizable



(a) Rotor field at middle air gap radius $r_{ag,m}$

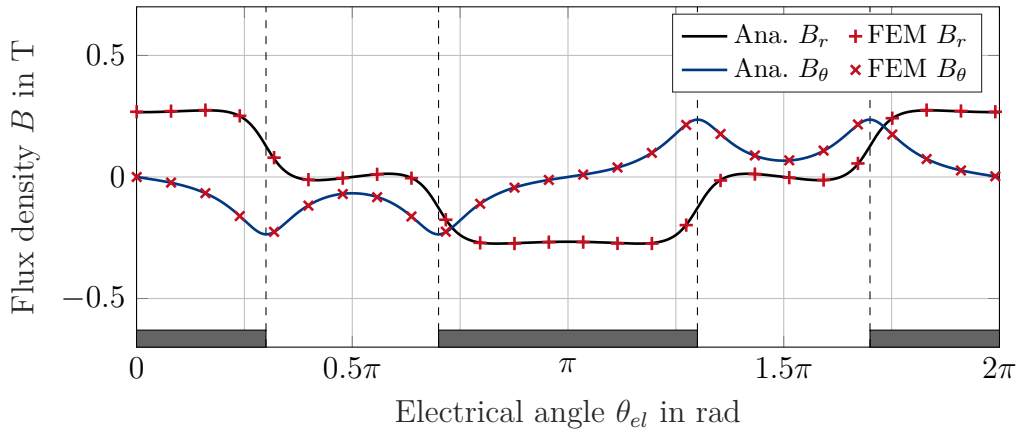


(b) Rotor field at middle rotor radius $r_{r,m}$

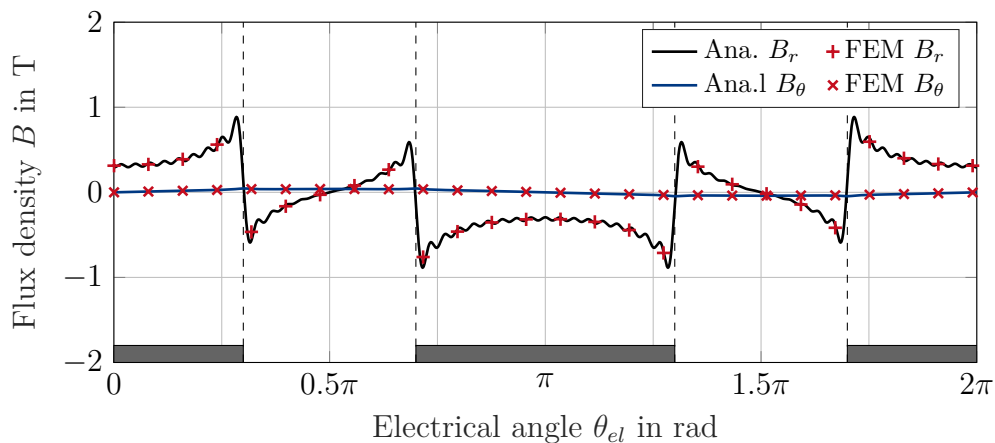
Figure 4.13.: Validation of the analytical machine model according to **config. 2** in Table 4.3 through a comparison with FEM over the radial and tangential flux density B_r and B_θ at different radii **with** exception np equals **2**. HTS bulks are used as rotor excitation and the position around the circumference is marked \blacksquare .

in Figure 4.13a and 4.13b. A mismatch is apparent at middle rotor radius in Figure 4.13b at zero crossing and the maximum of the absolute error is 0.18 T which corresponds to a relative error of 480 %. The mismatch arises in the 1st and 3rd harmonic. This high deviation occurs only if the exception comes into effect, as can be seen in Figure D.2 with 4 poles. Here, the absolute error is only 0.04 T which corresponds to a relative error of 7 %. In addition, the error has already decreased

at middle air gap radius in Figure 4.13a to a maximum relative error of 8%. The results of the flux density generated by a machine with permanent magnets in the rotor are calculated according to configuration 3 in Table 4.3 and are illustrated in Figure 4.14. The field by permanent magnets is displayed in the Figures 4.14a



(a) Rotor field at middle air gap radius $r_{ag,m}$

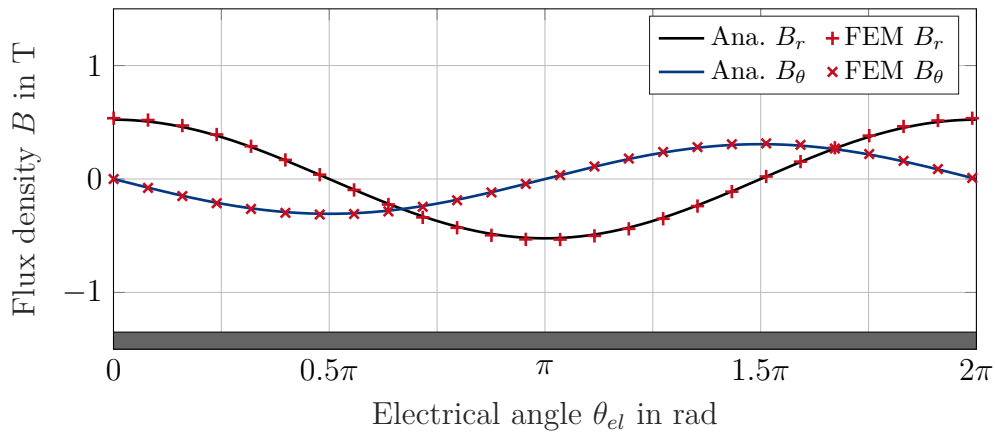


(b) Rotor field at middle rotor radius $r_{r,m}$

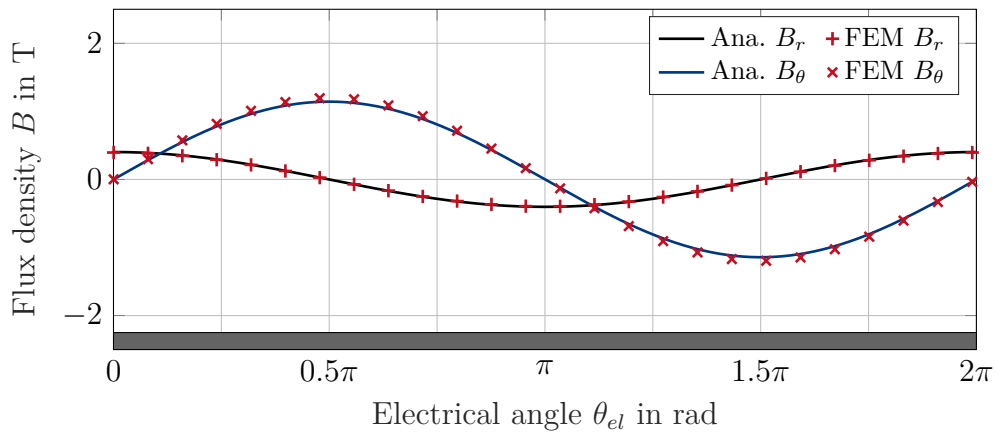
Figure 4.14.: Validation of the analytical machine model according to **config. 3** in Table 4.3 through a comparison with FEM over the radial and tangential flux density B_r and B_θ at different radii **without** exception np equals **2**. Permanent magnets are used as rotor excitation and the position around the circumference is marked \blacksquare .

and 4.14b at the middle air gap radius $r_{ag,m}$ and middle rotor radius $r_{r,m}$, respectively. The maximum relative error occurs in Figure 4.14b with 83%, because a high maximum harmonic order is necessary for the approximation of the sharp field profile. However, at the middle air gap radius the maximum relative error has already been reduced to 6%. This behavior is also shown in Figure D.3. The relative error in Figure D.3c at middle rotor radius $r_{r,m}$ is 108% and decreases to 5% at middle air gap radius $r_{ag,m}$ in Figure D.3b.

Finally, configuration 4, a machine with permanent magnets arranged to a perfect Halbach array, is discussed. Due to this fact, no harmonics occur and the field is



(a) Rotor field at middle air gap radius $r_{ag,m}$



(b) Rotor field at middle rotor radius $r_{r,m}$

Figure 4.15.: Validation of the analytical machine model according to **config. 4** in Table 4.3 through a comparison with FEM over the radial and tangential flux density B_r and B_θ at different radii. An Halbach array is used as rotor excitation and the position around the circumference is marked \blacksquare .

sinusoidal as it can be seen in Figure 4.15a and 4.15b. The maximum relative error amounts to 2.8%.

After all field profiles have been presented, the deviations are examined in more detail.

Error analysis

The absolute and relative errors mentioned in the validation examples occur always at field peaks. This behavior can also be seen in Figure 4.16, in which the radial flux density of the total field at middle stator radius $r_{s,m}$ of one pole is shown. Especially large absolute errors occur in each case during the transition from one stator coil to another. In this example, the error varies caused by the limited maximum harmonic

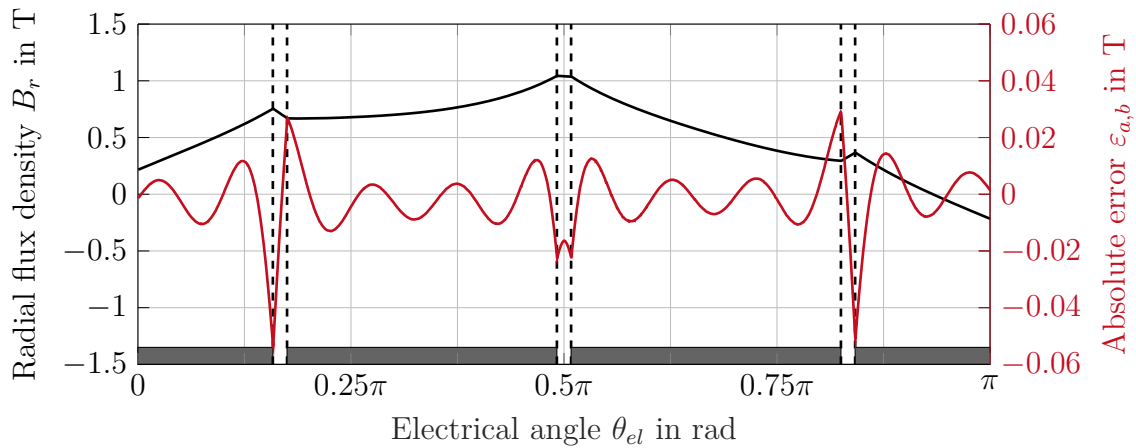


Figure 4.16.: Radial flux density B_r of the total field at middle stator radius $r_{s,m}$ calculated by FEM and the absolute error $\varepsilon_{a,b}$ between analytical machine model at n_{max} equals 19 and FEM of **config. 1** in Table 4.3. The position of the stator coils around the circumference of one pole is marked ■.

n_{max} of 19. This circumstance is advantageous for the accuracy of the calculation of the AC loss in the stator coils, because the loss occur only in the coils themselves and the accuracy is significantly higher there.

Now, the influence of the maximum harmonic on the absolute error ε_a and relative error ε_r is examined. For this purpose, configuration 1 from Table 4.3 is calculated for different maximum harmonics. This configuration is chosen because of the distinct peaks in the field profile and because the influence of the stator current density on the error can be investigated. The mismatch between analytical and finite element method is evaluated at the middle stator radius $r_{s,m}$ shown in Figure 4.2, because the accuracy in calculating the stator loss is particularly critical in this area.

Figure 4.17a presents the absolute and relative error $\varepsilon_{a,b}$ and $\varepsilon_{r,b}$ for the radial component of the flux density in dependence of the maximum harmonics. The error decreases steadily with increasing maximum harmonics apart from the result at n_{max} equal to 5. From n_{max} equal to 29, the relative error is less than 5%.

In Figure 4.17b the relative and absolute error is illustrated as a function of the stator current density J_s for different maximum harmonics. With increasing current density, the absolute error increases linearly because the peaks in the field profile becomes more distinctive. However, the relative error approaches with increasing current density to a constant relative error because the flux density increases simultaneously. If the maximum harmonics is 19, a relative error of less than 9% can be achieved. Up to a maximum harmonics of 59, the relative error drops to 2.6%.

The validation clearly shows the limits of the machine model. In machine designs with permanent magnets or HTS bulks and a pole pair number of 1 the accuracy decreases. For this reason, machines with a pole pair number of 1 are not supported by the model. The maximum harmonics must be chosen high enough to achieve the desired accuracy. It is assumed that a maximum harmonic of 19 is sufficient for large parameter analyses. If a pre-selection of machines has been done, the maximum

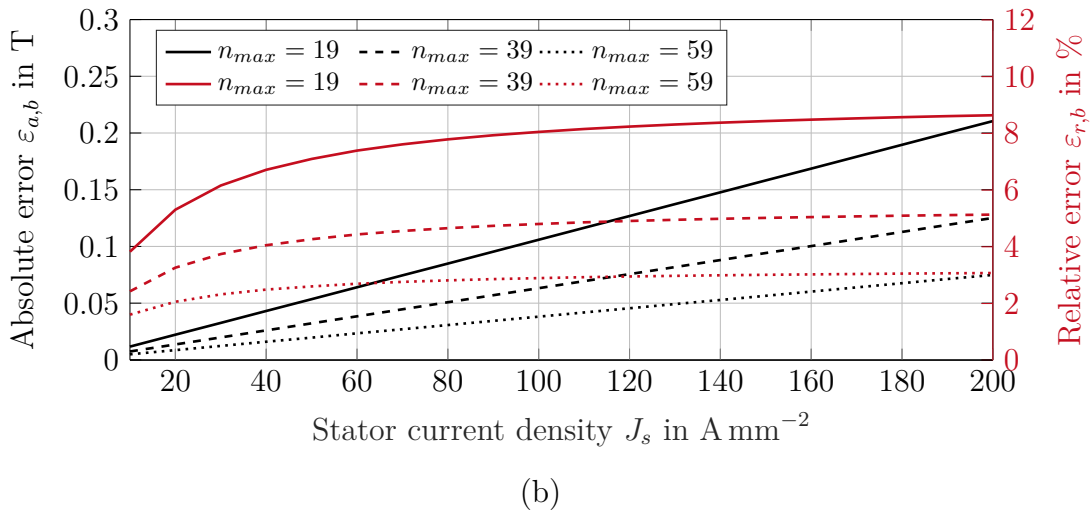
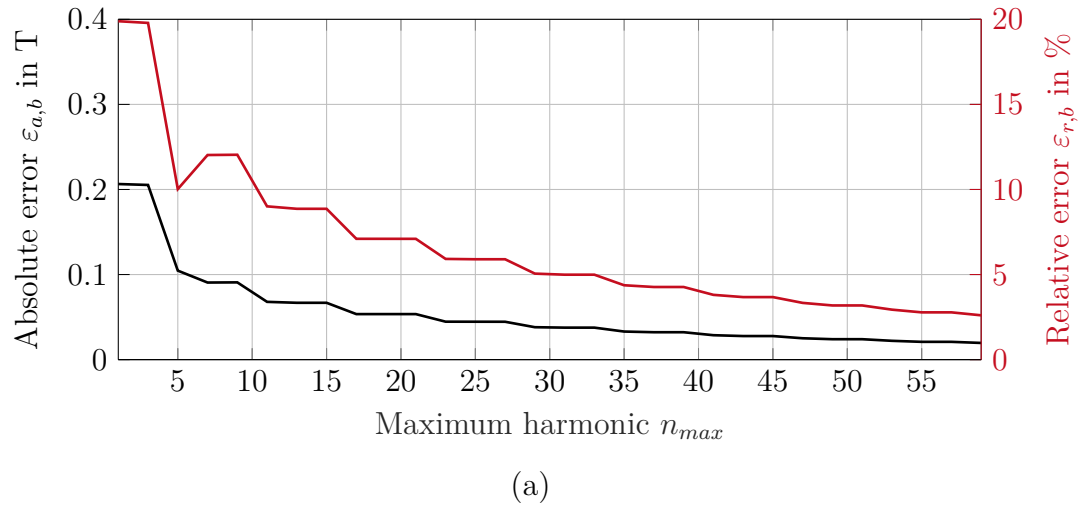


Figure 4.17.: Absolute error $\varepsilon_{a,b}$ and relative error $\varepsilon_{r,b}$ between analytical machine model and FEM as a function of the:

- (a) Maximum harmonic n_{max} .
- (b) Stator current density J_s .

Calculated are the radial flux density B_r of the total field at middle stator radius $r_{s,m}$ of **config. 1** in Table 4.3.

harmonic has to be increased. It must be noted that the product of harmonic n and number of pole pairs p in the exponent of the general solutions in Equation 4.41 and 4.52 are not higher than the maximum value of the used data type. Furthermore, the influence of the error on the AC loss of the stator coils, as presented in Section 5.3, is estimated to be low. This is due to the fact that the absolute error oscillates around its true value and thus has only a small effect on the average of the AC loss. In addition, the high relative errors occur mainly between the coils, where no AC loss is generated.

Overall, the accuracy of the calculation is sufficient for the analytical machine design and is used in the following chapters.

4.6. Torque Calculation

4.6.1. Analytical Calculation

The Lorentz force F_l on a current carrying conductor can be calculated by integrating the cross product of the current density \vec{J} and the flux density \vec{B} over its volume V :

$$F_l = \iiint_V \vec{J} \times \vec{B} dV \quad (4.73)$$

This approach is valid if the relative permeability μ_r of the stator coils equals to 1. It follows in Equation 4.74 that the mean torque \bar{M} can be calculated by integration of the tangential force in two steps [179]. Firstly, the volume integral of the cross product of the z -component of the current densities in all phases of the stator coils J_s and the radial component of the flux density generated by the rotor $B_{rot,r}$ is solved. Secondly, the time integral over one period of time T is calculated. The field generated by the stator does not produce any torque.

$$\bar{M} = \int_t \iiint_V J_s(\theta, t) \times B_{rot}(r, \theta, t) r dV dt = \frac{1}{T} \int_0^T l_{eff} \int_0^{2\pi} \int_{r_{s,i}}^{r_{s,o}} J_z B_{rot,r} r^2 dr d\theta dt \quad (4.74)$$

Solving the integrals leads to the mean torque for machines with excitations by magnets \bar{M}_m in Equation 4.75 and with excitations by coils \bar{M}_c in Equation 4.76. Spatial and time Fourier coefficients are F_n , M_n , $J_{s,n}$ as well as $J_{r,n}$ and are introduced in Sections 4.2 and 4.4. Further parameters are the number of phases m , the effective length of the machine l_{eff} and the load angle θ_{load} . Note that the coefficients A and C are different in both equations and given by solving the rotor field for magnets and coils, as presented in Section 4.5. The detailed calculation of the torque can be found in Appendix E.

$$\bar{M}_m = -\frac{1}{2}\pi \mu_0 m l_{eff} \sin(\theta_{load}) \sum_{n \text{ odd}} F_n M_n J_{s,n} \int_{r_{s,i}}^{r_{s,o}} A_{n,4} r^{np+1} - C_{n,4} r^{-np+1} dr \quad (4.75)$$

$$\bar{M}_c = \frac{1}{2}\pi \mu_0 m l_{eff} \sin(\theta_{load}) \sum_{n \text{ odd}} F_n J_{r,n} J_{s,n} \int_{r_{s,i}}^{r_{s,o}} A_{n,4} r^{np+1} + C_{n,4} r^{-np+1} dr \quad (4.76)$$

In this simplified form it can be seen that with a sinusoidal current, torque is generated only by the fundamental wave. This relationship makes the calculation much faster, because the sum is eliminated.

For machines with HTS bulks as excitation, the mean torque \bar{M}_m must be corrected by the flux factor f_Φ linked to the bulk geometry and introduced in Equation 4.33.

4.6.2. Validation

The torque calculation is compared with finite element method using the same example machines as presented in Table 4.3 and additionally the example machines

from Table D.1 in the appendix. For the results, it should be noted that these apply only to the example machines and their parameters are freely chosen. Furthermore, the different machine architectures should not be compared in this validation and the calculated torque refers to machines with an effective length l_{eff} of 1 m, respectively. The largest relative errors occur in configuration 2 and configuration 7 with 3.85 % and 8.93 %, respectively. Machines with a number of pole pairs of 1 are calculated in these configurations and thereby a singularity must be considered. This leads to the use of the exception to solve the differential equation and this causes the deviations as they occur also during the validation of the magnetic field in the section before.

Table 4.4.: Mean torque \overline{M} of the machine configurations from Table 4.3 and D.1 calculated by the analytical machine model and for comparison by FEM.

Parameter	Unit	Configuration						
		1	2	3	4	5	6	7
Analytical	N m	41227	23210	23010	44675	122934	24354	12028
FEM	N m	41240	22316	22847	45280	120970	23836	10954
Relative error	%	-0.03	+3.85	+0.70	-1.35	+1.60	+2.13	+8.93

4.7. Yoke Design

The yoke design includes the analytical determination of its thickness and the calculation of the iron loss. This is necessary because the mass of the yoke has a high influence on the power-to-weight ratio and the loss on the efficiency of the machine.

Yoke thickness

The following assumptions are made in the determination of the thickness of the yoke. Firstly, the stator yoke is not part of the field computation in the machine model. Secondly, the thickness of the yoke and the relative permeability of the yoke are first assumed as infinite, thereby the magnetic hysteresis of the yoke sheet metal is not considered. For this reason, only a radial field component is present at the transition to the yoke. However, the computational effort would grow significantly with the introduction of a finite thick yoke of finite permeability. In Addition, this assumption makes it impossible to calculate residual fields outside the machine.

The thickness of the yoke is adapted in the machine design process to saturate the yoke material up to a specific maximum flux density $B_{y,max}$ which is smaller than the saturation flux density $B_{y,sat}$ of the yoke sheet metal to prevent magnetic fields outside the machine.

The radial field component B_r is known, after the total field of the machine is solved. As a result of integrating the radial component of the flux density over a pole, the flux Φ_y through the cross section of the yoke is calculated. For simplification, Equation 4.77 displays the integration over a pole pair.

$$\Phi_y = \frac{1}{2} \int_0^{\frac{2\pi}{p}} |B_r| r_{y,i} l_{eff} d\theta \quad (4.77)$$

Using the flux Φ_y , the necessary thickness of the yoke d_y can be calculated, as shown in Equation 4.78.

$$d_y = \frac{\Phi_y}{B_{y,max} l_{eff}} \quad (4.78)$$

For machine excitations with HTS bulks, the flux Φ_y must be corrected by the flux factor f_Φ given in Equation 4.33, which leads to a reduction of the yoke thickness.

Iron loss

The iron loss $P_{v,fe}$ in the yoke iron is computed according to [188] and [189] in Equation 4.79 through a fit which is based on loss measurements for sinusoidal flux conditions with the volumetric density of the yoke sheet metal ρ_{fe} .

$$P_{v,fe} = \pi \left(r_{y,o}^2 - r_{y,i}^2 \right) l_{eff} \rho_{fe} p_{v,fe} \quad (4.79)$$

The approach is based on the subdivision of the total gravimetric iron loss $p_{v,fe}$ into the static hysteresis loss $p_{v,hys}$, the dynamic eddy current loss $p_{v,ec}$ and the excess loss $p_{v,exc}$ shown in Equation 4.80.

$$p_{v,fe} = p_{v,hys} + p_{v,ec} + p_{v,exc} \quad (4.80)$$

The excess loss considers the effect of the dynamic response of the domain structure to the applied field [189]. Equations 4.81, 4.82 and 4.83 describe the loss components, respectively. The advantage of this approach is that only the parameters C_{hys} and C_{exc} have to be fitted. Processing supplement factors are k_{hys} as well as k_{edd} and are chosen according to the manufacturing technology. Further parameters are the coercive field H_{co} , the electrical conductivity σ_{fe} , the thickness of the ferromagnetic sheets d_{fe} , the maximum sinusoidal flux density in the iron $B_{y,max}$ and electric frequency f_{el} . Furthermore, the permeability μ_{fe} must be known in dependence of the flux density and frequency.

$$p_{v,hys} = \frac{4 C_{hys} k_{hys} H_{co}}{\rho_{fe}} B_{y,max} f_{el} \quad (4.81)$$

$$p_{v,ec} = \frac{k_{edd} \pi^2 \sigma_{fe} d_{fe}}{6 \rho_{fe}} B_{y,max} f_{el}^2 \frac{3 \sinh(x) - \sin(x)}{x \cosh(x) - \cos(x)} \quad (4.82)$$

with $x = \sqrt{\pi f_{el} \sigma_{fe} \mu_{fe} d_{fe}}$

$$p_{v,exc} = \frac{C_{exc}}{\rho_{fe}} B_{y,max}^{1.5} f_{el}^{1.5} \quad (4.83)$$

This approach is compared in [190] with other analytical and numerical models and achieves good accuracy in the calculation of iron losses with only a few material parameters. As an example, the maximum error of the fit is 2.3% for untreated sheets of Vacodur [191] at a flux density of 1 T and frequencies less than 1000 Hz in comparison to the data sheet [192]. Therefore, this approach is assumed to be sufficient for this machine model.

4.8. Summary

An analytical model is developed for the electromagnetic design of a synchronous radial flux machine. This model is variable in all geometry and electromagnetic parameters. The stator is enclosed by a ferromagnetic iron yoke in order to shield the environment from electromagnetic fields. Furthermore, its thickness and iron loss is determined. The rotor does not have a ferromagnetic yoke, because this saves additional weight and is not required due to the high magnetic fields of superconducting DC coils and HTS bulks electromagnetically. This is also the case for an Halbach array, which is a further possibility to excite the machine. These different possibilities of excitation and the choice between stator coils made of copper or MgB_2 allow the design of both partially superconducting and fully superconducting machines. These topologies also differ in their air gap design, which influences the magnetically effective air gap between excitation and stator coils. For this reason, the radial thicknesses of the sleeve, the coil and magnet carriers and the cryo walls are calculated under consideration of mechanical and thermal boundary conditions.

The differential equations of the two-dimensional magnetic field calculation are solved in the frequency domain, which has the advantage of a fast computation compared to finite element method. Moreover, this offers the benefit that a large number of parameters can be evaluated in order to design optimized machines. A disadvantage compared to finite element method is that both coils and magnets have to be shaped due to the analytical approach and have no rectangular profile. Due to the complete implementation of all functionalities in Python the large amount of data can be efficiently computed and post processed. Therefore, the finite element method has an advantage when detailed investigations are carried out. However, the selection is always a compromise between accuracy, complexity and calculation time.

The field distribution of coils and magnets as well as the torque of the machine is compared with finite element method and shows good agreement with relative errors of less than 5% for maximum harmonics greater than or equal to 29. This is necessary to consider the high magnetic field sensitivity of MgB_2 , as presented in Chapter 2, correctly in the further design. It should be noted that machines with a pole pair number of 1 are not supported by the machine model due to a high inaccuracy in the field computation caused by singularities.

5. Design of Superconducting Machines for Flight Mission

This chapter describes the design process that uses the coupling of the electro-thermal model from Chapter 3 and the electromagnetic machine design model from Chapter 4 to design and optimize machines for aviation. At the beginning, the fundamental design process of a machine for a specific aircraft and flight mission is described. To account for the efficiency of the machines, the required amount of liquid hydrogen to cool the machines during a mission is considered. In order to include also the mass of a liquid hydrogen tank, an additional tank model is developed. Furthermore, it is discussed how the AC loss of a stator winding is calculated and how the total loss can be minimized by using an optimized control strategy to satisfy the different operational states during the entire mission.

5.1. Fundamental Design Process

Figure 5.1 presents the fundamental design process which is divided into 10 steps and each of them can contain subroutines. The abbreviations S and C in the steps links to the related subroutine and chapter, respectively. The goal is to design an optimal machine for a selected superconductor, taking into account the overall cooling and mission requirements. The description is made for a general superconductor and cooling medium, whereby liquid hydrogen (LH₂) is selected as coolant in this thesis.

A step-by-step explanation of the design process with a detailed description follows.

Step ①:

Firstly, a conductor and a machine topology according to Table 4.1 have to be selected. In general, each cylindrical shaped type of superconductor can be handled. However, in this thesis, only the 114 multifilament MgB₂ wire, presented in Section 2.1, is taken into account. A copper litz wire can also be selected. The geometric and material properties of the conductor are input parameters.

Step ②:

The main input parameters of the machine design are the power P and the speed n by which the torque M is determined. They are known from the aircraft design, the flight mission and various safety aspects that must be complied with, such as the redundancy of the drives. An exemplary flight mission is shown in Figure 5.2. The mission profile is represented by the altitude a as a function of the distance d including a diversion mission. This mission is flown e.g. in the case of a go-around of an aircraft when a landing approach is aborted. Furthermore, the additional jet fuel for this mission enables to circle for a while if no landing slot is free or to fly to an alternative airport. The cruising altitude is 35000 ft, which corresponds to 10668 m.

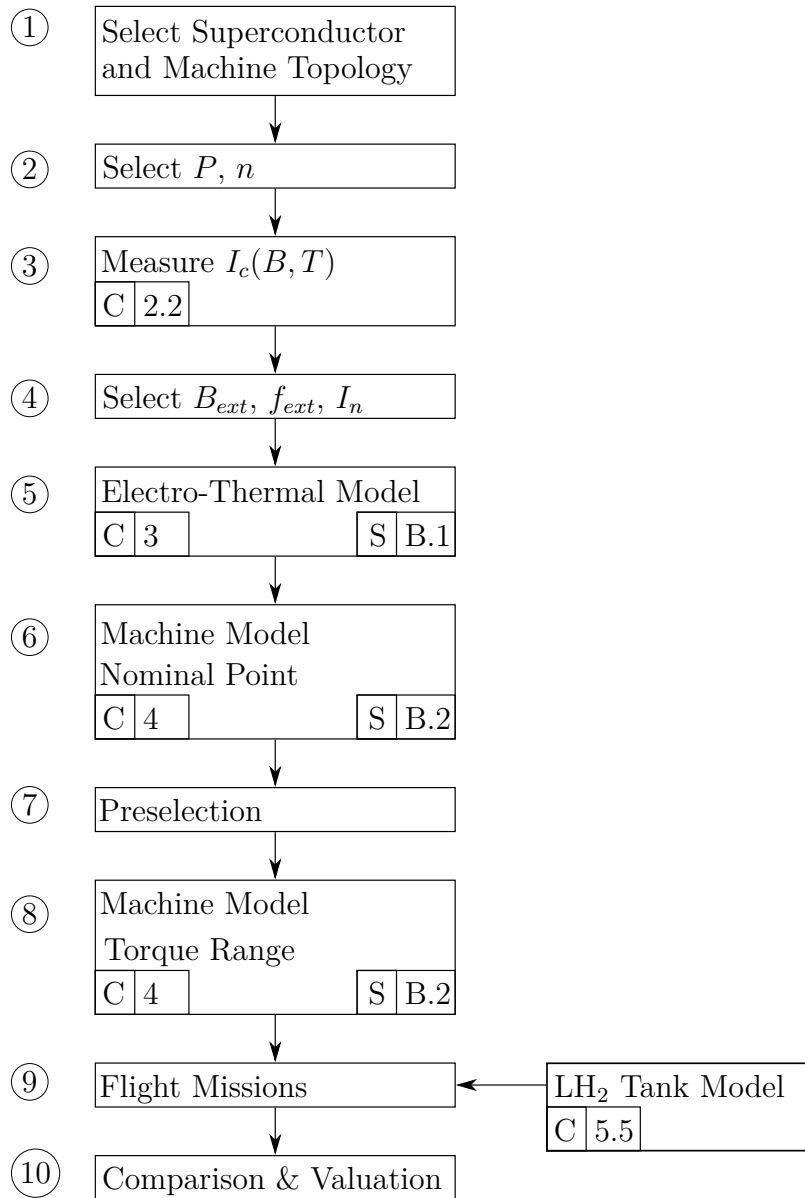


Figure 5.1.: Fundamental design process as flowchart with the related subroutines **S** and a link to the corresponding chapters **C**.

Step ③:

The determination of the critical current I_c of the superconductor as a function of the flux density B and the temperature T is indispensable for the further design process. This characterization of a superconductor is described in detail in Section 2.2 and is the basis of all further calculations. Furthermore, the conductor has to be characterized between the evaporation temperature of the cooling medium and the critical temperature of the superconductor. This range can also be made smaller depending on the choice of the superconductor and cooling medium. The flux density can be estimated from zero up to the saturation flux density of the yoke. However, the upper limit of the flux density can also be above the saturation flux density of the yoke, e.g. if yoke and stator coils are distanced from each other. Ironless

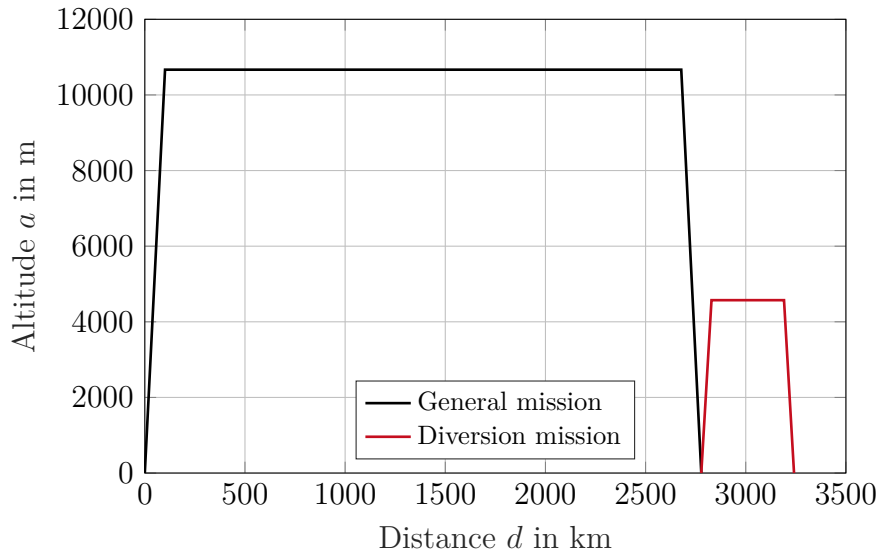


Figure 5.2.: Exemplary mission profile represented by the altitude a as a function of the distance d .

machines are not considered in this thesis in order to comply with electromagnetic compatibility (EMC) requirements.

Step ④:

Next, the input parameters of the electro-thermal model are chosen. The external flux density B_{ext} is limited in the same way as in the previous point and the associated external frequency f_{ext} should also be limited, such that the AC loss is not too high. In this work, this limit is set to 1000 Hz. Also, a variation of the number of pole pairs should be possible without exceeding the maximum frequency. For the normalized current I_n , a meaningful range is between 0 and 0.8. This ensures sufficient distance to the quench. The working point of the stator coils, described in Section 5.2, can be selected freely in the machine design in this normalized current range. In addition, this database forms the source of the stator coil AC loss calculation in Section 5.3.

Step ⑤:

Now the calculation of the electro-thermal model can start. A detailed description of this model can be found in Chapter 3, which also describes the corresponding subsequence in Figure B.1. The significant input parameters of the subfunctions cooling and superconductor behavior are collected in Table 5.1. Due to the given superconductor and the boundary conditions in a machine design, optimization is only possible by improving the flow conditions of the cooling medium. For every set of field and current conditions, the electro-thermal characterization of a specific superconductor must be done only once and can be reused for the design of different machine topologies. The same applies to the electro-thermal characterization of the copper litz wire.

Table 5.1.: Significant input parameters of the electro-thermal model for a chosen superconductor and coolant divided into the parts:

- (a) Cooling.
- (b) Superconductor behavior.

(a)

Symbol	Unit	Explanation
s_{lh2}	m	Cooling slot thickness for LH ₂
\dot{x}_{in}	–	Vapor quality at the beginning of cooling slot
\dot{x}_{out}	–	Vapor quality at the ending of cooling slot
l_s	m	Length of cooling slot
p_{out}	bar	Outlet pressure

(b)

Symbol	Unit	Explanation
B_{ext}	T	External flux density
f_{ext}	Hz	External frequency
I_n	–	Normalized current
I_c	A	Critical current
ρ	Ω m	Resistivities of all materials

Step ⑥:

The usage of the electromagnetic machine model from Chapter 4 with the corresponding subsequence in Figure B.2 follows. The model can be used to design machines for the nominal point or to characterize a specific machine over the entire torque range.

Firstly, an optimization of a machine with a chosen excitation for the nominal point is performed by varying the parameters in Table 5.2. These are divided into general, which are independent of the selected machine topology, and coil excitation as well as magnet excitation parameters. These significantly influence the stator current density as well as the exciting field profile of the rotor and thus the torque of a machine as well as the stator AC loss. The maximum normalized current in the stator $I_{n,max}$ defines the maximum spatial permissible normalized current I_n in the stator coils at the nominal point of the machine. Further parameters are the characteristics of the materials, as listed in Table 6.4. These are pre-defined and are not varied in this thesis in order to limit the amount of computing effort.

Step ⑦:

The results generated in the previous step are evaluated and rated. Depending on the application, exclusion criteria can exist. These include a minimum bending radius of the rotor coil as well as the stator coil and a specified installation space, for example. Economic boundary conditions can also be taken into account. The primary target parameters to be optimized are the power-to-weight ratio PTW and the stator AC

loss $P_{s,v}$. After this process a small number of machines remain, being investigated in further detail.

Table 5.2.: Significant input parameters of the machine design model divided into the parts:

- (a) General.
- (b) Coil excitation.
- (c) Magnet excitation.

(a)

Symbol	Unit	Explanation
p	–	Number of pole pairs
f_{el}	Hz	Electrical frequency
m	–	Number of phases
$I_{n,max}$	–	Maximum normalized current in stator
$r_{r,i}$	m	Inner radius of rotor
α_0	%	Duty cycle of stator coils
$d_{s,c}$	m	Thickness of stator coils
$B_{y,max}$	T	Maximum flux density of yoke
f_{csr}	–	Stator coil support ratio
θ_{load}	deg	Load angle

(b)

Symbol	Unit	Explanation
J_r	A mm ²	Current density in rotor coils
d_{mag}	m	Thickness of rotor coils
α_2	deg	Inner angle of rotor coil
α_3	deg	Angle between adjacent rotor coils

(c)

Symbol	Unit	Explanation
B_{rem}	T	Remanence flux density of rotor magnets
B_{peak}	T	Peak flux density of rotor magnets
d_{mag}	m	Thickness of rotor magnets
α_1	%	Duty cycle of rotor magnets

Step ⑧:

The AC loss of the stator coils of these selected machines is computed at various torque requirements according to the mission profile. This includes the identification of the AC loss-optimal control of machines with rotor coils, as described in

Section 5.4. In this way, the total hydrogen consumption can be obtained.

Step ⑨:

The flight mission can now be evaluated regarding the consumption of hydrogen in order to determine the hydrogen tank size. Various safety factors are taken into account, both for the design of the tank and the required hydrogen volume. The tank design is described in detail in Section 5.5. Furthermore, the available space for the tanks can be defined by re-equipping a selected aircraft.

The cooling of the superconductor is taken into account in the overall design and the power-to-weight ratio can be related to the total mass of the machine and liquid hydrogen tank. Furthermore, the maximum length of the flight mission due to stator AC loss is calculated. It should be noted, that the entire system design is not discussed in this thesis.

Step ⑩:

Finally, the results are evaluated and different machine topologies are compared. This allows to recommend a specific technology that works most effectively with the selected superconductor. Additionally, the results from the machine design can be used in the system design of the entire electrical propulsion system.

5.2. Stator Coil Working Point

At the beginning of the machine design, the operational current density of the stator coils is not known since the magnetic field penetrating the coils has not been computed yet. This point is defined as working point (WP) at the maximum flux density in the stator coil area and is named as working point flux density B_{wp} . A total field distribution of the stator coils is shown for example in Figure 5.5b. In this example, the working point flux density is detected at the inner stator radius $r_{s,i}$. In general, it can be found at various stator phases and radii. Furthermore, the working point defines the related current density J_{wp} . Since the working point depends strongly on the machine geometry and the rotor excitation, it must be redetermined for each new design.

The flowchart for determining the working point is shown in Figure 5.3. First, the characteristic of the engineering current density J_e in dependency of the external flux density B_{ext} is loaded from the results of the electro-thermal model for a specific maximum normalized current $I_{n,max}$ and external frequency f_{ext} . A characteristic is shown for example in Figure 5.4 for normalized currents I_n of 0.3, 0.5, 0.7 and 1.0. Next, the machine characteristic has to be calculated. Therefore, the maximum flux density in the stator coil area at the minimum engineering current density $J_{e,min}$ and maximum engineering current density $J_{e,max}$ of the stator coils defined by the electro-thermal model are calculated. Normally, these are $J_{e,min}$ which occurs at the maximum flux density B_{max} and $J_{e,max}$ at zero field, as shown in Figure 5.4.

Three termination conditions can occur during the calculation and these are illustrated in Figure 5.4. Firstly, if the maximum stator flux density at zero stator current density $B_{s,max}|_{J_e=0}$ is greater than the maximum flux density of the electro-thermal model results B_{max} . In this case, the rotor flux density B_{rot} alone is too strong for

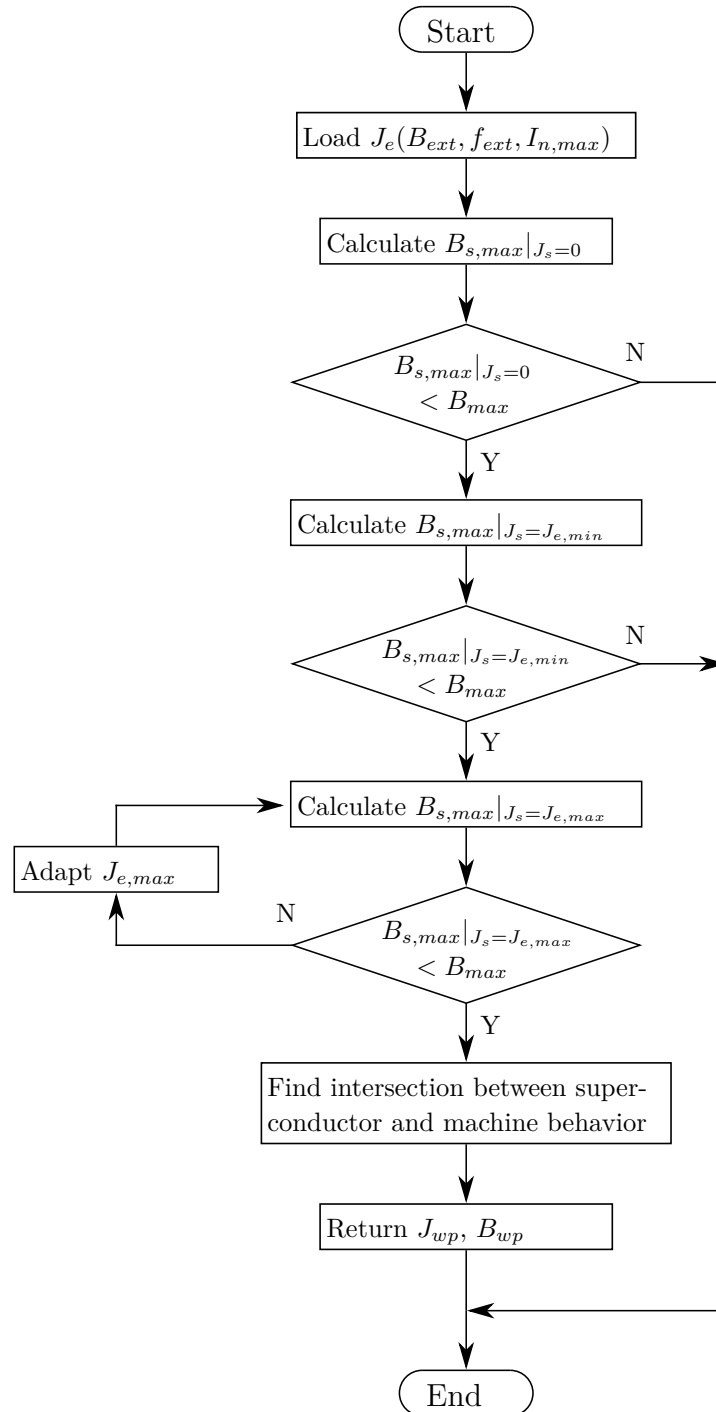


Figure 5.3.: Flowchart of the working point determination for a selected external frequency f_{ext} and maximum normalized current $I_{n,max}$ between the electro-thermal model of a chosen superconductor and an investigated machine geometry.

the stator coils. Secondly, if the maximum stator flux density at minimum stator current density $B_{s,max}|_{J_s=J_{e,min}}$ is greater than B_{max} . A third condition is defined, if the maximum stator flux density at maximum stator current density $B_{s,max}|_{J_s=J_{e,max}}$ is greater than B_{max} . This means that the stator field is too strong due to the maxi-

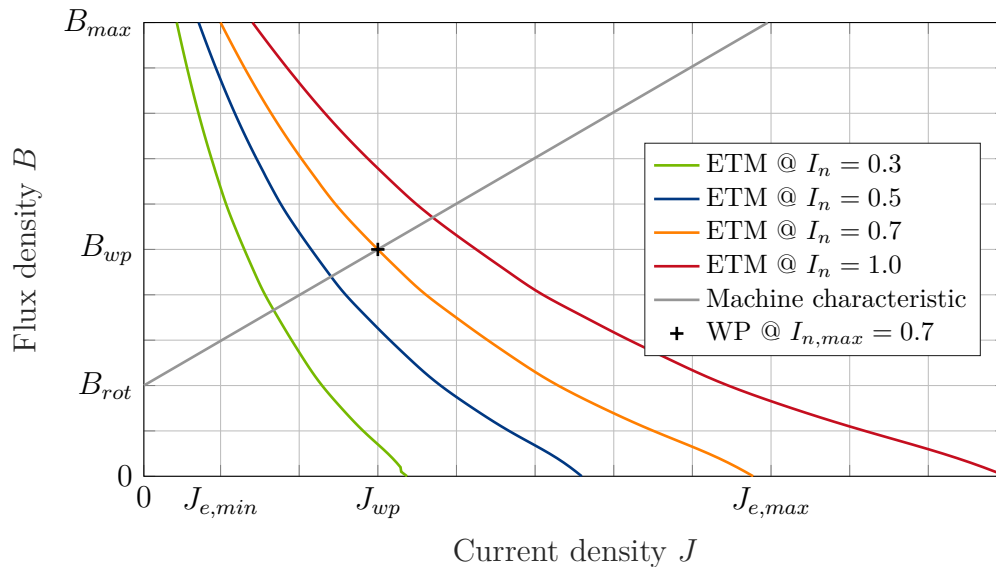


Figure 5.4.: Current density J as a function of the flux density B calculated by the electro-thermal model for the normalized currents I_n of 0.3, 0.5, 0.7 and 1.0. The machine characteristic is presented by the maximum flux density $B_{s,max}$ occurring at the stator coils as a function of the engineering current density of the stator coils J_e for a specific machine geometry at a maximum normalized current $I_{n,max}$ of 0.7. The working point is marked.

imum stator current density. In this case, the stator current density can be adjusted iteratively to a lower value.

The straight line through these points intersects the y-axis at the rotor flux density and the working point of the stator coils results from the intersection of the two characteristics. This is shown for example in Figure 5.4 for a maximum normalized current $I_{n,max}$ of 0.7. The electro-thermal characteristic at a normalized current of 1.0 illustrates the margin to the critical point of the superconductor. This is considered to be sufficient at a normalized current of 0.7. Finally, the current density J_{wp} and flux density B_{wp} of the working point are returned to the superordinate process, as presented in Figure B.2.

Since the total field has to be calculated for every adapted stator current density, the determination of the working point is a time consuming iterative process. In addition, the magnetic air gap of the machine varies, because the cryo wall design is dependent on the machine length, as described in Section 4.3.2. Furthermore, the high sensitivity of the current density in dependence of the flux density requires more iterations in the design of a superconducting stator compared to a normal conducting stator. This effect increases with decreasing number of pole pairs, because the area of the stator coil increases and thus the generated self field. In the worst case, this results in an oscillating machine design which converges very slowly or not at all. However, many times a solution is found after 5 iterations and a design process is terminated after 20 iterations.

5.3. Stator Coil AC Loss

The basics of the AC loss calculation are described in Chapter 2 and 3. However, single conductors and single coils are described there, which are penetrated by a spatially constant field. This assumption is now no longer valid, because the magnetic field changes in an electric machine both spatially and over time. For this reason the stator coils are discretized in tangential and radial direction.

Additionally, the liquid hydrogen consumption is determined. This defines the necessary volumetric size of the liquid hydrogen tank and greatly influences the mass of the entire drive system.

The following simplifications have been made in the calculation, which is based on [142]. Firstly, the AC loss in the winding heads is not considered by the two-dimensional model. Due to the large air gap and the high magnetic fields of superconducting machines, these should be considered by finite element method in a further more detailed design step. However, it is assumed that this loss component is much smaller compared to the loss in the winding segment in the air gap, because the field, which penetrates the stator winding heads, is much smaller than the air gap field. Furthermore, a field shield can also be designed to reduce the AC loss in the winding heads. Secondly, the support structure of the stator coils is taken into account by the correction factor f_{csr} and is not specified in detail due to the variability in the machine geometry. Thirdly, shielding effects of the superconducting coil are not considered, due to the loss calculation approach for a single wire, as described in Chapter 2.

Figure 5.5 illustrates the two-dimensional step by step AC loss calculation at an example machine with MgB₂ stator coils and HTS rotor coils at a load angle of 90 deg. The ideal stator current density distribution J_s of the 3-phase winding system is illustrated in Figure 5.5a for one pole pair. The areas of zero current density correspond to the value of α_0 and the coil transitions are marked.

The calculation starts with the creation of a mesh in the stator coil area between the inner stator radius $r_{s,i}$ and the outer stator radius $r_{s,o}$. Due to the small gradient in radial direction, as shown in Figure 5.5b, the local resolution can be much lower than in tangential direction. One sample is chosen per millimeter in the radial direction and 5000 samples per pole pair in tangential direction. This enables a tangential sample rate of more than 4 samples per mm if the outer stator radius is less than 400 mm and the pole pair number greater than 2. However, the tangential sample rate can be increased if necessary, because it does not have a great influence on the computation time, such as the radial sample rate.

Afterwards, the radial and tangential component of the flux density B are calculated at the meshed points according to Section 4.5. Figure 5.5b shows the spatial distribution of the absolute value of the total flux density $|B|$ in the stator coils. The absolute value of the flux density is sufficient for the calculation because the critical current density of the MgB₂ wire can be considered independent of the field angle, as presented in Section 2.3.3. This cannot be assumed for anisotropic coated superconductors, such as YBCO tapes. The angle of the penetrating field must be taken into account in the computation additionally [84].

In the next step, the normalized current I_n in the stator coils is determined by using the calculation results of the electro-thermal model for the 114 filament MgB₂

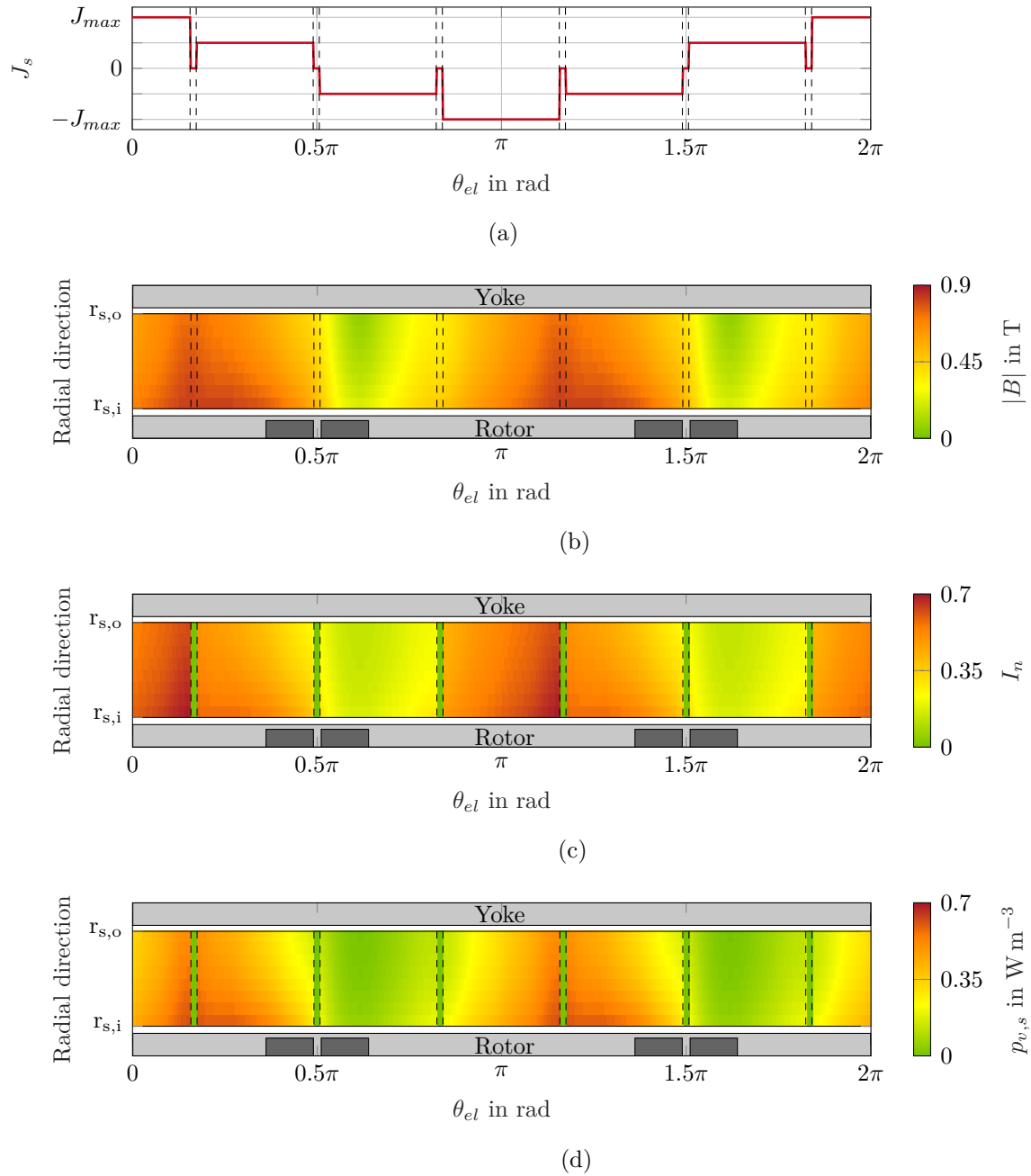


Figure 5.5.: Results of an exemplary calculation of the stator AC loss presented between the inner stator radius $r_{s,i}$ and outer stator radius $r_{s,o}$ for a fully superconducting machine with MgB_2 stator coils and HTS rotor coils:

- (a) Stator current density J_s as a function of the electrical angle θ_{el} .
- (b) Absolute value of the flux density $|B|$ as a function of the radial direction r and the electrical angle θ_{el} .
- (c) Normalized current I_n as a function of the radial direction r and the electrical angle θ_{el} .
- (d) Total loss density in the stator coils $p_{v,s}$ as a function of the radial direction r and the electrical angle θ_{el} .

The yoke and the rotor carrier are marked \square , the rotor coils are marked \blacksquare as well as the coil edges are marked $---$. [142]

wire. The spatial distribution of the normalized current is shown in Figure 5.5c. The normalized current distribution does not exceed its maximum value $I_{n,max}$ of 0.7. In this example, these are located in phase with the highest current density as well as opposite of the center of the rotor coils and at the inner stator radius $r_{s,i}$. However, the highest magnetic fields do not occur there, due to the load angle of 90° . Furthermore, the current-free areas between the coils are visible.

In the last step, the total loss density in the stator coils $p_{v,s}$ is deduced by using the results of the electro-thermal model again. A loss hot spot is detected at the inner stator radius $r_{s,i}$ in Figure 5.5d. The hot spots do not necessarily have to occur in the coil which currently carries the highest current, since the losses strongly depend on the magnetic field. This is the case in the example of Figure 5.5d, where the highest loss density occurs at the location of the highest flux density.

Subsequently, the total AC loss $P_{v,s}$ in the stator coils is calculated by integration of the total loss density over the stator coil area of one pole pair p in Equation 5.1 with the effective machine length l_{eff} and the stator coil support ratio f_{csr} .

$$P_{v,s} = f_{csr} p l_{eff} \int_0^{\frac{2\pi}{p}} \int_{r_{s,i}}^{r_{s,o}} p_{v,s} r dr d\theta \quad (5.1)$$

Similarly, the mass flow \dot{M}_s of liquid hydrogen in the stator can be calculated by integration of the mass flow rate \dot{m}_{lh2} in Equation 5.2.

$$\dot{M}_s = f_{csr} p l_{eff} \int_0^{\frac{2\pi}{p}} \int_{r_{s,i}}^{r_{s,o}} \dot{m}_{lh2} r dr d\theta \quad (5.2)$$

Furthermore, the temperature distribution T_s in the stator coil is determined. In the standard machine design process only the maximum stator temperature $T_{s,max}$ is evaluated.

The calculation of the stator AC loss and the mass flow can be done in a similar way for a copper coil and is therefore not explained. Due to the strong field dependence of the stator AC loss, a more detailed investigation of the field influencing parameters is given in the following section.

5.4. Maximum Torque per AC Loss

Various control strategies are known for normal conducting synchronous machines, such as maximum torque per ampere (MTPA), maximum torque per volt (MTPV) or loss minimization (LM) [193]. In this chapter the stator AC loss of superconducting machines is minimized, in order to minimize the hydrogen consumption during a flight mission. In principle, this corresponds to loss minimization, whereby the analytical loss modeling is more detailed compared to normal conducting machines. It must be noted that the iron loss of the yoke is not included because it is not part of the cryogenic system. The quantities in this section are normalized to their maximum value in order to describe the machine behavior in general.

Due to the rotatory magnetic symmetry of all machine topologies in Table 4.1 and according to Chapter 4, the machines generate only a synchronous torque component. Moreover, the stator AC loss can be optimized at constant torque by the stator current, the rotor current and the load angle. The current limits are at a maximum

normalized stator current of 0.7 and a maximum normalized rotor current of 0.7, which corresponds to a rotor current density of 300 A mm^{-2} . The load angle is varied between 0° and 90° .

Figure 5.6 shows the normalized stator AC loss $P_{v,n,s}$ as a function of the normalized stator current $I_{n,s}$, the normalized rotor current $I_{n,r}$ and the load angle θ_{load} for a fully superconducting machine with MgB_2 stator coils and HTS rotor coils at a normalized torque M_n of 0.15. The minimum normalized stator AC loss of 0.22 in

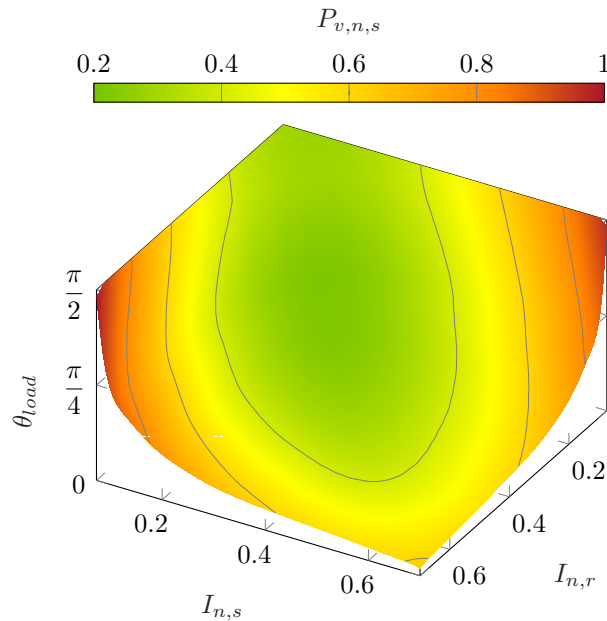


Figure 5.6.: Normalized stator AC loss $P_{v,n,s}$ as a function of the normalized stator current $I_{n,s}$, the normalized rotor current $I_{n,r}$ and the load angle θ_{load} for a fully superconducting machine with MgB_2 stator coils and HTS rotor coils at a normalized torque M_n of 0.15.

this example is achieved at a normalized stator current of 0.25, a normalized rotor current of 0.25 and a load angle of 34° . In contrast, at a constant load angle of 90° a minimum normalized stator AC loss of 0.25 is achieved.

In addition, Figure 5.7 presents the normalized torque M_n and the normalized stator AC loss per torque $P_{v,n,s}/M_n$ as a function of the load angle θ_{load} at a normalized stator and rotor current of 0.7 for the same machine design. With increasing load angle, the stator AC loss increases mainly linear and the torque increases sinusoidal, as described in Section 4.6. This increasing AC loss is linked to an increase of the total flux density in the stator coil area. The normalized stator AC loss per torque reaches a minimum at a load angle of approximately 60° where the normalized stator AC loss per torque is about 16% lower compared to an angle of 90° .

These two figures show that the load angle has to be taken into account when optimizing the machine control. However, this would increase the computing time due to the dependency of the stator AC loss on the machine geometry, especially if several machine designs have to be characterized. Furthermore, it is expected that the rotor current and the stator current have a greater influence on the stator AC loss than

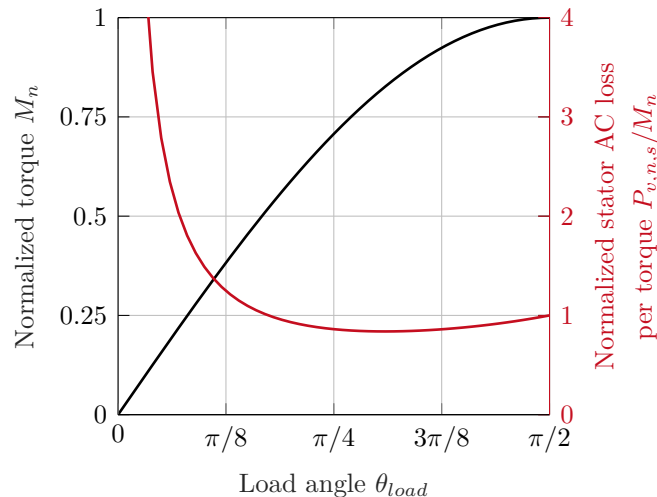


Figure 5.7.: Normalized torque M_n and normalized stator AC loss per torque $P_{v,n,s}/M_n$ as a function of the load angle θ_{load} at a normalized stator and rotor current of 0.7.

the load angle. For this reason, a load angle of 90° is applied for the following investigations. This assumption simplifies all machine architectures except architectures with excitation via rotor coils to a simple control strategy via the stator current and is therefore always optimal for magnetically symmetric machines [193]. It should be noted, that the rotor coils are not operated in persistent mode. This means that they are short-circuited and are energized once.

The derivation of the optimized machine control follows, starting with the calculation of the normalized torque for varying normalized rotor and stator current. Figure 5.8 presents hyperbolas of constant normalized torque M_n as a function of the normalized stator current $I_{n,s}$ and the normalized rotor current $I_{n,r}$ for the normalized torques of 0.25, 0.5 and 0.75. If the optimum points are determined for the entire torque spectrum, the trajectory of maximum normalized torque per normalized stator AC loss is obtained.

The marked optimal control point for the normalized current of rotor and stator at a normalized torque of 0.75 in Figure 5.8 is also shown in Figure 5.9 in dependence of the normalized stator AC loss $P_{v,n,s}$. The minimum pair of values is clearly recognizable in Figure 5.9. At this operating point the stator AC loss can be reduced by 18% compared to an unoptimized control. Furthermore, the highest stator AC loss is achieved when the rotor is operated with maximum normalized current and the stator is operated with minimum normalized current. When the normalized rotor current decreases, the stator current must increase in order to generate the same torque. After reaching the optimum, this behavior will change.

All optimized normalized currents together form the characteristic curve in Figure 5.10a. The optimized normalized stator current $I_{n,s,opt}$ initially increases linearly with increasing torque until 90% of the nominal torque is reached. At this point the normalized stator current has achieved its defined maximum of 0.7 and remains constant. The optimized normalized rotor current $I_{n,r,opt}$ also increases with increasing torque, but first with a higher gradient compared to the normalized stator current

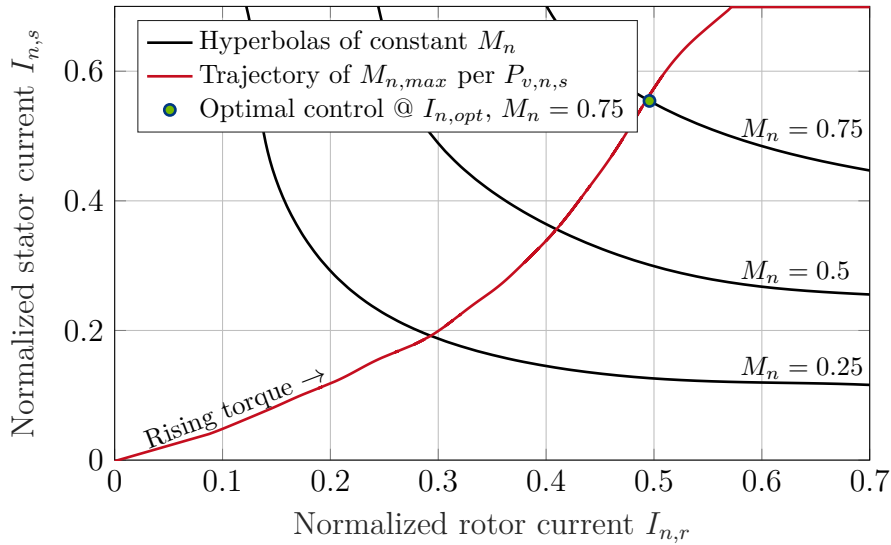


Figure 5.8.: Hyperbolas of constant normalized torque M_n in dependence of the normalized stator current $I_{n,s}$ and the normalized rotor current $I_{n,r}$. The trajectory of maximum normalized torque $M_{n,max}$ per normalized stator AC loss $P_{v,n,s}$ is shown and the optimized normalized current $I_{n,opt}$ at a normalized torque of 0.75 is marked which corresponds to Figure 5.9.

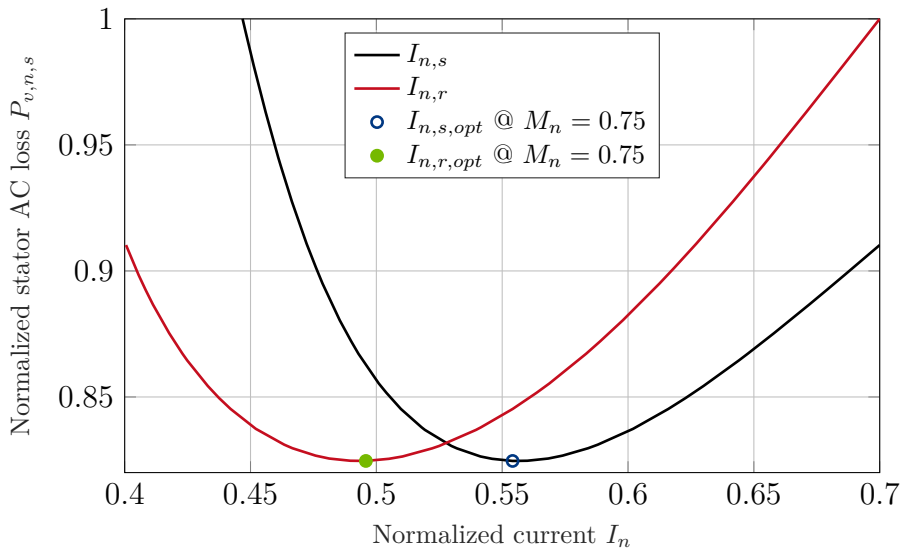


Figure 5.9.: Normalized stator AC loss $P_{v,n,s}$ as a function of normalized current I_n for the stator and rotor for a normalized torque M_n of 0.75. The optimal pair of values is marked.

and then after the first third of the torque with a smaller gradient. For a normalized torque between 0.9 and 1.0, the gradient of the rotor current rises sharply so that the torque continues to increase linearly at constant normalized stator current. This strong increase of the rotor current leads to an also strongly increasing rotor

flux density and is also detectable in the normalized stator AC loss $P_{v,n,s}$ in Figure 5.10b for the controlled normalized rotor current $I_{n,r}$. However, the stator AC loss increases approximately linearly for a normalized torque less than 0.9.

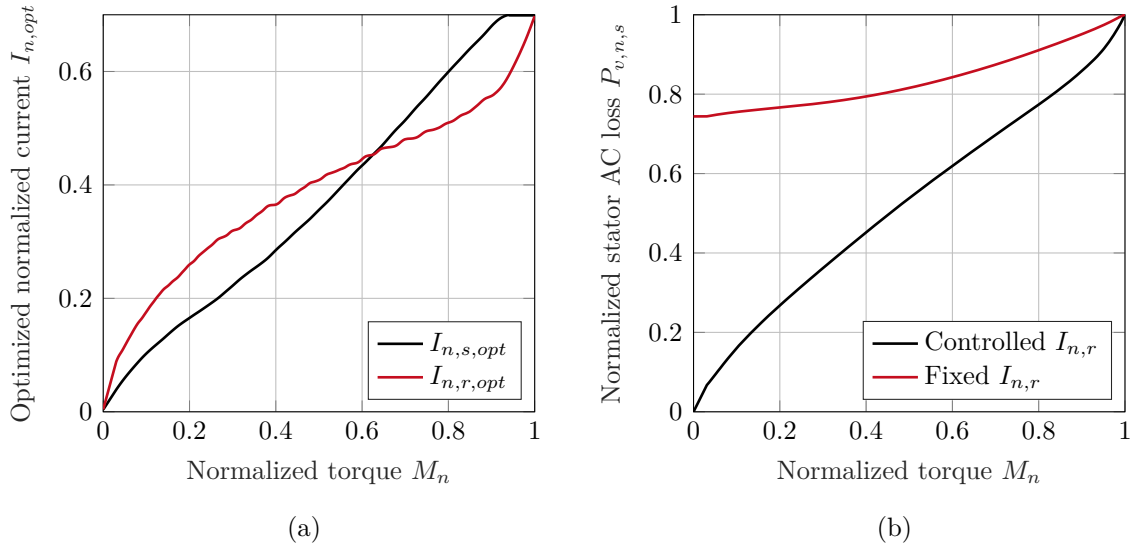


Figure 5.10.: (a) Optimized normalized current $I_{n,opt}$ as a function of the normalized torque M_n .
 (b) Comparison of the normalized stator AC loss $P_{v,n,s}$ as a function of the normalized torque M_n for a fully superconducting machine with a controlled rotor current and a fixed rotor current.

Comparing a controlled and a fixed operation of a fully superconducting machine, there are large differences and an optimization potential in the stator AC loss can be observed. It can be reduced by 34% with a controlled machine at 50% torque requirement, corresponding roughly to the operational point during the cruise phase of an aircraft. Even more extreme is the difference when the torque is zero and the machine continues to rotate at nominal speed. In this case, 78% of the maximum stator AC loss is still generated in the uncontrolled case, although this could be reduced to zero with a controlled rotor current.

The use of the optimized control strategy for superconducting stator machines and its influence on a flight mission is discussed in Chapter 6.

5.5. Liquid Hydrogen Tank Model

The liquid hydrogen tank provides the liquid hydrogen to cool the electric machines. In addition, further cryogenic components of the propulsion system can be cooled by hydrogen such as an inverter or a transmission cable. However, the design of this tank is an important step in the machine design, because it has a major impact on the mass of the propulsion system and the range of an aircraft.

Several aspects must be considered in the tank design. Temperature rise and thus evaporation of liquid hydrogen in the tank have to be prevented by thermal insulation. Additionally, the tank wall must withstand pressure deviations and hydrogen

embrittlement. Furthermore, the duration of the flight mission and the installation space in the aircraft influence the dimensions of the liquid hydrogen tank.

The energy density per volume of liquid hydrogen is about four times higher compared to jet fuel Jet A, as shown in Table 5.3. This indicates that the tank size is limited by the aircraft design. However, jet fuel weighs about 3 times more than liquid hydrogen for the same amount of energy. For this reason, a parametric tank model is necessary, which will design an optimized tank according to the above mentioned conditions. The complete model is based on work in [194] and described in the following.

Table 5.3.: Gravimetric and volumetric energy density of liquid hydrogen and jet fuel.

Property	Unit	Jet A	LH ₂
Gravimetric energy density	MJ/kg	42.8 [195]	120 [196]
Volumetric energy density	MJ/l	34.7 [195]	8.5 [196]

The basic shape of the tank is a cylinder with spherical ends, as shown in Figure 5.11, which must fit in the given dimensions h_t , b_t and l_t . This allows a variable integration of the tank into the fuselage of the aircraft. The tank consists mainly of three shells: the outer tank wall, the inner tank wall and the insulation between both, as illustrated in Figure 5.11 and 5.13. The thicknesses and distances of these layers are designed according to the mechanical and the thermal loads and requirements. These design steps are part of the calculation procedure, as presented in Figure 5.12. The computation of the mass of the tank m_t is the main result of the tank model. The schematic shows also the most important in- and output parameters of the model. These include the liquid hydrogen volume V_{lh_2} , the burst pressure p_{bur} , the liquid hydrogen mass m_{lh_2} , the ambient temperature T_a , the ambient pressure p_a and the boil-off-rate f_{bor} as input parameter. The boil-off-rate defines the amount of liquid

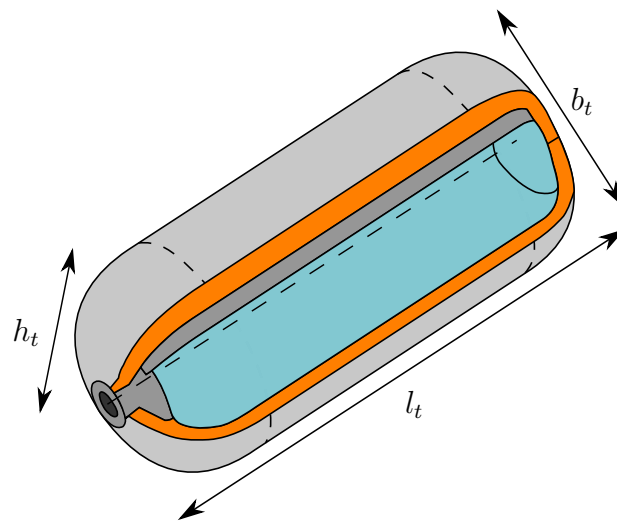


Figure 5.11.: Sketch of a liquid hydrogen tank with the outer tank wall \square , the foam insulation \blacksquare , the inner tank wall \blacksquare and the stored liquid hydrogen \blacksquare .

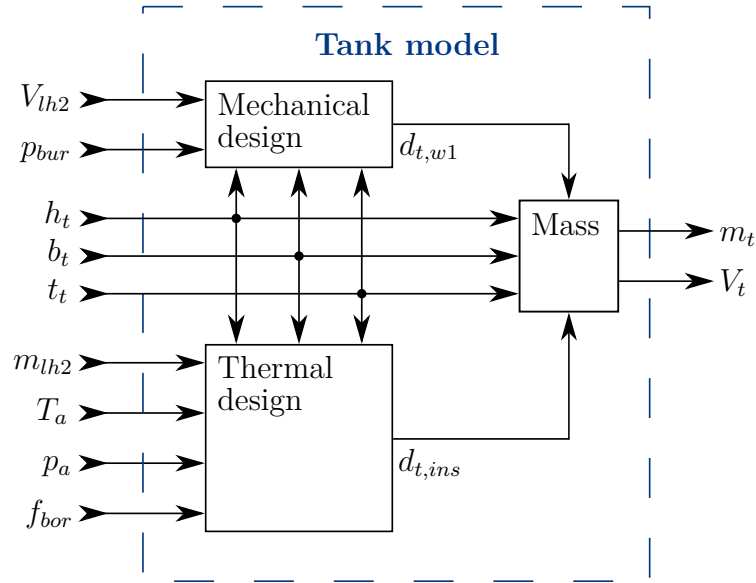


Figure 5.12.: Calculation procedure of the liquid hydrogen tank model.

hydrogen that is evaporating in the tank due to heat leakage. In addition, input parameters are the maximum accessible installation space, defined by the height h_t , width b_t and depth l_t . A further output parameter is the volume V_t of the tank. The sectional view through the wall of the tank is sketched in Figure 5.13. The temperature rises from the liquid hydrogen temperature T_{lh2} inside the tank to the ambient temperature T_a outside the tank. The main functionalities of the inner wall and the foam insulation are the mechanical stability and the thermal shielding, respectively. Both are described in the following sections. Moreover, the outer wall protects the insulation from damage by external influences and its thickness is assumed to be constant.

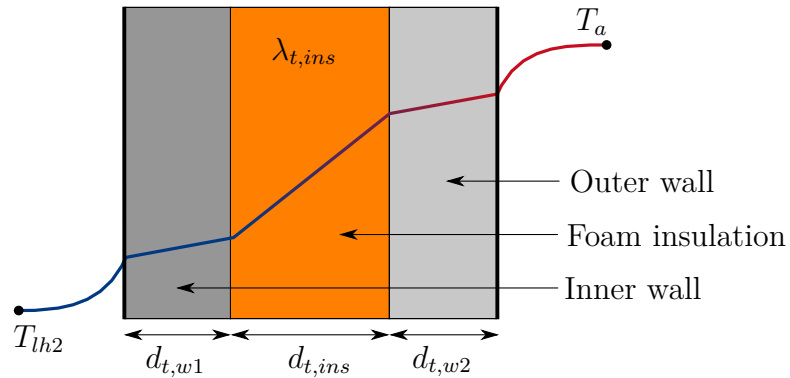


Figure 5.13.: Sectional view of a liquid hydrogen tank with foam insulation.

In order to achieve the design goals, materials with special properties such as low volumetric mass density, low thermal conductivity and high maximum allowable stress are required. It has been shown in literature [197, 198, 199], that high strength Al 2219 can act as tank wall and polyurethane (PU) foam as solid insulation. Moreover, Al 2219 is characterized by an insensitive hydrogen permeability [200].

5.5.1. Mechanical Design

The liquid hydrogen in the tank is stored at a pressure higher than the atmospheric pressure. Therefore, the internal pressurization must be considered in the tank design. This results in a pressure difference which stresses the wall of the tank. Barlow's formula in Equation 5.3 is used to calculate the thickness of a thin-walled cylinder under internal pressure [168]. Thus, the calculation differs only in the boundary condition compared to the design of the cryo wall in Section 4.3.2.

$$d_{t,w1} = \frac{p_{bur} d_{t,i} f_t}{2 \sigma_t} \quad (5.3)$$

It follows that the inner wall thickness $d_{t,w1}$ is designed according to the burst pressure p_{bur} and the maximum allowable stress σ_t of the wall material. In addition, the safety factor f_t and the inner diameter of the tank $d_{t,i}$ are considered in the mechanical design.

The internal pressure load is calculated from the maximum operating pressure of the tank system. This pressure is defined as vent pressure p_{vent} , because venting must be done to avoid over-pressurization. Furthermore, the burst pressure p_{bur} is calculated with the gravity g , the density of liquid hydrogen ρ_{lh2} and the ambient pressure p_a .

$$p_{bur} = p_{vent} + g \rho_{lh2} d_{t,i} - p_a \quad (5.4)$$

5.5.2. Thermal Design

In the thermal design, the heat transfer from the ambient air into the tank is calculated. Three fundamental principles of heat transfer are distinguished: radiant, conduction and convection heat. The total heat flow rate into the tank from the ambient air leads to evaporation of liquid hydrogen with the same amount. However, the heat flow rate into the tank cannot be prevented completely by the insulation and therefore a heat flow rate is defined with the percentage of boil-off per hour f_{bor} . The percentage of boil-off per hour or abbreviated boil-off rate is used to calculate the mass flow $\dot{M}_{b,off}$ due to boil-off.

$$\dot{M}_{b,off} = f_{bor} m_{lh2} \quad (5.5)$$

The incoming heat flow rate $\dot{Q}_{b,off}$ in Equation 5.6 is therefore considered to be equal to the mass flow through boil-off with the evaporation enthalpy Δh_v of liquid hydrogen.

$$\dot{Q}_{b,off} = \Delta h_v \dot{M}_{b,off} \quad (5.6)$$

Thermal conduction

Thermal conduction through the walls and the insulation of the tank is described by the thermal resistance R_{th} which depends on the geometry and material of each layer. The thermal resistance for a plane wall is given by Equation 5.7 with the thermal conductivity $\lambda_{t,w}$, the thickness $d_{t,w}$ and the surface $A_{t,w}$ of the layer.

$$R_{th} = \frac{d_{t,w}}{\lambda_{t,w} A_{t,w}} \quad (5.7)$$

Due to the curved shape of the layers of a cylindrical tank, its inner and outer surface are not equal. For this reason a correction factor is introduced by Equation 5.8 with the inner radius $r_{t,i}$ and the cylindrical length $l_{t,w}$ [144].

$$R_{th} = \frac{\ln\left(\frac{r_{t,i}+d_{t,w}}{r_{t,i}}\right)}{2\pi\lambda_{t,w}l_{t,w}} \quad (5.8)$$

Thermal natural convection

Between outer wall and ambient as well as inner wall and hydrogen, the heat is transferred mainly via natural convection. This heat transfer is due to a spatially inhomogeneous volumetric mass density distribution in liquids and gases, such as in the case of an uneven temperature distribution. The thermal resistance for this effect is given by Equation 5.9 with the heat transfer coefficient α and surface A .

$$R_{th} = \frac{1}{\alpha A} \quad (5.9)$$

The heat transfer coefficient for cylinders is calculated by Equation 5.10 with the Nußelt number Nu .

$$\alpha = \frac{2Nu\lambda}{\pi d_{t,w}} \quad (5.10)$$

In the case of natural convection, the Nußelt number is defined according to Equation 5.11 with the Rayleigh number Ra [144].

$$Nu = \left(0.752 + 0.387 Ra^{\frac{1}{6}} \left(1 + \left(\frac{0.559}{Pr}\right)^{\frac{9}{16}}\right)^{-\frac{8}{27}}\right)^2 \quad (5.11)$$

The Rayleigh number is given by Equation 5.12 with the temperature difference ΔT between wall and ambient air, the gravity g , the ambient temperature T_a , the dynamic viscosity η and the volumetric mass density ρ . The Prandtl number Pr is calculated with CoolProp, a library for fluid properties [201].

$$Ra = Pr \frac{g\rho^2}{\eta^2 T_a} \Delta T l_{t,w}^3 \quad (5.12)$$

Thermal radiation

Thermal radiation based on the electromagnetic radiation is emitted from each object and is proportional to the temperature difference of the object and its environment. Therefore, a hot object emits heat, which is absorbed by a colder object.

The radiation heat flow rate \dot{Q}_{rad} is calculated by Equation 5.13 with the Stefan–Boltzmann constant σ , the surface A and the temperature T_1 of the emitting surface and the temperature T_2 of the absorbing surface.

$$\dot{Q}_{rad} = \frac{A\sigma(T_1^4 - T_2^4)}{\frac{1}{\varepsilon_1 + \phi_{21}} \frac{1}{\varepsilon_2 - 1}} \quad (5.13)$$

Additionally, the view factor ϕ_{21} describes the proportion of radiation that leaves the emitting surface and hits the absorbing surface and the emissivities ε_1 and ε_2 describe the effectiveness of both objects in emitting energy as thermal radiation.

5.5.3. Parameter Study

Table 5.4 summarizes the input parameters for the following calculations. Aluminum 2219 and PU foam are used as wall and insulation material, respectively. The tank is designed 7.2% larger to withstand pressure changes due to boil-off and a safety factor f_t of 2 is considered [197].

Table 5.4.: Parameters of the liquid hydrogen tank model.

Parameter	Symbol	Value
Wall material	—	Al 2219
Insulation material	—	PU foam
Ambient temperature	T_a	293.15 K
LH ₂ temperature	T_{lh2}	20 K
Burst pressure	p_{bur}	10 bar
Fill level	f_{fill}	92.8 %
Safety factor of tank	f_t	2

Figure 5.14 presents hyperbolas of constant boil-off rate f_{bor} as a function of the tank mass m_t and the diameter-to-length ratio f_{dl} . The trajectory of minimum tank mass $m_{t,min}$ per boil-off rate is shown. With increasing boil-off rate the tank mass

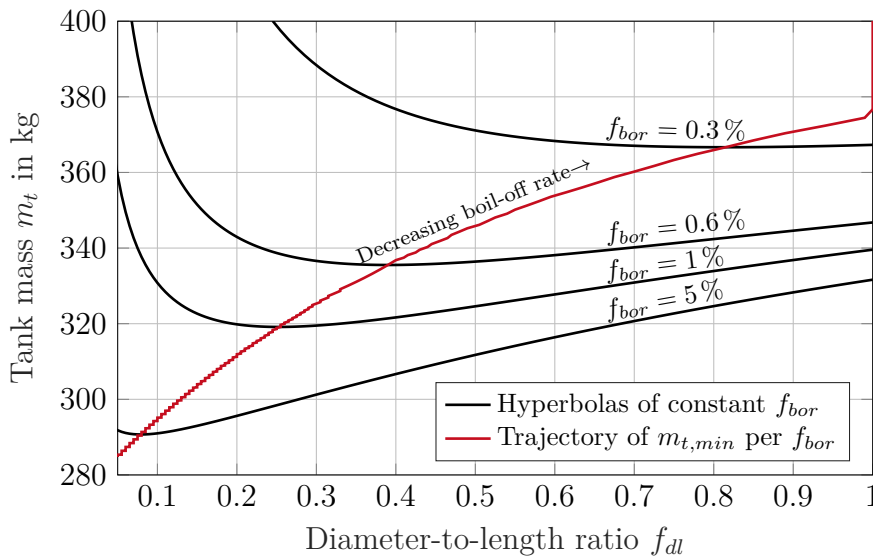


Figure 5.14.: Hyperbolas of constant boil-off rate f_{bor} in dependence of the tank mass m_t and the diameter-to-length ratio f_{dl} . The trajectory of minimum tank mass $m_{t,min}$ per boil-off rate is shown. The input parameters for this design are summarized in Table 5.4.

decreases, because the insulation can be designed thinner. This dependency stagnates, because the mechanical stability must still be guaranteed. In addition, the diameter-to-length ratio increases with increasing boil-off rate and reaches 1 for values smaller than 0.25 %, which corresponds to a sphere as tank shape. This is caused by the different conditions of thermal convection inside the tank.

Figure 5.15 presents results for the tank design with varying liquid hydrogen masses m_{lh_2} . With increasing liquid hydrogen mass and burst pressure p_{bur} the tank mass m_t increases, as shown in Figure 5.15a. At very low burst pressures, the minimum tank wall thickness is limited to 1 mm linked to manufacturing assumptions for aluminum, which can also be seen in the figure by a range of constant tank mass.

Figure 5.15b illustrates the tank mass m_t as a function of the boil-off rate f_{bor} . Boil-off rates lower than 1 % lead to high tank masses, since the thickness of the

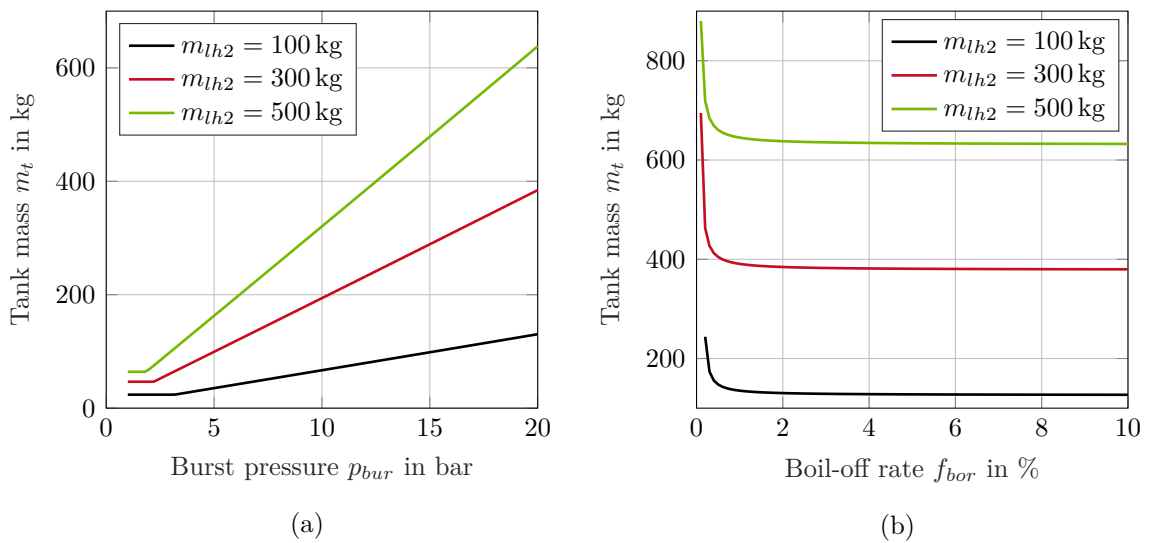


Figure 5.15.: Tank design results according to the boundary conditions in Table 5.4 and varying LH₂ masses m_{lh_2} :

- (a) Tank mass m_t as a function of the burst pressure p_{bur} .
- (b) Tank mass m_t as a function of the boil-off rate f_{bor} .

insulation must be increased extremely in order to strongly reduce the heat conduction. However, the boil-off rate reduction is limited due to the thermal radiation, which is independent of the insulation thickness. At boil-off rates much higher than 1 % the tank mass is relatively constant and is about 128 kg, 381 kg and 634 kg for 100 kg, 300 kg, and 500 kg liquid hydrogen, respectively.

Due to the limited flight time and the fact that not all cryogenic components have to be cooled with liquid hydrogen, a boil-off rate of 1 % is chosen for the calculations in the next section. This allows to design the tank especially light with a simultaneously low boil-off rate. Furthermore, a burst pressure of 10 bar is considered sufficient to ensure safe operation of the tank. Thus, the tank model can be used in the next chapter under real boundary conditions. For example, the ratio can usually not be selected freely, because the installation space of the tank is limited by an existing aircraft design.

5.6. Summary

This chapter describes the design process of superconducting machines for aircraft. It becomes apparent that an electro-thermal model and an electromagnetic machine design model, as presented in Chapters 3 and 4, respectively, are not sufficient for application in an aircraft. Additional models and procedures are necessary in order to achieve an efficient fundamental machine design and to consider the aeronautical boundary conditions.

The working point determination of the stator coils is essential in the machine design. Especially for superconducting stator coils a high sensitivity of the critical current density exists in relation to the flux density which penetrates the coils. For this reason, the working point must be calculated exactly to determine the torque of the machine correctly.

The exact field calculation is also necessary to determine the total AC loss of the stator coils in order to determine the hydrogen consumption. Rotor coils offer the advantage that the field of the rotor magnets can be freely adjusted from the nominal point down to zero, thus creating a further degree of freedom compared to permanent magnets. For this reason, the rotor current density is used to optimize the AC loss of the stator coils. Through this control strategy the AC loss is reduced by 34 % at torque requirement of 50 %. With this strategy, hydrogen consumption can be reduced considerably, but it requires a control of the rotor current.

Finally, a tank model is developed, which designs a cylindrical tank with spherical ends and given dimensions as boundary condition. Both, mechanics and thermodynamics are taken into account to determine the tank mass in the case of foam insulation. Optimal diameter-to-length ratios can be found depending on the boil-off rate, resulting in a minimum tank mass. However, the installation space of the tank is determined by the aircraft design in the following chapter. Furthermore, a boil-off rate of 1% can be allowed, because the flight time is a few hours only and thus has a minor influence on the hydrogen consumption on a flight mission. The tank can then be designed much lighter compared to smaller boil-off rates. Moreover, the hydrogen gas can be used to cool other components of the propulsion system.

6. Design Example for an Airbus A321neo-LR

The design of an electric machine for a commercial aircraft brings up challenges, in addition to a high power-to-weight ratio, that are usually not taken into account in the design. These are requirements which are specified by the aircraft design, such as the operation at high altitude, the integration of a flight mission or the transport of a coolant. Thus, machine and aircraft design must be combined in order to take into account the key requirements influencing each other. To integrate the most important boundary conditions into the machine design, the models and results of the Chapters 2 to 5 are applied to a use case. This includes the comparison and discussion of different machine topologies as well as the main design parameters.

To study the feasibility of the hybridization of a short- and medium-range commercial passenger aircraft, an Airbus A321neo-LR is electrified with superconducting machines which are cooled by liquid hydrogen. This aircraft is based on the Airbus A320neo, however, with a stretched fuselage and additional jet fuel tanks that are placed in the fuselage of the aircraft. The additional labeling neo identifies a re-equipped Airbus A320 with latest state-of-the-art and more efficient engines. This aircraft has an over-all length of 44.51 m, a maximum take-off weight of 101 t and a maximum payload of 25.5 t. [202]

Figure 6.1 presents this aircraft and the position as well as the size of the jet fuel tanks. In addition to the wing tanks and the center tank between the wings, the A321neo in the LR version has additional center tanks integrated in the front and rear in the fuselage. This is achieved by replacing a part of the cargo compartments with additional tanks. The total jet fuel capacity increases to 32943 l and the maximum design mission to 7400 km compared to 23580 l and 6500 km of the A321neo.

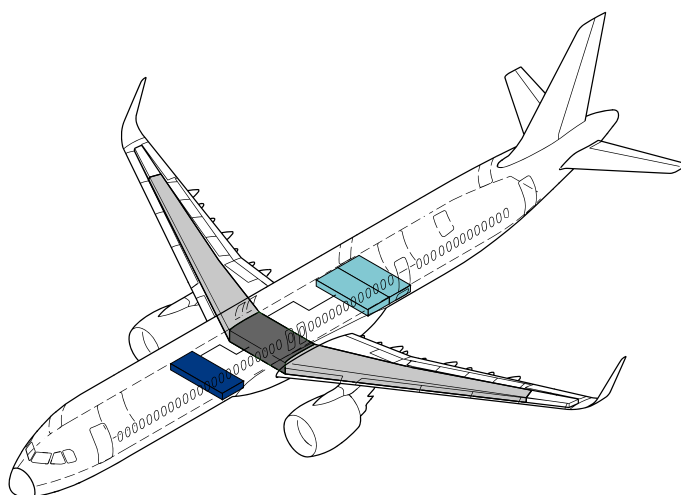


Figure 6.1.: Airbus A321neo-LR with the wing tanks ■, the center tank ■, the rear center tanks ■ and the front center tank ■ for jet fuel. Adapted from [203].

For a mission of 1222 km with full payload, the mean fuel consumption of this aircraft is estimated to be 3.36 kg km^{-1} or 50.91 min^{-1} [204]. However, the fuel consumption is influenced by many boundary conditions such as the take-off weight, the mission length or the weather conditions. Further properties of this aircraft are presented in Table 6.1.

Table 6.1.: Airbus A321neo-LR properties [203, 204, 205].

Property	Unit	Value
Length	m	44.51
Wingspan	m	35.80
Height	m	11.76
Maximum take-off weight	t	101
Maximum payload	t	25.5
Operating empty weight	t	50.1
Total fuel capacity	l	32943
Wing tank	l	7690
Center Tank	l	8200
Rear center tanks	l	6242
Front center tank	l	3121
Maximum speed	km h^{-1}	876
Range	km	7400
Maximum seating	–	244
Mean fuel burn	kg km^{-1}	3.36
	l min^{-1}	50.9
Fuel per seat	kg km^{-1}	0.0138

In the case study, the aircraft is electrified without any modifications to the fuselage, the wings or the dimensions of the engines. Therefore, the electric machine must be integrated into the existing engine. By this approach, the total empty mass of the aircraft can be increased, requiring an adaption of the aircraft mission range or payload. Furthermore, this can change the thrust requirements. These adaptations on the aircraft level are not considered in this study. Thus, the available space for all components of the electric propulsion system as well as the hydrogen tank is limited. This case study aims to investigate the suitability and feasibility of superconducting machines as propulsion unit. The approach is to replace the core engine of the actual turbofan. For a complete re-equipment of the aircraft, the machine design process would have to be integrated in the aircraft design process [206].

The main characteristics of the original turbofan engine are introduced in the following section. Afterwards, the hybrid-electric propulsion system is presented. An optimization for a turbo-electric propulsion system for such an aircraft can be found in [52], which used the machine design process developed in this thesis. Here, the focus is on the machine design and the comparison of different machine topologies. In addition, the required amount of hydrogen and its storage tank to comply with

the mission profile of the aircraft are included in the design process. Finally, a design proposal is given for a specific machine topology.

6.1. Turbofan

The Airbus A321neo-LR is powered by two Pratt & Whitney PW1133G turbofan engines and shown as a sketch of a sectional view in Figure 6.2. These are airbreath-

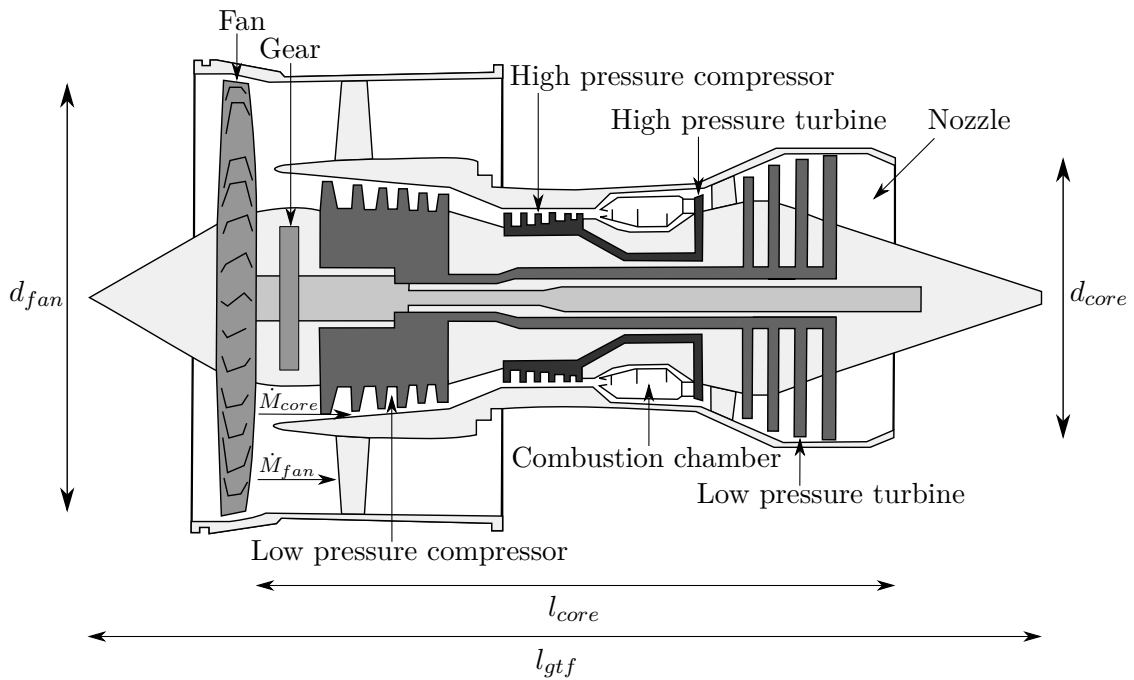


Figure 6.2.: Sketch of a sectional view of the Pratt & Whitney PW1133G geared turbofan. Adapted from [207].

ing jet engines and nearly all jet-powered civil aircraft are equipped with this engine type. This is due to the high efficiency and low noise emissions. It is based on the special engine design for Mach numbers Ma around 0.8 and is described in the following [208]. Specifically, the PW1133G is a geared turbofan engine, being the first engine of this type in commercial short range passenger aircraft [209]. The integrated gearbox decouples fan and core engine, thus enabling independent optimization of both components. This leads to more efficient engines with larger fan diameters and lower fan rotational speeds to avoid critical circumferential speeds [210]. Moreover, the diameter of the core engine cannot be reduced, as this would reduce its efficiency. For example, an engine with the same thrust as the Pratt & Whitney PW1133G and half bypass ratio would result in an approximately 15% higher fuel consumption [212].

The core engine consists of a combustion chamber that burns jet fuel and hence provides thermal energy. This energy is transformed into mechanical energy in a gas turbine which powers a compressor and a fan, usually located in front of the turbine. The mechanical energy is used to accelerate air rearwards. In contrast to a turbojet, not the entire air mass flow is passed through the combustion chamber, as shown in

Figure 6.2. The mass flow is split into the mass flow of the core engine \dot{M}_{core} and the mass flow which bypasses the core \dot{M}_{fan} . Furthermore, the fan compresses air into the by-pass while the inner part provides additional compression for the core engine. The pressure gradient at the engine outlet is finally converted completely into velocity through the nozzle. The ratio between both mass flows is defined as bypass ratio f_{bpr} according to Equation 6.1.

$$f_{bpr} = \frac{\dot{M}_{fan}}{\dot{M}_{core}} \quad (6.1)$$

The efficiency of the engine improves with increasing bypass ratio, resulting in modern turbofans with ratios greater 10. The PW1133G belongs to this category with a bypass ratio of 12.5. Thus, the bypassed mass flow provides with 92,6% the majority of the thrust, which is 147.28 kN at take-off condition and corresponds to a power of about 20 MW [213]. Further properties of the PW1133G are summarized in Table 6.2.

Table 6.2.: Pratt & Whitney PW1133G properties [45, 213, 214].

Property	Unit	Value
Power	MW	20
Take-off thrust	kN	147.28
Fan diameter	mm	2060
Core diameter	mm	582.7
Bypass ratio	–	12.5:1
Total length	mm	3401
Core length	mm	1800 ¹
Weight	kg	2857.6
Maximum fan speed	min ⁻¹	3500
Maximum N1 speed	min ⁻¹	10047
Maximum N2 speed	min ⁻¹	22300

¹ estimated

To allow a high by-pass ratio, the fan has a larger diameter compared to the core engine and this diameter is limited in order to avoid excessive circumferential speeds. For this reason, the fan rotates with 3500 min⁻¹ which is slower than the core engine. The speed reduction is achieved by several shafts and its respective compressor and turbine, as shown in Figure 6.2 as low-pressure and high pressure compressor as well as turbine for the PW1133G, respectively. These two shafts reach rotational speeds of 10047 min⁻¹ and 22300 min⁻¹ for the low-pressure shaft N1 and the high-pressure shaft N2, respectively. Further speed reduction for the fan is achieved by a gear, which is also integrated in the PW1133G. Hence, these engines are named geared turbofan (GTF). This allows both modules, fan and turbine, to achieve their respective optimum performance. Fuel consumption and noise emissions are significantly reduced. The PW1133G consists of a 3-stage low-pressure turbine, which drives a 3-stage low-pressure compressor and the fan via a planetary gear with a gear ratio

of 3:1. The gearbox weighs 113 kg at an efficiency of 99.5% and is therefore a weight reduction compared to further turbine stages [215, 216]. The combustion chamber is located between the high-pressure compressor and the high-pressure turbine. Furthermore, the entire engine mass m_{gtf} is 2857.6 kg and the entire engine length l_{gtf} is 3401 mm. This results in a power-to-weight ratio PTW of about 7 kW kg^{-1} for the entire propulsion system.

Since the bypass mass flow provides the majority of the total thrust of this engine, the thrust of the core engine can be neglected and it can be considered as a fan motor [215]. In this study, it is assumed that the core engine and gear box can be replaced by the superconducting electric machines that drive the shaft of the fan. To compensate the missing thrust by the core engine, the required power is increased to 21.6 MW. The limiting dimensions are given by the core diameter d_{core} of 582.7 mm, which is calculated by Equation 6.2.

$$d_{core} = \frac{d_{fan}}{\sqrt{f_{bpr}}} \quad (6.2)$$

The core length l_{core} is estimated to be 1800 mm. Thus, all necessary requirements are defined in order to design electric machines in the next section.

6.2. Hybrid-Electric Propulsion System Overview

The cryogenic propulsion system of the hybrid-electric Airbus A321neo-LR is a fully turbo-electric approach, as presented in Section 1.2.2 and in detail in [52]. A sketch of this approach is shown in Figure 6.3 and illustrates the relative dimensions of this aircraft and the positioning of the electric components as well as the liquid hydrogen tanks.

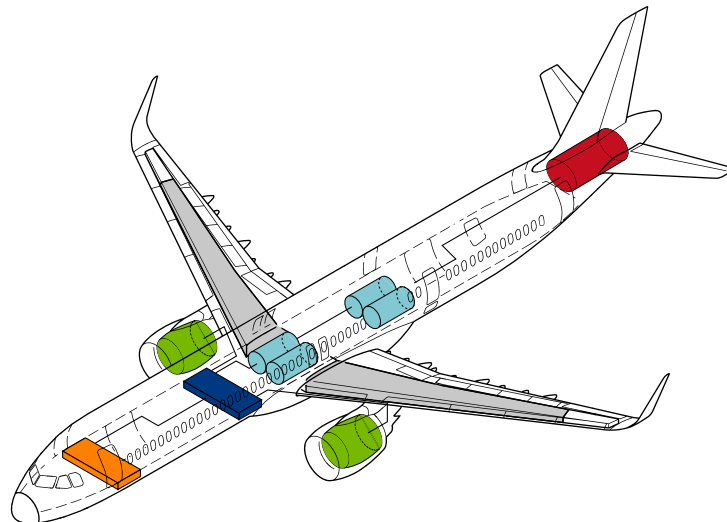


Figure 6.3.: Hybrid-electric Airbus A321neo-LR with battery unit ■, cryogenic electric power distribution center (CEPDC) ■, electric propulsion unit (EPU) ■, jet fuel tanks ■, liquid hydrogen tanks ■ and power generation unit (PGU) ■. Adapted from [203].

Two electric propulsion units (EPU) are integrated into the existing Pratt & Whitney PW1133G geared turbofans at each wing. Therefore, the core engines will be replaced by superconducting motors, which drive the fans and provide thrust to the aircraft. The engines remain at the same position as the propulsion units in the original aircraft. The inverter unit is also part of the electric propulsion unit and is installed close to the motors, as presented in Section 1.2.2. However, this thesis is focused on the motor and the optimal location of the inverters has to be investigated in future studies. Both electric propulsion units are connected with superconducting DC power lines to the cryogenic electric power distribution center (CEPDC). The electric power is generated in the power generation unit (PGU) by a gas turbine in combination with a superconducting generator placed in the aft of the aircraft fuselage. Additionally, a small share of the power can be provided by the battery unit in the front of the aircraft fuselage. Superconducting DC power lines also connect the power generation unit and the battery unit to the cryogenic electric power distribution center, which distributes the liquid hydrogen and contains circuit breakers. A comparison of the original aircraft in Figure 6.1 and the hybridized version in Figure 6.3 shows that jet fuel is stored only in the wings of the hybrid-electric Airbus A321neo-LR. The cryogenic electric power distribution center is placed in the space of the front center tank of the original aircraft and the liquid hydrogen storage is placed in the space of the rear center tanks. An additional front cargo compartment is required for the battery unit and the aft of the fuselage is used for the power generation unit, where the auxiliary power supply (APS) was originally located. Two hydrogen tanks are separated and fireproofed in the cargo compartment next to each other, as shown in the cross section of a hybrid-electric Airbus A321neo-LR fuselage in Figure 6.4. Moreover, the power generation unit, the electric propulsion

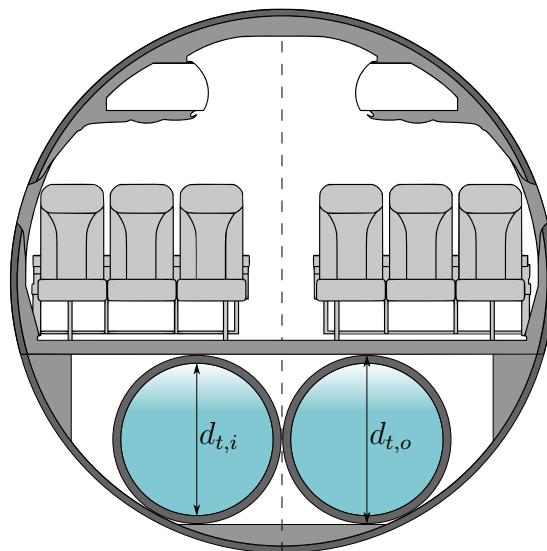


Figure 6.4.: Cross section of a hybrid-electric Airbus A321neo-LR fuselage with the interior arrangement \square , the stringers as well as the skin \square and further support structures \square . The hydrogen tanks \square are located below the passenger cabin in the rear of the aircraft as shown in Figure 6.3. Adapted from [203].

unit as well as the cryogenic electric power distribution center, as illustrated in Figure 1.6, have to be fireproof. This allows a nearly unchanged fuselage design, but strictly limits the outer tank diameter $d_{t,o}$ of 1230 mm for the Airbus A321neo-LR [203]. By using the space of two unit load devices (ULD) the maximum length of the tanks is 3260mm, which carry a maximum amount of 280 kg LH₂ per tank [217]. The boundary conditions for the tank design are given in Table 5.4 and a boil-off rate of 1% is chosen. This results in a thickness of the inner tank wall of 4.2 mm, a thickness of the tank insulation of 33.0 mm and a thickness of the outer tank wall of 0.5 mm. Thus, the hybrid-electric Airbus A321-LR contains four hydrogen tanks of the same size, which corresponds to 15819 l of liquid hydrogen and an energy amount of 134.5 GJ, according to Table 5.3. Furthermore, this corresponds to the energy amount of 3142 kg (3875 l) Jet A. The jet fuel tank volume is decreased by 14239 kg (17563 l) to 15380 kg (5486 l) due to the hybridization and only partially compensated by liquid hydrogen because of the lower volumetric energy density. This will reduce the maximum range of the aircraft to about 59% of the initial range, assuming that the efficiency of the gas turbine in combination with the further propulsion system is equal to the efficiency of the turbofan and independent of the mixing ratio between jet fuel and hydrogen.

It is shown in several studies that the efficiency of the combustion process of jet fuel can be optimized by adding 10%–20% of gaseous hydrogen. Furthermore, a continued increase of this mixing mass ratio does not lead to a significant degradation of this process. The average relative mass ratio of hydrogen in the jet fuel hydrogen mixture of this propulsion system is 6.8%. [218, 219]

To estimate the reduction of CO₂ emissions due to this cryogenic propulsion system, the production of liquid hydrogen must be taken into account. It is assumed that onshore wind power is used as energy source, which emits lifecycle CO₂ emissions of about 11 g kWh⁻¹ and is therefore one of the most environmentally friendly renewable energies [220, 221]. Furthermore, it is assumed that the efficiency is 64% for polymer electrolyte membrane (PEM) electrolysis and 50% for the hydrogen liquefaction process [222, 223, 224, 225]. In these large-scale processes, the energy consumption for the production of gaseous hydrogen is about 6 times higher than for the liquefaction. In summary, this aircraft concept inclusive hydrogen production maximally saves about 8.7 t of CO₂ emissions per flight and if it is assumed that the entire hydrogen is consumed as well as if energy and hydrogen transportation is neglected. Furthermore, the impact of other components, such as the power generation unit, of the propulsion system is not considered.

6.3. Flight Mission and Material Parameters

The performance requirements of an aircraft on a flight mission are very different. For this reason the liquid hydrogen consumption is calculated under consideration of a specific mission shown in Figure 6.5. The required power P is related to an Airbus A321neo-LR with a maximum take-off weight of 101 t, two PW1133G engines and is presented as a function of the time t . The flight time is 5 h 10 min and corresponds to a mission range of 4535 km. It is important to note that the mission also contains a diversion mission according to Figure 5.2, which includes an additional flight time

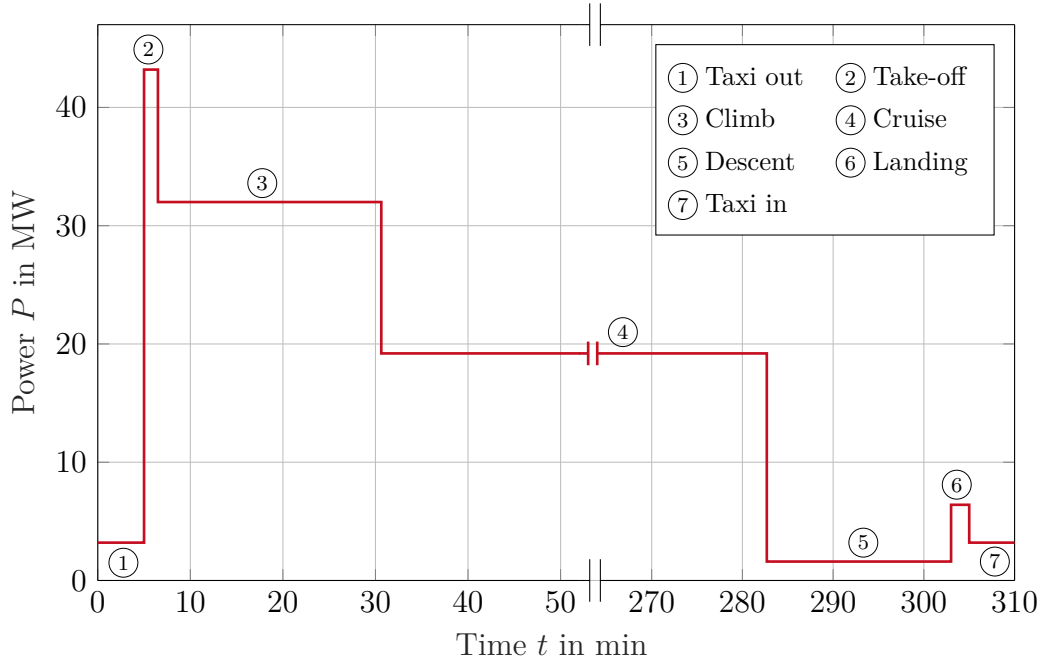


Figure 6.5.: Required power P for the hybrid-electric Airbus A321neo-LR as a function of the time t for a typical mission of 5 h 10 min according to Table 6.3. The cruise time is exemplary 4 h 12 min, but is in general variable as illustrated.

of 60 min. This mission phase is not illustrated in Figure 6.5. This enables to circle for a while if no landing slot is free or to fly to an alternate airport. This flight mission includes the power requirements for taxi in and taxi out as well as descent and landing, as summarized in Table 6.3. The highest power is required at the take-off

Table 6.3.: Performance requirements of the hybrid-electric Airbus A321neo-LR for an exemplary mission, as shown in Figure 6.5.

Mission phase	Time range	Power
Taxi out	300 s	3.2 MW
Take-off	90 s	43.2 MW
Climb	1448 s	32.0 MW
Cruise ¹	15 120 s	19.2 MW
Descent	1219 s	1.6 MW
Landing	120 s	6.4 MW
Taxi in	300 s	3.2 MW

¹ variable parameter in the flight mission

and climb with 43.2 MW and 32 MW, respectively. This is followed by a long cruise with about half the power compared to take-off. In this study, the duration of the cruise phase is kept variable to calculate the maximum flight time for a given fuel mix consisting of hydrogen gas and jet fuel.

For the machine design according to Chapter 4, materials must be selected for the

different components of the electric machine. The total mass of the machine is influenced by their volumetric densities. The selected materials are listed in Table 6.4 including their density and they are divided into rotor and stator materials.

The 114 filament MgB_2 wire, as presented in Section 2.1 in detail, is selected for the MgB_2 stator coils. Moreover, the silicone oil Novec is used as liquid coolant for stators made of the copper litz wire, as defined in Section 3.5.1, and the input parameters are chosen according to Table 3.4 [155]. In addition, carbon fiber reinforced polymer CFRP is used as support material in the stator. This is a cost-effective fiber-reinforced plastic that can be subjected to high mechanical stress at cryogenic temperature and under static and cyclic loading [237]. Additionally, it is particularly lightweight, non-conductive and non-magnetic.

The rotor sleeve is assumed to be made of Inconel 718 [231]. Stator and rotor housing, as well as carrier, are assumed to consist of aluminum Al-2219-T87 [226]. Both alloys combine high strength and an insensitive hydrogen permeability [234, 200].

Vacodym 745 HR with a remanence flux density B_{rem} of 1.44 T and a coercive field $H_{co,B}$ of 1115 kA m^{-1} at a temperature of 20°C is selected as permanent magnetic material based on NdFeB alloy [228]. The second generation of YBCO HTS tape with 12 mm width is assumed for HTS coils in the rotor with characteristics comparable to [235, 236]. The HTS bulks are assumed to be made of YBCO in the shape and size, as defined in Section 4.4.

As the yoke sheet metal, the commercially available soft magnetic cobalt-iron alloy Vacoflux 48 is assumed with a strip thickness of 0.35 mm [191]. It is characterized by a high magnetic saturation of up to 2.3 T and therefore the yoke can be designed particularly thin. Since the machine housing is not in contact with hydrogen, titanium Ti-6Al-4V is used instead of aluminum. Titanium offers a higher strength compared to aluminum, enabling a particularly thin housing design [233].

Table 6.4.: Materials for the machine parts subdivided into rotor and stator.

	Part	Material	Density ¹
Rotor	Carrier	Al 2219-T87	2840 [226, 227]
	PM magnet	Vacodym 745 HR	7600 [228]
	HTS coil	YBCO tape	8300 [229]
	HTS bulk	YBCO	6383 [230]
	Sleeve	Inconel 718	8193 [231]
	Housing	Al 2219-T87	2840
Stator	Carrier	Al 2219-T87	2840
	Housing	Al 2219-T87	2840
	MgB_2 coil	114F MgB_2 wire	8673^2
	Cu coil	Cu litz wire	6510 [154]
	Support	CFRP	2000 [232]
	Yoke	Vacoflux 48	8120 [191]
	Machine housing	Ti-6Al-4V	4430 [233]

¹ in kg m^{-3}

² calculated with the values given by Table 2.1 and 2.2

6.4. Topology Comparison

For the most promising machine topologies and architectures of Table 4.1 with respect to mass and efficiency, a detailed comparison is performed. Therefore, the partially and fully superconducting machines, as listed in Table 6.5, are disused in this section. Normal conducting machines and architectures with permanent magnets are not considered.

Table 6.5.: Investigated machine topologies for the design of a fan motor.

Generic term	Topology	Architecture
Fully superconducting	SC stator / SC rotor	MgB ₂ coil / HTS coil
		MgB ₂ coil / HTS bulk
Partially superconducting	SC stator / NC rotor	MgB ₂ coil / HA
	NC stator / SC rotor	Cu coil / SC coil
		Cu coil / HTS bulk

Based on previous sections, the requirements and boundary conditions linked to the aircraft and the installation of the fan are summarized for the machine design in Table 6.6. The rated power and rotational speed of the machine are 21.6 MW and 3500 min⁻¹. Additionally, technical limits of the wires, such as the minimum admissible bending radius, have to be taken into account. A critical bending radius of the stator coils $r_{s,b,c}$ of 48 mm, as optimistic limit and calculated in Section 2.2, is considered in the design. The impact of a critical bending radius of the stator coils of 80 mm, as pessimistic limit, on the design is discussed later in this section. The critical bending radius of rotor coils $r_{r,b,c}$ made of HTS tapes is 5 mm [238]. Furthermore, a minimum diameter-to-length aspect of the machine is defined to 1/3.

Table 6.6.: Requirements and boundary conditions for the machine design of a fan motor.

Symbol	Value	Unit	Explanation
P	21.6	MW	Power
n	3500	min ⁻¹	Rotational speed
$d_{m,max}$	0.5827	m	Maximum machine diameter
$l_{m,max}$	1.8	m	Maximum machine length
$(d_m/l_m)_{min}$	1/3	–	Minimum diameter-to-length aspect
$r_{s,b,c}$	48	mm	Critical stator bending radius (MgB ₂)
$r_{r,b,c}$	5	mm	Critical rotor bending radius (HTS tape) [238]

In addition to the material parameters in Table 6.4, further constant input parameters for the machine design are given by Table 6.7. They also include parameters that are suitable for optimization, but which are kept constant for this study. These

Table 6.7.: Constant input parameters for the machine design of a fan motor.

Symbol	Value	Unit	Explanation
m	3	–	Number of phases
$I_{n,s}$	0.7	–	Normalized stator current
α_0	95	%	Coverage of stator coils
α_1	$f(r_{ri})^1$	%	Coverage of rotor surface
α_3	$f(r_{ri})^1$	deg	Adjacent coil angle of rotor coil
f_{csr}	1/3	–	Coil support ratio
θ_{laod}	90	deg	Load angle of machine
$B_{y,max}$	2.1	T	Maximum flux density of iron yoke
$B_{y,sat}$	2.3	T	Saturation flux density of iron yoke
B_{rem}	1.44	T	Remanence flux density of magnet [228]
μ_r	1.027727	–	Relative permeability of magnet [228]
J_r	300	A mm ⁻²	Rotor current density [239]
n_{max}	19	–	Maximum harmonic

¹ is given as a function of the rotor inner radius to achieve a distance of 10 mm between the adjacent components

include the number of phases m and the normalized stator current $I_{n,s}$.

A constant value of 300 A mm⁻² is assumed for the rotor current density J_r , which has been achieved in practice for HTS coils at flux densities greater than 3 T and at an operational temperature corresponding to LH₂ cooling [239]. The fact that the self-field of the coil reduces the critical current density is neglected in this model. It is assumed that the rotor current density is independent of the coil geometry and external influences such as other magnetic fields or transient events. Furthermore, it is estimated that the rotor fields are below 3 T, explained by the field sensitive stator current density, as presented in Section 3.5. There, the investigations are limited to 2 T, due to the fact that the stator current densities are significantly reduced at such high fields.

It should be noted that, in contrast to the machine model description in Chapter 4, the coverage of rotor surface α_1 and the adjacent coil angle of rotor coil α_3 are calculated as a function of the inner rotor radius $r_{r,i}$. Therefore, a constant distance of 10 mm between adjacent magnets or coils in the rotor is assumed for the following reasons. Firstly, the resulting rotor carrier bar between these magnets or coils supports the force transmission and improves mechanical strength. Secondly, this distance also provides a safety margin if the coils are not manufactured bent and thus requires additional installation space between two adjacent coils in tangential direction.

The ratio between support structure and conductor inclusive cooling slot is considered by the coil support ratio f_{csr} of 1/3. The maximum flux density of the iron yoke $B_{y,max}$ is assumed to be 2.1 T. This provides a margin of 0.2 T to the saturation flux density $B_{y,sat}$ of the iron and thus prevents field leakage at the outer yoke radius. Finally, the maximum harmonic n_{max} of the field calculation is 19, as recommended in Section 4.5.5.

The remaining optimization parameters are summarized in Table 6.8. The essential parameters, which are investigated in all machine topologies, are the number of pole pairs p , the inner rotor radius $r_{r,i}$ and the stator coil thickness $d_{s,c}$. Depending on the type of rotor excitation, the characteristic parameters for the rotor are different. For rotor coils, the inner angle of rotor coil α_2 is mainly varied.

In the case of fully superconducting machines, the thickness of rotor coils is fixed to 12 mm, the typical width of commercially available second generation of YBCO HTS tapes. Combined with the specified rotor current density of 300 A mm^{-2} , sufficiently high magnetic fields are achieved. However, thicker coils that generate larger fields are possible, but lead to high AC loss and strongly decreased current density in the MgB_2 stator coils. The sensitivity of Cu coils on external field or AC loss is not as high. Therefore, double pancake HTS rotor coils with a thickness of 24 mm are also considered for partial superconducting machines with Cu stator coils. Other coil thicknesses based on other tape widths are feasible with this model.

In the case of HTS bulk rotors the peak flux density B_{peak} is varied up to 3.2 T and the bulk thickness is set to 10 mm. This flux density is below the achieved values at 20 K and is considered to be available independent of the bulk radius [174, 175]. However, one challenge is the magnetization of the bulks by the stator coils, which has not been achieved so far for the maximum peak flux density [240, 241]. Additionally, the rotor inner radius is chosen larger than it would be necessary according to the boundary conditions in order to find the global maximum.

All combinations of the input parameters are calculated to primarily increase the power-to-weight ratio (PTW) for each pole pair so that all boundary conditions are fulfilled. The power-to-weight ratio includes the active and passive mass of the machine, as introduced in Section 4.1. Secondly, the stator AC loss is minimized to realize a flight mission. This approach is known as brute-force search, which is simple to implement and will always find a solution. The disadvantage is that the number of variants rises quickly. However, this can be tolerated due to the holistic analytical approach and thus fast computation.

Furthermore, the range of the parameters in Table 6.8 are selected to achieve the maximum power-to-weight ratio for each parameter. This Cartesian product ensures that the global maximum is found. This approach is presented exemplary for the fully superconducting machine with MgB_2 stator coils and HTS rotor coils in Figure 6.6a for a pole pair number of 8 and without considering the boundary conditions in Table 6.6. The power-to-weight ratio PTW is shown as a function of the optimization parameters according to Table 6.8e, which are normalized to values between 0 and 1 for its minimum and maximum, respectively. It can be seen that a maximum power-to-weight ratio is achieved for each parameter. Thus, a weight-optimized machine for a pole pair number of 8 has been found for the given parameters. It should be noted, that the thickness of the stator coils is increased only until the maximum is reached. This is due to the fact that with increasing thickness the AC loss of the stator coil also increases and therefore no optimum machine according to their AC loss can be expected after this maximum.

Figure 6.6b shows how the variation of the parameters influences the working point flux density B_{wp} , which corresponds to the maximum flux density penetrating the stator coils at the nominal point of the machine, as presented in Section 5.2. A maxi-

Table 6.8.: Varied input parameters of the machine design for the machine architectures according to Table 6.5.

(a) Cu stator coils & HTS bulk rotor

Symbol	Range	Unit	Explanation
p	2–10	–	Number of pole pairs
$r_{r,i}$	75–300	mm	Inner radius of rotor
$d_{s,c}$	20–65	mm	Thickness of stator coil
B_{peak}	1.0–3.2	T	Peak flux density

(b) Cu stator coils & HTS rotor coils

Symbol	Range	Unit	Explanation
p	2–10	–	Number of pole pairs
$r_{r,i}$	75–300	mm	Inner radius of rotor
$d_{s,c}$	20–65	mm	Thickness of stator coil
d_{mag}	12, 24	mm	Thickness of rotor coil
α_2	40–80	deg	Inner angle of rotor coil

(c) MgB₂ stator coils & Halbach rotor array

Symbol	Range	Unit	Explanation
p	2–10	–	Number of pole pairs
$r_{r,i}$	75–300	mm	Inner radius of rotor
$d_{s,c}$	10–30	mm	Thickness of stator coil
d_{mag}	10–40	mm	Thickness of Halbach rotor array

(d) MgB₂ stator coils & HTS bulk rotor

Symbol	Range	Unit	Explanation
p	2–10	–	Number of pole pairs
$r_{r,i}$	75–300	mm	Inner radius of rotor
$d_{s,c}$	10–30	mm	Thickness of stator coil
B_{peak}	1.0–2.6	T	Peak flux density

(e) MgB₂ stator coils & HTS rotor coils

Symbol	Range	Unit	Explanation
p	2–10	–	Number of pole pairs
$r_{r,i}$	75–300	mm	Inner radius of rotor
$d_{s,c}$	10–30	mm	Thickness of stator coil
d_{mag}	12	mm	Thickness of rotor coil
α_2	45–87.5	deg	Inner angle of rotor coil

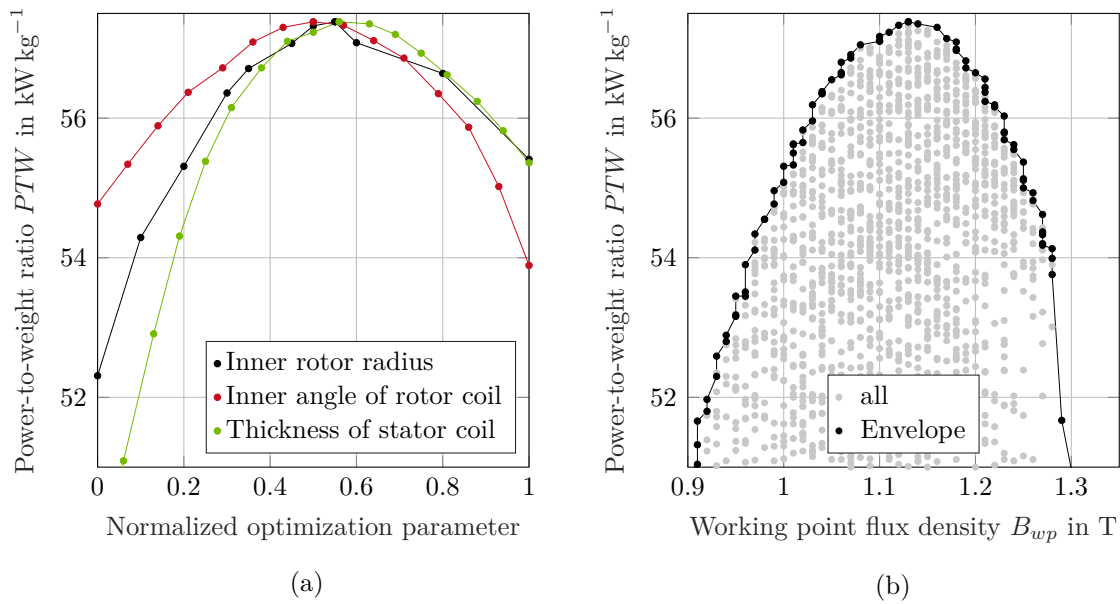


Figure 6.6.: Power-to-weight ratio PTW for the 21.6 MW and 3500 min^{-1} machine design at a pole pair number of 8 and in dependence of the:

- Normalized optimization parameters.
- Working point flux density B_{wp} .

imum power-to-weight ratio is clearly achieved in this example at a working point flux density of 1.1 T and decreases continuously from this point with increasing or decreasing flux density. As can be seen, the envelope also presents this correlation in a clear illustration for this large amount of data. For this reason, only the envelope or Pareto front is shown for different dependencies in the following topology comparison.

In the following sections, the results for partially and fully superconducting machines are presented, comparing the most important parameters power-to-weight ratio, stator AC loss and working point flux density. The analysis of the working point ensures that the flux density range for the AC loss and current density calculation in Chapter 3 is sufficiently large. Two data sets are presented in each figure. Firstly, the design results if the requirements and boundary conditions according to Table 6.6 are not considered. These are illustrated gray in the background of the figure. Secondly, the results if these conditions are considered, presented as the envelope for each numbers of pole pairs p . The influence of the boundary conditions is discussed in a separate section after introducing each machine topology.

6.4.1. Partially Superconducting Machines

Cu stator coils and HTS bulk rotor

Firstly, the suitability of partially superconducting machines with continuous HTS bulks as rotor excitation and Cu litz wires in the stator is investigated. In Figure 6.7a, the power-to-weight ratio PTW of such machines is shown as a function of the working point flux density B_{wp} for the optimization parameters according to Table 6.8a. If the boundary conditions according to Table 6.6 are not taken into

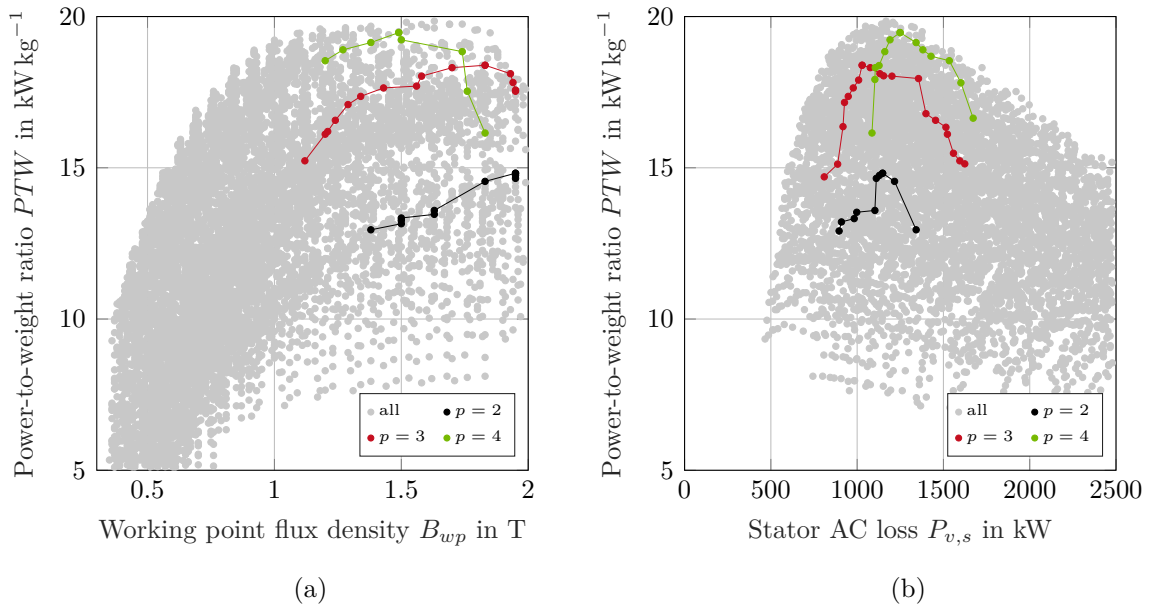


Figure 6.7.: Results for the machine architecture consisting of Cu stator coils and HTS rotor bulks according to the optimization parameters in Table 6.8a. Presented is the power-to-weight ratio PTW as a function of the:

- Working point flux density B_{wp} .
- Stator AC loss $P_{v,s}$.

account, power-to-weight ratios up to 19.9 kW kg^{-1} can be achieved in general with this machine architecture at a working point flux density of 1.63 T and a pole pair number of 4. However, if these boundaries are considered the maximum power-to-weight ratio decreases to 19.5 kW kg^{-1} at a working point flux density of 1.49 T and a pole pair number of 4. This is the lowest power-to-weight ratio in comparison of all examined machine architectures and the quantity of remaining machine designs with a pole pair number of 2, 3 and 4 is relatively small compared to the total solution space. This is due to the limited installation space of the machine. Moreover, the triangular field profile, as shown in Figure 4.13a, is disadvantageous, because its peak flux density leads to hot spots and thus limits the stator current density. Additionally, the fundamental wave of the radial flux density, which generates the torque, is lower than this peak. Increasing the peak flux densities beyond 3 T to increase the rotor flux is not feasible to compensate this disadvantages, because this lead also to hot spots in the stator coils. Nevertheless, the minimum stator AC loss is 809.3 kW at a power-to-weight ratio of 14.7 kW kg^{-1} and a pole pair number of 3, as shown in Figure 6.7b. This loss increases with increasing power-to-weight ratio and amounts to 1248.8 kW at maximum power-to-weight ratio.

This shows that a power-to-weight ratio of approximately 13 kW kg^{-1} is required for the limited installation space in the engine and that the following machine architectures must achieve much higher power-to-weight ratios to allow efficient machines as well. Furthermore, the requirements cannot be fulfilled with the cylindrical and rectangular bulk geometries, according to Section 4.4, due to the reduced magnetic flux of the bulk according to Equation 4.33.

Cu stator coils and HTS rotor coils

Secondly, the suitability of partial superconducting machines with HTS coils as rotor excitation and Cu litz wires as stator coils is investigated. In Figure 6.8, the machine design results are presented according to the optimization parameters in Table 6.8b.

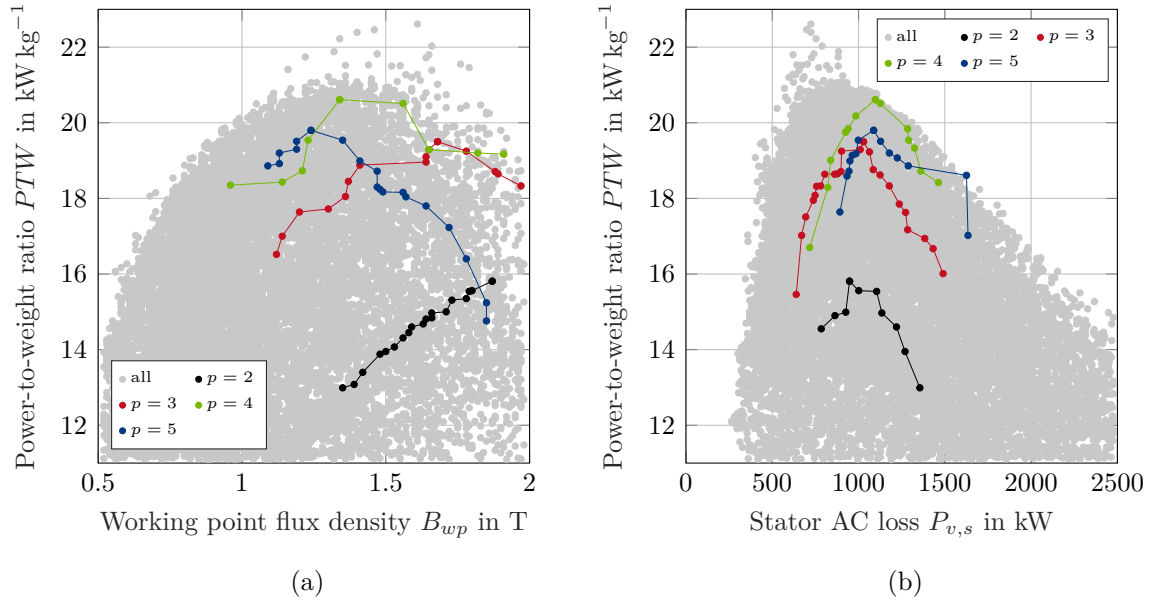


Figure 6.8.: Results for the machine architecture consisting of Cu stator coils and HTS rotor coils according to the optimization parameters in Table 6.8b. Presented is the power-to-weight ratio PTW as a function of the:

- (a) Working point flux density B_{wp} .
- (b) Stator AC loss $P_{v,s}$.

If the requirements and boundary conditions of Table 6.6 are not considered, a maximum power-to-weight ratio of 22.6 kW kg^{-1} is achieved at a working point flux density of 1.61 T and a pole pair number of 4. Taking the boundary conditions into account, the maximum power-to-weight ratio decreases to 20.6 kW kg^{-1} at the same pole pair number of 4 and a working point flux density of 1.34 T, as shown in Figure 6.8a. However, the power-to-weight ratio decreases with an increasing number of pole pairs above 4 and at a pole pair number of 6 and higher, no machine can be designed that fulfills the requirements, especially in the available installation space. This behavior is linked to the fact, that the electric frequency is directly proportional to the number of pole pairs. Therefore, the AC loss characteristic changes and results in a different current density for the copper litz wire, as described in Section 3.5.1. With decreasing pole pair number below 4 the power-to-weight ratio also decreases due to the rising thickness of the yoke. However, the lowest stator AC loss is achieved in this case at a pole pair number of 3, as shown in Figure 6.8b, with 639 kW at a power-to-weight ratio of 15.5 kW kg^{-1} . Theoretically, even more loss-optimized machines would be possible with a pole pair number of 2, but this is not feasible due to the decreasing power-to-weight ratio and limited installation space. Due to the increasing electrical frequency with rising pole pair numbers, the stator AC

loss increase strongly and reach 1097.8 kW at the maximum power-to-weight ratio of 20.6 kW kg^{-1} . Furthermore, both the lightest and the machine with the lowest stator AC loss are achieved at a rotor coil thickness of 12 mm.

MgB₂ stator coils and Halbach rotor array

The architecture consisting of MgB₂ stator coils and NdFeB magnets in an Halbach configuration is investigated according to the optimization parameters in Table 6.8c. The maximum power-to-weight ratio of 42.8 kW kg^{-1} is achieved at a working point flux density of 0.82 T and a pole pair number of 8 if the the boundary conditions in Table 6.6 are not considered, as shown in Figure 6.9a. This magnetic flux density

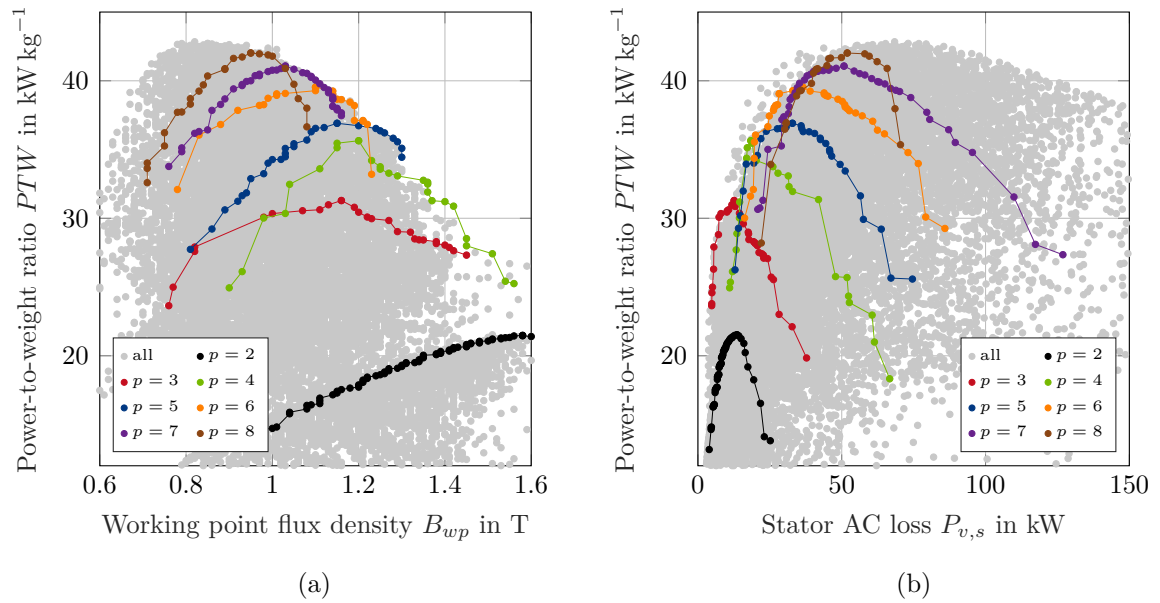


Figure 6.9.: Results for the machine architecture consisting of MgB₂ stator coils and Halbach rotor array according to the optimization parameters in Table 6.8c. Presented is the power-to-weight ratio PTW as a function of the:

- (a) Working point flux density B_{wp} .
- (b) Stator AC loss $P_{v,s}$.

is lower than in all other architectures due to the limited remanence of the magnetic material. Furthermore, this also leads to the fact that the working point flux density range for all investigated pole pair numbers of approximately 1 T is smaller compared to all other architectures. However, a maximum power-to-weight ratio of 42 kW kg^{-1} at a pole pair number of 8 and working point flux density of 0.95 T is achieved if the boundary conditions are considered. This most lightweight machine design generates an AC loss of about 51.9 kW at nominal operation. For designs with lower number of pole pairs, the AC loss is much smaller. The machine design with the lowest AC loss of 3.9 kW has 2 pole pairs and a power-to-weight ratio of 13.2 kW kg^{-1} .

The outliers above the maximum power-to-weight ratio can be explained by the limited accuracy of the working point determination. This design step is successful

if the torque change between two iterations is less than 0.5% of the target torque. Furthermore, the spatial resolution of the flux density calculation in the stator coil region is limited, as described in Section 5.2. In combination with the high sensitivity of the current density in relation to the flux density, outliers can occur. However, it is cross-checked that each working point matches the electro-thermal characteristic, as determined in Chapter 3 and shown in Figure 6.12a.

A comparison of all three architectures of partially superconducting machines shows that the combination of MgB₂ stator coils and Halbach rotor array achieves both the highest power-to-weight ratio and the lowest stator AC loss. This can be explained by the fact, that the reduced excitation flux generated by the Halbach array can be compensated to a large part by an increasing stator current density, so that the machine still achieves a high torque. Further advantages of this topology are the simple manufacturing and operation of a rotor with an Halbach array, in contrast to superconducting rotor excitations. These require either currents leads to the HTS coils and magnetization schemes for the HTS bulks or tape stacks in the machine environment [241, 242, 243, 244]. Moreover, implementing cryogenic cooling of the rotating parts is avoided. The minimum AC loss in the MgB₂ stator of 3.9 kW is about a factor of 164 lower compared to the Cu stator with AC loss of 639 kW.

A further challenge of the Cu stator is the transfer of its heat to the ambient air. For this reason, a heat exchanger has to be considered as additional mass in the propulsion system. Such a component is investigated and optimized for aviation applications in [245]. It is shown that maximum four kilowatts of power loss can be removed per kilogram of heat exchanger. Table 6.9 compares the masses between partially superconducting machines based on Cu or MgB₂ stator coils including the mass of the respective cooling system: heat exchanger or LH₂ tank. Presented are the lightest machine and the machine with lowest stator AC loss. The most efficient

Table 6.9.: Comparison of masses for machines with Cu or MgB₂ stator coils and HTS rotor coils considering the weight for cooling by a heat exchanger or LH₂ tank.

Mass ¹	Cu stator		MgB ₂ stator	
	max(<i>PTW</i>)	min(<i>P_{s,v}</i>)	max(<i>PTW</i>)	min(<i>P_{s,v}</i>)
Machine	1048.0	1397.0	380.3	1234.3
Cooling	274.5	159.8	103.8	103.8
Σ	1322.5	1556.8	484.1	1338.1

¹ in kg

machine which is based on Cu stator coils and HTS rotor coils requires a 159.8 kg heat exchanger, which in turn requires installation space and energy. In comparison, the liquid hydrogen tank weighs 207.6 kg and is designed to cool two machines with 280 kg of liquid hydrogen. The liquid hydrogen mass does not affect the weight balance because it is additionally used as fuel. A comparison of the total masses shows that MgB₂ stators are superior to Cu stators for both the lightest and most efficient machine. This is also indicated by the large difference in total masses between the lightest machine and the machine with lowest stator AC loss.

Due to these disadvantages, machine architectures based on Cu stators are not considered further and therefore only the Halbach array variant of partially superconducting machines is taken into account in the further design.

6.4.2. Fully Superconducting Machines

MgB₂ stator coils and HTS bulk rotor

The machine topology MgB₂ stator coils with HTS bulk rotor is evaluated according to the optimization parameters in Table 6.8d. The maximum power-to-weight ratio is reached at 53.5 kW kg⁻¹ at a working point flux density of 1.1 T and a pole pair number of 9 if the boundary conditions in Table 6.6 are not taken into account, as shown in Figure 6.10a. If the boundary conditions are considered, even a power-to-

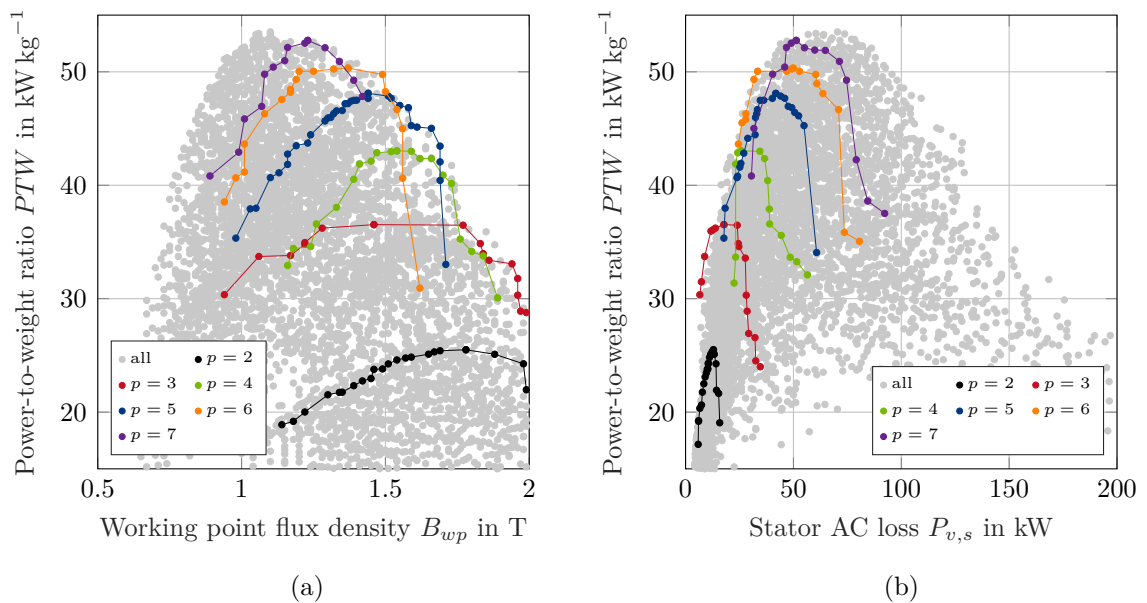


Figure 6.10.: Results for the machine architecture consisting of MgB₂ stator coils and HTS rotor bulks according to the optimization parameters in Table 6.8d. Presented is the power-to-weight ratio PTW as a function of the:

- (a) Working point flux density B_{wp} .
- (b) Stator AC loss $P_{v,s}$.

weight ratio of 52.8 kW kg⁻¹ is possible at a working point flux density of 1.23 T and a pole pair number of 7. It should also be noted that peak flux densities by the bulk of more than 2.0 T do not lead to optimal machines in terms of the power-to-weight ratio or the AC loss of the stator coils.

The stator AC loss of approximately 51.3 kW at the maximum power-to-weight ratio is at the same level compared to the combination of MgB₂ stator coils and Halbach array. Furthermore, the working point flux density is lower for the Halbach variant, but its maximum power-to-weight ratio is reached at a higher electrical frequency. However, the minimum stator AC loss is with about 5.9 kW higher as in the Halbach variant. In this minimum a power-to-weight ratio of 17.2 kW kg⁻¹ is achieved.

MgB₂ stator coils and HTS rotor coils

Figure 6.11 presents the machine design results for the architecture consisting of MgB₂ stator coils and HTS rotor coils. The optimization parameters are selected according to Table 6.8e. The maximum power-to-weight ratio of 57.5 kW kg^{-1} is

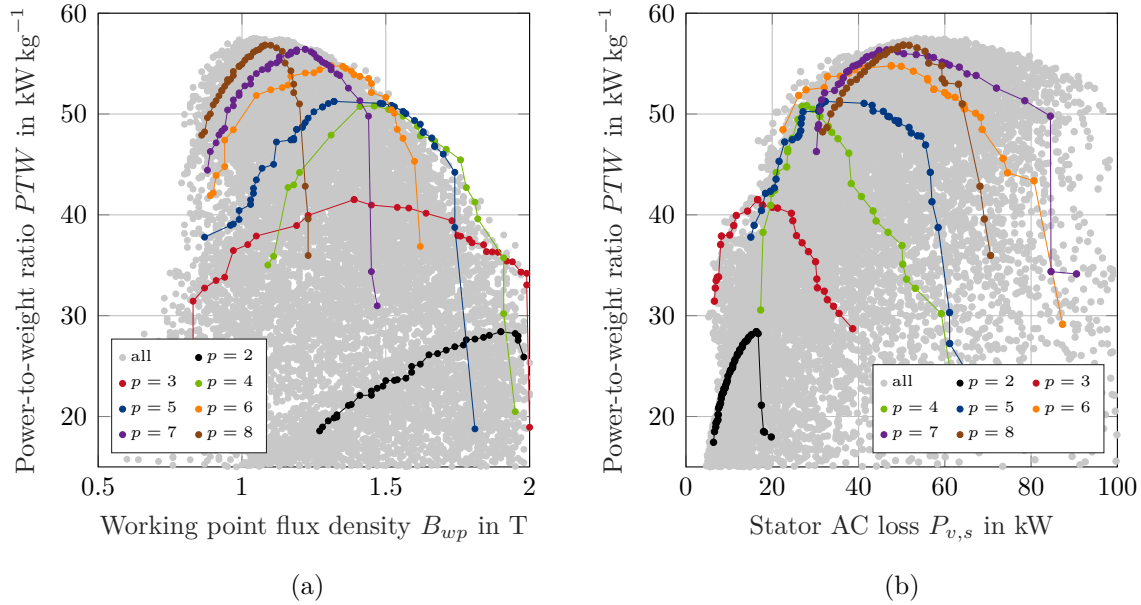


Figure 6.11.: Results for the machine architecture consisting of MgB₂ stator coils and HTS rotor coils according to the optimization parameters in Table 6.8e. Presented is the power-to-weight ratio PTW as a function of the:

- Working point flux density B_{wp} .
- Stator AC loss $P_{v,s}$.

achieved at a working point flux density of approximately 1.04 T at a pole pair number of 9 if the boundary conditions are not considered. By observing the boundary conditions, the power-to-weight ratio decreases to 56.8 kW kg^{-1} at a working point flux density of 1.08 T and a pole pair number of 8. This is the highest value of all architectures and is caused by the higher degree of freedom by which the excitation field can be adjusted compared to all other architectures. Thus, the field profile can be optimally configured for the MgB₂ stator coils to reach high power-to-weight ratios.

The minimum AC loss of 6.4 kW is achieved at a pole pair number of 2 and is thus higher compared to the Halbach rotor variant. However, at this point a power-to-weight ratio of 17.5 kW kg^{-1} is achieved, which is the best-in-class value of all architectures. At maximum power-to-weight ratio the stator AC loss increases to 50.3 kW.

Conclusion of the topology comparison

It is concluded that the power-to-weight ratio increases with increasing number of pole pairs until a maximum power-to-weight ratio is reached. This point is achieved for all architectures in the pole pair number range of 4–8. If the number of pole pairs is further exceeded, the power-to-weight ratio decreases, because the increasing

electrical frequency leads to increasing AC loss in the stator, which reduce the current carrying capacity of the stator coils. This effect is illustrated in Figure 6.12a for a machine architecture based on MgB₂ stator coils and HTS rotor coils. The correlation between working point current density J_{wp} and flux density B_{wp} corresponds to the electro-thermal characteristic of the 114 filament MgB₂ wire at a normalized current of 0.7, as discussed in Chapter 3.

In the case of a small number of pole pairs, the power-to-weight ratio increases mainly due to the reduction of the yoke thickness, as presented in Figure 6.12b. This effects saturate with increasing number of pole pairs. The optimum design

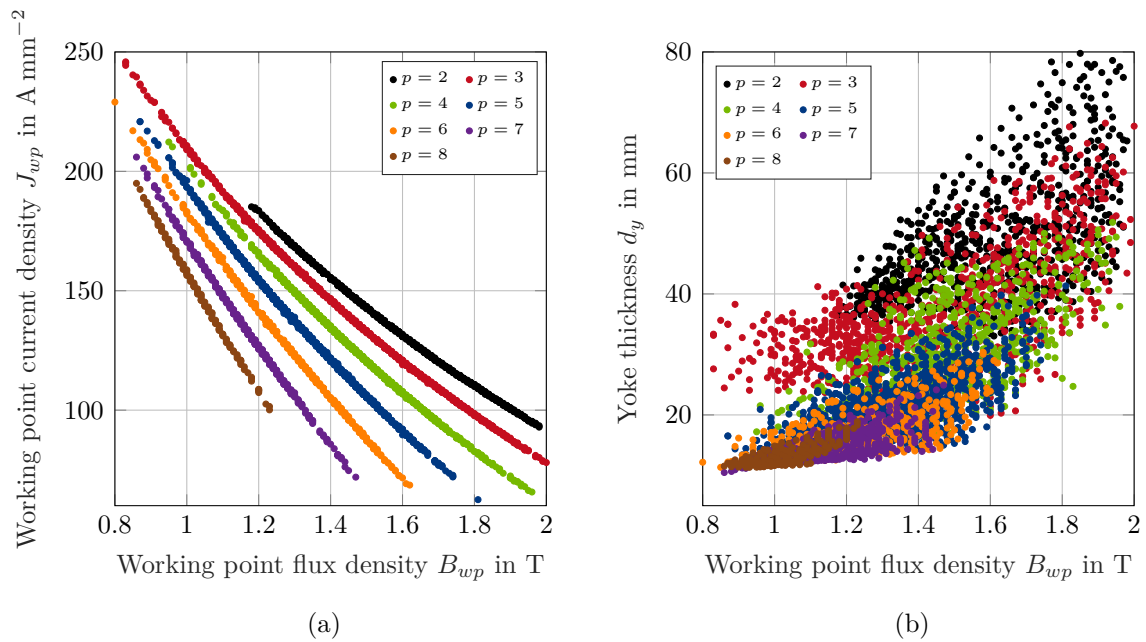


Figure 6.12.: Results for the machine architecture consisting of MgB₂ stator coils and HTS rotor coils according to the optimization parameters in Table 6.8e. Presented is the working point flux density B_{wp} as a function of the:
 (a) Working point current density J_{wp} at a normalized current of 0.7.
 (b) Yoke thickness d_y .

range concerning the working point flux density and the pole pair number is considerably smaller for fully superconducting machines than for partially superconducting machines, being even more pronounced at high power-to-weight ratios. This behavior can be attributed to the high sensitivity of the MgB₂ wire to AC loss. In the case of the partially superconducting rotor machines, the frequency-independent ohmic loss dominate the total loss in the copper Litz wire. This leads to a lower sensitive power-to-weight ratio of partially superconducting machines with Cu coils in terms of number of pole pairs and magnetic field. [142]

The highest power-to-weight ratio is achieved with a fully superconducting machine with MgB₂ stator coils and HTS rotor coils. Moreover, the working point flux density is 1.08 T and the pole pair number is 8, which corresponds to a electric frequency of 466.7 Hz. This leads to the conclusion that the MgB₂ wire performs best at this

value pair in the machine design and under the assumed conditions.

The lowest stator AC loss is obtained for all machines based on MgB₂ stator coils at a pole pair number of 2, which corresponds to a electric frequency of 116.7 Hz. Moreover, the most efficient stator coils are achieved by excitation with an Halbach array. Here, the AC loss is minimal 3.9 kW, a reduction of 39% compared to the excitation with HTS coils. This is due to the exclusively sinusoidal field profile of Halbach arrays, as shown in Figure 4.15a, resulting in no unnecessary hot spots in the stator coils by harmonics which in addition do not generate torque. However, the rotor current density is assumed to be constant in this study, resulting in a non-optimal adjustment of the field profile sharpness. Optimizing this parameter in combination with the inner angle of the rotor coil and the thickness of this coil will probably further reduce the AC loss of the stator. Moreover, a perfectly sinusoidal shape is not achievable for coils with constant current density distribution.

How the input parameters of Table 6.8 influence the target parameters, high power-to-weight ratio and low stator AC loss, is summarized in Table 6.10. For both architectures, a decreasing inner rotor radius $r_{r,i}$ has a positive effect on the power-to-weight ratio. The stator AC loss is mainly reduced in both architectures by a small number of pole pairs and thin stator coils. Furthermore, the excitation conditions are opposite, because a thicker Halbach array results in both high power-to-weight ratio and low stator AC loss. A significant influence of the sleeve thickness is not recognizable with increasing magnet thickness due to the medium rotational speed of 3500 min⁻¹ and the limited machine diameter. The inner angle of rotor coil α_2 should be as large as possible for low rotor fields and thus low stator AC loss, as long as the minimum power-to-weight ratio is not undershot. It should be noted that, the dependencies has been studied in the ranges listed in Table 6.8.

Table 6.10.: Impact of the varied input parameters in Table 6.8 for increasing power-to-weight ratio ($PTW \uparrow$) and decreasing stator AC loss ($P_{s,v} \downarrow$) of MgB₂ stator machines with Halbach array or HTS coil excitation.

Parameter	Halbach rotor array		HTS rotor coils	
	$PTW \uparrow$	$P_{s,v} \downarrow$	$PTW \uparrow$	$P_{s,v} \downarrow$
p	↗	↓	↗	↓
$r_{r,i}$	↓	↗	↓	↗
$d_{s,c}$	↗	↓	↗	↓
α_2	—	—	↘	↗
d_{mag}	↗	↑	—	—

So far, the focus of the result analysis was on the AC loss of the stator, because these mainly affect the coolant consumption on a flight mission. The iron loss of the yoke is additionally considered in the efficiency of the machine. It should be noted that the energy required to produce liquid hydrogen is not considered in the machine efficiency. Figure 6.13 shows the power-to-weight ratio PTW as a function of the efficiency η for all investigated machine architectures according to Table 6.5 and filtered by the requirements and boundary conditions in Table 6.6. The comparison

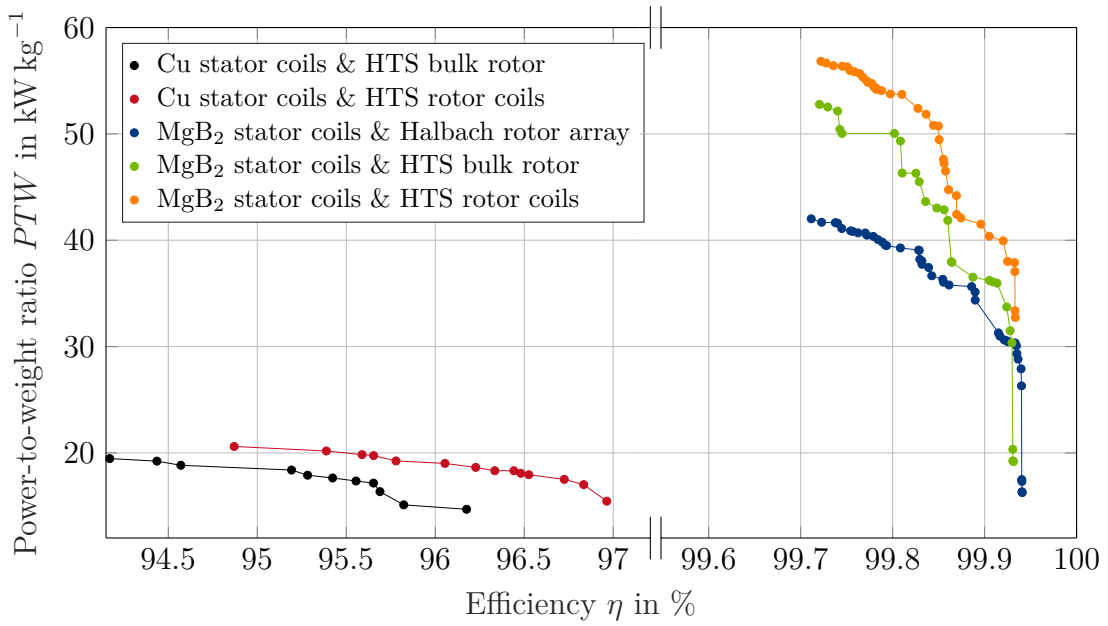


Figure 6.13.: Comparison of the power-to-weight ratio PTW as a function of the efficiency η of all machine architectures according to Table 6.5 and under consideration of the requirements as well as boundary conditions in Table 6.6.

between the efficiency of machines with MgB_2 and Cu stator coils reflects again the significant difference in stator AC loss of both technologies. Cu stators achieve a maximum efficiency of 96.96% at a PTW of 15.5 kW kg^{-1} with HTS rotor coils and MgB_2 stators achieve a maximum efficiency of 99.94% at a PTW of 16.3 kW kg^{-1} with Halbach rotor array.

Due to the lower efficiency of fully superconducting machines based on HTS bulks compared to the other machine architectures with MgB_2 stators, the machine architectures MgB_2 stator coils in combination with HTS rotor coils, as well as Halbach rotor array are only further investigated as the most promising solutions.

Preselection

A preselection is made, as shown in Figure 6.14, due to the large amount of data. Machines that fulfill all boundary conditions and have an optimal power-to-weight ratio as well as stator AC loss are further investigated in this design. The machines are selected by determining the Pareto optimality between both parameters. Since this would result in a very low number of machines, the Pareto front is determined three times, whereby the already selected machines are removed from the data set. This leads to a data set of about 150 machines for the architecture consisting of MgB_2 stator coils and Halbach rotor array as well as MgB_2 stator coils and HTS rotor coils, as shown in Figure 6.14a and 6.14b, respectively.

Impact of the boundary conditions

The results presented in the previous sections demonstrate a significant impact of the boundary conditions according to Table 6.6 on the power-to-weight ratio as well as the stator AC loss. In addition to the installation space for the machine, the

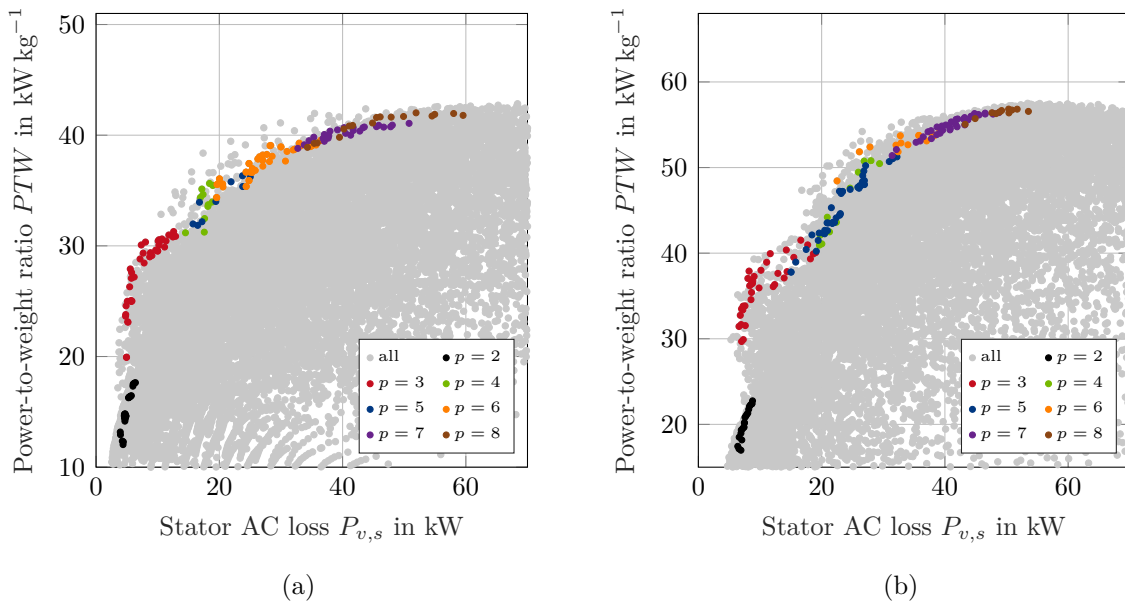


Figure 6.14.: Power-to-weight ratio PTW as a function of the stator AC loss $P_{v,s}$ filtered according to the machines with an optimal power-to-weight ratio as well as stator AC loss for the machine architectures:

- (a) MgB_2 stator coils and Halbach rotor array.
- (b) MgB_2 stator coils and HTS rotor coils.

bending radii of the rotor and stator coils as well as the diameter-to-length aspect of the machine are critical boundaries, as demonstrated in Figure 6.15. It should be noted, that both quantities are temporarily not considered as a boundary condition in the data sets of these figures, respectively.

Figure 6.15a and 6.15b show the power-to-weight ratio PTW as a function of the stator bending radius $r_{s,b}$ for the machine architectures consisting of MgB_2 stator coils and HTS rotor coils or Halbach rotor array, respectively. A critical bending radius range is defined for the 114 multifilament MgB_2 wire in Section 2.2, which is marked for the optimistic limit at 48 mm and the pessimistic limit at 80 mm in Figure 6.15a and 6.15b. It is clearly recognizable that the bending radius has a large influence on machines with MgB_2 stator coils and Halbach rotor array. If the pessimistic value is assumed, only machines with less than 5 pole pairs are possible. In case of the optimistic value, the pole pair number range increases to values lower than 9. This effect depends only on the wire properties and stator coil geometry and is therefore similar for machines with MgB_2 stator coils and HTS rotor coils. Thus, an increased mechanical stability of the sheath material of the wire would reduce this limitation, as described in Section 2.2.

The bending radius of the rotor coils is much less critical. A minimum bending radius of 30 mm is reached at a pole pair number of 8, which is 6 times higher than the critical value of 5 mm.

The diameter-to-length aspect d/l is in a similar range between 0.2 and 0.9 for both investigated architectures, as shown in Figure 6.15c and 6.15d. Since the minimum diameter-to-length aspect is defined as $1/3$, several machines in the range of all

pole pair numbers are not further considered. With increasing pole pair number and power-to-weight ratio, the diameter-to-length aspect tends to increase. Higher machine diameters as specified would thus lead to more optimal machines especially at low pole pair numbers.

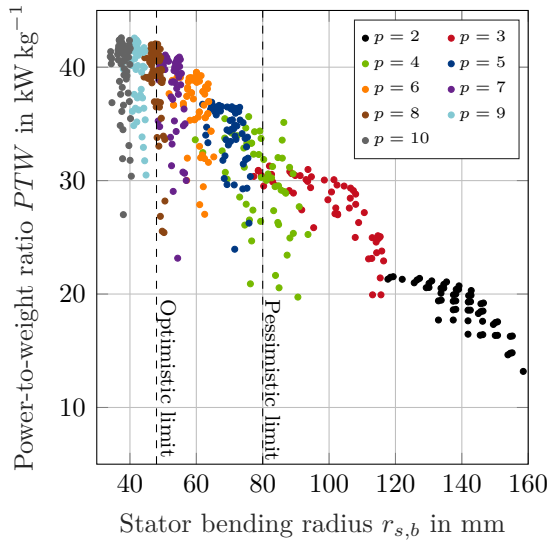
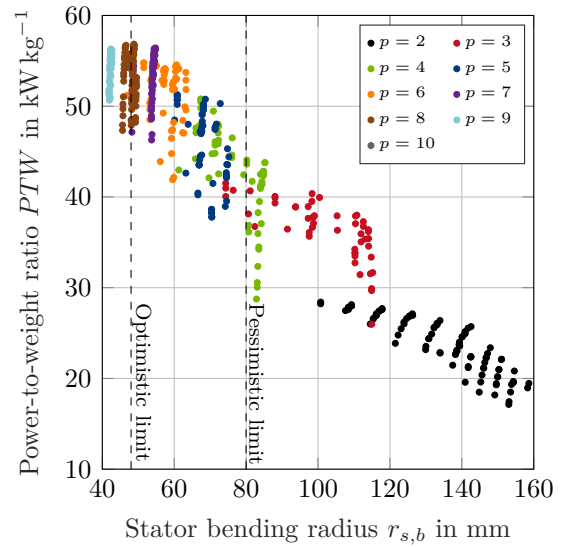
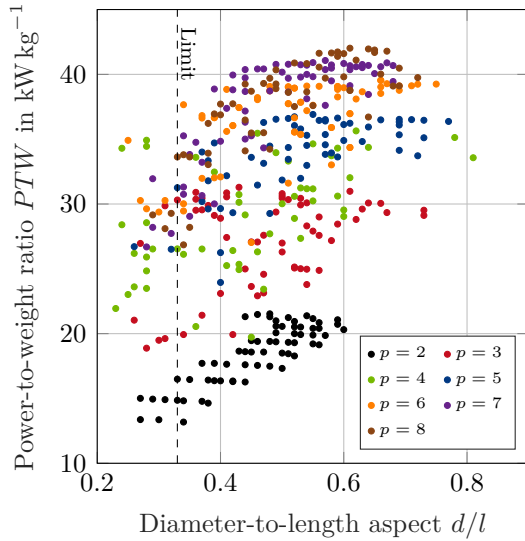
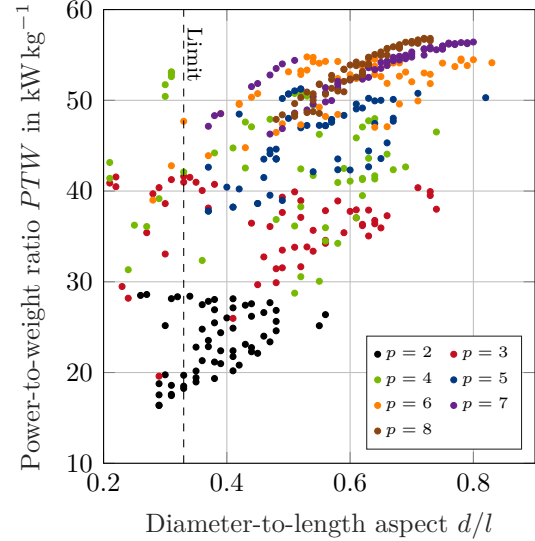
(a) MgB₂ stator coils & Halbach rotor array(b) MgB₂ stator coils & HTS rotor coils(c) MgB₂ stator coils & Halbach rotor array(d) MgB₂ stator coils & HTS rotor coils

Figure 6.15.: Results for the preselected machine architectures MgB₂ stator coils consisting of Halbach rotor array or HTS rotor coils. Presented are the power-to-weight ratio PTW as a function of the limiting parameters: (a) (b) Stator bending radius $r_{s,b}$. (c) (d) Diameter-to-length aspect d/l .

6.5. Influence of Flight Mission

In this section the amount of liquid hydrogen to cool the machines over a flight mission is evaluated. A flight mission consists of different power requirements for the propulsion system, as presented in Figure 6.5, and these also impact the stator AC loss. For this reason, the stator AC loss has been determined over a flight mission in order to size a liquid hydrogen tank. However, the tank size is specified with 280 kg of liquid hydrogen in this design example and therefore the maximum flight time is determined alternatively.

The take-off and landing phases, as given in Table 6.3, are summarized to about 58 min and are considered in the calculation as a constant and minimum share of the total flight mission. Thus, the maximum flight time is calculated by adjusting the cruise time. It should be noted that the maximum flight time does not include reserves, such as a diversion mission. The varying power demand on both machines is regulated by adjusting the normalized stator current. In addition, the control strategy maximum torque per AC loss is also applied for machines based on HTS rotor coils, as discussed in Section 5.4.

Figure 6.16 presents the stator AC loss $P_{s,v}$ at the nominal point of the machines as a function of the maximum flight time $t_{f,max}$ for the preselection of fully superconducting machines with HTS rotor coils and partially superconducting machines with Halbach rotor array. The number of pole pairs vary between 2–8, as shown in Figure 6.14a and 6.14b, respectively. The sum of take-off and landing phases are marked at about 58 min. Furthermore, the fuel range limit of the hybrid-electric Airbus A321-LR is marked at a maximum flight time of 378 min, which is calculated by the mean fuel burn given in Table 6.1. This is a reduction of the maximum range to about 59 % of the initial range of the Airbus A321-LR due to the reduced jet fuel capacity. At this maximum flight time, liquid hydrogen as coolant and the fuel, as a mixture of jet fuel and gaseous hydrogen (GH_2), are in equilibrium on board. This means that for shorter flight times, liquid hydrogen is used up as coolant before the fuel mixture. This is not desirable, because it shortens the flight mission.

Figure 6.16a shows that the machine architecture with Halbach rotor array achieves a maximum flight time of 600 min at a number of pole pairs of 2. The fuel range limit is also reached with a pole pair number of 3. As the number of pole pairs increases, the stator AC loss also increase and the maximum flight time decreases significantly. At a pole pair number of about 6 the AC loss is so high that theoretically only take-off and landing are possible. Even higher pole pair numbers lead to machines that can be cooled for only a few minutes.

The maximum flight time for MgB_2 stator machines with HTS rotor coils and non-minimized stator AC loss, as shown in Figure 6.16b, is shorter with about 329 min compared to machines with Halbach array excitation and also achieved at a pole pair number of 2. Consequently, the fuel range limit is not reached. This is due to the higher stator AC losses with minimum 6.4 kW in comparison to 3.9 kW. To realize a maximum flight time exceeding the fuel range limit, the AC loss have to be further reduced. This is possible for this architecture by using the control strategy maximum torque per AC loss. The influence of this control strategy in each mission phase for two design proposals, which are presented in the next section, is shown in Figure 6.18. Thus, a maximum flight time of 613 min is reached at a pole pair num-

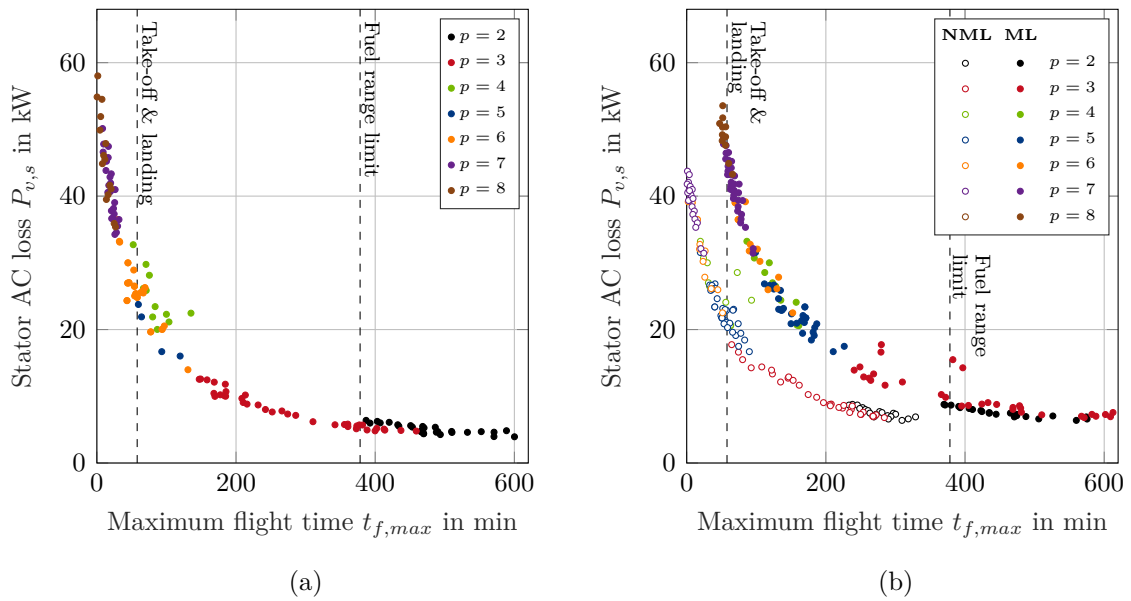


Figure 6.16.: Stator AC loss $P_{s,v}$ at the nominal point of the machine as a function of the maximum flight time $t_{f,max}$ for fully and partially superconducting machines. The maximum flight time is calculated according to the variable flight mission specified in Table 6.3 and the fuel range limit is marked. The machine architectures are divided into MgB_2 stator coils and:

- (a) Halbach rotor array.
- (b) HTS rotor coils with non-minimized (NML) and minimized (ML) stator AC loss.

ber of 3. This also represents a 2.1% improvement compared to the machine with Halbach array. With a pole pair number of 3, more efficient machines are achieved in contrast to machines with a pole pair number of 2, because the fundamental wave of the rotor field is more pronounced due to the smaller coil leg distance. The share of loss-generating harmonics is therefore greater at a pole pair number of 2 and overwhelms the AC loss reduction due to the lower electrical frequency.

In conclusion, both remaining machine architectures based on MgB_2 stator coils are successfully designed. All requirements and boundary conditions are fulfilled and the machines can be cooled over an entire flight mission of the hybrid-electric Airbus A321-LR. Since the fuel range limit is only exceeded by machines with a pole pair number of 2 or 3, the bending radius of the stator coils is non-critical.

6.6. Design Proposal

A design proposal is made for both remaining machine architectures: partially superconducting machines with MgB_2 stator coils and Halbach rotor array as well as fully superconducting machines with MgB_2 stator coils and HTS rotor coils. Therefore, all machines in Figure 6.16a and 6.16b, which reach a maximum flight time greater than the fuel range limit, are possible design proposals.

To make a proposal for both architectures, it is assumed that the most cost-effective

machine would be achieved by minimizing the superconducting and permanent magnet material. The target price of the stator coils P_s and rotor coils P_r are given by Equation 6.3 and 6.4, respectively, with the volume of superconducting coils V_{sc} and the critical current density J_c . It should be noted that nowadays the price performance ratio p_{sc} of the superconductor is highly dependent on the supplier and the volume of customer's order. However, the price performance ratio at a temperature of 20 K and flux density of 2 T of the second generation of YBCO HTS tape is forecasted to be $20 \text{ €kA}^{-1} \text{ m}^{-1}$ for a large commercial market in the year 2030 [246]. This is more expensive compared to MgB_2 wires with about $5 \text{ €kA}^{-1} \text{ m}^{-1}$ due to the more complex fabrication [83]. Furthermore, a price weight ratio of 250 €kg^{-1} is assumed for highly qualitative neodymium iron boron (NdFeB) magnets.

$$P_s = m p J_c p_{sc} V_{sc} \quad (6.3)$$

$$P_r = 2 p J_c p_{sc} V_{sc} \quad (6.4)$$

For both architectures, the machine with the minimum sum of stator and rotor coil or magnet costs is selected. Table 6.11 and 6.12 summarize the main input and output parameters for these design proposals. Additionally, Figure 6.17 presents the cross section of one magnetic machine pole for both design proposals to visualize the dimensions of the main parts. Both designs are close to the maximum machine diameter $d_{m,max}$, which demonstrates again the great influence of this boundary condition. Comparing the two design proposals further, it can be seen that the radial

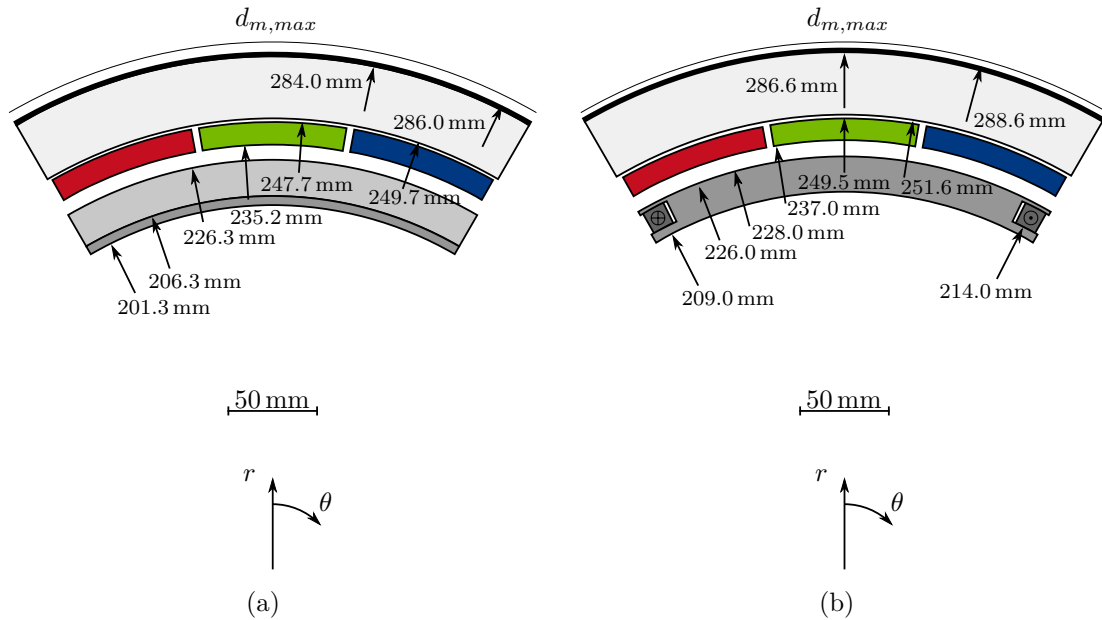


Figure 6.17.: Cross section to scale of one magnetic machine pole for the design proposals given in Table 6.11 and 6.12:

(a) MgB_2 stator coils and Halbach rotor array.

(b) MgB_2 stator coils and HTS rotor coils.

The radial distance is indicated by arrows.

Table 6.11.: Main input parameters of the proposed machine designs.

Symbol	Halbach array	HTS coil	Unit	Explanation
P	21.6	21.6	MW	Mechanical power
M	58.9	58.9	kNm	Torque
n	3500	3500	min ⁻¹	Rotational speed
m	3	3	–	Number of phases
p	3	3	–	Number of pole pairs
f_{el}	175	175	Hz	Electric frequency
$r_{r,i}$	206.3	214.0	mm	Inner radius of rotor
d_{mag}	20	12	mm	Thickness of rotor coil/magnet
$d_{s,c}$	12.5	12.5	mm	Thickness of the stator coil
α_0	95	95	%	Coverage of stator coil
α_1	100	–	%	Coverage of rotor surface
α_2	–	79	deg	Inner angle of rotor coil
α_3	–	1.3	deg	Adjacent coil angle of rotor coil
$I_{n,s}$	0.7	0.7	–	Normalized current of stator coil
J_r	–	300	A mm ⁻²	Current density of rotor coil
B_{rem}	1.44	–	T	Remanence flux density of magnet
f_{csr}	1/3	1/3	–	Coil support ratio
$B_{y,max}$	2.1	2.1	T	Maximum flux density of iron yoke
θ_{load}	90	90	deg	Load angle of the machine
n_{max}	59	59	–	Maximum harmonic

component of the fundamental wave of the flux density $B_{rot,r,1}$ generated by the rotor at outer rotor radius is very low with about 0.5 T for the Halbach variant and 0.71 T for the HTS coil variant. This can be explained by the fact that the AC loss of the MgB₂ multifilament wire is influenced stronger by the flux density than by its transport current. As a result, efficient machines are generally achievable at high stator current density and low rotor flux density as well as electrical frequency. The stator current density J_{wp} is therefore in the same range with 261.1 A mm⁻² and 236.1 A mm⁻² for the Halbach variant and HTS coil variant, respectively. Moreover, a large share of the working point flux density B_{wp} is generated by the stator.

The maximum magnetic field in permanent magnets generated by the stator coils previous to quenching $H_{s,mag}$, which is calculated at a normalized stator current of 1, is 758.6 kA m⁻¹ in the Halbach array and thus lower than the coercive field $H_{co,B}$ of 1115 kA m⁻¹ at a temperature of 20°C which avoids demagnetization [228]. However, eddy current loss in the permanent magnets can lead to heating of these if not sufficiently cooled, thus enabling demagnetization. Therefore, demagnetization, AC loss and cooling of the permanent magnet material as well as the quench behavior of the superconducting coils have to be studied in further investigations.

Due to the limited remanence flux density of NdFeB and the complete covering of the rotor, a large amount of magnetic material is required, which results in a higher

active mass m_a with 771.6 kg for the Halbach machine compared to the HTS coil machine with 496.7 kg. This also leads to a higher target price P_r for the active material in the rotor with 32.8 k€ in comparison to an excitation with HTS coils and 17.7 k€. However, the cooling effort has to be considered for a total cost evaluation. The MgB₂ stator coils are much cheaper with 8.6 k€ and 7.9 k€. Furthermore, the active mass of both machines is much larger than the passive mass m_p with 142.0 kg and 185.5 kg due to the low pole pair number and thus thick yoke with about 35 mm. It should be noted that, current leads and mechanical support are not considered in this study. The bending radii of the stator coils are 114.3 mm and 115.2 mm, which is above the pessimistic limit of 80 mm.

Figure 6.18 finally shows the stator AC loss $P_{v,s}$ for the respective flight mission phase of a single engine. The influence of the control strategy for the machine with HTS rotor coils is clearly visible. At take-off in nominal point of the machine, its stator AC loss is higher compared to the machine with Halbach array at 6.94 kW and 4.79 kW, each. The cruise requires a reduced power of 9.6 MW, which corresponds to 44.4% of the maximum power. In this mission phase the HTS coil variant already reaches lower stator AC loss of about 3.25 kW compared to the Halbach variant with 4.01 kW in this example. This corresponds to a stator AC loss reduction of

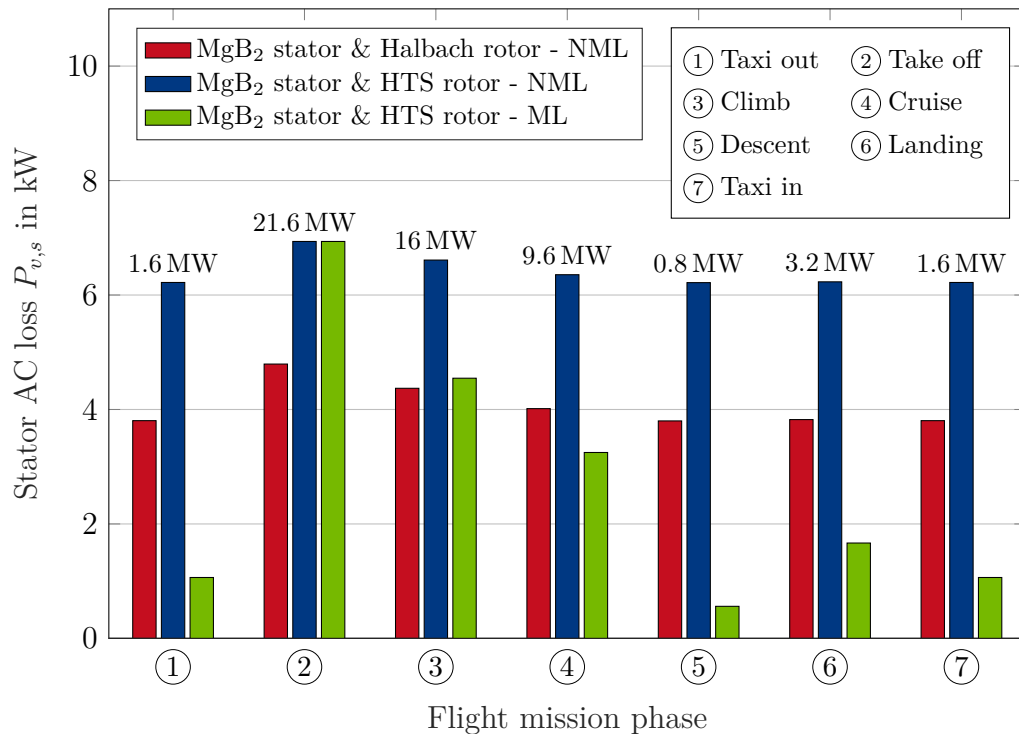


Figure 6.18.: Stator AC loss $P_{v,s}$ as a function of the flight mission phase according to Table 6.3. The required power P for a single engine is shown on the bars. Minimized (ML) and non-minimized (NML) stator AC loss are shown for machine architectures based on MgB₂ stator coils and HTS rotor coils as well as Halbach rotor array, respectively, and given as design proposals in Table 6.11 and 6.12.

Table 6.12.: Main output parameters of the proposed machine designs.

Symbol	Halbach array	HTS coil	Unit	Explanation
d_{air}	8.9	11.0	mm	Thickness of magnetic air gap
d_{c2y}	2.0	2.1	mm	Coil-to-yoke distance
d_y	34.3	35.0	mm	Thickness of yoke
J_{wp}	261.1	236.1	$A\text{ mm}^{-2}$	Working point current density
B_{wp}	0.76	0.87	T	Working point flux density
$B_{rot,r,1}$	0.50	0.71	T	Radial component of fundamental wave of magnetic flux density by rotor at outer rotor radius
$H_{s,mag}$	758.6	—	$kA\text{ m}^{-1}$	Maximum magnetic field previous to quenching by stator in magnets
d_m	571.9	577.1	mm	Diameter of machine
l_{eff}	1045.7	875.5	mm	Effective length of machine
l_m	1275.4	1106.9	mm	Length of machine
$r_{s,b}$	114.3	115.2	mm	Bending radius of stator coil
$r_{r,b}$	—	97.6	mm	Bending radius of rotor coil
m_a	771.6	496.7	kg	Active mass
m_p	142.0	185.5	kg	Passive mass
m_t	207.6	207.6	kg	Tank mass
PTW	23.6	31.7	$kW\text{ kg}^{-1}$	Power-to-weight ratio
TTW	64.5	86.4	$Nm\text{ kg}^{-1}$	Torque-to-weight ratio
$P_{s,v}$	4.79	6.94	kW	AC loss of stator coils at nominal point
$P_{v,fe}$	9.33	8.03	kW	Iron loss
η	99.935	99.931	%	Efficiency
\dot{M}_s	14.5	21.0	$g\text{ s}^{-1}$	Mass flow of LH_2 in stator at nominal point
$T_{s,max}$	21.1	21.2	K	Maximum temperature stator coils
$t_{f,max}$	459	609	min	Maximum flight time
P_s	8.6	7.9	k€	Target price of stator coils
P_r	32.8	17.7	k€	Target price of rotor coils/magnets
n_s	772	778	—	Single conductors per stator coil
$L_{s,t}$	1.91	1.58	μH	Self-inductance per turn of stator coil
$U_{i,t,1}$	113.6	96.7	V	Induced voltage of fundamental wave per turn of stator coil

53.2% compared to the nominal point. In general, machines with controlled HTS rotor coils are more efficient in this flight phase if identical maximum flight times are compared. Moreover, in the taxi, descent and landing phase the HTS coil ma-

chine is more efficient than the Halbach machine. This leads to the conclusion that the HTS coil machine with optimized control strategy has advantages for long-haul flights and the Halbach machine is more suitable for short-haul flights.

The power-to-weight ratio PTW of the machine is 23.6 kW kg^{-1} for the Halbach variant and 31.7 kW kg^{-1} for the HTS coil variant. Including the mass of the liquid hydrogen tank, the power-to-weight ratio is reduced to 21.2 kW kg^{-1} and 27.5 kW kg^{-1} , respectively. The target power-to-weight ratio defined in section 1.2 of around 7 kW kg^{-1} related to a conventional engine for an Airbus A320neo is thus exceeded by a factor of 3 for the Halbach variant and 4 for the HTS coil variant. That completes the design example on the hybrid-electric Airbus A321neo-LR and is followed by a summary, conclusion and outlook in the final chapter.

7. Summary, Conclusion and Outlook

The rapid increase of passengers in civil aviation led to rising CO₂ emissions, even taking into account technical advances. This requires new technical and environmentally friendly solutions. One promising approach for the future is to replace the conventional engines with a cryogenic hybrid-electric propulsion system. This reduces the emissions due to the decoupled optimization of electric propulsion unit and power generation unit, which allows the engine to be operated with optimized fossil fuel consumption. Moreover, stored liquid hydrogen is used to cool the electric components and burned afterwards as a mixture of jet fuel and gaseous hydrogen. With this approach, the refrigeration system adds no additional weight to the propulsion system. However, significant improvements in the power-to-weight ratio and the efficiency of all components of the electric propulsion system are required in order to achieve a higher overall efficiency compared to the conventional propulsion system.

The key enabling technology for lightweight electric machines is superconductivity. Superconductors have a high current carrying capacity and a negligible DC resistance. However, alternating fields and currents in electric machines generate AC loss, which heats up the superconductor and thus reduces its current carrying capacity. This effect is taken into account by the development and combination of several multiphysical models in the design of the machine as an innovation in this thesis, starting with the superconductor characteristics up to the consideration of aircraft requirements and flight mission.

Round superconductors are more suitable for alternating field applications compared to coated superconductors due to their thin filaments and twisted structure. Here, multifilament MgB₂ wires are investigated and characterized in terms of its critical current depending on the temperature and magnetic flux density as basis of the machine design. Using this measurements, the total AC loss of a MgB₂ wire with 114 filaments is calculated, taking into account the different loss mechanisms. Due to the alternating fields in electric machines a model is required to determine the AC loss in dependence of the transport current and the frequency as well as the flux density of an external field. The magnetization loss is calculated by the finite element method and integrated into the analytical loss computation, which further consists of coupling-current loss and eddy current loss. It is concluded that the coupling currents account for a major amount of the total AC loss, which is strongly dependent on frequency and flux density and less on the transport current.

A coupled electro-thermal model has been developed to consider the influence of the AC loss on the temperature of the wire. The MgB₂ wire is assumed to be cooled by a two-phase flow of liquid hydrogen and is arranged as a one-side cooled coil. It has been shown that the current density, which is related to the wire cross-section and cooling area, is up to 18 times higher compared to a copper litz wire at a hot spot temperature of 180°C cooled with a synthetic oil. Compared to the 114 filament MgB₂ wire, the copper litz wire is limited to a current density of 28.5 A mm⁻² and is less sensitive to the frequency and flux density of an external field due to the mainly ohmic loss. The engineering current density of this MgB₂ wire is highly dependent

on the thickness of its insulation, as this impedes heat dissipation. However, a comparison between MgB_2 and Cu wire at an external flux density of 1 T and frequency of 500 Hz shows that with 140.3 A mm^{-2} and 17.2 A mm^{-2} , respectively, the engineering current density is increased by approximately a factor of 8. This difference impacts directly on the torque density of a machine while aiming for low AC loss. Due to the high sensitivity of AC loss to alternating magnetic fields it is essential to calculate the field distribution in the machine design exactly, in order to determine the working point of the stator coils and its total AC loss. Therefore, a two-dimensional analytical model based on Laplace and Poisson equations is implemented to calculate the total flux density, which is generated by the stator coils and different possibilities of rotor excitation. These are permanent magnets, Halbach array, HTS bulks as well as HTS coils. Compared with FEM simulations, the analytical model shows an appropriate degree of accuracy. Furthermore, partially and fully superconducting machines are designed, based on Cu or MgB_2 stator coils. The thickness of the magnetic air gap between rotor excitation and stator coils influences the performance of the electric machine significantly. For this reason, components which depend on the topology, such as sleeve and cryo wall, are designed under consideration of thermal and mechanical aspects.

The fundamental design process of superconducting machines for a hybrid-electric propulsion system can be summarized into the following phases: characterization of the superconductor, computation of the electro-thermal behavior, machine design of the nominal point for a selection of input parameters and choice of a machine taking into account aircraft dependent boundary conditions as well as the flight mission. The stator AC loss can be further reduced for machines with rotor coils in the part-load range. This is obtained through an optimized control strategy of rotor and stator current compared to off-design points with constant excitement. Moreover, this control strategy increases the maximum flight time of the aircraft, if limited by the coolant.

To study the different machine topologies, an Airbus A321neo-LR is hybridized taking into account aircraft-specific requirements such as the installation space. The core engine is replaced by a 21.6 MW superconducting machine which directly propels the fan at a rotational speed of 3500 min^{-1} . Additionally, a hydrogen tank is designed, which is integrated into the fuselage. It is shown that partially superconducting machines based on continuous HTS bulks reach a maximum power-to-weight ratio of 19.9 kW kg^{-1} . Partially superconducting machines based on HTS coils achieve a maximum power-to-weight ratio of 20.6 kW kg^{-1} . A drawback is the stator loss of the Cu coils with minimum 639 kW for the HTS coil variant, being a factor of more than 160 higher compared to the most efficient MgB_2 coils. This requires an additional heat exchanger which is disadvantageous due to its additional mass and energy consumption. In comparison, the machine consisting of MgB_2 stator coils and Halbach rotor array generates a minimal AC loss of 3.9 kW while achieving a power-to-weight ratio of 13.2 kW kg^{-1} .

The fully superconducting machine based on MgB_2 stator coils and HTS bulk rotor achieves a maximum power-to-weight ratio of 52.8 kW kg^{-1} . This is lower compared to the machines consisting of MgB_2 stator coils and HTS rotor coils with a maximum power-to-weight ratio of 56.8 kW kg^{-1} . This architecture achieves a minimal AC loss

of approximately 6.4 kW at a power-to-weight ratio of 17.5 kW kg⁻¹.

Two machines are proposed for a more detailed design in the future. Firstly, the partially superconducting machine with MgB₂ stator coils and Halbach rotor array is presented due to their best in class stator AC loss. Furthermore, this topology features a simple mechanical design of the rotor, which operates at ambient temperature. Secondly, the fully superconducting machine with MgB₂ stator coils and HTS rotor coils is proposed, which obtains even longer flight times due to an optimized control strategy. While this machine architecture is the lightest, but also the one with the highest engineering and manufacturing effort. However, both architectures achieve a maximum flight time of about 600 min with a 280 kg hydrogen tank for both machines and the flight time is not limited by the amount of coolant in this design.

This concept maximally saves about 8.7 tons of CO₂ emissions per flight by using 1120 kg gaseous hydrogen as fuel and if it is assumed that the hybridization of the propulsion system has no effect on the total empty mass of the aircraft. However, due to seven times higher reaction rate of hydrogen compared to jet fuel, the combustor concept of the gas turbine has to be modified so that NO_x emissions are not as high as those of pure jet fuel [247].

In this thesis, it is shown that low AC losses at high power-to-weight ratios are realized in a machine design based on multifilament MgB₂ wires and magnetic fields less than 2 T. Consequently, it is concluded that material development should focus on improving the AC loss and bending properties of superconducting wires rather than achieving of extreme current carrying capacity for high magnetic fields by the rotor. [142]

Power and rotational speed are free parameters in the machine model and the design of machines for other applications such as ship propulsion and wind power are also supported [76].

In the future, the machine design has to be integrated into the aircraft design. Especially a coupling with a model of the fan promises optimization potential, because in this way the trade-off between rotational speed and diameter of both components can be solved. The machine characteristic can already be described, starting from the actual speed of 3500 min⁻¹. With increasing rotational speed, the power-to-weight ratio increases further but with a decreasing growth per speed increment. Furthermore, the maximum power-to-weight ratio moves to lower number of pole pairs because the rising mechanical frequency is thus compensated. This effect will have a maximum due to the increasing thickness of the yoke and subsequently lead to a decrease of the power-to-weight ratio. Accordingly, the conclusion is that also a gearbox should also be considered in such a system design.

Further potential for improvement exists in the electromagnetic design, which is discussed in the next section.

7.1. Extension Options for Machine Design

The extension options are intended for the electromagnetic design in Chapter 4 and describe the potential for improvements through a higher level of detail. It is feasible to transfer the entire AC loss calculation to FEM, which is described in Section 7.1.1, as well as to extend the analytical model to a multi shell stator coil, as presented in Section 7.1.2.

7.1.1. Stator Coils with Multifilament Coated Superconductor

In addition to MgB_2 multifilament wires, coated superconductors are also promising as stator coils in AC machines. The critical temperature and current density of HTS tapes is in general higher than with MgB_2 multifilament wires, making even higher power-to-weight ratios possible. However, these tapes generate significantly higher AC loss compared to MgB_2 , which would make hydrogen cooling on a flight mission less economical [84, 248, 249]. This loss could be greatly reduced by filamentation of the superconducting layer [250]. The general design of such partially and fully super-

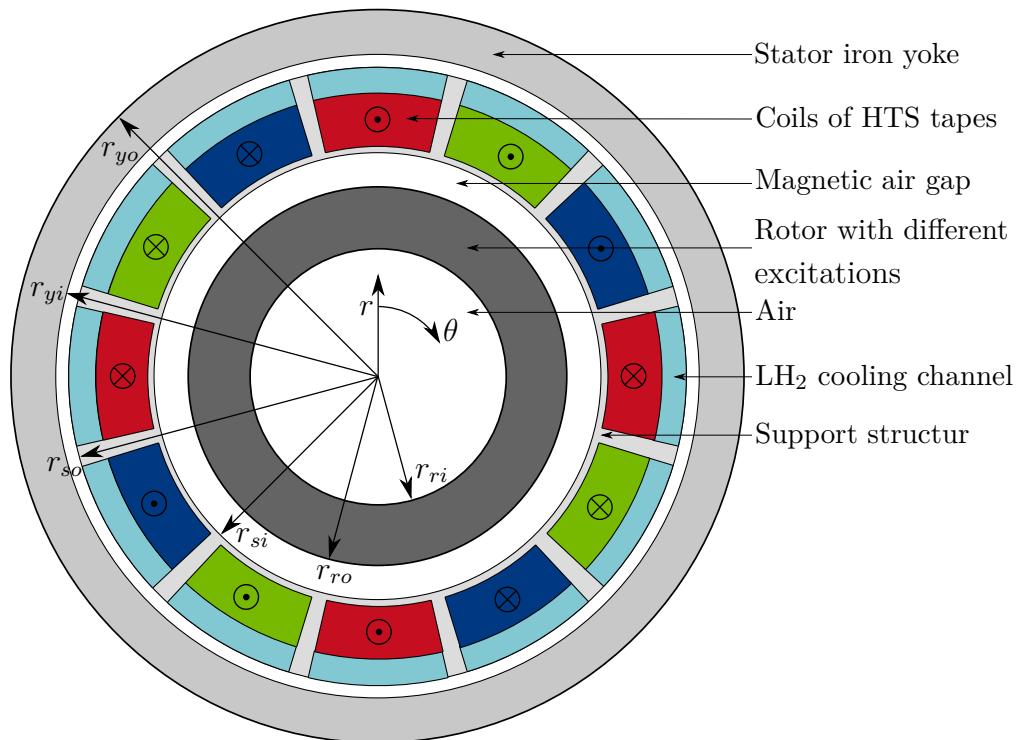


Figure 7.1.: Superconducting machine model with cold stator air gap windings made of HTS tapes and variable rotor excitation, as presented in Figure 4.8. Each coil leg is fixed by a support structure and is cooled by LH_2 through a channel between the coil and the yoke.

conducting machines has been discussed and pre-designed in [84]. There is currently no possibility to calculate the magnetization loss with sufficient accuracy using an analytical approach due to its angle dependence. Consequently, this loss component is computed by FEM. The T-A formulation allows the AC loss of entire coils to be calculated in more reasonable time compared to MgB_2 coils [251, 252, 253, 254].

By coupling of an analytical machine model with FEM software, the heating of the superconducting coil by its AC loss can be considered in the design similar to the approach in this thesis. However, this formulation can only be applied for flat conductors and is therefore not feasible for round MgB_2 wires.

Figure 7.1 presents the general machine model consisting of coils made of HTS tapes. The LH_2 cooling channels are located between the coil leg and the stator yoke, which is separated from the cryogenic area by a cryo wall.

Advantages are expected in a less critical bending radius compared to MgB_2 multifilament wires. As a result, machines with smaller diameters and power can also be realized. The speed of such a model will be much lower compared to the model in this thesis. Therefore, no large parameter studies can be realized.

7.1.2. Multi Shell Stator Coils

The analytical approach for the calculation of the electro-magnetic fields from Section 4.5 allows the separation of the stator coils presented in Figure 4.2. This enables to differentiate between cooling channel, support structure and coil, as shown in Figure 7.2. Consequently, the electro-magnetic fields are calculated more precisely and the winding heads are modeled more accurate. Due to the increasing number of shells from 6 to 12 compared with the approach in Chapter 4, the computational effort increases strongly. Thus, this approach should be used after the first parameter studies with the model of this thesis.

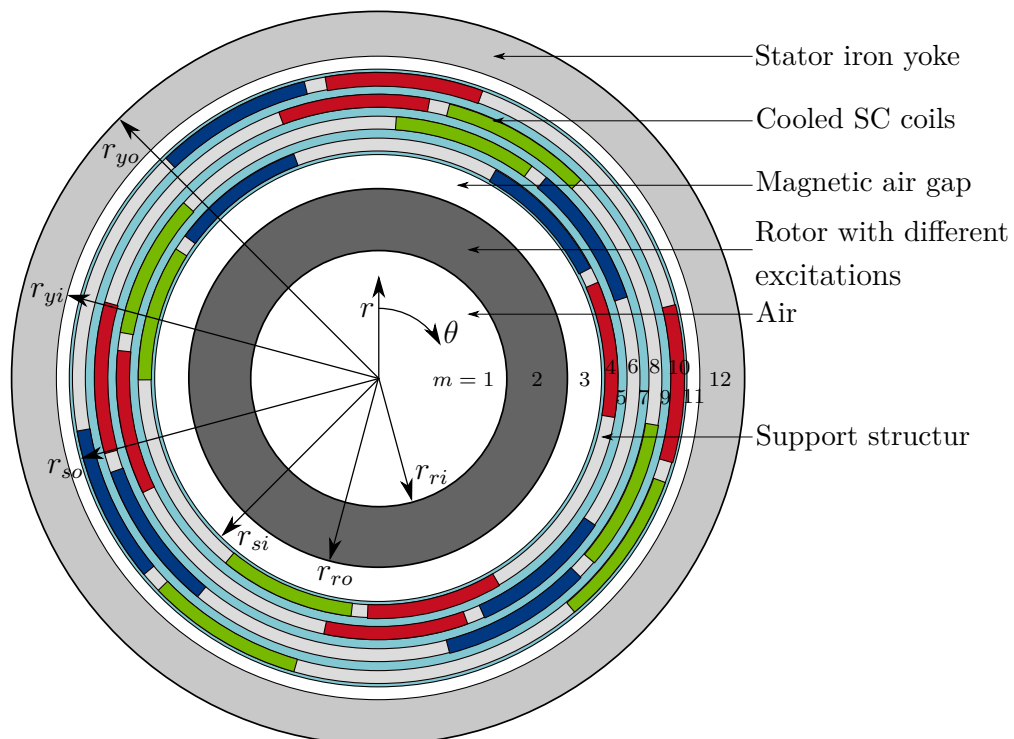


Figure 7.2.: Superconducting machine model with cold flat stator air gap windings and variable rotor excitation, as presented in Figure 4.8. The regions correspond to the parameter m in Section 4.5.

7.2. Next Steps

As a result of the investigations in this thesis it can be noted that superconducting AC machines are particularly suitable for cryogenic hybrid-electric propulsion systems. The focus of this work is to investigate the feasibility of partially and fully superconducting AC machines with different excitations and to integrate the influence of the AC loss generated by the superconductor into the machine design. These machines support low mass and a much higher power-to-weight ratio compared to conventional normal conducting machines. Furthermore, the stator AC loss can be reduced by multifilament MgB_2 wires, such that cooling during several flight hours with a few hundred kilogram of hydrogen is enabled for an aircraft with 244 seats. However, more work needs to be done to realize a first machine demonstrator based on MgB_2 wires in this power range and the results of this thesis could serve as a basis for such development.

An intermediate step could be the manufacturing of a MgB_2 coil which includes the investigation of winding techniques and the integration into the coil support structure. This requires thermal, electrical and mechanical tests under the effect of external magnetic fields and cryogenic temperatures while using hydrogen cooling. In this step, the AC loss of the stator coil as well as the heat transfer of the two-phase cooling should be verified. Furthermore, the cryostats have to be designed in detail and manufactured. In order to evaluate the availability and reliability of such machines, the quench and short-circuit behavior have to be analyzed. A further point is the machine optimization within the system design. Among other things, this includes the investigation of influences by the converter and the choice of a DC-link voltage.

Appendix

A. Temperature Distribution by Thermal Conduction

Differential equations are solved for the calculation of the one-dimensional temperature distribution by thermal conduction in Section 3.4. The coefficients for the general solutions are summarized for Cartesian and polar coordinates in the following sections.

A.1. Cartesian Coordinate System

The coefficients $C_{n,1}$ and $C_{n,2}$ are given for a Cartesian coordinate system and the general solution in Equation 3.34 by Equation A.1 and A.2 for the currently considered stage n . Figure A.1 shows the minimal sketch with several stages and the respective heat flux \dot{q} , thermal conductivity λ and volumetric mass density ρ . The transition to the cooling medium is characterized by the wall temperature T_w , the fluid temperature T_{fl} and the heat transfer coefficient α_w . Furthermore, the total number of stages is defined by the parameter n_{max} .

$$C_{n,1} = \begin{cases} \frac{\alpha}{\lambda_n} (T_{fl} - T_{w_n}) + \frac{\dot{q}_n}{\lambda_n} x_n & \text{if } n = n_{max} \\ \frac{\lambda_{n+1}}{\lambda_n} \left(C_{n+1,1} - \frac{\dot{q}_{n+1}}{\lambda_{n+1}} x_n \right) + \frac{\dot{q}_n}{\lambda_n} x_n & \text{if } 1 < n < n_{max} \\ 0 & \text{if } n = 1 \end{cases} \quad (\text{A.1})$$

$$C_{n,2} = \begin{cases} T_{w_n} - C_{n,1} x_n + \frac{\dot{q}_n}{2 \lambda_n} x_n^2 & \text{if } n = n_{max} \\ C_{n+1,1} x_n + C_{n+1,2} - \frac{\dot{q}_{n+1}}{2 \lambda_{n+1}} x_n^2 - C_{n,1} x_n + \frac{\dot{q}_n}{2 \lambda_n} x_n^2 & \text{if } 1 < n < n_{max} \\ C_{n+1,1} x_1 + C_{n+1,2} - \frac{\dot{q}_{n+1}}{2 \lambda_{n+1}} x_1^2 + \frac{\dot{q}_n}{2 \lambda_n} x_1^2 & \text{if } n = 1 \end{cases} \quad (\text{A.2})$$

A.2. Polar Coordinate System

In the same way, the coefficients for a polar coordinate system and the general solution in Equation 3.40 are given in Equation A.3 and A.4.

$$C_{n,1} = \begin{cases} \frac{\alpha}{\lambda_n} (T_{fl} - T_{w_n}) r_n + \frac{\dot{q}_n}{2 \lambda_n} r_n^2 & \text{if } n = n_{max} \\ \frac{\lambda_{n+1}}{\lambda_n} \left(\frac{C_{n+1,1}}{r_n} - \frac{\dot{q}_{n+1}}{2 \lambda_{n+1}} r_n \right) r_n + \frac{\dot{q}_n}{2 \lambda_n} r_n^2 & \text{if } 1 < n < n_{max} \\ 0 & \text{if } n = 1 \end{cases} \quad (\text{A.3})$$

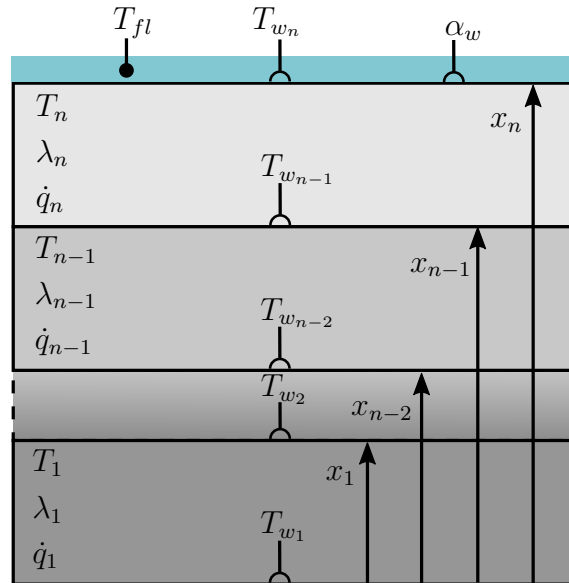


Figure A.1.: Minimal sketch for heat conduction calculation in a Cartesian coordinate system.

$$C_{n,2} = \begin{cases} T_{w_n} - C_{n,1} \ln(r_n) + \frac{\dot{q}_n}{4\lambda_n} r_n^2 & \text{if } n = s \\ \left(\frac{\dot{q}_n}{4\lambda_n} - \frac{\dot{q}_{n+1}}{4\lambda_{n+1}} \right) r_n^2 + (C_{n+1,1} - C_{n,1}) \ln(r_n) + C_{n+1,2} & \text{if } 1 < n < s \\ \left(\frac{\dot{q}_n}{4\lambda_n} - \frac{\dot{q}_{n+1}}{4\lambda_{n+1}} \right) r_n^2 + C_{n+1,1} \ln(r_n) + C_{n+1,2} & \text{if } n = 1 \end{cases} \quad (\text{A.4})$$

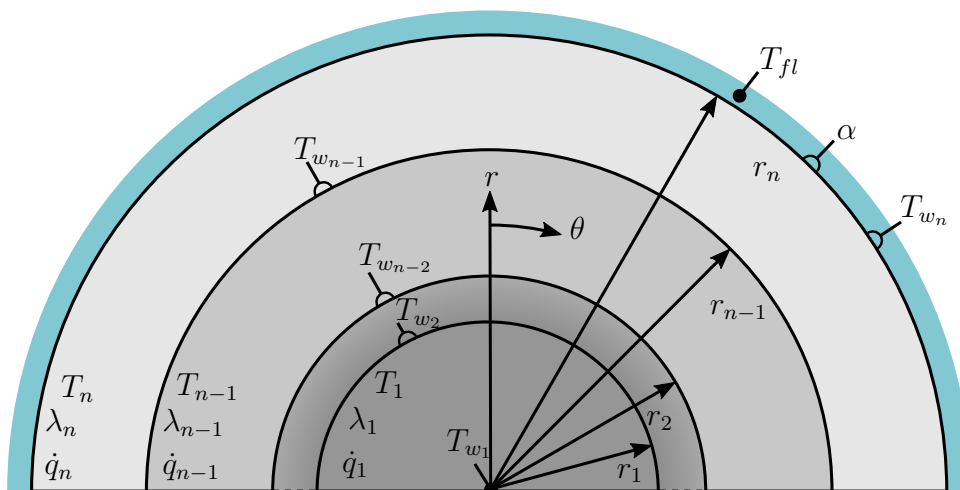


Figure A.2.: Minimal sketch for heat conduction calculation in a polar coordinate system.

B. Detailed Calculation Procedures

B.1. Electro-Thermal Model

Figure B.1 shows the flowchart of the current density calculation procedure, as presented in Chapter 3.

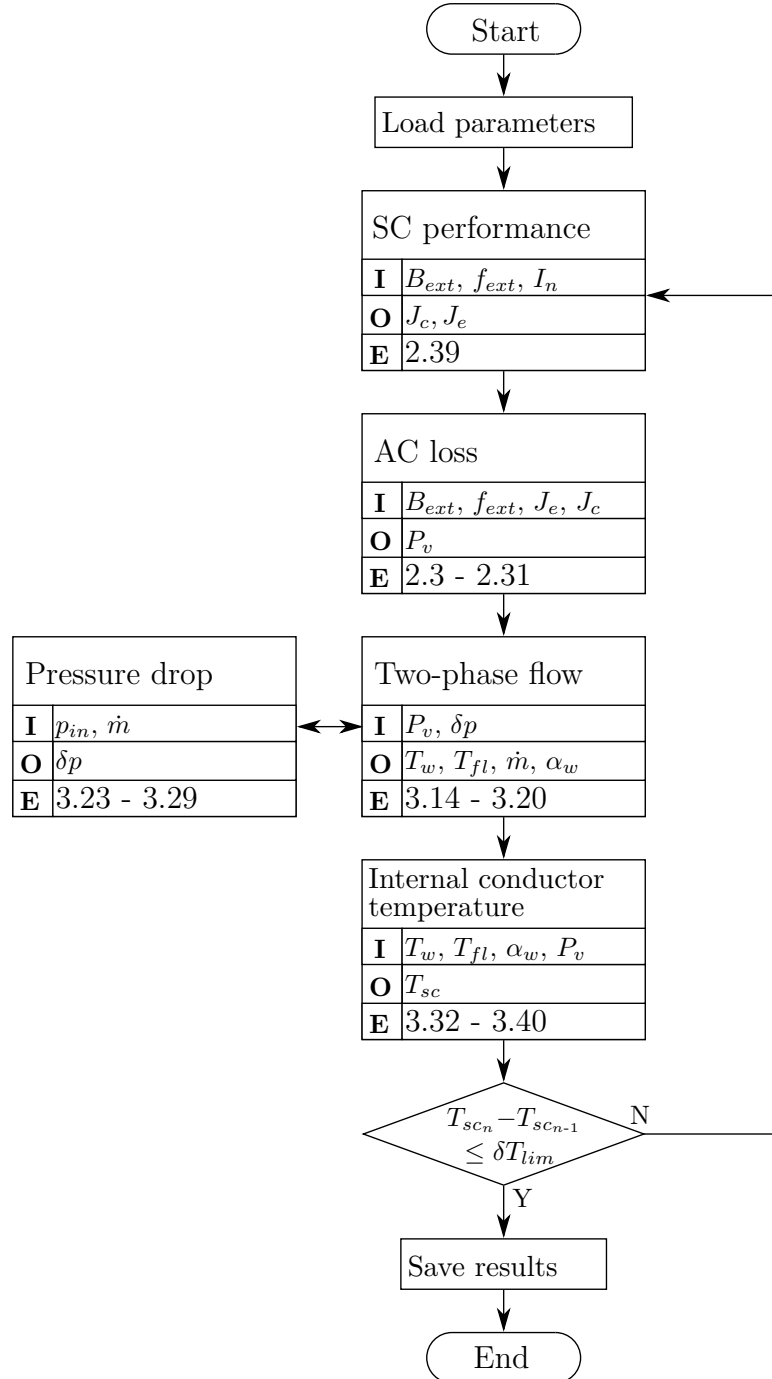


Figure B.1.: Current density calculation procedure with the input **I**, output **O** and related equation **E** of different functions as flowchart for the iteration n of the temperature of the superconductor T_{sc} .

B.2. Machine Design Model

Figure B.2 presents the flowchart of the machine design procedure, as discussed in Chapter 4.

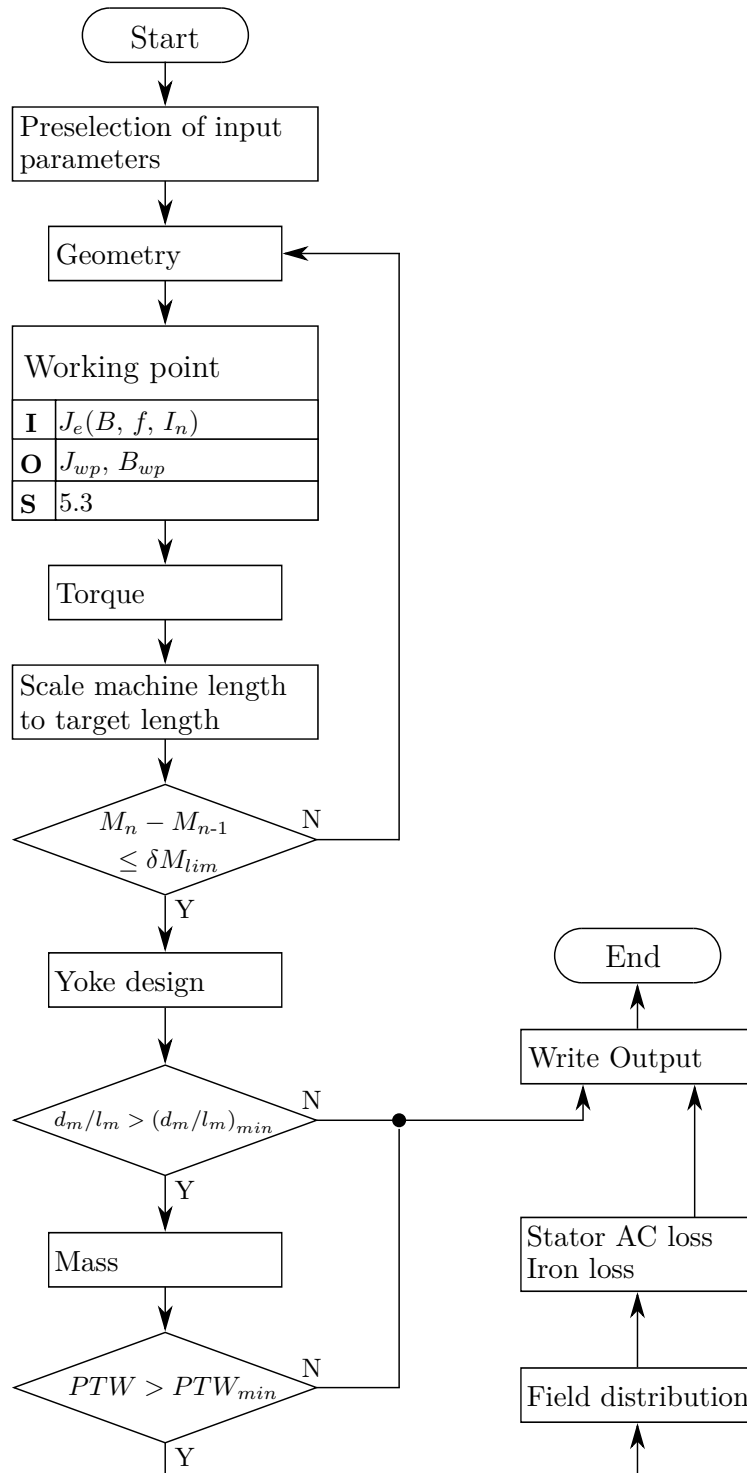


Figure B.2.: Detailed machine design procedure with the input **I**, output **O** and related equation **E** or subsequence **S** of different functions as flowchart for the iteration n of the torque M .

C. Properties of Various Materials

C.1. Magnesiumdiborid

Thermal conductivity

The thermal conductivity of magnesium diboride (MgB_2) λ_{sc} is investigated in dependence of the temperature T in $[100, 255]$ between 7.8 K and 39.0 K, as shown in Figure C.1. The linear fitting from this data results in Equation C.1 with the fit parameters given in Table C.1.

$$\lambda_{sc} = P_0 + P_1 T \quad (\text{C.1})$$

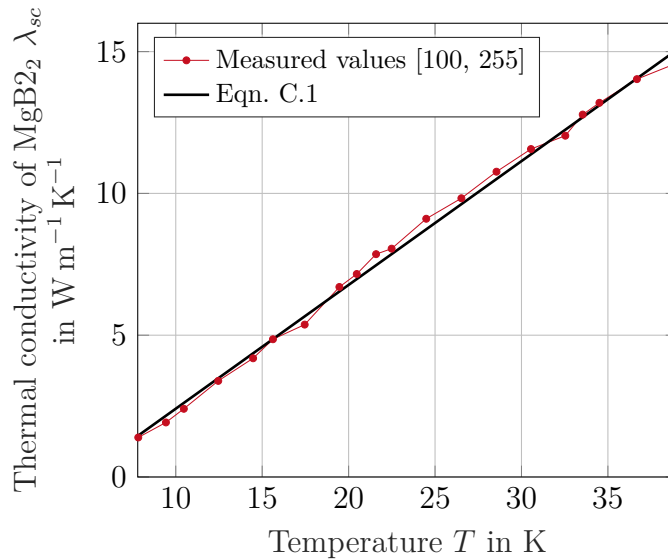


Figure C.1.: Thermal conductivity of MgB_2 λ_{sc} as a function of the temperature T .

Table C.1.: Fit parameters for the thermal conductivity of MgB_2 in Equation C.1.

Parameter	Value	Parameter	Value
P_0	-1.957	P_1	0.4365

C.2. Copper

Electrical resistivity

The electrical resistivity of copper (Cu) $\rho_{cu,1}$ is studied by [101] under consideration of the temperature T and the residual-resistance ratio RRR and is given in Equation C.2. All fit parameters from the equations below are summarized in Table C.2.

$$\rho_{cu,1}(T, RRR) = \rho_1 + \rho_2 + \rho_3 \quad (\text{C.2})$$

The summands ρ_1 , ρ_2 and ρ_3 are defined through:

$$\rho_1 = \frac{P_1 T^{P_2}}{1 + P_1 P_3 T^{P_2 - P_4} e^{-\left(\frac{P_4}{T}\right)^{P_6}}}$$

$$\rho_2 = \frac{1.553 \cdot 10^{-8}}{RRR}$$

$$\rho_3 = P_7 \frac{\rho_i \rho_0}{\rho_i + \rho_0}$$

The relationship presented in Equation C.2 can be extended by a flux density dependence

$$\rho_{cu,2}(T, RRR, B) = \rho_{cu,1} (1 + 10^a) \quad (\text{C.3})$$

with the exponent a .

$$a = \sum_{n=0}^4 a_n \left(\log \frac{P_0 B}{\rho_{cu,1}} \right)^n \quad (\text{C.4})$$

It is important to highlight, that the polynomial in Equation C.4 exhibits a minimum, if the argument of the common logarithm reaches the value 0.589. If this boundary is reached, the resistivity would increase with decreasing magnetic induction. Therefore, there is a minimum flux density $B_{min}(T)$ at which Equation C.3 begins to fail and which decreases with lower temperatures depending on RRR. The minimum flux density B_{min} at 20 K is approximately 6.3 mT and thereby not in the studied flux density range in this thesis [256].

Table C.2.: Fit parameters for the electrical resistivity of Cu in Equation C.2 and C.3.

Parameter	Value	Parameter	Value
P_0	$1.553 \cdot 10^{-8}$	P_7	0.4531
P_1	$1.171 \cdot 10^{-17}$	a_0	-2.662
P_2	4.49	a_1	0.3168
P_3	$3.841 \cdot 10^{10}$	a_2	0.6229
P_4	1.14	a_3	-0.1839
P_5	50	a_4	0.018271
P_6	6.428		

Thermal conductivity

The thermal conductivity of Cu λ_{cu} depending on the temperature T and RRR is given in Equation C.5 [101].

$$\lambda_{cu} = \frac{1}{\lambda_1 + \lambda_2 + \lambda_3} \quad (\text{C.5})$$

The parameters to calculate the following summands λ_1 , λ_2 and λ_3 are summarized in Table C.3.

$$\lambda_1 = \frac{\beta_0}{T}$$

$$\lambda_2 = \frac{P_1 T^{P_2}}{1 + P_1 P_3 T^{P_2+P_4} e^{-\left(\frac{P_5}{T}\right)^{P_6}}$$

$$\lambda_3 = P_7 \frac{\lambda_1 \lambda_2}{\lambda_1 + \lambda_2}$$

Figure C.2 presents the electrical resistivity ρ_{cu} and the thermal conductivity λ_{cu} of Cu as a function of the temperature T for Cu with a RRR of 1000. The magnetic flux density varies between 0 T and 2 T.

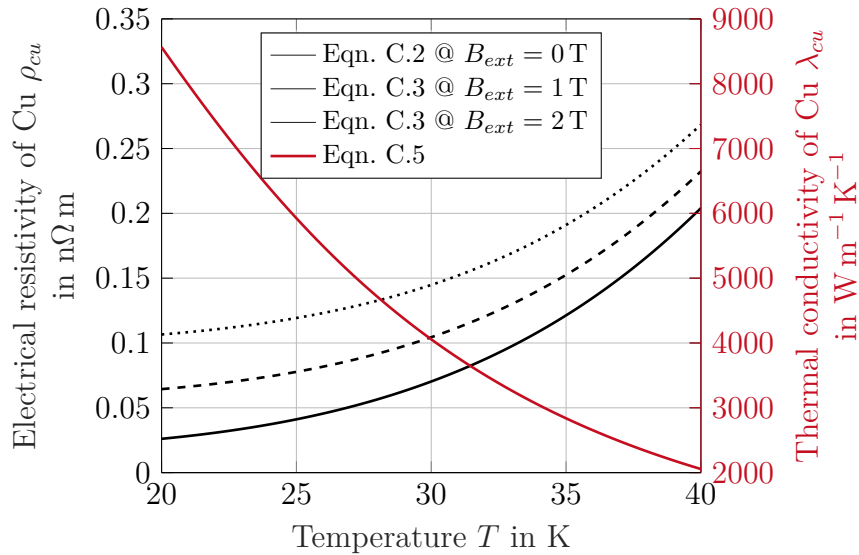


Figure C.2.: Electrical resistivity ρ_{cu} and the thermal conductivity λ_{cu} of Cu as a function of the temperature T at a RRR of 1000 and external flux densities between 0 T and 2 T.

Table C.3.: Fit parameters for the thermal conductivity of Cu in Equation C.5.

Parameter	Value	Parameter	Value
P_1	$1.754 \cdot 10^{-8}$	P_6	1.756
P_2	2.763	P_7	$0.838/\beta_2^{0.1661}$
P_3	1102	β_1	$0.634/RRR$
P_4	-0.165	β_2	$\beta_1/0.00039$
P_5	70		

C.3. Insulation Material

Thermal conductivity

The thermal conductivity of a 76 μm polyimide film λ_{ins} is given in Equation C.6 with the fit parameters in Table C.5a [152, 258].

$$\log \lambda_{ins} = P_0 + P_1 \log(T) + P_2 \log(T)^2 + P_3 \log(T)^3 + P_4 \log(T)^4 + P_5 \log(T)^5 + P_6 (\log(T))^6 + P_7 (\log(T))^7 \quad (\text{C.6})$$

Table C.4.: Fit parameters for the thermal conductivity of the insulation materials:

(a) Polyimide.

(b) Kapton.

(a) Polyimide in Equation C.6

Parameter	Value	Parameter	Value
P_0	5.73101	P_4	50.9157
P_1	-39.5199	P_5	-17.9835
P_2	79.9313	P_6	3.42413
P_3	-83.8572	P_7	-0.27133

(b) Kapton in Equation C.7

Parameter	Value	Parameter	Value
P_0	$5.24 \cdot 10^{-3}$	P_1	1.02

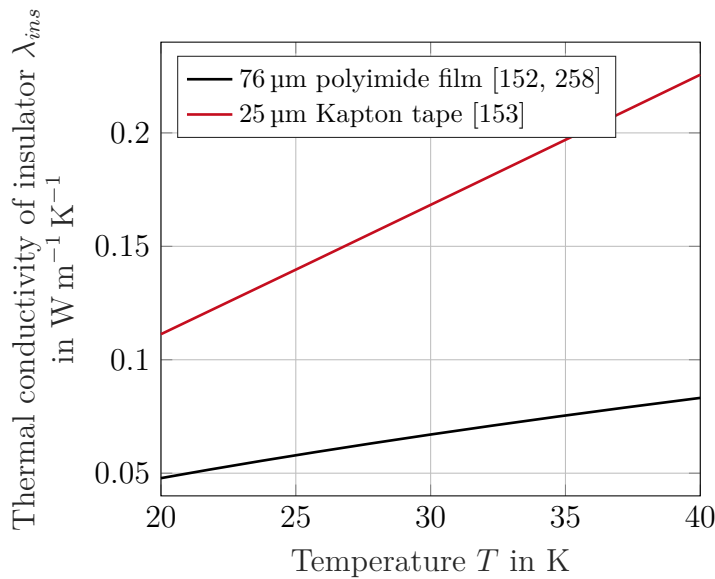


Figure C.3.: Thermal conductivity of polyimide and Kapton insulation λ_{ins} as a function of the temperature T .

Furthermore, the thermal conductivity of a 25 μm Kapton tape is given in Equation C.7 with the fit parameters in Table C.5b [153].

$$\lambda_{ins} = P_0 T^{P_1} \quad (\text{C.7})$$

In this work, the thermal conductivity of the Kapton tape according to Equation C.6 is used for the wire insulation.

C.4. Cupronickel

Electrical resistivity and thermal conductivity

Cupronickel (CuNi) alloys are divided in this work into Cu10Ni and Cu30Ni. The electrical resistivity of CuNi ρ_{cuni} is 140 n Ω m and 365 n Ω m at a temperature of 20 K for Cu10Ni and Cu30Ni, respectively [102]. The thermal conductivity of CuNi λ_{cuni} is 9.1 W m $^{-1}$ K $^{-1}$ for Cu30Ni and the thermal conductivity of Cu10Ni as a function of the temperature T is given in Figure C.4 [105, 107].

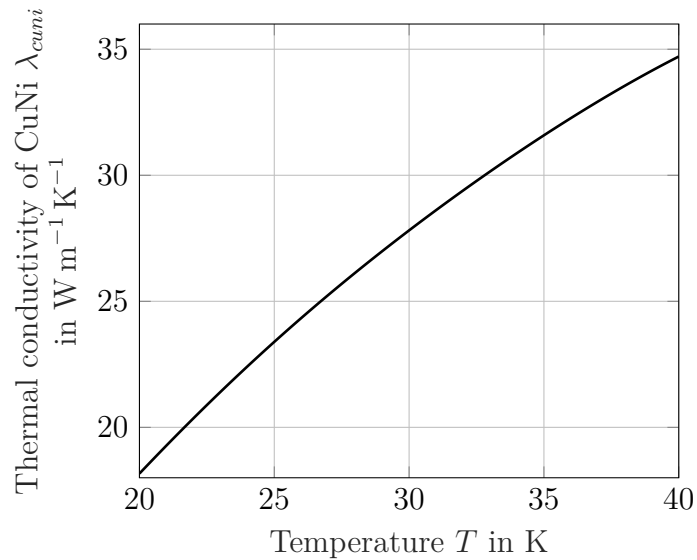


Figure C.4.: Thermal conductivity of Cu10Ni λ_{cuni} as a function of the temperature T .

C.5. Niobium

Electrical resistivity and thermal conductivity

The electrical resistivity ρ_{nb} and the thermal conductivity λ_{nb} of niobium (Nb) in dependence of the temperature T are presented in [257] and [103], respectively. Furthermore, linear interpolation is implemented to calculate values between the measuring points.

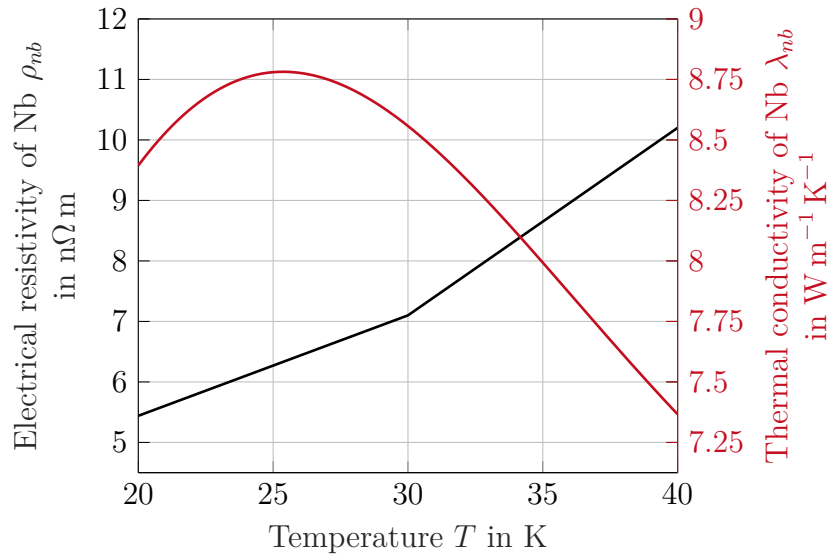


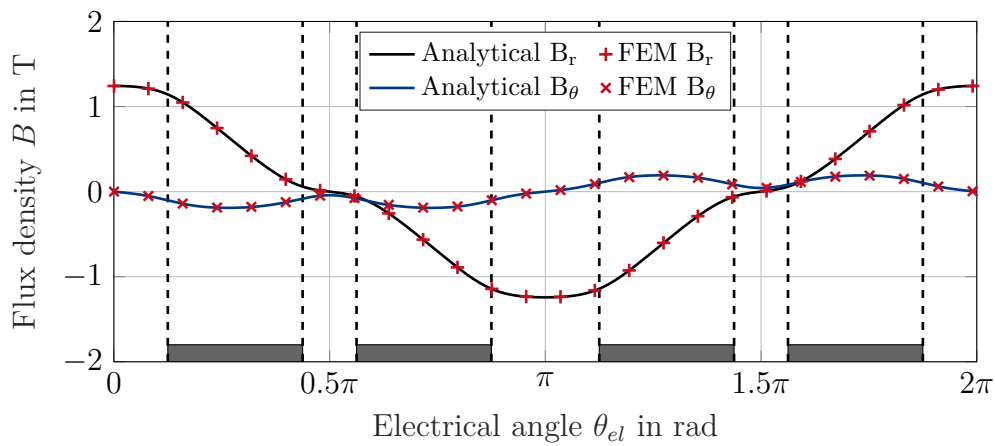
Figure C.5.: Electrical resistivity ρ_{nb} and the thermal conductivity λ_{nb} of Nb as a function of the temperature T [103, 257].

D. Magnetic Field Distributions for Validation

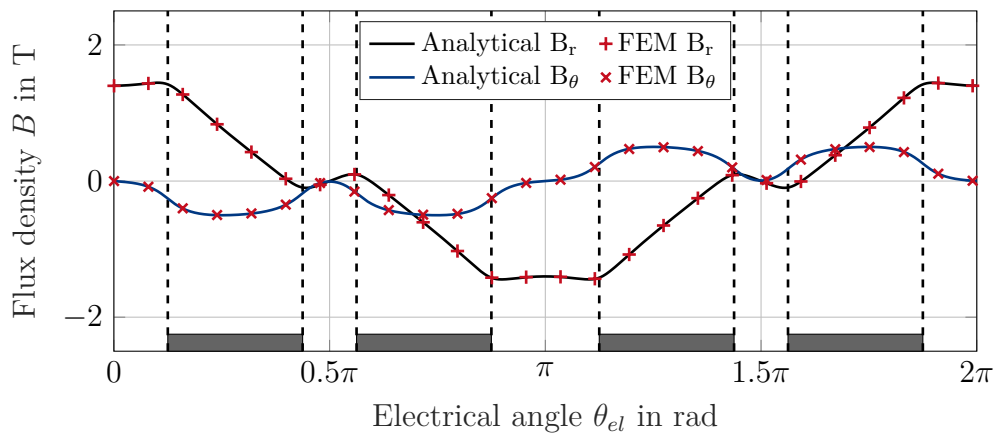
In this section, results of the validation of the analytical magnetic field distribution, which is discussed in Section 4.5.5, are summarized. The input parameters of this validation are listed Table D.1 and the field distributions are shown in Figure D.1, D.2 and D.3.

Table D.1.: Important input parameters of the electromagnetic machine model for validation.

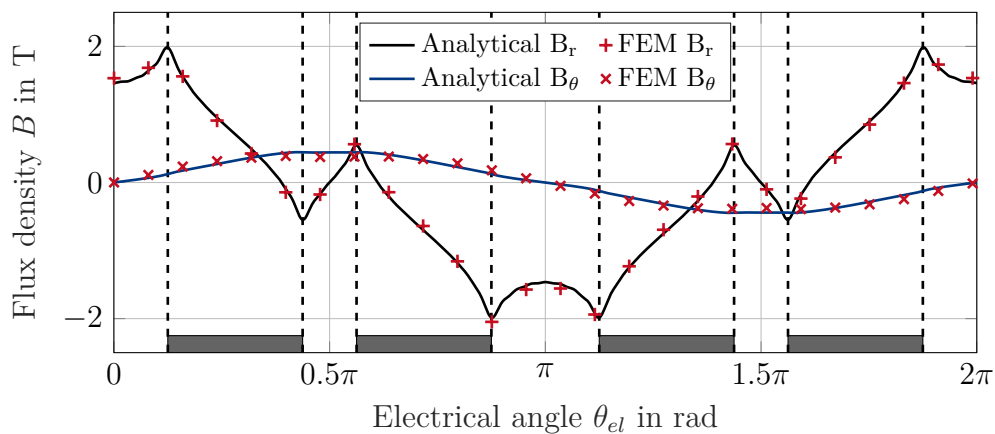
Parameter	Unit	Config. 5	Config. 6	Config. 7
Rotor	-	HTS coil	HTS bulk	PM
p	-	2	2	1
m	-	3	3	3
$r_{r,i}$	mm	150.0	150.0	150.0
$r_{r,o}$	mm	170.0	170.0	170.0
$r_{ag,m}$	mm	177.5	177.5	177.5
$r_{s,i}$	mm	185.0	185.0	185.0
$r_{s,o}$	mm	205.0	205.0	205.0
$r_{y,i}$	mm	210.0	210.0	210.0
J_s	A mm ⁻²	50	50	50
J_r	A mm ⁻²	100	-	-
B_{peak}	T	-	1.0	-
B_{rem}	T	-	-	1.44
α_0	%	95	95	95
α_1	%	-	80	60
α_2	deg	22.5	-	-
α_3	deg	11.25	-	-
n_{max}	-	59	59	59



(a) Rotor field at middle stator radius $r_{s,m}$

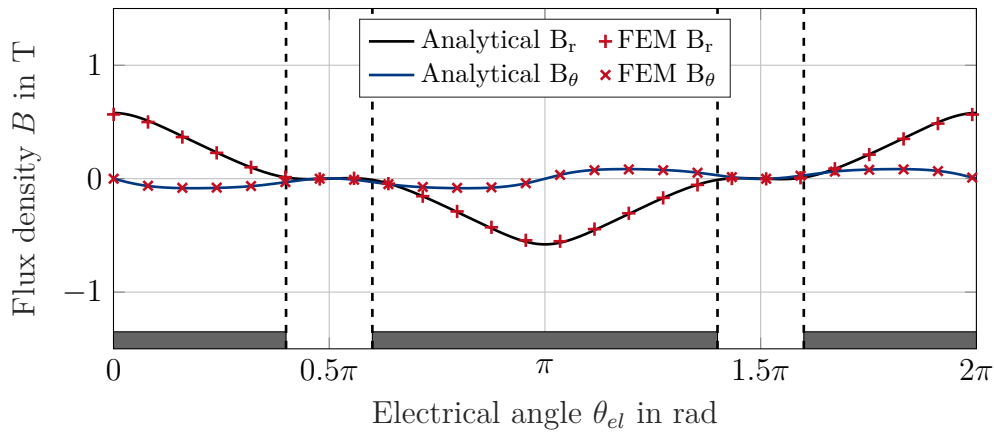


(b) Rotor field at middle air gap radius $r_{ag,m}$

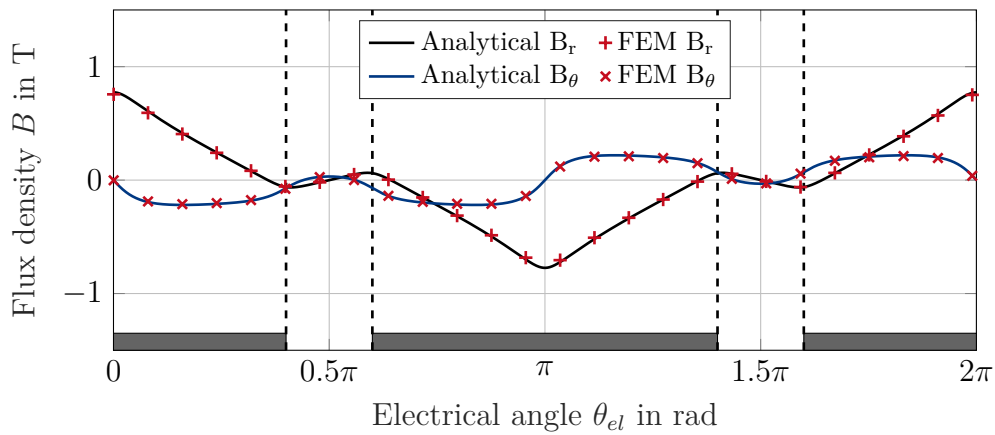


(c) Rotor field at middle rotor radius $r_{r,m}$

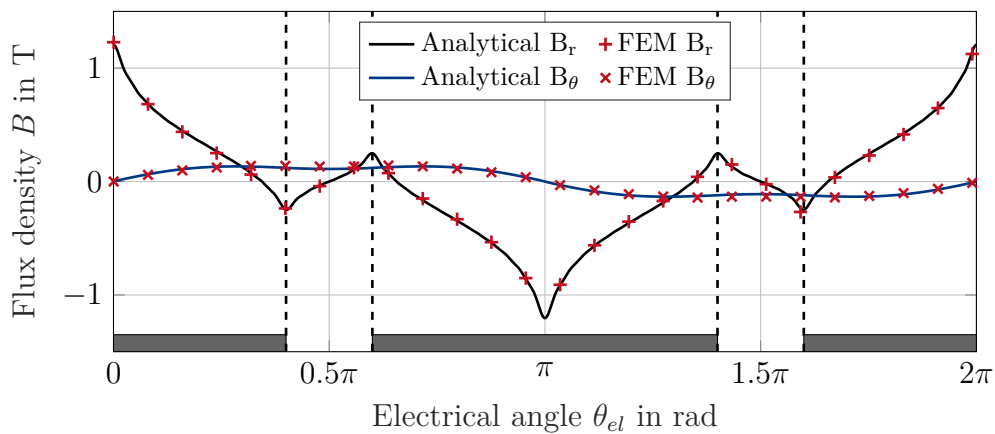
Figure D.1.: Validation of the analytical machine model according to **config. 5** in Table D.1 through a comparison with FEM over the radial and tangential flux density B_r and B_θ at different radii **with** exception np equals **2**. Coils are used as rotor excitation and the position around the circumference is marked \blacksquare .



(a) Rotor field at middle stator radius $r_{s,m}$

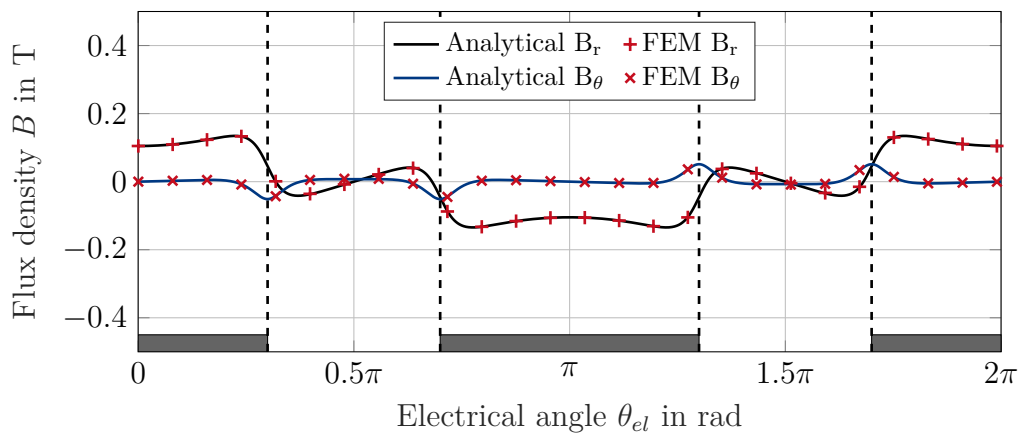


(b) Rotor field at middle air gap radius $r_{ag,m}$

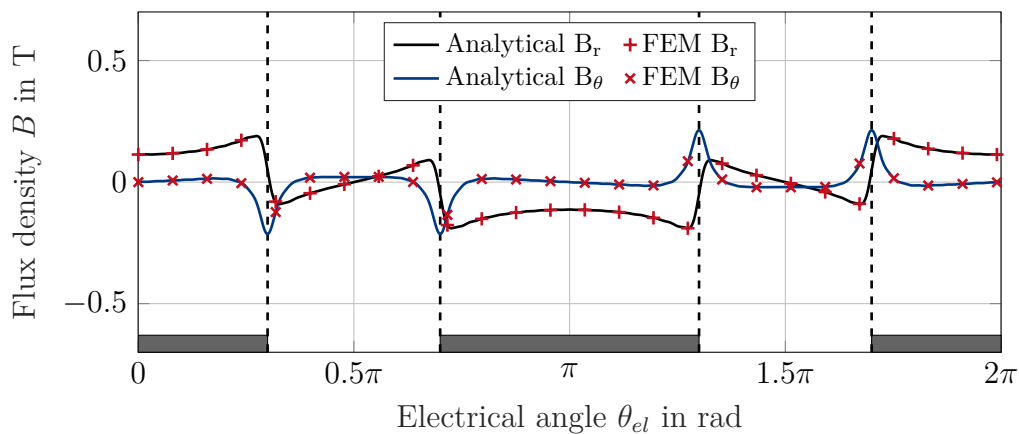


(c) Rotor field at middle rotor radius $r_{r,m}$

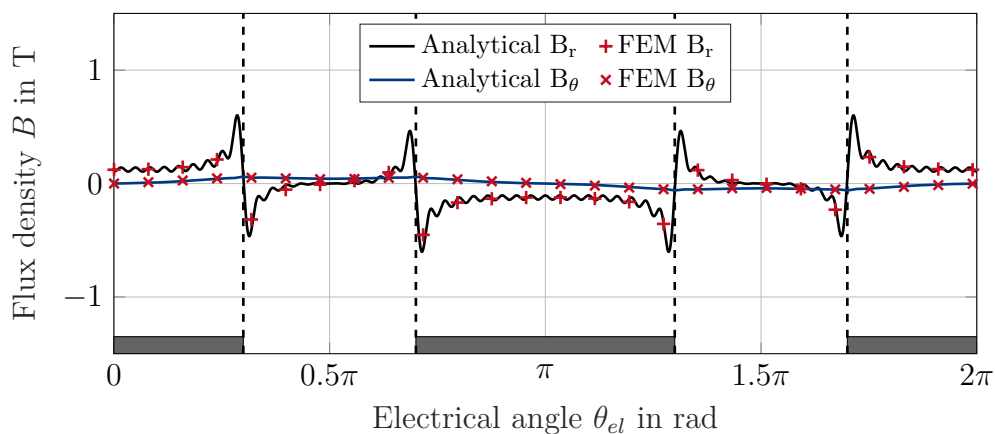
Figure D.2.: Validation of the analytical machine model according to **config. 6** in Table D.1 through a comparison with FEM over the radial and tangential flux density B_r and B_θ at different radii **without** exception np equals **2**. HTS bulks are used as rotor excitation and the position around the circumference is marked \blacksquare .



(a) Rotor field at middle stator radius $r_{s,m}$



(b) Rotor field at middle air gap radius $r_{ag,m}$



(c) Rotor field at middle rotor radius $r_{r,m}$

Figure D.3.: Validation of the analytical machine model according to **config. 7** in Table D.1 through a comparison with FEM over the radial and tangential flux density B_r and B_θ at different radii **with** exception n_p equals **2**. Permanent magnets are used as rotor excitation and the position around the circumference is marked \blacksquare .

E. Derivation of Mean Torque

The mean torque \overline{M} over a period of time T is calculated through the Lorentz force [179]. The general expression can be simplified due to periodic quantities. Furthermore, the relationships in Equation E.1 are used in the calculation [259]:

$$\begin{aligned} \cos(a \pm b) &= \cos(a) \cos(b) \mp \sin(a) \sin(b) \\ \int_0^T \begin{pmatrix} \cos(nx) \cos(nx+a) \\ \sin(nx) \sin(nx+a) \end{pmatrix} dx &= \frac{T}{2} \cos(a) \quad \text{if } n \in \mathbb{Z} \\ \int_0^T \cos(nx) \sin(nx) dx &= 0 \quad \text{if } n \in \mathbb{Z} \end{aligned} \quad (\text{E.1})$$

The derivation of the torque is different for machines with magnets or coils in the rotor and therefore the torque is subdivided in \overline{M}_m and \overline{M}_c , respectively. Firstly, the torque for machines with magnets is calculated.

The calculation begins with the cross product of the stator current density J_s introduced in Section 4.2 and the radial flux density B_r of the respective rotor excitement introduced in Section 4.5.

$$\begin{aligned} \overline{M}_m &= \int_t \iiint_V J_s(\theta, t) \times B_r(r, \theta, t) r dV dt \\ &= \frac{1}{T} \int_0^T l_{fe} \int_0^{2\pi} \int_{r_{si}}^{r_{so}} J_z B_{r,r} r^2 dr d\theta dt \\ &= -\mu_0 \mu_r \frac{l_{fe}}{T} \int_0^T \int_0^{2\pi} \int_{r_{si}}^{r_{so}} r^2 \sum_{k=0}^{m-1} \sum_n J_{r,n} \cos\left(n\left(p\theta - \frac{2\pi k}{m}\right)\right) F_n \cos\left(n\left(p\omega t - \frac{2\pi k}{m}\right)\right) \\ &\quad \cdot \sum_n M_n np \left(A_{n,4} r^{np-1} - C_{n,4} r^{-np-1}\right) \cos(np(\theta - \omega t - \theta_{load})) dr d\theta dt \\ &= -\mu_0 \mu_r \frac{l_{fe}}{T} \sum_{k=0}^{m-1} \sum_n J_{r,n} F_n M_n np \\ &\quad \cdot \int_0^{2\pi} \cos\left(n\left(p\theta - \frac{2\pi k}{m}\right)\right) \int_0^T \cos\left(n\left(p\omega t - \frac{2\pi k}{m}\right)\right) \cos(np(\theta - \omega t - \theta_{load})) dt d\theta \\ &\quad \cdot \int_{r_{si}}^{r_{so}} r^2 \left(A_{n,4} r^{np-1} - C_{n,4} r^{-np-1}\right) dr \end{aligned}$$

$$\begin{aligned}
\overline{M}_m &= -\mu_0 \mu_r \frac{l_{fe}}{T} \sum_{k=0}^{m-1} \sum_n J_{r,n} F_n M_n np \\
&\cdot \int_0^{2\pi} \cos(np\theta) \cos\left(n\frac{2\pi k}{m}\right) + \sin(np\theta) \sin\left(n\frac{2\pi k}{m}\right) \\
&\cdot \int_0^T \left(\cos(np\omega t) \cos\left(n\frac{2\pi k}{m}\right) + \sin(np\omega t) \sin\left(n\frac{2\pi k}{m}\right) \right) \\
&\cdot (\cos(np\theta - \theta_{load}) \cos(np\omega t) + \sin(np\theta - \theta_{load}) \sin(np\omega t)) dt d\theta \\
&\cdot \int_{r_{si}}^{r_{so}} r^2 (A_{n,4} r^{np-1} - C_{n,4} r^{-np-1}) dr \\
&= -\mu_0 \mu_r \frac{l_{fe}}{T} \sum_{k=0}^{m-1} \sum_n J_{r,n} F_n M_n np \\
&\cdot \int_0^{2\pi} \cos(np\theta) \cos\left(n\frac{2\pi k}{m}\right) + \sin(np\theta) \sin\left(n\frac{2\pi k}{m}\right) \\
&\cdot \frac{T}{2} \cos(\theta_{load}) \left(\cos\left(n\frac{2\pi k}{m}\right) \cos(np\theta) + \sin\left(n\frac{2\pi k}{m}\right) \sin(2p\theta) \right) d\theta \\
&\cdot \int_{r_{si}}^{r_{so}} r^2 (A_{n,4} r^{np-1} - C_{n,4} r^{-np-1}) dr \\
&= -\mu_0 \mu_r \frac{l_{fe}}{2} \sum_{k=0}^{m-1} \sum_n J_{r,n} F_n M_n np \pi \cos(\theta_{load}) \left(\cos\left(n\frac{2\pi k}{m}\right)^2 + \sin\left(n\frac{2\pi k}{m}\right)^2 \right) \\
&\cdot \int_{r_{si}}^{r_{so}} r^2 (A_{n,4} r^{np-1} - C_{n,4} r^{-np-1}) dr \\
&= -\frac{1}{2} \pi \mu_0 m l_{fe} \cos(\theta_{load}) \sum_{n \text{ odd}} F_n M_n J_{s,n} \int_{r_{si}}^{r_{so}} A_{n,4} r^{np+1} - C_{n,4} r^{-np+1} dr
\end{aligned}$$

Now follows the calculation of \overline{M}_c for machines with coils in the rotor.

$$\begin{aligned}
\overline{M}_c &= \int_t \iiint_V J_s(\theta, t) \times B_r(r, \theta, t) r dV dt \\
&= \frac{1}{T} \int_0^T l_{fe} \int_0^{2\pi} \int_{r_{si}}^{r_{so}} J_z B_{s,r} r^2 dr d\theta dt \\
&= \mu_0 \mu_r \frac{l_{fe}}{T} \int_0^T \int_0^{2\pi} \int_{r_{si}}^{r_{so}} r^2 \sum_{k=0}^{m-1} \sum_n J_{r,n} \cos\left(n\left(p\theta - \frac{2\pi k}{m}\right)\right) F_n \cos\left(n\left(p\omega t - \frac{2\pi k}{m}\right)\right) \\
&\cdot \sum_n J_{s,n} np (A_{n,m} r^{np} + C_{n,m} r^{-np}) \cos(np(\theta - \omega t - \theta_{load})) dr d\theta dt
\end{aligned}$$

$$\begin{aligned}
 \overline{M}_c &= \mu_0 \mu_r \frac{l_{fe}}{T} \sum_{k=0}^{m-1} \sum_n J_{r,n} F_n J_{s,n} np \\
 &\quad \cdot \int_0^{2\pi} \cos \left(n \left(p\theta - \frac{2\pi k}{m} \right) \right) \int_0^T \cos \left(n \left(p\omega t - \frac{2\pi k}{m} \right) \right) \cos (np(\theta - \omega t - \theta_{load})) dt d\theta \\
 &\quad \cdot \int_{r_{si}}^{r_{so}} r^2 \left(A_{n,4} r^{np-1} + C_{n,4} r^{-np-1} \right) dr \\
 &= \mu_0 \mu_r \frac{l_{fe}}{T} \sum_{k=0}^{m-1} \sum_n J_{r,n} F_n J_{s,n} np \\
 &\quad \cdot \int_0^{2\pi} \cos (np\theta) \cos \left(n \frac{2\pi k}{m} \right) + \sin (np\theta) \sin \left(n \frac{2\pi k}{m} \right) \\
 &\quad \cdot \int_0^T \left(\cos (np\omega t) \cos \left(n \frac{2\pi k}{m} \right) + \sin (np\omega t) \sin \left(n \frac{2\pi k}{m} \right) \right) \\
 &\quad \cdot (\cos (np\theta - \theta_{load}) \cos (np\omega t) + \sin (np\theta - \theta_{load}) \sin (np\omega t)) dt d\theta \\
 &\quad \cdot \int_{r_{si}}^{r_{so}} r^2 \left(A_{n,4} r^{np-1} + C_{n,4} r^{-np-1} \right) dr \\
 &= \mu_0 \mu_r \frac{l_{fe}}{T} \sum_{k=0}^{m-1} \sum_n J_{r,n} F_n J_{s,n} np \\
 &\quad \cdot \int_0^{2\pi} \cos (np\theta) \cos \left(n \frac{2\pi k}{m} \right) + \sin (np\theta) \sin \left(n \frac{2\pi k}{m} \right) \\
 &\quad \cdot \frac{T}{2} \cos (\theta_{load}) \left(\cos \left(n \frac{2\pi k}{m} \right) \cos (np\theta) + \sin \left(n \frac{2\pi k}{m} \right) \sin (2p\theta) \right) d\theta \\
 &\quad \cdot \int_{r_{si}}^{r_{so}} r^2 \left(A_{n,4} r^{np-1} + C_{n,4} r^{-np-1} \right) dr \\
 &= \mu_0 \mu_r \frac{l_{fe}}{2} \sum_{k=0}^{m-1} \sum_n J_{r,n} F_n J_{s,n} np \pi \cos (\theta_{load}) \left(\cos \left(n \frac{2\pi k}{m} \right)^2 + \sin \left(n \frac{2\pi k}{m} \right)^2 \right) \\
 &\quad \cdot \int_{r_{si}}^{r_{so}} r^2 \left(A_{n,4} r^{np-1} + C_{n,4} r^{-np-1} \right) dr \\
 &= \frac{1}{2} \pi \mu_0 m l_{fe} \cos (\theta_{load}) \sum_{n \text{ odd}} F_n J_{r,n} J_{s,n} \int_{r_{si}}^{r_{so}} A_{n,4} r^{np+1} + C_{n,4} r^{-np+1} dr
 \end{aligned}$$

Depending on the definition of the load angle θ_{load} , the expression $\cos(\theta_{load})$ can also be changed into $\sin(\theta_{load})$. In this thesis, the load angle is defined over the spatial angular displacement from the fundamental wave of stator field and rotor field, which requires the expression $\sin(\theta_{load})$.

F. Collection of Superconducting Machines from Various Areas

The main properties of superconducting machines of the areas wind, utility and marine, which are discussed in Section 1.4 and presented in Figure 1.8, are collected in Table F.1, F.2 and F.3.

Table F.1.: Main properties of the superconducting machines for wind turbines corresponding to Figure 1.8.

Year	Power ¹	Speed ²	PTW ³	Efficiency ⁴	SC	Temp. ⁵	Source
2007	8.0	12	–	–	YBCO	30	[260]
2011	5.0	10	0.147	–	BSCCO	40	[261]
2011	10.0	10	0.066	96.0	YBCO	30	[262]
2012	10.0	10	0.070	96.0	NbTi	4.3	[263]
2013	10.0	10	0.192	98.0	MgB ₂	20	[264]
2014	10.0	9.65	–	97.7	MgB ₂	10	[265]
2015	0.0105	600	–	–	REBCO	30	[266]
2015	10.0	8	–	–	YBCO	30	[267]
2015	10.0	10	0.066	97.6	REBCO	40	[268]
2015	13.2	9	0.066	96.2	NbTi	4.2	[269]
2016	12.0	8.4	0.063	–	REBCO	20	[270]
2016	12.0	10	0.086	98.0	YBCO	15	[271]
2017	10.0	10	–	99.8	MgB ₂	20	[69]
2017	10.0	10	–	99.0	Nb ₃ Sn	4.0	[69]
2018	10.0	10	0.179	96.0	YBCO	30	[161]
2019	3.0	15	0.046	–	REBCO	30	[272]
2019	3.6	15	–	–	REBCO	30	[273]
2019	11.6	10	0.064	92.9	YBCO	65	[274]

¹ in MW

² in min⁻¹

³ in kW kg⁻¹

⁴ in %

⁵ in K

Table F.2.: Main properties of the superconducting machines for utility corresponding to Figure 1.8.

Year	Power ¹	Speed ²	PTW ³	Efficiency ⁴	SC	Temp. ⁵	Source
1978	20	3600	0.17	99.3	NbTi	4	[275]
1978	1200	3600	3.97	99.6	NbTi	4	[276]
1982	250	3000	–	–	NbTi	5	[277]
1984	300	3600	1.83	99.4	NbTi	4	[276]
1997	78.7	3600	–	98.15	NbTi	4	[278]
1997	200	3600	–	99.05	NbTi	4	[278]
2002	50	3600	–	–	BSCCO	35-40	[279]
2003	1.5	3600	–	–	BSCCO	20-40	[280]
2003	100	3600	–	–	BSCCO	20-40	[280]
2005	8	1800	–	98.8	BSCCO	–	[281]

¹ in MW

² in min⁻¹

³ in kW kg⁻¹

⁴ in %

⁵ in K

Table F.3.: Main properties of the superconducting machines for marine corresponding to Figure 1.8.

Year	Power ¹	Speed ²	PTW ³	Efficiency ⁴	SC	Temp. ⁵	Source
1983	2.25	1200	–	–	NbTi	4	[63]
2002	25	120	0.417	97.0	BSCCO	35-40	[279]
2004	5	230	0.25	96	BSCCO	32	[282]
2005	37	120	–	97.3	NbTi	4	[283]
2006	0.4	1500	–	96.8	BSCCO	27	[284, 285, 286]
2006	4	3600	0.58	98.7	BSCCO	25	[284, 285, 286]
2009	0.0075	360	–	–	YBCO	30	[287]
2010	1	190	–	98	BSCCO	30	[288]
2010	4	120	0.11	94.6	BSCCO	30	[289]
2011	36.5	120	0.49	97.3	BSCCO	32	[290]
2012	3	160	–	98	BSCCO	30	[291]
2012	20	90	–	–	BSCCP	37	[291]
2013	0.4	250	–	98	BSCCO	40	[292]
2015	3.6	1800	–	–	YBCO	–	[267]
2016	5	213	0.23	98	REBCO	27	[293]
2016	40	120	0.496	99.4	BSCCO\MgB ₂	20-35	[294]

¹ in MW

² in min⁻¹

³ in kW kg⁻¹

⁴ in %

⁵ in K

List of Figures

1.1.	Global annual fossil CO ₂ emissions for the year 2018 divided into main activity sectors and aviation operations as well as aircraft class.	1
1.2.	Total passenger CO ₂ emission and the carbon intensity as a function of the mission length.	2
1.3.	CO ₂ emission and revenue passenger kilometers as a function of the year <i>yr</i> .	3
1.4.	Forecast of CO ₂ emission of the civil aviation for the years between 2020 and 2050.	4
1.5.	Topologies of hybrid-electric propulsion systems divided into turbo-electric, serial-hybrid and parallel-hybrid.	6
1.6.	Cryogenic hybrid-electric propulsion system consists of the subsystems cryogenic electric power distribution center, power generation unit and electric propulsion unit.	8
1.7.	Critical temperature T_c and the year of discovery for bardeen-cooper-schrieffer superconductors, cuprates and iron-based superconductors.	9
1.8.	Power P as a function of the rotational speed n of superconducting machines from the areas marine, wind, utility and aerospace which are divided into the development stages concept and demonstrator.	11
1.9.	Minimal sketch of radial flux synchronous machines with an air gap stator winding of copper and superconducting rotor coil as well as slotted superconducting stator and permanent magnet rotor.	13
1.10.	Content of this thesis which is surrounded by the main topics superconductivity, electric machine and hybrid-electric aircraft.	15
2.1.	Cross section of the 114 filament MgB ₂ wire shown as microscopic image and adapted geometry for FEM simulations.	18
2.2.	Cross section of the 54 filament MgB ₂ wire shown as microscopic image and adapted geometry for FEM simulations.	19
2.3.	Measured temperature T at the sample of the 54 filament wire as a function of the time t .	20
2.4.	Magnetic field H as a function of the temperature T for type-I and type-II superconductors.	21
2.5.	Measured electric field E of the 114 filament wire as a function of the transport current I_t to determine the critical current I_c .	22
2.6.	Critical current I_c as a function of the external flux density B_{ext} for the 114 multifilament wire and 54 multifilament wire.	23
2.7.	Sketch illustrating the different loss components in superconducting filaments, normal conducting sheath material and stabilizer.	25
2.8.	Loss factor Γ for the magnetization loss density per cycle and per unit volume as a function of normalized flux density amplitude β in different shapes of superconductors.	27

2.9.	Magnetization loss results for an exemplary filament of the 114 filament wire divided into magnetization loss density $Q_{v,mag}$ as a function of the normalized flux density amplitude β and the normalized current I_n as well as magnetization loss per unit length and per transport current $P'_{v,mag}/I_t$ as a function of filament radius r_{fil}	28
2.10.	Eddy current loss per unit length $P'_{v,e}$ as a function of the resistivity ρ_{nc} for a normal conducting material with circular cross-section.	31
2.11.	Sketch of the current path of coupling currents between two filaments embedded in a matrix and penetrated by a perpendicular magnetic field in a non-twisted and twisted conductor.	32
2.12.	Cable consisting of multifilament wires with superconducting filaments and normal conducting matrix in three twisting stages.	33
2.13.	Multifilament wire divided into the inner matrix core, the filamentary zone and the outer sheath.	34
2.14.	Coupling current loss per unit length $P'_{v,cc}$ as a function of the external flux density B_{ext} at different external frequencies f_{ext} for the 114 filament wire.	35
2.15.	Magnetization loss results divided into the influence of the filament radius r_{fil} on the magnetization loss per unit length and per transport current $P'_{v,mag}/I_t$ of a monofilament wire as well as the comparison of the magnetization loss per unit length $P'_{v,mag}$ between the monofilament and the 114 filament wire depending on the external flux density B_{ext}	40
2.16.	Instantaneous transport current i_t , the instantaneous critical current i_c and the instantaneous magnetization loss per unit length $p'_{v,mag}$ as a function of the time t for the 114 filament wire for a phase angle of 0° and 90° between external field and transport current.	42
2.17.	Magnetization loss results for the 114 filament wire divided into the magnetization loss per unit length $P'_{v,mag}$ as a function of the rotation angle θ_{sc} and the magnetization loss per unit length $P'_{v,mag}$ as a function of the external frequency f_{ext}	43
2.18.	Magnetization loss density $Q_{v,mag}$ of the 114 filament wire as a function of the external flux density B_{ext} and the normalized current I_n for different temperatures T	44
2.19.	Magnetization loss density $Q_{v,mag}$ of the 114 filament wire as a function of the temperature T and different external flux densities B_{ext} as well as normalized currents I_n	45
2.20.	Comparison of the loss components per unit length of the 114 filament wire depending on the external frequency f_{ext} and the flux density B_{ext} at a normalized current I_n of 0.7 and a temperature T of 20 K.	46
3.1.	Calculation procedure of the electro-thermal model divided into superconductor behavior and cooling.	47
3.2.	Three-dimensional view of a multifilament MgB ₂ wire with a normal conducting matrix cooled with evaporating liquid hydrogen in axial flow direction through the whole superconductor surface.	48

3.3.	T - s diagram of hydrogen with a descriptive determination of the evaporation enthalpy at different pressures and vapor qualities.	49
3.4.	Phase diagram of hydrogen.	50
3.5.	Heat transfer coefficient α_w and wall temperature T_w as a function of the wire length l_w for an exemplary wire cooling at single-phase and two-phase flow.	54
3.6.	Minimal sketch for the heat conduction calculation through a shell model in a Cartesian coordinate system and cylindrical coordinate system.	57
3.7.	Temperature profile of the perfect cooled round wire model and the round shell model.	60
3.8.	Temperature distribution in r -direction of the round wire model and in y -direction of the quadratic wire model.	60
3.9.	Temperature profile of the one-side cooled quadratic 114 filament wire and the quadratic shell model.	61
3.10.	Single one-side cooled arrangement of a potted and pressed copper litz wire including insulation.	62
3.11.	Engineering current density of copper J_{cu} and pressure drop Δp as a function of cooling slot height h_s for a slot with double one-side cooling.	63
3.12.	Current density of the copper litz wire J_{cu} as a function of external flux density B_{ext} and frequency f_{ext}	64
3.13.	Minimal sketch of periodic cooling arrangements in the MgB ₂ stator based on the insulated 114 filament wire and divided into single one-side cooling and double one-side cooling.	65
3.14.	Engineering current density $J_{e,sc}$ of the 114 filament MgB ₂ wire and the maximum MgB ₂ temperature $T_{sc,max}$ as a function of the insulation thickness d_{ins} for a slot with double one-side cooling.	66
3.15.	Engineering current density $J_{e,sc}$ of the 114 filament MgB ₂ wire and the inlet pressure p_{in} as a function of the cooling slot height h_s for a slot with double one-side cooling.	67
3.16.	Current density J of the 114 filament MgB ₂ wire in the cases single one-side cooled as well as perfect cooled and the measured values.	67
3.17.	Engineering current density J_e of the 114 filament MgB ₂ wire in the cases single one-side cooled as well as double one-side cooled and the copper litz wire.	68
3.18.	Current density ratio between the 114 filament MgB ₂ wire double one-side cooled and single one-side cooled as well as the 114 filament MgB ₂ wire double one-side cooled and the copper litz wire.	69
4.1.	Calculation procedure of the analytical machine design model including results by the electro-thermal model. [142]	71
4.2.	General superconducting machine model with a cold air gap winding and variable rotor excitation.	73
4.3.	Sketch of a flat coil with the top view and the cross section.	74
4.4.	Spatial stator current density distribution of a three-phase system in a ideal model under load and in comparison with a limited model.	76

4.5. Exemplary air gap design with marked temperature areas for cryogenic and ambient temperature of fully superconducting machines, partially superconducting rotor machines, partially superconducting stator machines and normal conducting machines.	78
4.6. Press-fit model of a rotor section with rotor carrier, segmented magnets and covered by a sleeve.	79
4.7. Sketch of a cryo wall in cylindrical form under overpressure and negative pressure.	82
4.8. Rotor excitation of the general superconducting machine model with superconducting coil, HTS bulk, permanent magnet and Halbach array.	85
4.9. HTS bulk arrangements for one pole distinguished in continuous, rectangular and cylindrical.	86
4.10. Spatial shape of the current density J in rotor coils and the remanence M of conventional permanent magnets and HTS bulks as a function of the electrical angle θ_{el} over a pole pair.	87
4.11. Machine model with 4 pole pairs and specific circular arcs for the validation of the analytical calculation.	94
4.12. Validation of the analytical machine model according to config. 1 through a comparison with FEM over the radial and tangential flux density B_r and B_θ at different radii without exception.	96
4.13. Validation of the analytical machine model according to config. 2 through a comparison with FEM over the radial and tangential flux density B_r and B_θ at different radii with exception.	97
4.14. Validation of the analytical machine model according to config. 3 through a comparison with FEM over the radial and tangential flux density B_r and B_θ at different radii without exception.	98
4.15. Validation of the analytical machine model according to config. 4 through a comparison with FEM over the radial and tangential flux density B_r and B_θ at different radii with exception.	99
4.16. Radial flux density B_r of the total field at middle stator radius $r_{s,m}$ calculated by FEM and the absolute error between analytical machine model and FEM of config. 1.	100
4.17. Absolute error $\varepsilon_{a,b}$ and relative error $\varepsilon_{r,b}$ of the radial flux density B_r of the total field at middle stator radius $r_{s,m}$ between analytical machine model and FEM as a function of the maximum harmonic n_{max} and stator current density J_s	101
5.1. Fundamental design process as flowchart with the related subroutines S and a link to the corresponding chapters C.	108
5.2. Exemplary mission profile represented by the altitude a as a function of the distance d	109
5.3. Flowchart of the working point determination for a selected external frequency f_{ext} and maximum normalized current $I_{n,max}$ between the electro-thermal model of a chosen superconductor and an investigated machine geometry.	113

5.4.	Current density J as a function of the flux density B calculated by the electro-thermal model for the normalized currents I_n of 0.3, 0.5, 0.7 and 1.0. The machine characteristic is presented by the maximum flux density $B_{s,max}$ occurring at the stator coils as a function of the engineering current density of the stator coils J_e for a specific machine geometry at a maximum normalized current $I_{n,max}$ of 0.7. The working point is marked.	114
5.5.	Results of an exemplary calculation of the stator AC loss presented between the inner stator radius $r_{s,i}$ and outer stator radius $r_{s,o}$ for a fully superconducting machine with MgB ₂ stator coils and HTS rotor coils. Presented are the stator current density J_s as a function of the electrical angle θ_{el} , the flux density B as a function of the radial direction r and the electrical angle θ_{el} , the normalized current I_n as a function of the radial direction r and the electrical angle θ_{el} as well as the total AC loss density in stator coils $p_{v,s}$ as a function of the radial direction r and the electrical angle θ_{el} . The yoke, the rotor carrier, the rotor coils as well as coil edges are marked.	116
5.6.	Normalized stator AC loss $P_{v,n,s}$ as a function of the normalized stator current $I_{n,s}$, the normalized rotor current $I_{n,r}$ and the load angle θ_{load} for a fully superconducting machine with MgB ₂ stator coils and HTS rotor coils at a normalized torque M_n of 0.15.	118
5.7.	Normalized torque M_n and normalized stator AC loss per torque $P_{v,n,s}/M_n$ as a function of the load angle θ_{load} at a normalized stator and rotor current of 0.7.	119
5.8.	Hyperbolas of constant normalized torque M_n in dependence of the normalized stator current $I_{n,s}$ and the normalized rotor current $I_{n,r}$. The trajectory of maximum normalized torque $M_{n,max}$ per normalized stator AC loss $P_{v,n,s}$ is shown and the optimized normalized current $I_{n,opt}$ at a normalized torque of 0.75 is marked.	120
5.9.	Normalized stator AC loss $P_{v,n,s}$ as a function of normalized current I_n for the stator and rotor for a normalized torque M_n of 0.75.	120
5.10.	Optimized normalized current $I_{n,opt}$ as a function of the normalized torque M_n as well as the comparison of the normalized stator AC loss $P_{v,n,s}$ as a function of the normalized torque M_n for a fully superconducting machine with a controlled rotor current and a fixed rotor current.	121
5.11.	Sketch of a liquid hydrogen tank with the outer tank wall, the foam insulation, the inner tank wall and the stored liquid hydrogen.	122
5.12.	Calculation procedure of the liquid hydrogen tank model.	123
5.13.	Sectional view of a liquid hydrogen tank with foam insulation.	123
5.14.	Hyperbolas of constant boil-off rate f_{bor} in dependence of the tank mass m_t and the diameter-to-length ratio f_{dl} . The trajectory of minimum tank mass $m_{t,min}$ per boil-off rate is shown.	126
5.15.	Tank design results according to the boundary conditions and varying LH ₂ masses m_{lh2} . Presented are the tank mass m_t as a function of the burst pressure p_{bur} as well as the boil-off rate f_{bor}	127

6.1.	Airbus A321neo-LR with the wing tanks, the center tank, the rear center tanks and the front center tank for jet fuel.	129
6.2.	Sketch of a sectional view of the Pratt & Whitney PW1133G geared turbofan.	131
6.3.	Hybrid-electric Airbus A321neo-LR with battery unit, cryogenic electric power distribution center, electric propulsion unit, jet fuel tanks, liquid hydrogen tanks and power generation unit.	133
6.4.	Cross section of a hybrid-electric Airbus A321neo-LR fuselage with the interior arrangement, the stringers as well as the skin and further support structures. The hydrogen tanks are located below the passenger cabin in the rear of the aircraft.	134
6.5.	Required power P for the hybrid-electric Airbus A321neo-LR as a function of the time t for a typical mission of 5 h 10 min. The cruise time is exemplary 4 h 12 min, but is in general variable as illustrated.	136
6.6.	Power-to-weight ratio PTW for the 21.6 MW and 3500 min^{-1} machine design at a pole pair number of 8 and in dependence of the normalized optimization parameters as well as the working point flux density B_{wp}	142
6.7.	Results for the machine architecture consisting of Cu stator coils and HTS rotor bulks. Presented is the power-to-weight ratio PTW as a function of the working point flux density B_{wp} as well as the stator AC loss $P_{v,s}$	143
6.8.	Results for the machine architecture consisting of Cu stator coils and HTS rotor coils. Presented is the power-to-weight ratio PTW as a function of the working point flux density B_{wp} as well as the stator AC loss $P_{v,s}$	144
6.9.	Results for the machine architecture consisting of MgB_2 stator coils and Halbach rotor array. Presented is the power-to-weight ratio PTW as a function of the working point flux density B_{wp} as well as the stator AC loss $P_{v,s}$	145
6.10.	Results for the machine architecture consisting of MgB_2 stator coils and HTS rotor bulks. Presented is the power-to-weight ratio PTW as a function of the working point flux density B_{wp} as well as the stator AC loss $P_{v,s}$	147
6.11.	Results for the machine architecture consisting of MgB_2 stator coils and HTS rotor coils. Presented is the power-to-weight ratio PTW as a function of the working point flux density B_{wp} as well as the stator AC loss $P_{v,s}$	148
6.12.	Results for the machine architecture consisting of MgB_2 stator coils and HTS rotor coils. Presented is the working point flux density B_{wp} as a function of the working point current density J_{wp} at a normalized current of 0.7 as well as the yoke thickness d_y	149
6.13.	Comparison of the power-to-weight ratio PTW as a function of the efficiency η of all machine architectures and under consideration of the requirements as well as boundary conditions.	151

6.14. Power-to-weight ratio PTW as a function of the stator AC loss $P_{v,s}$ filtered according to the machines with an optimal power-to-weight ratio as well as stator AC loss for the machine architectures MgB ₂ stator coils and Halbach rotor array as well as MgB ₂ stator coils and HTS rotor coils.	152
6.15. Results for the preselected machine architectures MgB ₂ stator coils consisting of Halbach rotor array or HTS rotor coils. Presented are the power-to-weight ratio PTW as a function of the limiting parameters stator bending radius $r_{s,b}$ and the diameter-to-length aspect d/l	153
6.16. Stator AC loss $P_{s,v}$ at the nominal point of the machine as a function of the maximum flight time $t_{f,max}$ for fully and partially superconducting machines. The maximum flight time is calculated according to the variable flight mission and the fuel range limit is marked. The machine architectures are divided into MgB ₂ stator coils and Halbach rotor array as well as HTS rotor coils with non-minimized and minimized stator AC loss.	155
6.17. Cross section to scale of one magnetic machine pole for the design proposals MgB ₂ stator coils and Halbach rotor array as well as HTS rotor coils.	156
6.18. Stator AC loss $P_{v,s}$ as a function of the flight mission phase. The required power P for a single engine is shown on the bars. Minimized and non-minimized stator AC loss are shown for machine architectures based on MgB ₂ stator coils and HTS rotor coils as well as Halbach rotor array, respectively, and given as design proposals.	158
7.1. Superconducting machine model with cold stator air gap windings made of HTS tapes and variable rotor excitation. Each coil leg is fixed by a support structure and is cooled by LH ₂ through a channel between the coil and the yoke.	164
7.2. Superconducting machine model with cold flat stator air gap windings and variable rotor excitation.	165
A.1. Minimal sketch for heat conduction calculation in a Cartesian coordinate system.	168
A.2. Minimal sketch for heat conduction calculation in a polar coordinate system.	168
B.1. Current density calculation procedure as flowchart.	169
B.2. Machine design procedure as flowchart.	170
C.1. Thermal conductivity of MgB ₂ λ_{sc} as a function of the temperature T	171
C.2. Electrical resistivity ρ_{cu} and thermal conductivity λ_{cu} of Cu as a function of the temperature T at different external flux densities.	173
C.3. Thermal conductivity of polyimide and Kapton insulation λ_{ins} as a function of the temperature T	174
C.4. Thermal conductivity of Cu10Ni λ_{cuni} as a function of the temperature T	175
C.5. Electrical resistivity ρ_{nb} and the thermal conductivity λ_{nb} of Nb as a function of the temperature T	176

- D.1. Validation of the analytical machine model according to config. 5 through a comparison with FEM over the radial and tangential flux density B_r and B_θ at different radii with exception. 178
- D.2. Validation of the analytical machine model according to config. 6 through a comparison with FEM over the radial and tangential flux density B_r and B_θ at different radii without exception. 179
- D.3. Validation of the analytical machine model according to config. 7 through a comparison with FEM over the radial and tangential flux density B_r and B_θ at different radii with exception. 180

List of Tables

1.1.	Main properties of the superconducting machines for aerospace application.	12
2.1.	Geometric properties of the 54 filament and 114 filament MgB ₂ wire.	19
2.2.	Material properties of the investigated multifilament MgB ₂ wires. . .	20
2.3.	AC loss components in a superconducting wire with the major influence parameters and point of origin.	25
2.4.	Input parameters for the analytical magnetization loss calculation of the 114 filament wire.	29
2.5.	Fit parameters for the critical current density of the 114 filament wire.	38
2.6.	Input parameters for the analytical and FEM magnetization loss calculation for a monofilament and the 114 filament wire.	41
3.1.	Constants and normalization values of evaporating hydrogen for the heat transfer coefficient calculation.	53
3.2.	Input parameters for a benchmark cooling calculation for single-phase flow and two-phase flow of liquid hydrogen.	53
3.3.	Input parameters of the temperature distribution calculation.	59
3.4.	Input parameters of the electro-thermal calculation for an exemplary copper litz wire.	64
3.5.	Input parameters of the electro-thermal calculation for the 114 filament MgB ₂ wire.	65
4.1.	Machine topologies and corresponding architectures in the machine design model.	76
4.2.	Design points of the sleeve thickness at different temperature T , angular speed ω and mean torque \overline{M}	81
4.3.	Important input parameters of the electromagnetic machine model for validation.	95
4.4.	Mean torque \overline{M} of the machine configurations calculated by the analytical machine model and for comparison by FEM.	103
5.1.	Significant input parameters of the electro-thermal model for a chosen superconductor and coolant divided into the parts cooling and superconductor behavior.	110
5.2.	Significant input parameters of the machine design model divided into the parts general, coil excitation and magnet excitation.	111
5.3.	Gravimetric and volumetric energy density of liquid hydrogen and jet fuel.	122
5.4.	Parameters of the liquid hydrogen tank model.	126
6.1.	Airbus A321neo-LR properties.	130
6.2.	Pratt & Whitney PW1133G properties.	132
6.3.	Performance requirements of the hybrid-electric Airbus A321neo-LR for an exemplary mission.	136

6.4.	Materials for the machine parts subdivided into rotor and stator. . . .	137
6.5.	Investigated machine topologies for the design of a fan motor. . . .	138
6.6.	Requirements and boundary conditions for the machine design of a fan motor.	138
6.7.	Constant input parameters for the machine design of a fan motor. . .	139
6.8.	Varied input parameters of the machine design for the machine architectures Cu stator coils & HTS bulk rotor, Cu stator coils & HTS rotor coils, MgB ₂ stator coils & Halbach rotor array, MgB ₂ stator coils & HTS bulk rotor and MgB ₂ stator coils & HTS rotor coils. . . .	141
6.9.	Comparison of masses for machines with Cu or MgB ₂ stator coils and HTS rotor coils considering the weight for cooling by a heat exchanger or LH ₂ tank.	146
6.10.	Impact of the varied input parameters for increasing power-to-weight ratio PTW and decreasing stator AC loss $P_{s,v}$ of MgB ₂ stator machines with Halbach array or HTS coil excitation.	150
6.11.	Main input parameters of the proposed machine designs.	157
6.12.	Main output parameters of the proposed machine designs.	159
C.1.	Fit parameters for the thermal conductivity of MgB ₂	171
C.2.	Fit parameters for the electrical resistivity of Cu.	172
C.3.	Fit parameters for the thermal conductivity of Cu.	173
C.4.	Fit parameters for the thermal conductivity of the insulation materials polyimide and Kapton.	174
D.1.	Important input parameters of the electromagnetic machine model for validation.	177
F.1.	Main properties of the superconducting machines for wind turbines. .	184
F.2.	Main properties of the superconducting machines for utility.	185
F.3.	Main properties of the superconducting machines for marine.	185

Abbreviations

AC	alternating current
Al	aluminum
ana	analytical, analytically
APS	auxiliary power supply
B	boron
BCS	bardeen-cooper-schrieffer
BSCCO	bismuth strontium calcium copper oxide
C	carbon
CEPDC	cryogenic electric power distribution center
CFRP	carbon fiber reinforced polymer
Cu	copper
CuNi	cupronickel
DC	direct current
CO ₂	carbon dioxide
EMC	electromagnetic compatibility
EPDC	electric power distribution center
EPU	electric propulsion unit
eqn	equation
ETM	electro-thermal model
Fe	iron
FEM	finite element method
GH ₂	gaseous hydrogen
GTF	geared turbofan
H ₂ O	water
HA	Halbach array
HTS	high-temperature superconductor
IMD	internal magnesium diffusion
LH ₂	liquid hydrogen
LHe	liquid helium
LM	loss minimization
LTS	low-temperature superconductor
Mg	magnesium
MgB ₂	magnesium diboride
ML	minimized loss
MTPA	maximum torque per ampere
MTPV	maximum torque per volt
NML	non-minimized loss
Nb	niobium
NC	normal conducting, normal conductor

NdFeB	neodymium iron boron
Ni	nickel
NO _x	nitrogen oxide
PDE	partial differential equations
PGU	power generation unit
PIT	powder in tube
PTW	power-to-weight ratio
PM	permanent magnet
PU	polyurethane
REBCO	rare-earth barium copper oxide
RPK	revenue passenger kilometer
RRR	residual-resistance ratio
RT	room temperature
SC	superconducting, superconductor
Si	silicon
SiC	silicon carbide
SO _x	sulfur oxide
Ti	titanium
ULD	unit load device
WP	working point
Y	yttrium
YBCO	yttrium barium copper oxide

Index of Symbols

Symbol	Unit	Explanation
a	m	Altitude, height
A	m ²	Area, surface
A_{cab}	m ²	Cable area
A_{con}	m ²	Shell surface of conductor
A_{fil}	m ²	Filament area
A_{fl}	m ²	Cross section of cooling slot or non-circular tube
A_h	m ²	Hysteresis curve area
$A_{t,w}$	m ²	Surface of tank wall layer
$A_{n,o}$	–	Fourier coefficient of n^{th} harmonic and o^{th} region
\vec{B}	T	Magnetic flux density
B_{\perp}	T	Perpendicular magnetic flux density
B_{\parallel}	T	Parallel magnetic flux density
B_{ext}	T	External magnetic flux density
B_{max}	T	Maximum magnetic flux density
B_p	T	Penetration flux density
B_{peak}	T	Peak flux density in HTS bulks
B_r	T	Radial component of magnetic flux density
$B_{r,o}$	T	Radial component of magnetic flux density in o^{th} region
B_{rem}	T	Remanance flux density of magnet
B_{rot}	T	Magnetic flux density by rotor
$B_{rot,r}$	T	Radial component of magnetic flux density by rotor
$B_{rot,r,1}$	T	Radial component of fundamental wave of magnetic flux density by rotor at outer rotor radius
$B_{s,max}$	T	Maximum flux density at stator coils
B_{θ}	T	Tangential component of magnetic flux density
$B_{\theta,o}$	T	Tangential component of magnetic flux density in o^{th} region
B_{wp}	T	Working point flux density of stator coil
$B_{y,sat}$	T	Saturation flux density of yoke
$B_{y,max}$	T	Maximum flux density of yoke
B_0	T	Parameter for critical current calculation
B_1	T	Parameter for critical current calculation
b	m	Width
b_s	m	Width of cooling slot
$b_{s,c}$	m	Width of stator coil
$b_{s,c,i}$	m	Inner diameter of stator coil
b_t	m	Width of tank

Symbol	Unit	Explanation
b_w	m	Width of wire
c_p	$\text{J kg}^{-1} \text{K}^{-1}$	Specific heat capacity
$c_{p,m}$	$\text{J kg}^{-1} \text{K}^{-1}$	Specific heat capacity at average temperature
C_1	–	Parameter of heat transfer calculation
C_2	–	Parameter of heat transfer calculation
C_{exc}	–	Parameter for excess loss in yoke
C_{fe}	–	Constant for ferromagnetic loss calculation
C_{hys}	–	Parameter for hysteresis loss in yoke
C_n	–	Constant value of heat transfer coefficient calculation
$C_{n,o}$	–	Fourier coefficient of n^{th} harmonic and o^{th} region
C_p	–	Factor in eddy current loss calculation
C_s	–	Factor in eddy current loss calculation
d	m	Distance, diameter, thickness
d_{air}	m	Thickness of magnetic air gap
d_b	m	Thickness of contact resistive barrier
d_{c2y}	m	Coil-to-yoke distance
d_{con}	m	Diameter of conductor
d_{core}	m	Diameter of GTF core
d_{cw}	m	Thickness of cryo wall
d_{fan}	m	Diameter of fan
d_{fe}	m	Thickness of ferromagnetic sheets
d_{fil}	m	Filament diameter
d_h	m	Hydraulic diameter
$d_{h,ann}$	m	Hydraulic diameter for annular gap
$d_{h,rec}$	m	Hydraulic diameter for rectangular gap
d_{in}	m	Inner diameter
d_{ins}	m	Insulation thickness
d_m	m	Machine diameter
$d_{m,max}$	m	Maximum machine diameter
d_{mag}	m	Thickness of rotor coil / magnet
d_n	m	Normalized diameter of heat transfer coefficient calculation
d_{of}	m	Distance of outer filament from neutral axis
d_{out}	m	Outer diameter
d_{rot}	m	Thickness of rotor carrier
$d_{s,c}$	m	Thickness of stator coil
d_{sh}	m	Thickness of sheath
d_{sl}	m	Thickness of sleeve
$d_{t,i}$	m	Inner diameter of tank
$d_{t,ins}$	m	Thickness of tank insulation

Symbol	Unit	Explanation
$d_{t,o}$	m	Outer diameter of tank
$d_{t,w}$	m	Thickness of tank wall
$d_{t,w1}$	m	Thickness of inner tank wall
$d_{t,w2}$	m	Thickness of outer tank wall
d_y	m	Thickness of yoke
d/l	–	Diameter-to-length aspect
\vec{E}	V m^{-1}	Electric field
E_c	V m^{-1}	Critical electric field
E_z	V m^{-1}	Electric field in z -direction
E	N m^{-2}	Young's modulus
E_{cw}	N m^{-2}	Young's modulus of cryo wall
E_{mag}	N m^{-2}	Young's modulus of magnet
E_{rot}	N m^{-2}	Young's modulus of rotor carrier
$E_{sl,r}$	N m^{-2}	Radial Young's modulus of sleeve
$E_{sl,\theta}$	N m^{-2}	Tangential Young's modulus of sleeve
f	Hz	Frequency
f_{el}	Hz	Electrical frequency
f_{ext}	Hz	External frequency
F_l	N	Lorentz force
f_ω	–	Whirl safety factor
f_Φ	–	Flux factor in HTS bulks
f_{bor}	–	Boil-off-rate
f_{bpr}	–	Bypass ratio
f_{cw}	–	Safety factor of cyro wall
f_{csr}	–	Stator coil support ratio
f_{dl}	–	Diameter-to-length ratio of tank
f_{fil}	–	Fill factor of copper litz wire
f_m	–	Non-slip safety factor
F_n	–	Fourier coefficient of n^{th} harmonic
$f_{sl,\sigma}$	–	Stress safety factor of sleeve
f_{sp}	–	Fanning friction factor at single-phase flow
f_t	–	Safety factor of tank
f_{tp}	–	Coefficient for pressure drop calculation of two-phase flow
f_{fill}	%	Fill level of tank
g	m s^{-2}	Gravity
GEO	–	Geometry data set
\vec{H}	A m^{-1}	Magnetic field
H_θ	A m^{-1}	Tangential component of magnetic field
$H_{\theta,o}$	A m^{-1}	Tangential component of magnetic field in o^{th} region

Symbol	Unit	Explanation
H_c	A m^{-1}	Critical magnetic field
H_{c2}	A m^{-1}	Upper critical magnetic field
H_{c1}	A m^{-1}	Lower critical magnetic field
H_{co}	A m^{-1}	Coercive magnetic field
$H_{co,B}$	A m^{-1}	Coercive magnetic field related to flux density
$H_{r,o}$	A m^{-1}	Radial component of magnetic field in o^{th} region
$H_{s,mag}$	A m^{-1}	Maximum magnetic field previous to quenching by stator in magnets
h_s	m	Height of cooling slot
$h_{s,c}$	m	Height of stator coil
h_t	m	Height of tank
h_w	m	Height of wire
h_l	J kg^{-1}	Specific enthalpy at boiling point
h_v	J kg^{-1}	Specific enthalpy at dew point
i	A	Instantaneous current
I	A	Current
i_c	A	Instantaneous critical current
I_c	A	Critical current
i_{coup}	A	Coupling current
I_{ext}	A	External current
I_k	A	Current in k^{th} filament
i_t	A	Instantaneous transport current
I_t	A	Transported current
I_n	—	Normalized current
$I_{n,max}$	—	Maximum normalized current in stator coils
$I_{n,opt}$	—	Optimized normalized current
$I_{n,r}$	—	Normalized rotor current
$I_{n,r,opt}$	—	Optimized normalized rotor current
$I_{n,s}$	—	Normalized stator current
$I_{n,s,opt}$	—	Optimized normalized stator current
I_a	m^4	Second moment of area
i	—	Imaginary number
\vec{J}	A m^{-2}	Current density
J_c	A m^{-2}	Critical current density
$J_{c,fil}$	A m^{-2}	Critical current density of filament
J_{c0}	A m^{-2}	Critical current density at zero external field
J_{cu}	A m^{-2}	Current density of copper litz wire
J_e	A m^{-2}	Engineering current density
$J_{e,max}$	A m^{-2}	Maximum engineering current density of stator coil
$J_{e,min}$	A m^{-2}	Minimum engineering current density of stator coil

Symbol	Unit	Explanation
$J_{e,sc}$	A m^{-2}	Engineering current density of MgB ₂
$J_{e,sc,d}$	A m^{-2}	Engineering current density of MgB ₂ with double one-side cooling
$J_{e,sc,s}$	A m^{-2}	Engineering current density of MgB ₂ with single one-side cooling
J_{max}	A m^{-2}	Maximum current density
J_r	A m^{-2}	Rotor current density
J_s	A m^{-2}	Stator current density
J_{wp}	A m^{-2}	Working point current density of stator coil
J_z	A m^{-2}	Current density in z -direction
$J_{z,k}$	A m^{-2}	Current density in z -direction and k^{th} filament
J_n	–	Fourier coefficient of n^{th} harmonic
$J_{r,n}$	–	Fourier coefficient of n^{th} harmonic for rotor coil
$J_{s,n}$	–	Fourier coefficient of n^{th} harmonic for stator coil
J_ν	–	ν^{th} Bessel function
\vec{K}	A m^{-1}	Surface current density
K_{cw}	Pa	Structural strength of cyro wall
k	–	Index of summation
K_{Bei}	–	Kelvin function
K_{Ber}	–	Kelvin function
k_{edc}	–	Factor for eddy current loss in yoke
k_{hys}	–	Factor for hysteresis loss in yoke
l	m	Length
l_c	m	Critical length
l_{core}	m	Length of GTF core
l_{cw}	m	Length of cryo wall
l_{eff}	m	Effective machine length
l_{gtf}	m	Length of GTF
l_m	m	Machine length
$l_{m,max}$	m	Maximum machine length
l_s	m	Length of cooling slot
l_t	m	Depth of tank
$l_{t,w}$	m	Cylindrical length of tank wall
l_{tw}	m	Twist pitch length
$l_{tw,n}^*$	m	Effective twist pitch length of n^{th} twisting stage
$l_{tw,n}$	m	Twist pitch length of n^{th} twisting stage
l_w	m	Length of wire or conductor
$L_{s,t}$	μH	Self-inductance per turn of stator coil
m	–	Number of phases
M_n	–	Normalized torque

Symbol	Unit	Explanation
M_n	–	Fourier coefficient of n^{th} harmonic
$M_{n,max}$	–	Maximum normalized torque
$M_{rec,n}$	–	Fourier coefficient of n^{th} harmonic for HTS bulk
$M_{tri,n}$	–	Fourier coefficient of n^{th} harmonic for HTS bulk
M	N m	Torque
\overline{M}	N m	Mean torque
\overline{M}_c	N m	Mean torque with excitation by coil
\overline{M}_m	N m	Mean torque with excitation by magnet
M_n	N m	Torque of n^{th} loop
\dot{M}	kg s ⁻¹	Mass flow
$\dot{M}_{b,off}$	kg s ⁻¹	Mass flow due to boil-off
\dot{M}_{core}	kg s ⁻¹ m ⁻²	Mass flow of core engine
\dot{M}_{fan}	kg s ⁻¹ m ⁻²	Bypass mass flow
\dot{M}_s	kg s ⁻¹	Mass flow of LH ₂ in stator
\dot{m}	kg s ⁻¹ m ⁻²	Mass flow rate
\dot{m}_n	kg s ⁻¹ m ⁻²	Normalized mass flow rate of heat transfer coefficient calculation
\dot{m}_{lh2}	kg s ⁻¹ m ⁻²	Mass flow rate of LH ₂
\dot{m}_v	kg s ⁻¹ m ⁻²	Vapor mass flow rate
\vec{M}	A m ⁻¹	Remanence
$M_{hal,r}$	A m ⁻¹	Radial component of remanence in Halbach array
$M_{hal,\theta}$	A m ⁻¹	Tangential component of remanence in Halbach array
M_r	A m ⁻¹	Radial component of remanence
$M_{rec,\theta}$	A m ⁻¹	Tangential component of remanence in permanent magnet
$M_{rec,r}$	A m ⁻¹	Radial component of remanence in permanent magnet
$M_{tri,r}$	A m ⁻¹	Radial component of remanence in HTS bulk
$M_{tri,\theta}$	A m ⁻¹	Tangential component of remanence in HTS bulk
M_{max}	A m ⁻¹	Maximum remanence in permanent magnet
m_a	kg	Active machine mass
m_{gtf}	kg	Mass of GTF
m_{lh2}	kg	Mass of LH ₂
m_m	kg	Machine mass
m_p	kg	Passive machine mass
m_t	kg	Mass of tank
$m_{t,min}$	kg	Minimum tank mass
Ma	–	Mach number
n	min ⁻¹	Rotational speed
\vec{n}	–	Normal vector
n	–	Harmonic number

Symbol	Unit	Explanation
n	–	Index of summation, iteration or loop
n	–	Number of twisting stages
n	–	Exponent in power-law E(J) relation
n	–	Exponent in ferromagnetic loss calculation
n_{cw}	–	Order of buckling wave
n_{max}	–	Maximum harmonic or stages
n_s	–	Single conductors per stator coil
n^*	–	Exponent of heat transfer coefficient calculation
Nu	–	Nusselt number
Nu_l	–	Nusselt number of liquid at boiling point
Nu_{sp}	–	Nusselt number at single-phase flow
$Nu_{sp,int}$	–	Nusselt number at intermediate flow and single-phase flow
$Nu_{sp,lam}$	–	Nusselt number at laminar flow and single-phase flow
$Nu_{sp,tur}$	–	Nusselt number at turbulent flow and single-phase flow
Nu_v	–	Nusselt number of vapor at dew point
o	–	Region of machine model
p	bar	Pressure
p_a	bar	Ambient pressure
p_{bur}	bar	Burst pressure
p_c	bar	Critical pressure
$p_{cw,e}$	bar	Buckling pressure in case of elastic buckling
$p_{cw,i}$	bar	Inner pressure of cryo wall
$p_{cw,o}$	bar	Outer pressure of cryo wall
$p_{cw,p}$	bar	Buckling pressure in case of plastic buckling
p_i	bar	Inner pressure
p_{in}	bar	Inlet pressure
p_o	bar	Outer pressure
p_{out}	bar	Outlet pressure
$p_{tot,i}$	bar	Total inner pressure
$p_{tot,o}$	bar	Total outer pressure
p_{tri}	bar	Pressure at triple point
p_{vent}	bar	Vent pressure
PTW	$W\ kg^{-1}$	Power-to-weight ratio
p_v	$W\ m^{-3}$	Loss density
$p_{v,s}$	$W\ m^{-3}$	Total loss density in stator coils
$p_{v,ec}$	$W\ kg^{-3}$	Gravimetric eddy current loss
$p_{v,exc}$	$W\ kg^{-3}$	Gravimetric excess loss
$p_{v,fe}$	$W\ kg^{-3}$	Total gravimetric iron loss
$p_{v,hys}$	$W\ kg^{-3}$	Gravimetric hysteresis loss

Symbol	Unit	Explanation
P'_v	W m^{-1}	Loss per unit length
p'_v	W m^{-1}	Instantaneous loss per unit length
$P'_{v,cc}$	W m^{-1}	Coupling current loss per unit length
$P'_{v,e}$	W m^{-1}	Eddy current loss per unit length
$P'_{v,fe}$	W m^{-1}	Ferromagnetic loss per unit length
$P'_{v,mag}$	W m^{-1}	Magnetization loss per unit length
$P'_{v,oc}$	W m^{-1}	Overcurrent transport loss per unit length
$P'_{v,tot}$	W m^{-1}	Total AC loss per unit length
$p_{c,n}$	N m^{-2}	Normalized critical pressure of heat transfer coefficient calculation
P	W	Mechanical power
P_v	W	Loss
$P_{v,cc}$	W	Coupling current loss
$P_{v,e}$	W	Eddy current loss
$P_{v,fe}$	W	Iron loss
$P_{v,fe}$	W	Ferromagnetic loss
$P_{v,mag}$	W	Magnetization loss
$P_{v,oc}$	W	Overcurrent transport loss
$P_{v,s}$	W	Stator loss
$P_{v,tot}$	W	Total AC loss
Pr	W	Prandtl number
P_r	€	Target price of rotor coils / magnets
P_s	€	Target price of stator coils
p_{sc}	€A ⁻¹ m ⁻¹	Price performance ratio of superconductor
p	–	Number of pole pairs
p^*	–	Normalized pressure
$P_{v,n,s}$	–	Normalized stator AC loss
\dot{q}	W m^{-2}	Heat flux
\dot{q}_b	W m^{-2}	Heat flux of barrier
$\dot{q}_{cr,PB}$	W m^{-2}	Reference heat flux of heat transfer coefficient calculation
\dot{q}_{cu}	W m^{-2}	Heat flux of Cu
\dot{q}_{ins}	W m^{-2}	Heat flux of insulation
\dot{q}_{ma}	W m^{-2}	Heat flux of matrix
\dot{q}_{sc}	W m^{-2}	Heat flux of MgB ₂
\dot{q}_n	W m^{-2}	Normalized heat flux of heat transfer coefficient calculation
\dot{q}_{on}	W m^{-2}	Heat flux to overheat wall
\dot{q}_{sh}	W m^{-2}	Heat flux of sheath
$\dot{Q}_{b,off}$	W	Heat flow rate due to boil-off

Symbol	Unit	Explanation
\dot{Q}_{rad}	W	Heat flow rate due to radiation
$Q_{v,fe}$	J m^{-3}	Ferromagnetic loss density
$Q_{v,cc}$	J m^{-3}	Coupling current loss density
$Q_{v,mag}$	J m^{-3}	Magnetization loss density
r	m	Radius
r_b	m	Bending radius
$r_{b,c}$	m	Critical bending radius
r_{co}	m	Radius of wire core
$r_{cw,o}$	m	Outer radius of cryo wall
$r_{cw,i}$	m	Inner radius of cryo wall
r_{fc}	m	Radius of filamentary core
r_{fil}	m	Filament radius
r_i	m	Inner radius
$r_{mag,i}$	m	Inner radius of magnet
$r_{mag,o}$	m	Outer radius of magnet
R_n	m	Outer radius of n^{th} twisting stage
r_n	m	Twist radius of n^{th} twisting stage
r_{nc}	m	Radius of normal conductor
r_o	m	Outer radius
$r_{ag,m}$	m	Middle air gap radius
$r_{r,b}$	m	Bending radius of rotor coil
$r_{r,b,c}$	m	Critical rotor bending radius
$r_{r,b,i}$	m	Inner bending radius of rotor coil
$r_{r,b,o}$	m	Outer bending radius of rotor coil
$r_{r,i}$	m	Inner radius of rotor
$r_{r,m}$	m	Middle radius of rotor
$r_{r,o}$	m	Outer radius of rotor
$r_{rot,i}$	m	Inner radius of rotor carrier
$r_{rot,o}$	m	Outer radius of rotor carrier
$r_{s,b}$	m	Bending radius of stator coil
$r_{s,b,c}$	m	Critical stator bending radius
$r_{s,b,i}$	m	Inner bending radius of stator coil
$r_{s,b,o}$	m	Outer bending radius of stator coil
$r_{s,m}$	m	Middle radius of stator
$r_{s,o}$	m	Outer radius of stator
r_{sc}	m	Radius of superconductor
$r_{s,i}$	m	Inner radius of stator
$r_{sl,i}$	m	Inner radius of sleeve
$r_{sl,o}$	m	Outer radius of sleeve
$r_{t,i}$	m	Inner radius of tank

Symbol	Unit	Explanation
$r_{t,w}$	m	Radius of tank wall
$r_{y,i}$	m	Inner radius of yoke
$r_{y,o}$	m	Outer radius of yoke
R_w	m	Roughness of wall surface
$R_{w,n}$	m	Normalized roughness of wall surface of heat transfer coefficient calculation
r_{wire}	m	Outer radius of wire
R_{dc}	Ω	DC resistance
R_{nc}	Ω	Resistance of normal conductor
R'_{dc}	$\Omega \text{ m}^{-1}$	DC resistance per unit length
R'_{nc}	$\Omega \text{ m}^{-1}$	Resistance of normal conductor per unit length
R_{th}	K W^{-1}	Thermal resistance
Ra	–	Rayleigh number
Re	–	Reynolds number
RRR	–	Residual-resistance ratio
s	m	Length
s	m	Cooling gap thickness
s_{lh2}	m	LH ₂ cooling slot thickness
s	$\text{J kg}^{-1} \text{ K}^{-1}$	Specific entropy
t	s	Time
T	s	Period of time
$t_{f,max}$	s	Maximum flight time
T	K	Temperature
T_a	K	Ambient temperature
T_c	K	Critical temperature
T_{fl}	K	Temperature of fluid
T_{hot}	K	Temperature at hot spot
T_{in}	K	Inlet temperature
T_{lh2}	K	LH ₂ temperature
T_{max}	K	Maximum temperature
T_{out}	K	Outlet temperature
$T_{r,min}$	K	Minimum operation temperature of rotor
$T_{r,max}$	K	Maximum operation temperature of rotor
T_{rt}	K	Room temperature
T_s	K	Temperature distribution in stator coils
$T_{s,max}$	K	Maximum temperature in stator coils
T_{sc}	K	Temperature of superconductor
$T_{sc,max}$	K	Maximum SC temperature
T_{tri}	K	Temperature at triple point
T_w	K	Wall temperature

Symbol	Unit	Explanation
TTW	Nm kg^{-1}	Torque-to-weight ratio
U	V	Voltage
$U_{i,t,1}$	V	Induced voltage of fundamental wave per turn of stator coil
U_{fl}	m	Circumference of non-circular tube
u_{cw}	–	Out of roundness factor of cryo wall
V	m^3	Volume
V_{lh2}	m^3	Volume of LH ₂
V_{sc}	m^3	Volume of superconducting coils
V_t	m^3	Volume of tank
\dot{V}	$\text{m}^3 \text{s}^{-1}$	Volume flow rate in cooling slot
w_m	m s^{-1}	Flow velocity at average temperature / mean flow velocity
w_{sp}	m s^{-1}	Flow velocity of single-phase flow
\dot{x}	–	Vapor quality
\dot{x}_{in}	–	Vapor quality at the beginning of cooling channel
\dot{x}_{out}	–	Vapor quality at the ending of cooling channel
x_{ana}	–	Analytical specific physical quantity
x_{fem}	–	Specific physical quantity by FEM
X_{tt}	–	Martinelli parameter of turbulent flow in both phases
yr	yr	Year
z	m	Length in z -direction
α	–	Parameter for critical current calculation
α	$\text{W m}^{-2} \text{K}^{-1}$	Heat transfer coefficient
α_b	$\text{W m}^{-2} \text{K}^{-1}$	Heat transfer coefficient of nucleate boiling
α_k	$\text{W m}^{-2} \text{K}^{-1}$	Heat transfer coefficient of convective boiling
α_{l0}	$\text{W m}^{-2} \text{K}^{-1}$	Heat transfer coefficient at liquid phase
α_{v0}	$\text{W m}^{-2} \text{K}^{-1}$	Heat transfer coefficient at vapor phase
α_{sp}	$\text{W m}^{-2} \text{K}^{-1}$	Heat transfer coefficient of single-phase flow
α_0	%	Coverage of stator with coils
α_1	%	Coverage of rotor with magnets
α_2	deg	Inner angle of rotor coil
α_3	deg	Angle between adjacent rotor coils
$\alpha_{mag,t,r}$	K^{-1}	Radial thermal expansion coefficient of magnets
$\alpha_{rot,t,\theta}$	K^{-1}	Tangential thermal expansion coefficient of rotor carrier
$\alpha_{sl,t,\theta}$	K^{-1}	Tangential thermal expansion coefficient of sleeve
α_t	K^{-1}	Thermal expansion coefficient
α_n	$\text{W m}^{-2} \text{K}^{-1}$	Normalized heat transfer coefficient of heat transfer coefficient calculation
α_{tp}	$\text{W m}^{-2} \text{K}^{-1}$	Heat transfer coefficient at two-phase flow

Symbol	Unit	Explanation
α_w	$\text{W m}^{-2} \text{K}^{-1}$	Heat transfer coefficient at wall
β	–	Normalized flux density amplitude
β	–	Parameter for critical current calculation
Γ	–	Loss factor in magnetization loss calculation
δ_s	m	Skin depth
$\delta_{\omega,r}$	m	Radial displacement due to centrifugal force
$\delta_{mag,r}$	m	Radial displacement in magnet
$\delta_{p,r}$	m	Radial displacement due to inner or outer pressure
$\delta_{rot,r}$	m	Radial displacement in rotor carrier
$\delta_{sl,r}$	m	Radial displacement in sleeve
$\delta_{t,r}$	m	Radial displacement due to thermal expansion
$\delta_{tot,r}$	m	Total radial displacement
Δl_w	m	Length of cooling channel section
Δp	bar	Pressure drop, pressure difference
Δp_{acce}	bar	Accelerational pressure drop
Δp_{fric}	bar	Frictional pressure drop
Δp_{grav}	bar	Gravitational pressure drop
Δp_{sp}	bar	Pressure drop at single-phase flow
Δp_{tot}	bar	Total pressure drop
Δp_{tp}	bar	Pressure drop at two-phase flow
ΔT	K	Temperature difference
Δh_v	J kg^{-1}	Evaporation enthalpy
$\Delta \dot{x}$	–	Change of vapor quality
ε	–	Emissivity
ε_a	–	Absolute error
$\varepsilon_{a,b}$	T	Absolute error of flux density
$\varepsilon_{b,c}$	%	Critical bending strain
ε_f	–	Fraction of filaments in filamentary core
ε_n	–	Average void fraction of n^{th} stage
ε_r	%	Relative error
$\varepsilon_{r,b}$	%	Relative error of flux density
η	$\text{kg m}^{-1} \text{s}^{-1}$	Dynamic viscosity
η_l	$\text{kg m}^{-1} \text{s}^{-1}$	Dynamic viscosity of liquid at boiling point
η_m	$\text{kg m}^{-1} \text{s}^{-1}$	Dynamic viscosity at average temperature
η_v	$\text{kg m}^{-1} \text{s}^{-1}$	Dynamic viscosity of vapor at dew point
η	%	Efficiency
η_n	–	Contact area ratio of n^{th} twisting stage
θ	deg, rad	Mechanical angle, angular coordinate
θ_{el}	deg, rad	Electrical angle
θ_{load}	deg, rad	Load angle of machine

Symbol	Unit	Explanation
θ_{sc}	deg, rad	Rotation angle of superconductor
λ	$\text{W m}^{-1} \text{K}^{-1}$	Thermal conductivity
λ_b	$\text{W m}^{-1} \text{K}^{-1}$	Thermal conductivity of barrier
λ_{cu}	$\text{W m}^{-1} \text{K}^{-1}$	Thermal conductivity of Cu
λ_{cuni}	$\text{W m}^{-1} \text{K}^{-1}$	Thermal conductivity of CuNi
λ_{ins}	$\text{W m}^{-1} \text{K}^{-1}$	Thermal conductivity of insulation
λ_l	$\text{W m}^{-1} \text{K}^{-1}$	Thermal conductivity of liquid at boiling point
λ_m	$\text{W m}^{-1} \text{K}^{-1}$	Thermal conductivity at average liquid temperature
λ_{ma}	$\text{W m}^{-1} \text{K}^{-1}$	Thermal conductivity of matrix
λ_{nb}	$\text{W m}^{-1} \text{K}^{-1}$	Thermal conductivity of Nb
λ_{sc}	$\text{W m}^{-1} \text{K}^{-1}$	Thermal conductivity of MgB_2
λ_{sh}	$\text{W m}^{-1} \text{K}^{-1}$	Thermal conductivity of sheath
$\lambda_{t,ins}$	$\text{W m}^{-1} \text{K}^{-1}$	Thermal conductivity of tank insulation
$\lambda_{t,w}$	$\text{W m}^{-1} \text{K}^{-1}$	Thermal conductivity of tank wall
$\lambda_{t,w1}$	$\text{W m}^{-1} \text{K}^{-1}$	Thermal conductivity of inner tank wall
$\lambda_{t,w2}$	$\text{W m}^{-1} \text{K}^{-1}$	Thermal conductivity of outer tank wall
λ_v	$\text{W m}^{-1} \text{K}^{-1}$	Thermal conductivity of vapor at dew point
λ_w	$\text{W m}^{-1} \text{K}^{-1}$	Thermal conductivity of wire
μ_0	$\text{Vs A}^{-1} \text{m}^{-1}$	Vacuum permeability
μ_{fe}	–	Permeability of yoke
μ_r	–	Relative permeability
μ_σ	–	Static friction coefficient between magnet and rotor carrier
ν	–	Poisson's ratio
ν	–	Order of harmonic, ν^{th} order of Bessel function
ν_{sl}	–	Poisson's ratio of sleeve
ν_{cw}	–	Poisson's ratio of cryo wall
ν_{rot}	–	Poisson's ratio of rotor carrier
ξ	–	Factor for Nusselt number calculation
ξ	–	Relative thickness in eddy current loss calculation
π	–	Number π
ρ	Ωm	Electrical resistivity
ρ_b	Ωm	Effective resistivity of wires
ρ_{co}	Ωm	Electrical resistivity of core
ρ_{cu}	Ωm	Electrical resistivity of Cu
ρ_{cuni}	Ωm	Electrical resistivity of CuNi
$\rho_{m,eff}$	Ωm	Effective transverse resistivity of matrix
ρ_n^*	Ωm	Effective resistivity of n^{th} twisting stage
ρ_{nb}	Ωm	Electrical resistivity of Nb
ρ_{nc}	Ωm	Electrical resistivity of normal conductor

Symbol	Unit	Explanation
ρ_{sh}	$\Omega \text{ m}$	Electrical resistivity of sheath
ρ_{st}	$\Omega \text{ m}$	Electrical resistivity of stabilizer
ρ	kg m^{-3}	Volumetric mass density
ρ_{cw}	kg m^{-3}	Volumetric mass density of cryo wall
ρ_{fe}	kg m^{-3}	Volumetric mass density of yoke sheet metal
ρ_l	kg m^{-3}	Volumetric mass density of liquid at boiling point
ρ_{lh_2}	kg m^{-3}	Volumetric mass density of LH ₂
ρ_m	kg m^{-3}	Volumetric mass density at average temperature
$\rho_{m,lv}$	kg m^{-3}	Mean volumetric mass density between liquid and vapor state
ρ_{mag}	kg m^{-3}	Volumetric mass density of magnet
ρ_{rot}	kg m^{-3}	Volumetric mass density of rotor carrier
ρ_{sl}	kg m^{-3}	Volumetric mass density of sleeve
ρ_v	kg m^{-3}	Volumetric mass density of vapor at dew point
σ	$\text{W m}^{-2} \text{ K}^{-4}$	Stefan-Boltzmann constant
σ_l	N m^{-1}	Surface tension of liquid
σ_{fe}	S m^{-1}	Electrical conductivity of yoke
$\sigma_{\theta,sl,allow}$	Pa	Allowable tangential stress in sleeve
$\sigma_{cw,\omega,\theta}$	Pa	Tangential stress due to centrifugal forces in cryo wall
$\sigma_{cw,p,\theta}$	Pa	Tangential stress due to external pressure in cryo wall
$\sigma_{cw,\theta}$	Pa	Tangential stress in cryo wall
$\sigma_{sl,\theta}$	Pa	Tangential stress in sleeve
σ_t	Pa	Maximum allowable stress of tank wall
$\tau_{m,\theta}$	Pa	Tangential shear stress due to torque
τ_n	s	Coupling time constant of n^{th} twisting stage
τ_{tot}	s	Total coupling time constant
ϕ	A	Magnetic scalar potential
ϕ_o	A	Magnetic scalar potential in region o
$\vec{\Phi}$	V m s^{-1}	Magnetic vector potential
$\Phi_{z,o}$	V m s^{-1}	Magnetic vector potential in z -direction and region o
Φ_y	Wb	Flux through cross section of yoke
$\Phi_{l,tt}^2$	—	Lockhart-Martinelli multiplier of liquid phase and turbulent flow in both phases
ϕ_{21}	—	View factor
ω	Hz, s^{-1}	Angular frequency, angular speed
ω_n	Hz, s^{-1}	Nominal angular speed
ω_w	Hz, s^{-1}	Whirl angular speed

Bibliography

- [1] M. S. Hossain: *Panel estimation for CO₂ emissions, energy consumption, economic growth, trade openness and urbanization of newly industrialized countries*, Energy Policy, 39(11):6991–6999, 2011.
- [2] N. L. Bindoff, P. A. Stott, K. M. AchutaRao, M. R. Allen, N. Gillett, D. Gutzler, K. Hansingo, G. Hegerl, Y. Hu, S. Jain, I. I. Mokhov, J. Overland, J. Perlwitz, R. Sebbari, X. Zhang et al.: *Chapter 10 - Detection and Attribution of Climate Change: from Global to Regional*, Climate Change 2013: The Physical Science Basis, Cambridge, U.K., 2013.
- [3] T. R. Anderson, E. Hawkins and P. D. Jones: *CO₂, the greenhouse effect and global warming: from the pioneering work of Arrhenius and Callendar to today's Earth System Models*, Endeavour, 40(3):178–187, 2016.
- [4] M. Crippa, G. Oreggioni, D. Guizzardi, M. Muntean, E. Schaaf, E. Lo Vullo, E. Solazzo, F. Monforti-Ferrario, J. G. J. Olivier and E. Vignati: *Fossil CO₂ and GHG emissions of all world countries - 2019 report*, EUR 29849 EN, Publications Office of the European Union, Luxembourg, 2019.
- [5] International Energy Agency: *Transport sector CO₂ emissions by mode in the Sustainable Development Scenario: 2000-2030*, URL: <https://www.iea.org/data-and-statistics/charts/transport-sector-co2-emissions-by-mode-in-the-sustainable-development-scenario-2000-2030>, 15.12.2019.
- [6] B. Graver, K. Zhang and D. Rutherford: *CO₂ emissions from commercial aviation, 2018*, The international council on clean transportation, 2019.
- [7] D. S. Lee, D. W. Fahey, P. M. Forster, P. J. Newton, R. C. N. Wit, L. L. Lim, B. Owen and R. Sausen: *Aviation and global climate change in the 21st century*, Atmospheric Environment, 43(22-23):3520-3537, 2009.
- [8] J. E. Penner, D. H. Lister, D. J. Griggs, D. J. Dokken and M. McFarland: *IPCC Special Report on Aviation and the Global Atmosphere*, Intergovernmental Panel on Climate Change, Geneva, Switzerland, 1999.
- [9] R. Derwent, W. Collins, C. Johnson and D. Stevenson: *Global Ozone Concentrations and Regional Air Quality*, Environmental science & technology, 36(19):379A–382A, 2002.
- [10] European Aviation Safety Agency: *Type Certificate Data Sheet for Noise (TCDN): No. EASA.A.064.3 for AIRBUS A320*, 2020.
- [11] International Civil Aviation Organization: *Environmental technical manual: Volume I Procedures for the Noise Certification of Aircraft*, 9501 AN/929, 2nd edition, Montréal, Canada, 2015.

- [12] M. K. Bradley and C. K. Droney: *Subsonic Ultra Green Aircraft Research: Phase I Final Report*, National Aeronautics and Space Administration, NASA/CR-2011-216847, 2011.
- [13] N. Shibahara, H. Kato and Y. Hayashi: *A Methodology for Identifying Lower Carbon Transport Systems for Inter-regional Passengers: Rail vs Aviation*, 12th World Conference on Transport Research, Lisbon, Portugal, 2010.
- [14] Airbus S.A.S.: *Global market forecast: Cities, Airports & Aircraft 2019-2038*, Blagnac Cedex, France, 2019.
- [15] B. Owen and D. S. Lee: *Allocation of International Aviation Emissions from Scheduled Air Traffic—Future Cases, 2005 to 2050*, Centre for Air Transport and the Environment, Manchester Metropolitan University, U.K., 2006.
- [16] R. Berghof, A. Schmitt, C. Eyers, K. Haag, J. Middel, M. Hepting, A. Grübler and R. Hancox: *CONSAVE 2050 Final Technical Report*, DLR, Köln, Germany, 2005.
- [17] Aislelabs: *How Airports Globally are Responding to Coronavirus*, URL: <https://new.engineering.com/eng/story/fully-superconducting-motor-prepares-for-testing>, 25.10.2019.
- [18] S. V. Gudmundsson, M. Cattaneo and R. Redondi: *Forecasting recovery time in air transport markets in the presence of large economic shocks: COVID-19*, SSRN 3623040, 2020.
- [19] M. Darecki, C. Edelstenne, T. Enders, E. Fernandez, P. Hartman, J. P. Herteman, M. Kerkloh, I. King, P. Ky, M. Mathieu et al.: *Flightpath 2050 Europe's Vision for Aviation*, European Commission, Publications Office of the European Union, Luxembourg, 2011.
- [20] J. Faber, D. Greenwood, D. Lee, M. Mann, P. M. de Leon, D. Nelissen, B. Owen, M. Ralph, J. Tilston, A. van Velzen et al.: *Lower NO_x at Higher Altitudes: Policies to Reduce the Climate Impact of Aviation NO_x Emission*, CE Delft Solutions for environment, economy and technology, Delft, The Netherlands, 2008.
- [21] J. Delfs, L. Bertsch, C. Zellmann, L. Rossian, E. Kian Far, T. Ring and S. Langer: *Aircraft Noise Assessment—From Single Components to Large Scenarios*, *Energies*, 11(2):429, 2018.
- [22] L. Leylekian, M. Lebrun and P. Lempereur: *An Overview of Aircraft Noise Reduction Technologies*, *AerospaceLab Journal* 7, 2014.
- [23] European Aviation Safety Agency: *European aviation environmental report 2019* Publications Office of the European Union, Luxembourg, 2019.
- [24] ASTM D4054-17: *Standard Practice for Qualification and Approval of New Aviation Turbine Fuels and Fuel Additives*, ASTM International, West Conshohocken, U.S.A., 2017.

-
- [25] ASTM D7566-20: *Standard Specification for Aviation Turbine Fuel Containing Synthesized Hydrocarbons*, ASTM International, West Conshohocken, U.S.A., 2020.
- [26] M. C. Vásquez, E. E. Silva and E. F. Castillo: *Hydrotreatment of vegetable oils: A review of the technologies and its developments for jet biofuel production*, *Biomass and Bioenergy*, 105:197–206, 2017.
- [27] P. Schmidt, V. Batteiger, A. Roth, W. Weindorf and T. Raksha: *Power-to-Liquids as Renewable Fuel Option for Aviation: A Review*, *Chemie Ingenieur Technik*, 90(1-2):127–140, 2018.
- [28] B. Sarlioglu and C. T. Morris: *More Electric Aircraft: Review, Challenges and Opportunities for Commercial Transport Aircraft*, *IEEE Transactions on Transportation Electrification*, 1(1):54–64, 2015.
- [29] M. Sinnett: *787 No-Bleed Systems: Saving Fuel and Enhancing Operational Efficiencies*, *Aero Quarterly*, 18:6–11, 2007.
- [30] F. Re: *Viability and state of the art of environmentally friendly aircraft taxiing systems*, 2012 IEEE Electrical Systems for Aircraft, Railway and Ship Propulsion, 1–6, 2012.
- [31] F. Re: *Model-based Optimization, Control and Assessment of Electric Aircraft Taxi Systems*, PhD thesis, Technical University of Darmstadt, Darmstadt, Germany, 2017.
- [32] B. Lukasik and W. Wisniowski: *All-electric propulsion for future business jet aircraft: A feasibility study*, *Proceedings of the Institution of Mechanical Engineers, Part G: Journal of Aerospace Engineering*, 231(12):2203–2213, 2017.
- [33] A. H. Epstein and S. M. O’Flarity: *Considerations for Reducing Aviation’s CO₂ with Aircraft Electric Propulsion*, *Journal of Propulsion and Power*, 35(3):572–582, 2019.
- [34] J. Christensen, P. Albertus, R. S. Sanchez-Carrera, T. Lohmann, B. Kozinsky, R. Liedtke, J. Ahmed and A. Kojic: *A Critical Review of Li/Air Batteries*, *Journal of The Electrochemical Society*, 159(2):R1–R30, 2011.
- [35] T. Kadyk, C. Winnefeld, R. Hanke-Rauschenbach and U. Krewer: *Analysis and Design of Fuel Cell Systems for Aviation*, *Energies*, 11(2):375, 2018.
- [36] E. Middelmann, W. Kout, B. Vogelaar, J. Lenssen and E. de Waal: *Bipolar plates for PEM fuel cells*, *Journal of Power Sources*, 118(1-2):44–46, 2003.
- [37] J. L. Felder, G. V. Brown, H. Dae Kim and J. Chu: *Turboelectric Distributed Propulsion in a Hybrid Wing Body Aircraft*, 20th International Society for Airbreathing Engines, 2011.

- [38] J. Welstead and J. L. Felder: *Conceptual Design of a Single-Aisle Turboelectric Commercial Transport with Fuselage Boundary Layer Ingestion*, 54th AIAA Aerospace Sciences Meeting, 1027, 2016.
- [39] M. Filipenko, S. Biser, M. Boll, M. Corduan, M. Noe and P. Rostek: *Comparative Analysis and Optimization of Technical and Weight Parameters of Turbo-Electric Propulsion Systems*, *Aerospace*, 7(8):107, 2020.
- [40] K. R. Antcliff, M. D. Guynn, T. Marien, D. P. Wells, S. J. Schneider and M. J. Tong: *Mission Analysis and Aircraft Sizing of a Hybrid-Electric Regional Aircraft*, 54th AIAA Aerospace Sciences Meeting, 1028, 2016.
- [41] R. Rings, J. Ludowicy, D. F. Finger and C. Braun: *Sizing studies of light aircraft with parallel hybrid propulsion systems*, 67. Deutscher Luft-und Raumfahrtkongress DLRK, 2018.
- [42] A. M. Stoll, J. B. Bevirt, M. D. Moore, W. J. Fredericks and N. K. Borer: *Drag Reduction Through Distributed Electric Propulsion*, 14th AIAA Aviation Technology, Integration, and Operations Conference, 2851, 2014.
- [43] N. K. Borer, M. D. Patterson, J. K. Viken, M. D. Moore, S. Clarke, M. E. Redifer, R. J. Christie, A. M. Stoll, A. Dubois, J. B. Bevirt, A. R. Gibson, T. J. Foster and P. G. Osterkamp: *Design and Performance of the NASA SCEPTOR Distributed Electric Propulsion Flight Demonstrator*, 16th AIAA Aviation Technology, Integration, and Operations Conference, 3920, 2016.
- [44] J. Schömann: *Hybrid-electric propulsion systems for small unmanned aircraft*, PhD thesis, Technical University of Munich, Munich, Germany, 2014.
- [45] European Aviation Safety Agency: *Type Certificate data sheet: No. IM.E.093 for PW1100G-JM Series Engines*, 2019.
- [46] F. Berg, J. Palmer, P. Miller and G. Dodds: *HTS System and Component Targets for a Distributed Aircraft Propulsion System*, *IEEE Transactions on Applied Superconductivity*, 27(4):1–7, 2017.
- [47] P. Wheeler: *Technology for the More and All Electric Aircraft of the Future*, 2016 IEEE International Conference on Automatica (ICA-ACCA), 1–5, IEEE, 2016.
- [48] M. Abdel-Salam, H. Anis, A. El-Morshedy and R. Radwan: *High-Voltage Engineering: Theory and Practice, Second Edition, Revised and Expanded*, CRC Press, 2018
- [49] I. Cotton, A. Nelms and M. Husband: *Higher Voltage Aircraft Power Systems*, *IEEE Aerospace and Electronic Systems Magazine*, 23(2):25–32, 2008.
- [50] B. H. Nya, J. Brombach and D. Schulz: *Benefits of Higher Voltage Levels in Aircraft Electrical Power Systems*, 2012 IEEE Electrical Systems for Aircraft, Railway and Ship Propulsion, 1–5, 2012.

-
- [51] G. A. Whyatt and L. A. Chick: *Electrical Generation for More-Electric Aircraft using Solid Oxide Fuel Cells*, No. PNNL-21382, Pacific Northwest National Laboratory, Richland, U.S.A., 2012.
- [52] M. Boll, M. Corduan, S. Biser, M. Filipenko, Q. H. Pham, S. Schlachter, P. Rostek and M. Noe: *A holistic system approach for short range passenger aircraft with cryogenic propulsion system*, *Superconductor Science and Technology*, 33(4):044014, 2020.
- [53] H. K. Onnes: *Further experiments with liquid helium. C. On the change of electric resistance of pure metals at very low temperatures etc. IV. The resistance of pure mercury at helium temperatures*, *KNAW, Proceedings*, 13, 1274-1276, Amsterdam, 1911.
- [54] W. Buckel and R. Kleiner: *Supraleitung: Grundlagen und Anwendungen*, John Wiley & Sons, 7. Auflage, Weinheim, Germany, 2013.
- [55] K. Fossheim and A. Sudbø: *Superconductivity: Physics and Applications*, John Wiley & Sons, Chichester, U.K., 2005.
- [56] P. J. Ray: *Structural Investigation of $La(2-x)Sr(x)CuO(4+y)$: Following a Staging as a Function of Temperature*, Master thesis, University of Copenhagen, Copenhagen, Denmark, 2015.
- [57] Z. Fisk, J. D. Thompson, E. Zirngiebl, J. L. Smith and S-W. Cheong: *Superconductivity of rare earth-barium-copper oxides*, *Solid State Communications*, 62(11):743–744, 1987.
- [58] G. F. Sun, K. W. Wong, B. R. Xu, Y. Xin and D. F. Lu: *T_c enhancement of $HgBa_2Ca_2Cu_3O_{8+\delta}$ by Tl substitution*, *Physics Letters A*, 192(1):122–124, 1994.
- [59] P. Kittel: *Cryocooler Performance Estimator*, *International Cryocooler Conference*, 14:777–780, 2007.
- [60] J. Pyrhönen, T. Jokinen, V. Hrabovcová and H. Niemelä: *Design of Rotating Electrical Machines*, John Wiley & Sons, Chichester, U.K., 2014.
- [61] A. Binder: *Elektrische Maschinen und Antriebe: Grundlagen, Betriebsverhalten*, Springer, Berlin and Heidelberg, 2012.
- [62] X. Zhang and K. S. Haran: *High-Specific-Power Electric Machines for Electrified Transportation Applications—Technology Options*, 2016 IEEE Energy Conversion Congress and Exposition, 1–8, 2016.
- [63] R. A. Marshall: *3000 horsepower superconductive field acyclic motor*, *IEEE Transactions on Magnetics*, 19(3):876–879, 1983.
- [64] B. B. Gamble and T. A. Keim: *High-Power-Density Superconducting Generator*, *Journal of Energy*, 6(1):38–44, 1982.

- [65] K. Sivasubramaniam, T. Zhang, M. Lokhandwalla, E. T. Laskaris, J. W. Bray, B. Gerstler, M. R. Shah and J. P. Alexander: *Development of a High Speed HTS Generator for Airborne Applications*, IEEE Transactions on Applied Superconductivity, 19(3):1656–1661, 2009.
- [66] C. A. Luongo, P. J. Masson, T. Nam, D. Mavris, H. D. Kim, G. V. Brown, M. Waters and D. Hall: *Next Generation More-Electric Aircraft: A Potential Application for HTS Superconductors*, IEEE Transactions on Applied Superconductivity, 19(3):1055–1068, 2009.
- [67] K. Kovalev, N. Ivanov, I. Kobzeva and E. Tulinova: *High specific power HTS electric machines*, Przegląd Elektrotechniczny, 93(11):125–128, 2017.
- [68] P. C. Michael, J. Kvitkovic, S. V. Pamidi, P. J. Masson and L. Bromberg: *Development of MgB₂-Cabled Conductors for Fully Superconducting Rotating Electric Machines*, IEEE Transactions on Applied Superconductivity, 27(4):1–5, 2017.
- [69] M. Feddersen, K. S. Haran and F. Berg: *AC Loss Analysis of MgB₂-Based Fully Superconducting Machines*, IOP Conference Series: Materials Science and Engineering, 279:012026, 2017.
- [70] C. D. Manolopoulos, M. F. Iacchetti, A. C. Smith, P. M. Tuohy, X. Pei, M. Husband and P. Miller: *Design of Superconducting AC Propulsion Motors for Hybrid Electric Aerospace*, AIAA/IEEE Electric Aircraft Technologies Symposium, 1–9, 2018.
- [71] R. H. Jansen, Y. de Jesus-Arce, P. Kascak, R. Dyson, A. Woodworth, J. Scheidler, R. Edwards, E. Stalcup, J. Wilhite, K. Duffy, P. Passe and S. McCormick: *High Efficiency Megawatt Motor Conceptual Design*, 2018 Joint Propulsion Conference, 2018.
- [72] J. Muelaner: *Fully Superconducting Motor Prepares for Testing: Extreme power-to-weight ratio and efficiency will be key to electrification of aviation*, URL: <https://new.engineering.com/eng/story/fully-superconducting-motor-prepares-for-testing>, 10.12.2019.
- [73] A. Perez, R. R. van der Woude and R. Dekker: *Rotor Cooling Concept for the ASuMED Superconductive Motor*, IOP Conference Series: Materials Science and Engineering, 502:012139, 2019.
- [74] F. Grilli, T. Benkel, J. Hänisch, M. Lao, T. Reis, E. Berberich, S. Wolfstädler, C. Schneider, P. Miller, C. Palmer, B. Glowacki, V. Climente-Alarcon, A. Smara, L. Tomkow, J. Teigelkötter, A. Stock, J. Büdel, Loïc Jeunesse, M. Staempflin, G. Delautre, B. Zimmermann, R. van der Woude, A. Perez, S. Samoilenkov, A. Molodyk, E. Pardo, M. Kapolka, S. Li and A. Dadhich: *Superconducting motors for aircraft propulsion: The Advanced Superconducting Motor Experimental Demonstrator project*, Journal of Physics: Conference Series, 1590(1):012051, 2020.

-
- [75] Y. Terao, A. Seta, H. Ohsaki, H. Oyori and N. Morioka: *Lightweight Design of Fully Superconducting Motors for Electrical Aircraft Propulsion Systems*, IEEE Transactions on Applied Superconductivity, 29(5):1–5, 2019.
- [76] K. S. Haran, S. Kalsi, T. Arndt, H. Karmaker, R. Badcock, B. Buckley, T. Haugan, M. Izumi, D. Loder, J. W. Bray, P. Masson and E. W. Stautner: *High power density superconducting rotating machines—development status and technology roadmap*, Superconductor Science and Technology, 30(12):123002, 2017.
- [77] M. Filipenko, L. Kühn, T. Gleixner, M. Thummet, M. Lessmann, D. Möller, M. Böhm, A. Schröter, K. Häse, J. Grundmann, M. Wilke, M. Frank, P. van Hasselt, J. Richter, M. Herranz-Garcia, C. Weidemann, A. Spangolo and M. Klöpzig: *Concept design of a high power superconducting generator for future hybrid-electric aircraft*, Superconductor Science and Technology, 33(5):054002, 2020.
- [78] M. Komiya, T. Aikawa, H. Sasa, S. Miura, M. Iwakuma, T. Yoshida, T. Sasayama, A. Tomioka, M. Konno and T. Izumi: *Design Study of 10 MW REBCO Fully Superconducting Synchronous Generator for Electric Aircraft*, IEEE Transactions on Applied Superconductivity, 29(5):1–6, 2019.
- [79] P. M. Grant: *Potential Electric Power Applications for Magnesium Diboride*, Materials Research Society Proceedings Library Archive, 689:E1.1, 2001.
- [80] R. Wesche: *Physical Properties of High-Temperature Superconductors*, John Wiley & Sons, Chichester, U.K., 2015.
- [81] A. Ballarino and R. Flükiger: *Status of MgB_2 wire and cable applications in Europe*, Journal of Physics: Conference Series, 871:012098, 2017.
- [82] R. F. Service: *MgB_2 Trades Performance for A Shot at the Real World*, Science, 295(5556):786–788, 2002.
- [83] M. Tomsic: *Commercial Rules for Making Money with Superconducting Applications*, NIST Physical Measurement Laboratory, Gaithersburg, U.S.A., 08.09.2015.
- [84] Q. H. Pham: *Modellierung elektrischer Maschinen mit HTS Statorwicklungen*, Master thesis, Karlsruher Institut für Technologie, Karlsruhe, Deutschland, 2020.
- [85] M. Tomsic, M. A. Rindfleisch, J. Yue, K. McFadden, D. Doll, J. Phillips, M. D. Sumption, M. Bhatia, S. Bohnenstiehl and E. W. Collings: *Development of magnesium diboride (MgB_2) wires and magnets using in situ strand fabrication method*, Physica C: Superconductivity, 456(1-2):203–208, 2007.
- [86] F. Wan, M. D. Sumption, M. A. Rindfleisch, M. J. Tomsic and E. W. Collings: *Architecture and Transport Properties of Multifilamentary MgB_2 Strands for MRI and Low AC Loss Applications*, IEEE Transactions on Applied Superconductivity, 27(4):1–5, 2017.

- [87] M. D. Sumption, F. Wan, M. A. Rindfleisch and M. J. Tomsic: *AC Loss of Superconducting Materials- refined loss estimates for very high density motors and generators for hybrid-electric aircraft: MgB₂ wires, Coated conductor tapes and wires*, AIAA Propulsion and Energy 2019 Forum, 4495, 2019.
- [88] J. Nagamatsu, N. Nakagawa, T. Muranaka, Y. Zenitani and J. Akimitsu: *Superconductivity at 39 K in magnesium diboride*, nature, 410(6824):63–64, 2001.
- [89] Z. Q. Ma and Y. C. Liu: *Low-temperature synthesis of MgB₂ superconductors*, International Materials Reviews, 56(5-6):267–286, 2011.
- [90] G. Grasso, A. Malagoli, M. Modica, A. Tumino, C. Ferdeghini, A. S. Siri, C. Vignola, L. Martini, V. Previtalli and G. Volpini: *Fabrication and properties of monofilamentary MgB₂ superconducting tapes*, Superconductor Science and Technology, 16(2):271–275, 2003.
- [91] A. Malagoli, V. Braccini, N. Scati, S. Roncallo, A. S. Siri and G. Grasso: *Fabrication and superconducting properties of powder-in-tube processed MgB₂ tapes*, Physica C: Superconductivity, 372-376:1245–1247, 2002.
- [92] M. D. Sumption, X. Peng, E. Lee, M. Tomsic and E. W. Collings: *Transport Current in MgB₂ based Superconducting Strand at 4.2 K and Self-Field*, arXiv preprint cond-mat/0102441, 2001.
- [93] Y. Feng, Y. Zhao, A. K. Pradhan, L. Zhou, P. X. Zhang, X. H. Liu, P. Ji, S. J. Du, C. F. Liu, Y. Wu and N. Koshizuka: *Fabrication and superconducting properties of MgB₂ composite wires by the PIT method*, Superconductor Science and Technology, 15(1):12–15, 2002.
- [94] B. A. Glowacki, M. Majoros, M. Vickers, J. E. Evetts, Y. Shi and I. McDougall: *Superconductivity of powder-in-tube MgB₂ wires*, Superconductor Science and Technology, 14(4):193–199, 2001.
- [95] H. Kumakura, A. Matsumoto, H. Fujii and K. Togano: *High transport critical current density obtained for powder-in-tube-processed MgB₂ tapes and wires using stainless steel and Cu–Ni tubes*, Applied Physics Letters, 79(15):2435–2437, 2001.
- [96] B. Brunner: *MgB₂ Wires Made by Diffusion Method and Their Properties*, PhD thesis, Slovak University of Technology, Bratislava, Slovakia, 2016.
- [97] J. M. Hur, K. Togano, A. Matsumoto, H. Kumakura, H. Wada and K. Kimura: *Fabrication of high-performance MgB₂ wires by an internal Mg diffusion process*, Superconductor Science and Technology, 21(3):032001, 2008.
- [98] G. Giunchi, S. Ceresara, G. Ripamonti, A. Di Zenobio, S. Rossi, S. Chiarelli, M. Spadoni, R. Wesche and P. L. Bruzzone: *High performance new MgB₂ superconducting hollow wires*, Superconductor Science and Technology, 16(2):285–291, 2003.

-
- [99] C. Buzea and T. Yamashita: *Review of the superconducting properties of MgB₂*, Superconductor Science and Technology, 14(11):R115–R146, 2001.
- [100] E. Bauer, C. Paul, S. Berger, S. Majumdar, H. Michor, M. Giovannini, A. Saccone and A. Bianconi: *Thermal conductivity of superconducting MgB₂*, Journal of Physics: Condensed Matter, 13(22):L487, 2001.
- [101] E. S. Drexler, N. J. Simon and R. P. Reed: *Properties of Copper and Copper Alloys at Cryogenic Temperatures: Final report*, National Institute of Standards and Technology, PB-92-172766/XAB, NIST/MONO-177, 1992.
- [102] P. Eckels: *CryoComp Rapid Cryogenic Design: 98 Materials in Properties Database*, CryoComp Rapid Design.
- [103] J. E. Jensen, W. A. Tuttle, R. B. Stewart, H. Brechna and A. G. Prodell: *Brookhaven National Laboratory selected cryogenic data notebook: Volume 1, Sections I-IX*, Brookhaven National Laboratory, BNL-10200-R (Vol. 1), 1980.
- [104] J. H. Devletian and M. J. Sullivan: *Flux Cored Arc Welding of CuNi 90/10 Piping with CuNi 70/30 Filler Metal*, National Shipbuilding Research Program, 2006.
- [105] R. Linz, A. Bouley, R. Klaffky and D. Damon: *The electrical and thermal conductivities of Cu-4, 10, and 20 at.% Ni from 1-25 K*, IEEE Transactions on Magnetics, 11(2):305–308, 1975.
- [106] Special Metals Corporation: *MONEL alloy 400*, 2005.
- [107] J. E. Campbell, E. A. Eldridge and J. K. Thompson: *Handbook on materials for superconducting machinery*, Battelle Columbus Laboratories, MCIC-HB-04, 1974.
- [108] National Research Council: *Opportunities in high magnetic field science*, National Academies Press, Washington, U.S.A., 2005.
- [109] A. Gurevich, S. Patnaik, V. Braccini, K. H. Kim, C. Mielke, X. Song, L. D. Cooley, S. D. Bu, D. M. Kim, J. H. Choi, L. J. Belenky, J. Giencke, M. K. Lee, W. Tian, X. Q. Pan, A. Siri, E. E. Hellstrom, C. B. Eom and D. C. Larbalestier: *Very high upper critical fields in MgB₂ produced by selective tuning of impurity scattering*, Superconductor Science and Technology, 17(2):278–286, 2004.
- [110] M. Lao, J. Hänisch, S. Kauffmann-Weiss, R. Gehring, H. Fillinger, A. Drechsler and B. Holzapfel: *High current variable temperature electrical characterization system for superconducting wires and tapes with continuous sample rotation in a split coil magnet*, Review of Scientific Instruments, 90(1):015106, 2019.
- [111] Y. B. Kim, C. F. Hempstead and A. R. Strnad: *Flux-Flow Resistance in Type-II Superconductors*, Physical Review, 139(4A):A1163–A1172, 1965.

- [112] M. Hanna, H. Fang, Y. X. Zhou, M. Alessandrini, P. T. Putman and K. Salama: *Mechanical properties of superconducting MgB₂ wire*, Journal of Materials Processing Technology, 181(1-3):44–47, 2007.
- [113] P. Kováč, L. Kopera, J. Kováč, T. Melišek, W. Haessler, D. Wang and Y. Ma: *Current densities and strain tolerances of filamentary MgB₂ wires made by an internal Mg diffusion process*, Superconductor Science and Technology, 32(9):095006, 2019.
- [114] P. Alknes, M. Hagner, R. Bjoerstad, C. Scheuerlein, B. Bordini, M. Sugano, J. Hudspeth and A. Ballarino: *Mechanical Properties and Strain-Induced Filament Degradation of Ex Situ and In Situ MgB₂ Wires*, IEEE Transactions on Applied Superconductivity, 26(3):1–5, 2016.
- [115] P. Kováč, I. Hušek, T. Melišek, M. Kulich and L. Kopera: *Bending strain tolerance of MgB₂ superconducting wires*, Superconductor Science and Technology, 29(4):045002, 2016.
- [116] P. Kováč, I. Hušek, T. Melišek, L. Kopera and M. Reissner: *Stainless steel reinforced multi-core MgB₂ wire subjected to variable deformations, heat treatments and mechanical stressing*, Superconductor Science and Technology, 23(6):065010, 2010.
- [117] M. P. Oomen: *AC loss in superconducting tapes and cables*, PhD thesis, University of Twente, Enschede, The Netherlands, 2000.
- [118] J. R. Reitz, F. J. Milford and R. W. Christy: *Foundations of Electromagnetic Theory*, Addison-Wesley, 4th edition, San Francisco, U.S.A., 2009.
- [119] M. N. Wilson: *Superconducting Magnets*, Clarendon Press, Oxford , U.K., 1983.
- [120] C. P. Bean: *Magnetization of Hard Superconductors*, Physical Review Letters, 8(6):250–253, 1962.
- [121] W. J. Carr Jr.: *AC Loss and Macroscopic Theory of Superconductors*, CRC Press, 2nd edition, London, U.K., 2001.
- [122] P. Dubots, A. Fevrier, J. Renard, J. Tavergnier, J. Goyer and H. G. Ky: *NbTi wires with ultra-fine filaments for 50 - 60 Hz use: Influence of the filament diameter upon losses*, IEEE Transactions on Magnetics, 21(2):177–180, 1985.
- [123] J. Lammeraner and M. Štafl: *Eddy currents*, CRC Press, Prague, Czech Republic, 1966.
- [124] F. W. J. Olver, D. W. Lozier, R. F. Boisvert and C. W. Clark: *The NIST handbook of mathematical functions*, Cambridge University Press, Cambridge, U.K., 2010.

-
- [125] K. V. Namjoshi and P. P. Biringer: *Low-frequency eddy-current loss estimation in long conductors by using the moment of inertia of cross sections*, IEEE Transactions on Magnetics, 24(5):2181–2185, 1988.
- [126] B. Seeber: *Handbook of Applied Superconductivity*, Institute of Physics Publishing, Bristol, U.K., 1998.
- [127] B. Turck: *Coupling losses in various outer normal layers surrounding the filament bundle of a superconducting composite*, Journal of Applied Physics, 50(8):5397, 1979.
- [128] B. Turck: *Effect of the respective positions of filament bundles and stabilizing copper on coupling losses in superconducting composites*, Cryogenics, 22(9):466–468, 1982.
- [129] F. Grilli, A. Chervyakov, V. Zermeno, A. Marian, G. Grasso, W. Goldacker and C. Rubbia: *Numerical modeling of MgB_2 conductors for high power AC transmission*, Physica C: Superconductivity, 504:167–171, 2014.
- [130] A. Stenvall, A. Korpela, R. Mikkonen and G. Grasso: *Quench analysis of MgB_2 coils with a ferromagnetic matrix*, Superconductor Science and Technology, 19(6):581–588, 2006.
- [131] P. C. Sen: *Principles of Electric Machines and Power Electronics*, John Wiley & Sons, 3rd edition, Chennai, India, 2014.
- [132] R. Brambilla, F. Grilli and L. Martini: *Development of an edge-element model for AC loss computation of high-temperature superconductors*, Superconductor Science and Technology, 20(1):16–24, 2006.
- [133] Y. B. Kim, C. F. Hempstead and A. R. Strnad: *Critical Persistent Currents in Hard Superconductors*, Physical Review Letters, 9(7):306–309, 1962.
- [134] F. Grilli, E. Pardo, A. Stenvall, D. N. Nguyen, W. Yuan and F. Gömöry: *Computation of Losses in HTS Under the Action of Varying Magnetic Fields and Currents*, IEEE Transactions on Applied Superconductivity, 24(1):78–110, 2013.
- [135] L. Rostila, G. Grasso, E. Demenčík, A. Tumino, S. Brisigotti and P. Kováč: *Low field critical current density of titanium sheathed magnesium diboride wires*, Journal of Physics: Conference Series, 234(2):022029, 2010.
- [136] M. Costa, E. Martinez, C. Beduz, Y. Yang, F. Grilli, B. Dutoit, E. Vinot and P. Tixador: *3D modeling of coupling between superconducting filaments via resistive matrix in AC magnetic field*, IEEE Transactions on Applied Superconductivity, 13(2):3634–3637, 2003.
- [137] G. Escamez, F. Sirois, V. Lahtinen, A. Stenvall, A. Badel, P. Tixador, B. Ramdane, G. Meunier, R. Perrin-Bit and C.-E. Bruzek: *3-D Numerical Modeling of AC Losses in Multifilamentary MgB_2 Wires*, IEEE Transactions on Applied Superconductivity, 26(3):1–7, 2016.

- [138] F. Grilli, S. Stavrev, Y. LeFloch, M. Costa-Bouzo, E. Vinot, I. Klutsch, G. Meunier, P. Tixador and B. Dutoit: *Finite-Element Method Modeling of Superconductors: From 2-D to 3-D*, IEEE Transactions on Applied Superconductivity, 15(1):17–25, 2005.
- [139] E. Demenčík, A. Godfrin, V. M. R. Zermeno and F. Grilli: *Determination of I–V Curves of HTS Tapes From the Frequency-Dependent AC Transport Loss*, IEEE Transactions on Applied Superconductivity, 26(3):1–4, 2016.
- [140] A. Cubero, R. Navarro, P. Kováč, L. Kopera, M. Rindfleisch and E. Martínez: *Quench dynamics in MgB₂ Rutherford cables*, Superconductor Science and Technology, 31(4):045009, 2018.
- [141] J. Hartwig, B. Fraser, G. Brown, L. Kohlman, D. Koci, K. Hunker, C. Bowman, P. Schrum and D. Matten: *New Test Rig to Measure Alternating Current Losses of Both Low and High Critical Temperature Superconductors*, National Aeronautics and Space Administration, NASA/TM-2019-220046, 2019.
- [142] M. Corduan, M. Boll, R. Bause, M. P. Oomen, M. Filipenko and M. Noe: *Topology Comparison of Superconducting AC Machines for Hybrid Electric Aircraft*, IEEE Transactions on Applied Superconductivity, 30(2):1–10, 2020.
- [143] E. W. Lemmon, I. H. Bell, M. L. Huber and M. O. McLinden: *NIST Standard Reference Database 23: Reference Fluid Thermodynamic and Transport Properties-REFPROP, Version 10.0*, National Institute of Standards and Technology, 2018.
- [144] VDI e.V.: *VDI-Wärmeatlas*, Springer Vieweg, Berlin, 11th edition, 2013.
- [145] J. P. Lewis, J. H. Goodykoontz and J. F. Kline: *Boiling heat transfer to liquid hydrogen and nitrogen in forced flow*, National Aeronautics and Space Administration, NASA-TN-D-1314, 1962.
- [146] S. G. Kandlikar, V. K. Dhir, Y. Iida and R. H. Heist: *Handbook of Phase Change: Boiling and Condensation*, Taylor and Francis, first edition, Philadelphia, U.S.A., 1999.
- [147] G. Yadigaroglu and G. F. Hewitt: *Introduction to Multiphase Flow: Basic Concepts, Applications and Modelling*, Springer, Cham, Switzerland, 2018.
- [148] R. W. Lockart and R. C. Martinelli: *Proposed Correlation of Data for Isothermal Two-Phase, Two-Component Flow in Pipes*, Chemical Engineering Progress, 45(1):39–48, 1949.
- [149] D. R. MacFarlane: *An analytic study of the transient boiling of sodium in reactor coolant channels*, Argonne National Laboratory, Illinois, U.S.A., 1966.
- [150] T. L. Bergman, F. P. Incropera, D. B. Dewitt and A. S. Lavine: *Fundamentals of Heat and Mass Transfer*, John Wiley & Sons, 4th edition, New York, U.S.A., 1996.

-
- [151] DuPont Films: *Corona Resistant Kapton CR Takes Electrical Insulation Design and Reliability to New Levels: Technical Information*, Dupont Co Technical Information, U.S.A., 1996.
- [152] D. L. Rule, D. R. Smith and L. L. Sparks: *Thermal conductivity of polypyromellitimide film with alumina filler particles from 4.2 to 300 K*, *Cryogenics*, 36(4):283–290, 1996.
- [153] D. J. Benford, T. J. Powers and S. H. Moseley: *Thermal conductivity of Kapton tape*, *Cryogenics*, 39(1):93–95, 1999.
- [154] F. Kurte: *Modell-Entwicklung zur Beschreibung der Wärmeleitfähigkeit von verpressten Litzen zur Optimierung von Wicklungen elektrischer Maschinen*, Master thesis, University of Erlangen–Nuremberg, Erlangen, Germany, 2018.
- [155] 3M: *Datenblatt 3M™ Novec™ 7500 High-Tech-Flüssigkeit: Datenblatt*, 3M Deutschland GmbH, Germany, 2014.
- [156] H. Woodson, Z. J. Stekly and E. Halas: *A Study of Alternators with Superconducting Field Windings: I - Analysis*, *IEEE Transactions on Power Apparatus and Systems*, PAS-85(3):264–274, 1966.
- [157] A. Rahideh and T. Korakianitis: *Analytical Magnetic Field Calculation of Slotted Brushless Permanent-Magnet Machines With Surface Inset Magnets*, *IEEE Transactions on Magnetics*, 48(10):2633–2649, 2012.
- [158] T. Lubin, S. Mezani and A. Rezzoug: *Exact Analytical Method for Magnetic Field Computation in the Air Gap of Cylindrical Electrical Machines Considering Slotting Effects*, *IEEE Transactions on Magnetics*, 46(4):1092–1099, 2010.
- [159] L. J. Wu, Z. Li, X. Huang, Y. Zhong, Y. Fang and Z. Q. Zhu: *A Hybrid Field Model for Open-Circuit Field Prediction in Surface-Mounted PM Machines Considering Saturation*, *IEEE Transactions on Magnetics*, 54(6):1–12, 2018.
- [160] A. Tessarolo: *Leakage Field Analytical Computation in Semiclosed Slots of Unsaturated Electric Machines*, *IEEE Transactions on Energy Conversion*, 30(2):431–440, 2015.
- [161] Y. Liu: *Design of a superconducting DC wind generator*, PhD thesis, Karlsruhe Institute of Technology, Karlsruhe, Germany, 2018.
- [162] M. H. Rashid: *Power electronics handbook*, Butterworth-Heinemann, 4th edition, U.S.A., 2017.
- [163] G. Aubert, J. F. Jacquinet and D. Sakellariou: *Eddy current effects in plain and hollow cylinders spinning inside homogeneous magnetic fields: Application to magnetic resonance*, *The Journal of chemical physics*, 137(15):154201, 2012.

- [164] S. Jumayev, A. Borisavljevic, K. Boynov, E. A. Lomonova and J. Pyrhönen: *Analysis of rotor eddy current losses in slotless high-speed permanent magnet machines*, 2014 16th European Conference on Power Electronics and Applications, 1–10, 2014.
- [165] A. P. Boresi and R. J. Schmidt: *Advanced mechanics of materials*, John Wiley & Sons, 6th edition, New York, U.S.A., 2003.
- [166] M. R. Eslami, R. B. Hetnarski, J. Ignaczak, N. Noda, N. Sumi and Y. Tanigawa: *Theory of Elasticity and Thermal Stresses: Explanations, Problems and Solutions*, Springer, Dordrecht, The Netherlands, 2013.
- [167] Siemens AG: *Press-fit model of a sleeve*, Internal document, Munich, Germany, 2018.
- [168] D. Gleich and R. Weyl: *Apparatelemente: Praxis der sicheren Auslegung*, Springer-Verlag, Berlin, Germany, 2006.
- [169] Verband der TÜV e.V.: *AD 2000-Code B 0: Design of pressure vessels*, Beuth Verlag GmbH, Berlin, Germany, 2014.
- [170] Verband der TÜV e.V.: *AD 2000-Code B 1: Cylindrical and spherical shells subjected to internal overpressure*, Beuth Verlag GmbH, Berlin, Germany, 2000.
- [171] Verband der TÜV e.V.: *AD 2000-Code B 6: Cylindrical shells subjected to external overpressure*, Beuth Verlag GmbH, Berlin, Germany, 2006.
- [172] E. J. Hearn: *Mechanics of Materials 2: An Introduction to the Mechanics of Elastic and Plastic Deformation of Solids and Structural Materials*, Butterworth-Heinemann, 3rd edition, Oxford, U.K., 2001.
- [173] Z. Shen, M. D. Ainslie, A. M. Campbell and D. A. Cardwell: *Computation of the Field in an Axial Gap, Trapped-Flux Type Superconducting Electric Machine*, IEEE Transactions on Applied Superconductivity, 25(3):1–5, 2015.
- [174] J. H. Durrell, A. R. Dennis, J. Jaroszynski, M. D. Ainslie, K. G. B. Palmer, Y.-H. Shi, A. M. Campbell, J. Hull, M. Strasik, E. E. Hellstrom and D. A. Cardwell: *A trapped field of 17.6 T in melt-processed, bulk Gd-Ba-Cu-O reinforced with shrink-fit steel*, Superconductor Science and Technology, 27(8):082001, 2014.
- [175] S. Gruss, G. Fuchs, G. Krabbes, P. Verges, G. Stöver, K.-H. Müller, J. Fink and L. Schultz: *Superconducting bulk magnets: Very high trapped fields and cracking*, Applied Physics Letters, 79(19):3131–3133, 2001.
- [176] T. Nakamura, Y. Itoh, M. Yoshikawa, T. Oka and J. Uzawa: *Development of a superconducting magnet for nuclear magnetic resonance using bulk high-temperature superconducting materials*, Concepts in Magnetic Resonance Part B: Magnetic Resonance Engineering, 31B(2):65–70, 2007.

-
- [177] J. Ogawa, M. Iwamoto, K. Yamagishi, O. Tsukamoto, M. Murakami and M. Tomita: *Influence of AC external magnetic field perturbation on trapped magnetic field in HTS bulk*, Physica C: Superconductivity, 386:26–30, 2003.
- [178] T. Hlásek and V. Plecháček: *Trapped Field in Different Shapes of RE-Ba-Cu-O Single Grains for the Use in Production of Superconducting Bearings*, IEEE Transactions on Applied Superconductivity, 25(3):1–4, 2015.
- [179] R. Bause, M. D. Ainslie, M. Corduan, M. Boll, M. Filipenko and M. Noe: *Electromagnetic design of a superconducting electric machine with bulk HTS material*, arXiv:1903.08906, 2019.
- [180] M. Zhang, W. Wang, Y. R. Chen and T. Coombs: *Design Methodology of HTS Bulk Machine for Direct-Driven Wind Generation*, IEEE Transactions on Applied Superconductivity, 22(3):5201804, 2012.
- [181] P. B. Osgood: *Lecture Notes for EE 261 the Fourier Transform and Its Applications*, Electrical Engineering Department, Stanford University, 2014.
- [182] K. Halbach: *Design of permanent multipole magnets with oriented rare earth cobalt material*, Nuclear Instruments and Methods, 169(1):1–10, 1980.
- [183] Z. Q. Zhu and D. Howe: *Halbach permanent magnet machines and applications: A review*, IEE Proceedings - Electric Power Applications, 148(4):299, 2001.
- [184] S.-M. Jang, S.-S. Jeong, D.-W. Ryu and S.-K. Choi: *Design and analysis of high speed slotless PM machine with Halbach array*, IEEE Transactions on Magnetics, 37(4):2827–2830, 2001.
- [185] Y. Liu, M. Noe, J. Ou, P. Breining, M. Veigel and M. Doppelbauer: *Measurement of Magnetic Materials at Room and Cryogenic Temperature for Their Application to Superconducting Wind Generators*, IEEE Transactions on Applied Superconductivity, 28(3):1–6, 2018.
- [186] Z. Q. Zhu, D. Howe, E. Bolte and B. Ackermann: *Instantaneous magnetic field distribution in brushless permanent magnet DC motors. I. Open-circuit field*, IEEE Transactions on Magnetics, 29(1):124–135, 1993.
- [187] Z. P. Xia, Z. Q. Zhu and D. Howe: *Analytical Magnetic Field Analysis of Halbach Magnetized Permanent-Magnet Machines*, IEEE Transactions on Magnetics, 40(4):1864–1872, 2004.
- [188] G. Bertotti, G. Di Schino, A. Ferro Milone and F. Fiorillo: *On the effect of grain size on magnetic losses of 3% non-oriented SiFe*, Le Journal de Physique Colloques, 46(6):C6–385–C6–388, 1985.
- [189] G. Bertotti: *Physical interpretation of eddy current losses in ferromagnetic materials. II. Analysis of experimental results*, Journal of Applied Physics, 57(6):2118–2126, 1985.

- [190] A. Krings and J. Soulard: *Overview and Comparison of Iron Loss Models for Electrical Machines*, Journal of Electrical Engineering, 10:162–169, 2010.
- [191] Vacuumschmelze: *Soft magnetic Cobalt-iron Alloys: Vacoflux and Vacodur: Datasheet*, Vacuumschmelze GmbH & Co. KG, Hanau, Germany, 2016.
- [192] W. R. Candlers: *Berechnung von Eisenverluste: Physikalisch Basierter Ansatz Nach Bertottis Theorie*, Technical University of Braunschweig, Braunschweig, Germany, 2011.
- [193] D. Schröder: *Elektrische Antriebe - Regelung von Antriebssystemen*, Springer-Verlag, 2nd edition, Berlin, Heidelberg, Germany, 2015.
- [194] P. Weber: *Parametric Modelling of a Liquid Hydrogen Tank for Future Cryogenic Hybrid-Electric Short-Range Aircraft*, Master thesis, University of Stuttgart, Stuttgart, Germany, 2019.
- [195] ASTM D1655-20b: *Standard Specification for Aviation Turbine Fuels*, ASTM International, West Conshohocken, U.S.A., 2019.
- [196] R. D. McCarty, J. Hord and H. M. Roder: *Selected properties of hydrogen (engineering design data). Final report*, National Bureau of Standards, PB-81-211492, 1981.
- [197] G. D. Brewer: *Hydrogen Aircraft Technology*, CRC Press, 1st edition, Boca Roca, U.S.A., 1991.
- [198] C. Winnefeld, T. Kadyk, B. Bensmann, U. Krewer and R. Hanke-Rauschenbach: *Modelling and Designing Cryogenic Hydrogen Tanks for Future Aircraft Applications*, Energies, 11(1):105, 2018.
- [199] P. R. Sekaran, A. S. Gohardani, G. Doulgeris and R. Singh: *Liquid hydrogen tank considerations for turboelectric distributed propulsion*, Aircraft Engineering and Aerospace Technology, 86(1):67–75, 2013.
- [200] R. J. Walter and W. T. Chandler: *Influence of gaseous hydrogen on metals*, National Aeronautics and Space Administration, NASA-CR-124410, 1973.
- [201] I. H. Bell, J. Wronski, S. Quoilin and V. Lemort: *Pure and Pseudo-pure Fluid Thermophysical Property Evaluation and the Open-Source Thermophysical Property Library CoolProp*, Industrial & Engineering Chemistry Research, 53(6):2498–2508, 2014.
- [202] Airbus S.A.S.: *A321neo: Unbeatable fuel efficiency*, URL: <https://www.airbus.com/aircraft/passenger-aircraft/a320-family/a321neo.html>, 10.10.2019.
- [203] Airbus S.A.S.: *A321: Aircraft Characteristics Airport and Maintenance Planning*, Blagnac Cedex, France, 2020.

-
- [204] V. Bhaskara: *Analysis: A320neo vs. 737 MAX: Airbus is Leading (Slightly) - Part 2*, Airways News, URL: <https://airinsight.com/wp-content/uploads/2016/02/airwaysnews02052016.pdf>, 02.05.2016.
- [205] Airbus S.A.S.: *Figures Family: April 2019 Edition*, Airbus Print Centre, France, 2019.
- [206] A. Sgueglia: *Methodology for sizing and optimising a Blended Wing-Body with distributed electric ducted fans*, PhD thesis, University of Toulouse, Toulouse, France, 2019.
- [207] Jeppesen: *A&P technician powerplant textbook*, Jeppesen, Englewood, U.S.A., 2011.
- [208] K. Hünecke: *Jet engines: Fundamentals of Theory, Design and Operation*, Motorbooks International, 6th edition, Osceola, U.S.A., 2003.
- [209] Pratt & Whitney: *Pratt & Whitney GTF Engine*, URL: <http://prattwhitney.com/products-and-services/products/commercial-engines/Pratt-and-Whitney-GTF-Engine>, 04.05.2020.
- [210] J. Kurzke: *Fundamental Differences Between Conventional and Geared Turbofans*, Proceedings of the ASME Turbo Expo 2009: Power for Land, Sea, and Air, 48821:145–153, 2009.
- [211] Pratt & Whitney: *Geared Turbofan - PW1100G-JM*, 2018.
- [212] M. Koppe: *Kraftstoffverbräuche von Turbofan, Propfan und Turboprop im Vergleich*, PhD thesis, Hamburg University of Applied Sciences, Hamburg, Germany, 2012.
- [213] R. Blockley, W. Shyy, R. Agarwal, F. Collier, A. Schaefer and A. Seabridge: *Green Aviation*, John Wiley & Sons, 2016.
- [214] Pratt & Whitney: *Geared Turbofan - PW1100G-JM*, 2018.
- [215] W. J. G. Bräunling: *Flugzeugtriebwerke: Grundlagen, Aero-Thermodynamik, ideale und reale Kreisprozesse, thermische Turbomaschinen, Komponenten, Emissionen und Systeme*, Springer Vieweg, 4. Auflage, Berlin, Deutschland, 2015.
- [216] A. Epstein: *The Pratt & Whitney PurePower Geared Turbofan Engine*, Academie de l’Air et de l’Espace, Paris, France, 2015.
- [217] H. Mensen: *Planung, Anlage und Betrieb von Flugplätzen*, Springer-Verlag, 2. Auflage, Heidelberg, Deutschland, 2013.
- [218] L. N. Bortnikov: *Combustion of a gasoline-hydrogen-air mixture in a reciprocating internal combustion engine cylinder and determining the optimum gasoline-hydrogen ratio*, Combustion, Explosion, and Shock Waves, 43(4):378–383, 2007.

- [219] Y. M. Annushkin and G. F. Maslov: *Efficiency of combustion of hydrogen-kerosene fuel in a straight duct*, Combustion, Explosion, and Shock Waves, 21(3):297–298, 1985.
- [220] T. Lauf, M. Memmler and S. Schneider: *Emissionsbilanz erneuerbarer Energieträger: Bestimmung der vermiedenen Emissionen im Jahr 2018*, Umweltbundesamt, Dessau-Roßlau, Deutschland, 2019.
- [221] O. Edenhofer: *Climate change 2014: Mitigation of climate change : Working Group III contribution to the Fifth assessment report of the Intergovernmental Panel on Climate Change*, Cambridge University Press, Cambridge, U.K., 2014.
- [222] M. Kopp, D. Coleman, C. Stiller, K. Scheffer, J. Aichinger and B. Scheppat: *Energiepark Mainz: Technical and economic analysis of the worldwide largest Power-to-Gas plant with PEM electrolysis*, International Journal of Hydrogen Energy, 42(19):13311–13320, 2017.
- [223] A. Tremel: *Electricity-based Fuels*, Springer International Publishing, Cham, 2018.
- [224] D. O. Berstad, J. H. Stang and P. Neksa: *Large-scale hydrogen liquefier utilizing mixed-refrigerant pre-cooling*, International Journal of Hydrogen Energy, 35(10):4512–4523, 2010.
- [225] S. Krasae-in: *Efficient Hydrogen Liquefaction Processes*, PhD thesis, Norwegian University of Science and Technology, Trondheim, Norway, 2013.
- [226] J. R. Davis and ASM International: *Properties and Selection: Nonferrous Alloys and Special-purpose Materials*, ASM International, Materials Park, Ohio, 6. print edition, 2000.
- [227] Department of Defense of the United States of America: *MIL-HDBK-5H Metallic Materials and Elements for Aerospace Vehicle Structures*, 3-244, 1998.
- [228] Vacuumschmelze: *Rare Earth Permanent Magnets: Vacodym, VACOMax*, Vacuumschmelze GmbH & Co. KG, 2014.
- [229] C. D. Sanabria von Walter: *Design of high-torque-density synchronous drives for propulsion of rotary-wing aircraft*, PhD thesis, Delft University of Technology, Delft, The Netherlands, 2016.
- [230] J.-S. Wang and S.-Y. Wang: *High temperature superconducting magnetic levitation*, De Gruyter and Peking University Press, Berlin and Beijing, 2018.
- [231] Special Metals Corporation: *INCONEL Alloy 718*, 2007.
- [232] A. Zingoni: *Insights and Innovations in Structural Engineering, Mechanics and Computation*, Proceedings of the Sixth International Conference on Structural Engineering, Mechanics and Computation, CRC Press, Cape Town, South Africa, 2016.

-
- [233] M. J. Donachie: *Titanium: A technical guide*, ASM International, Materials Park, Second Edition, 2000.
- [234] W. M. Robertson: *Hydrogen permeation and diffusion in inconel 718 and incoloy 903*, Metallurgical Transactions A, 8(11):1709–1712, 1977.
- [235] Theva Dünnschichttechnik: *Theva Pro-Line HTS Wire*, THEVA Pro-Line, Theva Dünnschichttechnik GmbH, 2020.
- [236] S. C. Wimbush and N. M. Strickland: *A Public Database of High-Temperature Superconductor Critical Current Data*, IEEE Transactions on Applied Superconductivity, 27(4):1–5, 2017.
- [237] S. Kubo, K. Okubo and T. Fujii: *Characteristic behaviors of CFRP and GFRP at cryogenic temperature under static and cyclic loadings*, WIT Transactions on The Built Environment, 85:179–188, 2006.
- [238] S. J. Otten: *Characterisation of REBCO Roebel cables*, PhD thesis, Karlsruhe Institute of Technology, Karlsruhe, Germany, 2019.
- [239] M. P. Oomen: *HTS rotor coils and joints for high power density rotating machines*, European Conference on Applied Superconductivity 2019, Glasgow, U.K., 03.09.2019.
- [240] T. Sano, Y. Kimura, D. Sugyo, K. Yamaguchi, M. Izumi, T. Ida, H. Sugimoto and M. Miki: *Pulsed-field magnetization study for Gd123 bulk HTS cooled with condensed neon for axial-gap type synchronous motor*, Journal of Physics: Conference Series, 97:012194, 2008.
- [241] Z. Huang, H. S. Ruiz, Y. Zhai, J. Geng, B. Shen and T. A. Coombs: *Study of the Pulsed Field Magnetization Strategy for the Superconducting Rotor*, IEEE Transactions on Applied Superconductivity, 26(4):1–5, 2016.
- [242] M. D. Ainslie and H. Fujishiro: *Corrigendum: Modelling of bulk superconductor magnetisation*, Superconductor Science and Technology, 30(3):039501, 2017.
- [243] M. Watasaki, M. Miki, B. Felder, K. Tsuzuki, R. Sato, S. Kase, M. Izumi and T. Ida: *Trapped Magnetic Flux of Bulk HTS Magnets in the External AC Magnetic Field at Low Temperatures*, IEEE Transactions on Applied Superconductivity, 23(3):8201604, 2013.
- [244] A. Patel, A. Baskys, S. C. Hopkins, V. Kalitka, A. Molodyk and B. A. Glowacki: *Pulsed-Field Magnetization of Superconducting Tape Stacks for Motor Applications*, IEEE Transactions on Applied Superconductivity, 25(3):1–5, 2015.
- [245] J. W. Chapman, S. L. Schnulo and M. P. Nitzsche: *Development of a Thermal Management System for Electrified Aircraft*, AIAA Scitech 2020 Forum, 0545, 2020.

- [246] B. G. Marchionini, Y. Yamada, L. Martini and H. Ohsaki: *High-Temperature Superconductivity: A Roadmap for Electric Power Sector Applications, 2015–2030*, IEEE Transactions on Applied Superconductivity, 27(4):1–7, 2017.
- [247] C. J. Marek, T. D. Smith and K. Kundu: *Low Emission Hydrogen Combustors for Gas Turbines Using Lean Direct Injection*, 41st AIAA/ASME/SAE/ASEE Joint Propulsion Conference & Exhibit, Tucson, U.S.A., 2012.
- [248] M. D. Ainslie, Y. Jiang, W. Xian, Z. Hong, W. Yuan, R. Pei, T. J. Flack and T. A. Coombs: *Numerical analysis and finite element modelling of an HTS synchronous motor*, Physica C: Superconductivity and its Applications, 470(20):1752–1755, 2010.
- [249] S. Fukuda, K. Yun, M. Iwakuma, S. Miura, S. Sato, K. Yoshida, A. Tomioka, M. Konno and T. Izumi: *Design Study of 2-MW Fully Superconducting Synchronous Motors*, IEEE Transactions on Applied Superconductivity, 28(4):1–6, 2018.
- [250] F. Grilli and A. Kario: *How filaments can reduce AC losses in HTS coated conductors: A review*, Superconductor Science and Technology, 29(8):083002, 2016.
- [251] F. Liang, S. Venuturumilli, H. Zhang, M. Zhang, J. Kvitkovic, S. Pamidi, Y. Wang and W. Yuan: *A finite element model for simulating second generation high temperature superconducting coils/stacks with large number of turns*, Journal of Applied Physics, 122(4):043903, 2017.
- [252] H. Zhang, M. Zhang and W. Yuan: *An efficient 3D finite element method model based on the T–A formulation for superconducting coated conductors*, Superconductor Science and Technology, 30(2):024005, 2017.
- [253] E. Berrospe-Juarez, V. M. R. Zermeño, F. Trillaud and F. Grilli: *Real-time simulation of large-scale HTS systems: Multi-scale and homogeneous models using the T–A formulation*, Superconductor Science and Technology, 32(6):065003, 2019.
- [254] E. Pardo, L. Shuo, F. Grilli, Y. Liu, T. Benkel, S. Wolfstädler, E. Berberich and T. Reis: *AC loss in the distributed stator winding of a 1 MW motor for aviation*, European Conference on Applied Superconductivity 2019, Glasgow, U.K., 03.09.2019.
- [255] G. P. Malik and U. Malik: *Thermal Conductivity of Superconducting MgB₂*, World Journal of Condensed Matter Physics, 04(01):39–47, 2014.
- [256] J. N. Schwerg: *Numerical calculation of transient field effects in quenching superconducting magnets*, PhD thesis, Technical University of Berlin, Berlin, Germany, 2010.
- [257] L. A. Hall: *Survey of Electrical Resistivity Measurements on 16 Pure Metals in the Temperature Range 0 to 273 K*, US Department of Commerce, National Bureau of Standards, 365, 1968.

-
- [258] E. D. Marquardt, J. P. Le and R. Radebaugh: *Cryogenic Material Properties Database*, Cryocoolers 11, 681–687, 2002.
- [259] H.-J. Bartsch and M. Sachs: *Taschenbuch mathematischer Formeln für Ingenieure und Naturwissenschaftler*, Fachbuchverlag Leipzig im Carl Hanser Verlag, München, 24. überarbeitete Auflage, 2018.
- [260] C. Lewis and J. Müller: *A Direct Drive Wind Turbine HTS Generator*, 2007 IEEE Power Engineering Society General Meeting, 1–8, 2007.
- [261] A. B. Abrahamsen, B. B. Jensen, E. Seiler, N. Mijatovic, V. M. Rodriguez-Zermeno, N. H. Andersen and J. Østergård: *Feasibility study of 5 MW superconducting wind turbine generator*, Physica C: Superconductivity and its applications, 471(21-22):1464–1469, 2011.
- [262] G. Snitchler, B. Gamble, C. King and P. Winn: *10 MW Class Superconductor Wind Turbine Generators*, IEEE Transactions on Applied Superconductivity, 21(3):1089–1092, 2011.
- [263] R. Fair, W. Stautner, M. Douglass, R. Rajput-Ghoshal, M. Moscinski, P. Riley, D. Wagner, J. Kim, S. Hou, F. Lopez, K. Haran, J. Bray, T. Laskaris, J. Rochford and R. Duckworth: *Superconductivity for Large Scale Wind Turbines*, Applied Superconductivity Conference 2012, Portland, U.S.A., 2012.
- [264] S. S. Kalsi: *Superconducting Wind Turbine Generator Employing MgB₂ Windings Both on Rotor and Stator*, IEEE Transactions on Applied Superconductivity, 24(1):47–53, 2014.
- [265] A. B. Abrahamsen, N. Magnusson, D. Liu, E. Stehouwer, B. Hendriks and H. Polinder: *Design study of a 10 MW MgB₂ superconductor direct drive wind turbine generator*, European Wind Energy Conference & Exhibition 2014, 2014.
- [266] A. Kim, K.-M. Kim, H. Park, G.-H. Kim, T.-J. Park, M. Park, S. Kim, S. Lee, H. Ha, S. Yoon and H. Lee: *Performance Analysis of a 10-kW Superconducting Synchronous Generator*, IEEE Transactions on Applied Superconductivity, 25(3):1–4, 2015.
- [267] H. Karmaker, D. Sarandria, M. T. Ho, J. Feng, D. Kulkarni and G. Rupertus: *High-Power Dense Electric Propulsion Motor*, IEEE Transactions on Industry Applications, 51(2):1341–1347, 2015.
- [268] H. Yamasaki and M. Furuse: *Feasibility study project to realize the merits of 10 MW class superconducting wind turbine generators*, Cryogenic Engineering Conference and International Cryogenic Materials Conference 2015, Tucson, U.S.A., 01.07.2015.
- [269] J. Wang, R. Qu, Y. Tang, Y. Liu, B. Zhang, J. He, Z. Zhu, H. Fang and L. Su: *Design of a Superconducting Synchronous Generator With LTS Field Windings for 12 MW Offshore Direct-Drive Wind Turbines*, IEEE Transactions on Industrial Electronics, 63(3):1618–1628, 2016.

- [270] H.-J. Sung, M. Park, B.-S. Go and I.-K. Yu: *A study on the required performance of a 2G HTS wire for HTS wind power generators*, Superconductor Science and Technology, 29(5):054001, 2016.
- [271] H. J. Sung, R. A. Badcock, Z. Jiang, J. Choi, M. Park and I. K. Yu: *Design and Heat Load Analysis of a 12 MW HTS Wind Power Generator Module Employing a Brushless HTS Exciter*, IEEE Transactions on Applied Superconductivity, 26(4):1–4, 2016.
- [272] X. Song, C. Bührer, P. Brutsaert, J. Krause, A. Ammar, J. Wiezoreck, J. Hansen, A. V. Rebsdorf, M. Dhallé, A. Bergen, T. Winkler, S. Wessel, M. ter Brake, J. Kellers, H. Putz, M. Bauer, H. Kylling, H. Boy and E. Seitz: *Designing and Basic Experimental Validation of the World’s First MW-Class Direct-Drive Superconducting Wind Turbine Generator*, IEEE Transactions on Energy Conversion, 34(4):2218-2225, 2019.
- [273] A. Bergen, R. Andersen, M. Bauer, H. Boy, M. ter Brake, P. Brutsaert, C. Bührer, M. Dhallé, J. Hansen, H. ten Kate, J. Kellers, J. Krause, E. Krooshoop, C. Kruse, H. Kylling, M. Pilas, H. Pütz, A. Rebsdorf, M. Reckhard, E. Seitz, H. Springer, X. Song, N. Tzabar, S. Wessel, J. Wiezoreck, T. Winkler and K. Yagotyntsev: *Design and in-field testing of the world’s first ReBCO rotor for a 3.6 MW wind generator*, Superconductor Science and Technology, 32(12):125006, 2019.
- [274] K. Kails, Q. Li and M. Mueller: *Mass reduction of superconducting power generators for large wind turbines*, The Journal of Engineering, 2019(17):3972–3975, 2019.
- [275] T. A. Keim, T. E. Laskaris, J. A. Fealey and P. A. Rios: *Design and Manufacture of a 20 MVA Superconducting Generator*, IEEE Transactions on Power Apparatus and Systems, PAS-104(6):1474–1483, 1985.
- [276] J. H. Parker and R. A. Towne: *Superconducting Generator Design: Final Report*, Westinghouse Electric Corporation, Large Rotating Apparatus Division, 1977.
- [277] J. Sabrie and J. Goyer: *Technical overview of the French program*, IEEE Transactions on Magnetics, 19(3):529–532, 1983.
- [278] K. Yamaguchi, M. Takahashi, R. Shiobara, T. Taniguchi, H. Tomeoku, M. Sato, H. Sato, Y. Chida, M. Ogihara, R. Takahashi and H. Kusafuka: *70 MW class superconducting generator test*, IEEE Transactions on Applied Superconductivity, 9(2):1209–1212, 1999.
- [279] S. S. Kalsi: *Development status of superconducting rotating machines*, 2002 IEEE Power Engineering Society Winter Meeting, Conference Proceedings (Cat. No.02CH37309), 401–403, 2002.

-
- [280] J. A. Urbahn, R. A. Ackermann, X. Huang, E. T. Laskaris, K. Sivasubramaniam and A. Steinbach: *The Thermal Performance of a 1.5 MVA HTS Generator*, AIP Conference Proceedings, 710(1):849–858, 2004.
- [281] S. S. Kalsi, D. Madura, T. MacDonald, M. Ingram and I. Grant: *Operating Experience of Superconductor Dynamic Synchronous Condenser*, 2005/2006 IEEE/PES Transmission and Distribution Conference and Exhibition, 899–902, 2006.
- [282] G. Snitchler, B. Gamble and S. S. Kalsi: *The Performance of a 5 MW High Temperature Superconductor Ship Propulsion Motor*, IEEE Transactions on Applied Superconductivity, 15(2):2206–2209, 2005.
- [283] K. M. Schaubel, A. R. Langhorn, W. P. Creedon, N. W. Johanson, S. Sheynin and R. J. Thome: *Development of a Superconducting Magnet System for the ONR/General Atomics Homopolar Motor*, AIP Conference Proceedings, 823(1):1819–1826, 2006.
- [284] H. W. Neumüller, W. Nick, B. Wacker, M. Frank, G. Nerowski, J. Fraunhofer, W. Rządki and R. Hartig: *Advances in and prospects for development of high-temperature superconductor rotating machines at Siemens*, Superconductor Science and Technology, 19(3):114–117, 2006.
- [285] W. Nick, M. Frank, G. Klaus, J. Fraunhofer and H.-W. Neumüller: *Operational Experience With the World's First 3600 rpm 4 MVA Generator at Siemens*, IEEE Transactions on Applied Superconductivity, 17(2):2030–2033, 2007.
- [286] M. Frank, J. Fraunhofer, B. Gromoll, P. van Haßelt, W. Nick, G. Nerowski, H.-W. Neumüller, H.-U. Häfner and G. Thummes: *Thermosyphon Cooling System for the Siemens 400kW HTS Synchronous Machine*, AIP Conference Proceedings, 710(1):859–866, 2004.
- [287] M. Iwakuma, Y. Hase, T. Satou, A. Tomioka, M. Konno, Y. Iijima, T. Saitoh, Y. Yamada, T. Izumi and Y. Shiohara: *Production and Test of a REBCO Superconducting Synchronous Motor*, IEEE Transactions on Applied Superconductivity, 19(3):1648–1651, 2009.
- [288] K. Umemoto, K. Aizawa, M. Yokoyama, K. Yoshikawa, Y. Kimura, M. Izumi, K. Ohashi, M. Numano, K. Okumura, M. Yamaguchi, Y. Gocho and E. Kosuge: *Development of 1 MW-class HTS motor for podded ship propulsion system*, Journal of Physics: Conference Series, 234(3):032060, 2010.
- [289] W. Nick, M. Frank, P. Kummeth, J. J. Rabbers, M. Wilke and K. Schleicher: *Development and construction of an HTS rotor for ship propulsion application*, Journal of Physics: Conference Series, 234(3):032040, 2010.

- [290] B. Gamble, G. Snitchler and T. MacDonald: *Full Power Test of a 36.5 MW HTS Propulsion Motor*, IEEE Transactions on Applied Superconductivity, 21(3):1083–1088, 2011.
- [291] T. Yanamoto, M. Izumi, M. Yokoyama and K. Umemoto: *Electric Propulsion Motor Development for Commercial Ships in Japan*, Proceedings of the IEEE, 103(12):2333–2343, 2015.
- [292] K. Sato: *Research, Fabrication and Applications of Bi-2223 HTS Wires*, World Scientific Series in Applications of Superconductivity and Related Phenomena, World Scientific, 2016.
- [293] H. Moon, Y.-C. Kim, H.-J. Park, I.-K. Yu and M. Park: *An introduction to the design and fabrication progress of a megawatt class 2G HTS motor for the ship propulsion application*, Superconductor Science and Technology, 29(3):034009, 2016.
- [294] S. S. Kalsi: *Ship Propulsion Motor Employing Bi-2223 and MgB₂ Superconductors*, Kenichi Sato, Research, Fabrication and Applications of Bi-2223 HTS Wires, volume 1 of World scientific series in applications of superconductivity and related phenomena, 427–449, World Scientific, 2016.